Different manifestations of accretion onto compact objects

ACADEMISCH PROEFSCHRIFT

ter verkrijging van de graad van doctor
aan de Universiteit van Amsterdam
op gezag van de Rector Magnificus
prof. dr. D. C. van den Boom
ten overstaan van een door het college voor promoties
ingestelde commissie,
in het openbaar te verdedigen in the Aula der Universiteit
op woensdag 23 april 2008, te 10:00 uur.

door

Diego Altamirano

geboren te La Plata, Argentinië

Promotiecommissie:

Promotor:	Prof. dr. M. van der Klis
Overige leden:	Prof. dr. M. Méndez
	dr. R. Wijnands
	Prof. dr. E. P. J van den Heuvel
	Prof. dr. R. A. M. J. Wijers
	Prof. dr. H. B. van Linden van den Heuvell
	Prof. dr. W. Hermsen

Faculteit der Natuurwetenschappen, Wiskunde en Informatica

The research reported in this thesis was carried out at the Astronomical Institute "Anton Pannekoek", at the Universiteit van Amsterdam, The Netherlands.

A Nona y a Mamá,
a Tata y a Papá

Contents

1 Introduction

Insignificante, pero lo disimulo con elegancia

Juan Feu

In this thesis I discuss phenomena that occur in systems that are referred to as low–mass X-ray binaries. These systems emit radiation over a large range of wavelengths but here I focus only on the X-ray emission. In this chapter, I briefly explain what these systems are, I introduce some of the main phenomena that arise in them and I discuss the methods by which these systems are studied.

1.1 Low–Mass X-ray binaries

Most of the stars in our universe occur in binary systems, i.e., systems of two stars in orbit around a common center of mass. If one of the members of these systems is a compact object (neutron star or black hole), and the system components are sufficiently close to exchange matter causing them to become very bright in X-rays, then they are called X-ray binaries. Compact objects are formed by supernova explosions; I note, however, that it has also been suggested that neutron stars can be formed from the accretion–induced collapse of a white dwarf (Whelan & Iben 1973), and that black holes might be the result of the merger of two neutron stars (King 2006), events whose signature in terms of supernova phenomenology is uncertain.

X-ray binaries can be divided into high-mass X-ray binaries (HMXBs) and low-mass X-ray binaries (LMXBs) depending on the mass of the companion star. The companion to the X-ray source in HMXBs is a luminous star of spectral type O or B with mass typically larger than 10 $M_{\odot}$, necessarily belonging to a young stellar population as these types of stars do not live longer than about $\sim 10^7$ years. In LMXBs the companion is a faint star of mass lower than 1 $M_\odot$ and tends to belong to a much older stellar population, with ages that can be hundreds of millions of years.

In this thesis, I concentrate on the study of the LMXBs (see Figure 1.1 for an artist's impression) in which mass transfer from the companion star to the compact object is due to Roche-lobe overflow, i.e., material from the companion star that passes beyond the so called Roche-lobe radius flows onto the compact object. Since the Roche-lobe radius is a function only of the orbital separation and the masses of the two stars, the onset of Roche-lobe overflow requires that either the envelope of the companion star expands (due to stellar evolution), or that the binary separation shrinks (as a result of orbital angular momentum losses). In any case, due to conservation of angular momentum the gas cannot fall directly onto the compact object and so it spirals in, forming a rotating disk around the compact object. This process is called accretion and the disk is known as an *accretion disk*.

The most powerful phenomena we observe from LMXBs are directly related to these accretion disks, as a large amount of gravitational energy is released when the matter approaches the compact object. This causes the inner accretion disk to reach temperatures as high as 10^7 Kelvin and therefore to emit in (thermal) X-rays. So, the analysis of the X-ray emission from these sources is a fundamental tool we have to study the properties of compact objects and accretion disks. These sources become therefore, very good natural laboratories in which to test theories of gravity in extreme conditions (e.g. general relativity), and where to study physics of ultra-dense matter, in particular the equation of state (i.e., the mathematical description of the relations between temperature, pressure and density of matter) of neutron stars, where densities are thought to be higher than those in atomic nuclei.

1.2 Instrumentation and techniques

In this thesis I study low-mass X-ray binary systems by means of energy spectra and time variability analysis. The combination of these two methods has proven to be very useful in describing the X-ray behavior of LMXBs. Below, I briefly describe the instruments and techniques used.

1.2.1 The Rossi X-ray Timing Explorer

All the results presented in this thesis are based on data obtained with the *Rossi X-ray Timing Explorer* (*RXTE*, Bradt et al. 1993). It was launched

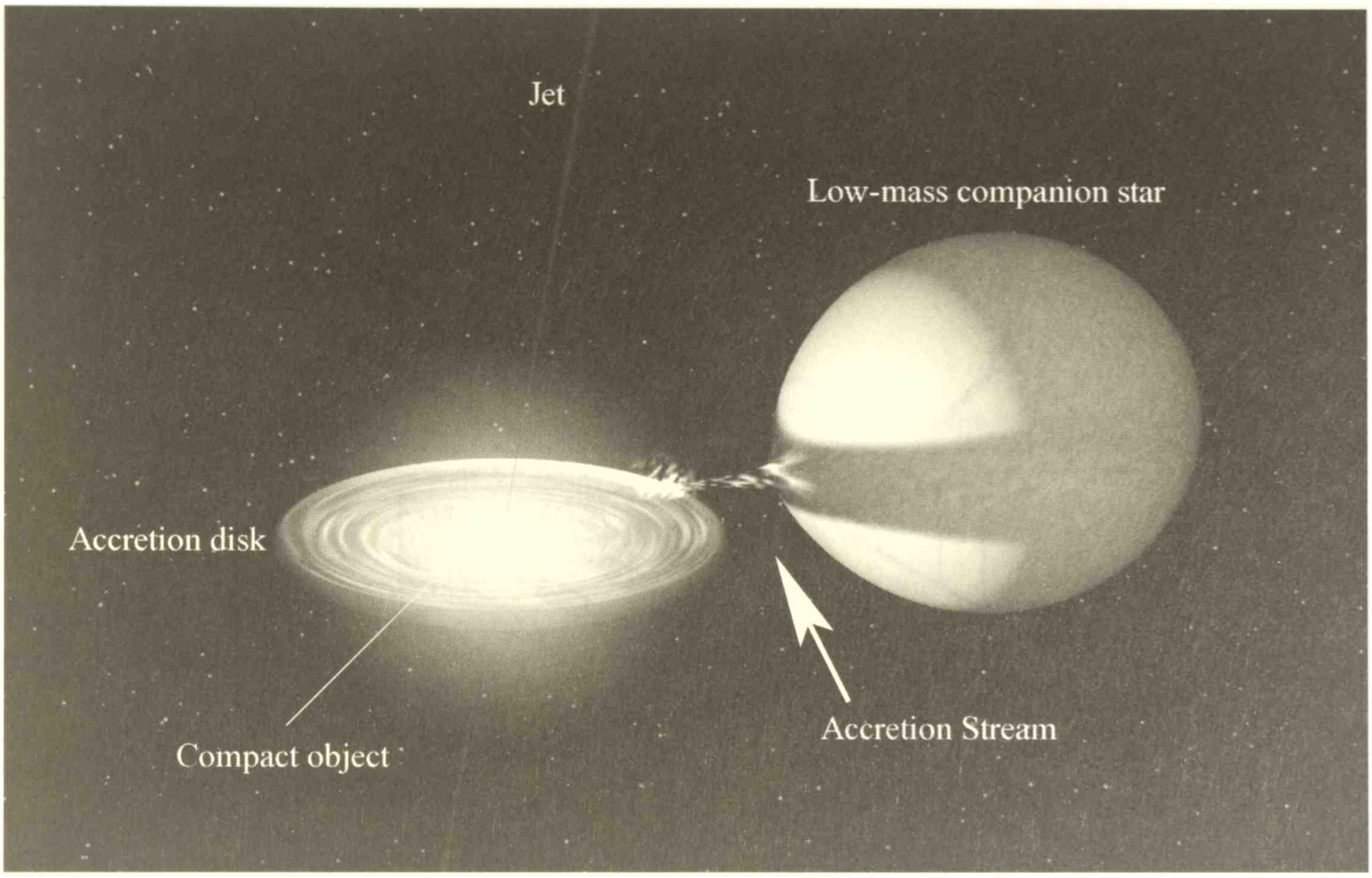

Figure 1.1: Artist's impression of a low-mass X-ray binary. The image was produced with the program BinSim (v0.8.1) developed by Rob Hynes.

on December 30^{th}, 1995 and, at the time this thesis goes to press, is still operating. Figure 1.2 shows a schematic view of the satellite.

There are three scientific instruments on board the satellite, namely the All Sky Monitor (ASM, Levine et al. 1996), the High Energy X-ray Timing Experiment (HEXTE, Gruber et al. 1996; Rothschild et al. 1998) and the Proportional Counter Array (PCA; Zhang et al. 1993; Jahoda et al. 2006).

The ASM observes ~80% of the sky each orbit with a spatial resolution of $3' \times 15'$, it operates in the 1.5–12 keV range and has a time resolution of 1/8 seconds. The ASM plays an important role in identifying state transitions and outbursts from transient sources, allowing us to trigger follow-up observations with other instruments within a few hours. The instrument also permits us to monitor the long-term intensity and behavior of the brightest X-ray sources (see, e.g., Chapters 4 & 8 and Figure 1.6 in this Chapter).

The HEXTE has a field of view of $\sim 1^{\circ}$ and operates in the 15–200 keV range. It consists of two photon counter detectors, each having an area of ~800 cm^2, an energy resolution of 18% at 60 keV, and a time resolution of 10 μs. Due to the large field of view and the lack of spatial resolution, background estimation can be an issue. This problem is solved by making both clusters oscillate ("rock") between on and off source positions (1.5° or 3° from the

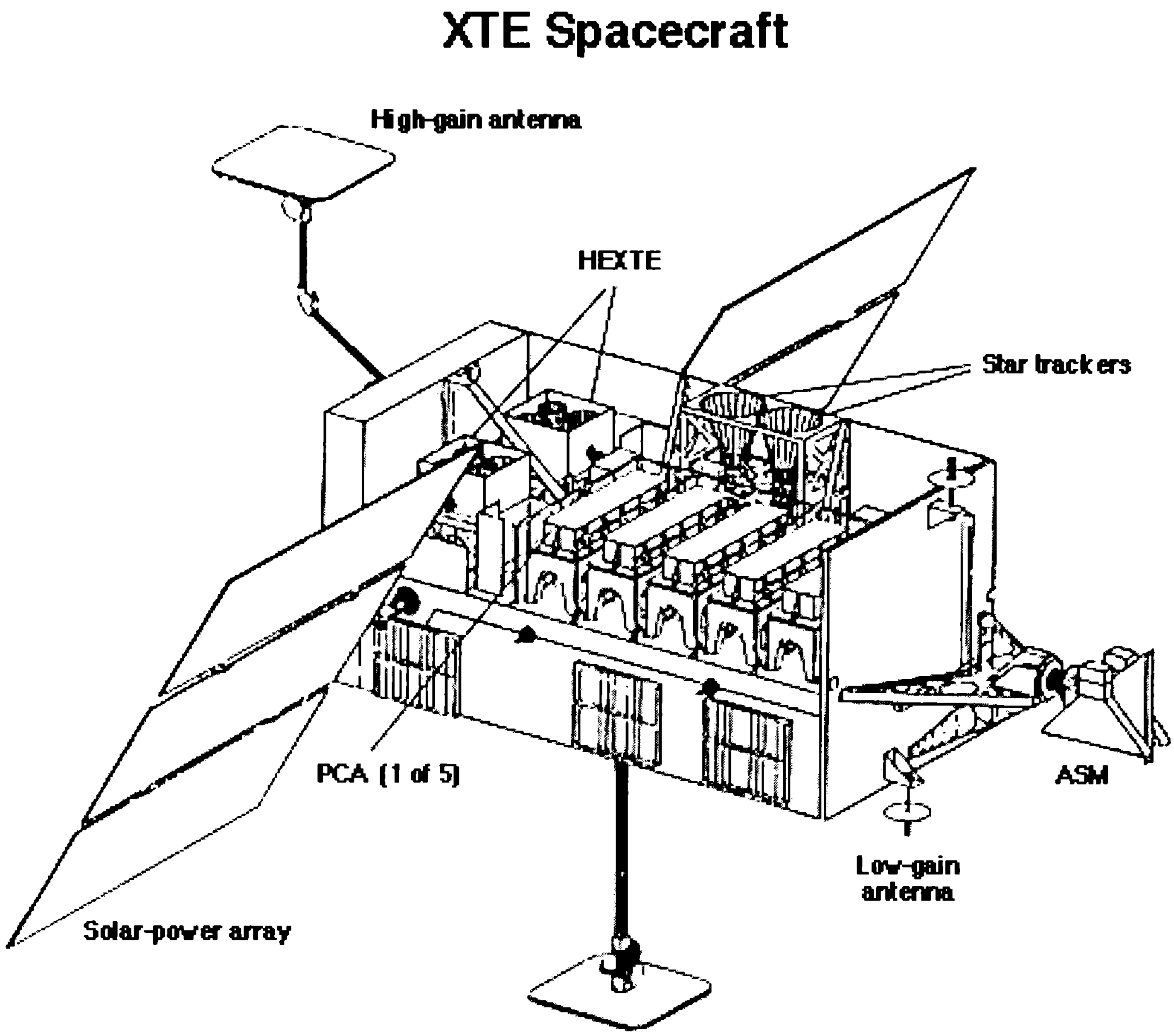

Figure 1.2: Diagram of the XTE spacecraft, with instruments labeled.

source), every 16 or 32 seconds. The data from this instrument have been used in this thesis mainly to better estimate the X-ray luminosity of sources.

The PCA is the main instrument on board *RXTE*. It is a pointed instrument, co-aligned with the HEXTE and having the same collimated field of view of $\sim$1°. It consists of five Proportional Counter Units (PCUs) with a total collecting area of $\sim$6250 cm^2, operates in the 2–60 keV range, has a nominal energy resolution of 18% at 6 keV and, most importantly for this thesis, a maximum time resolution of $\sim 1\mu$s. With the exception of regions near the center of the Galaxy, the source density on the sky is low enough to provide sufficient positional resolution and avoid source confusion.

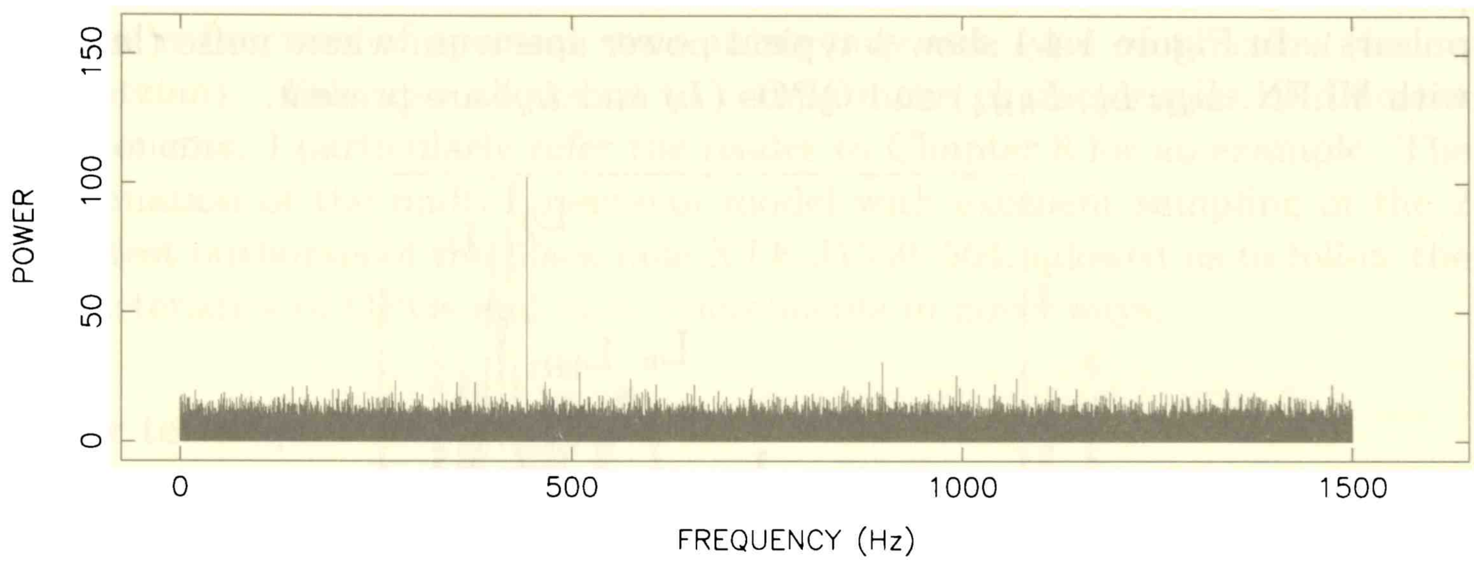

Figure 1.3: Typical power spectrum of a pulsar light curve. The high power represents the pulsar spin frequency ($\nu_s \sim 442$ Hz, in SAX J1748–2021, Chapters 4).

1.2.2 Timing analysis

The main tool I use for studying the timing properties of an X-ray source is the Fourier power spectrum of the count rate time series, in which data are transformed from the time to the frequency domain. This technique is particularly needed when the counting noise dominates the time series and it is only possible to study the averaged properties of the timing phenomena. It is not the aim of this introduction to give an extensive overview of how Fourier techniques are used in X-ray variability studies. For that, I refer to the "bible" by van der Klis (1989). Below, I briefly describe the main procedures.

For the Fourier timing analysis I use data from the PCA (recorded in Event, Good Xenon and/or Single Bit modes, Jahoda et al. 2006). Data are split up into blocks of equal time length and for each block the Fourier power spectrum is calculated. These power spectra are then averaged (generally per observation – I refer to Appendix I in Chapter 6 for a discussion on this). The frequency resolution is equal to the inverse of the time duration of each block. The maximum frequency in the resulting power spectrum is called the Nyquist frequency and is half the inverse of the time resolution of the data (generally, the time resolution I have used is 125μs, which allows the study of variability up to 4096 Hz).

Highly coherent signals, like pulsations, appear as a single frequency-bin spikes while aperiodic structures are spread over more frequency elements. Broad structures are usually called 'noise', while narrow–peaked features are called 'quasi-periodic oscillations' (QPOs). In Figure 1.3 I show an example of a power spectrum in which a clear spike appears at the spin period of the accreting millisecond pulsar SAX J1748–2021 (the spin frequency of this pulsar is $\nu_s \sim 442$ Hz, see Section 1.5.3 for a brief introduction to millisecond pulsars). In Figure 1.4 I show a typical power spectrum where noise (labeled with VLFN, L_{b2}, L_b, L_{hHz}) and QPOs (L_ℓ and L_u) are present.

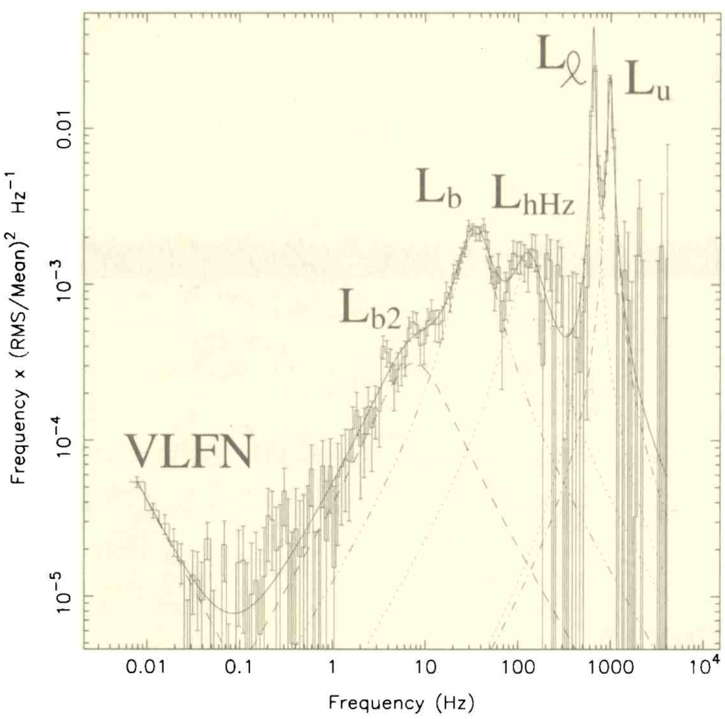

Figure 1.4: Typical averaged power spectrum where noise (VLFN, L_{b2}, L_b, L_{hHz}) and QPOs (L_ℓ and L_u) are present (this is a representative power spectrum from the Atoll source 4U 1636–53, see Chapter 6).

As can be seen in Figure 1.4, the power spectrum consists of a superposition of different components. Unfortunately, there is no physical model that describes all these components consistently, as the real processes behind the X-ray variability are still poorly understood. In order to have a unified phenomenological description of these timing features within a source and among different sources and source types, I fit noise and QPOs with a function consisting of one or multiple Lorentzians, each denoted as L_i, where i determines the type of component. The characteristic frequency (ν_{max}) of L_i is denoted ν_i. ν_{max} is the frequency where the component contributes most of its variance per logarithmic frequency interval and is defined as $\nu_{max} = \sqrt{\nu_0^2 + (FWHM/2)^2} = \nu_0\sqrt{1 + 1/4Q^2}$ (Belloni et al. 2002b). For the quality factor Q, I use the standard definition $Q = \nu_0/FWHM$. $FWHM$ is the full width at half maximum and ν_0 the centroid frequency of the Lorentzian.

I note that a Lorentzian is the Fourier power spectrum of an exponentially damped sinusoid, and although the multi-Lorentzian model usually gives good fits (but see Chapter 8 for exceptions), the original signal can still be different from a damped oscillation. Our choice of this over other models (such as a combination of power law and Gaussian functions) is motivated by the fact that the multi-Lorentzian model gives the possibility to identify and follow the characteristics of power spectral components as they evolve in time and as a function of spectral state using only one type of function (i.e., a Lorentzian). This also allows us to compare the characteristics of different components. I particularly refer the reader to Chapter 8 for an example. The combination of the multi-Lorentzian model with excellent sampling of the 2 brightest outbursts of the black hole XTE J1550–564, allowed us to follow the characteristics of QPOs and noise components in novel ways.

Other techniques used

In a few cases in my thesis I use other techniques, in addition to Fourier ones, in particular Lomb-Scargle periodograms (Lomb 1976; Scargle 1982; Press et al. 1992) as well as the phase dispersion minimization technique (PDM - see Stellingwerf 1978). The Lomb-Scargle technique is ideally suited to look for sinusoidal signals in unevenly sampled data. The phase dispersion minimization technique is well suited to the case of non-sinusoidal time variation covered by irregularly spaced observations.

1.2.3 Spectral analysis: Colors

In the best case scenario the X-ray energy spectrum of a given source can be described by the combination of one or more physically motivated mathematical functions, or models. However, the physical reality of these models is still uncertain and in many cases the data can be satisfactorily described by different models, making the results of such spectral analysis inconclusive. In this thesis I use another method, the so called *color analysis*, which makes use of color-color diagrams and hardness–intensity diagrams. This method is more sensitive to subtle changes in the X-ray spectra as it does not need to assume a certain model.

To calculate the colors, the X-ray spectrum is divided into energy bands. A color is defined as the ratio of count rates in two different energy bands. Different bands are typically chosen for neutron stars and black holes, which have different spectral variability characteristics.

To calculate X-ray colors, in this thesis I always use the 16-s time-resolution Standard 2 mode data of RXTE (see Section 1.2.1). For neutron stars I define soft and hard color as the 3.5–6.0 keV / 2.0–3.5 keV and 9.7–16.0 keV / 6.0–9.7 keV count rate ratio, respectively, and the intensity as the 2.0–16.0 keV count rate. For black hole systems, soft and hard color are the 6.0–16.0 / 2.0–6.0 keV and 16.0–20.0/ 2.0–6.0 keV count rate ratio, respectively and the intensity is the count rate in the 2.0–20 keV band. To correct for the gain changes (i.e., changes in the high voltage setting of the PCUs, Jahoda et al. 2006) as well as the differences in effective area between the PCUs themselves, we normalize our colors by the corresponding Crab Nebula color values that are closest in time but in the same RXTE gain epoch (see Kuulkers et al. 1994; van Straaten et al. 2003, see table 2 in Chapter 6 for average colors of the Crab Nebula per PCU). By applying this normalization, I assume that the spectrum of the Crab is constant, and that the energy spectrum from the source studied is similar to that of the Crab. In Figure 1.5 I show examples of a color–color and a hardness–intensity diagram for the atoll source 4U 1608–52.

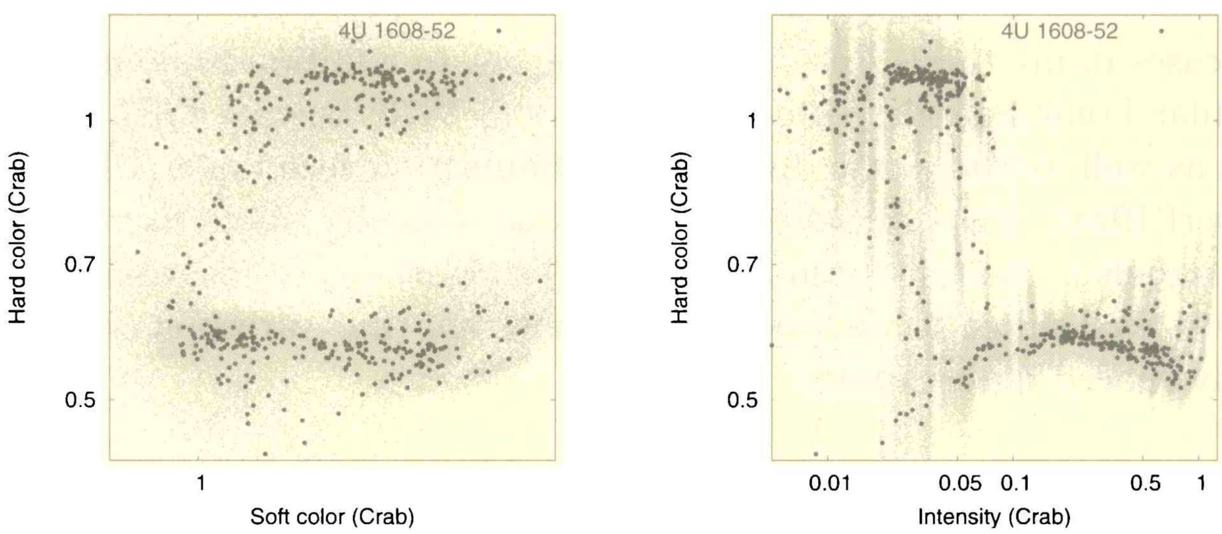

Figure 1.5: Color–color (left) and hardness–intensity (right) diagrams for the transient atoll source 4U 1608–52. Grey points represent the 16 seconds average color and black points the average color per observation (where an observation covers 1 to 5 consecutive satellite orbits. Usually, an orbit contains between 1 and 5 ksec of useful data separated by 1–4 ksec data gaps). Colors and intensities are normalized to the Crab Nebula.

1.3 Long term X-ray variability of LMXBs

In the context of X-ray variability at time scales of hours, days and up to years, low-mass X-ray binaries can be divided into two main classes: the so called *persistent* and *transient* sources. The persistent ones are those which have been "on" since the beginnings of X-ray astronomy while transient sources are those which are generally "off" (in what is called quiescent state) but occasionally show outbursts during which the count rate can increase by several orders of magnitude.

In Figure 1.6 I show the long-term variability of the persistent sources Serpens X-1 and 4U 1820–30 (top and middle panel, respectively) and of the transient source Aql X-1 (bottom panel). As can be seen, a persistent source can show almost no variability (Serpens X-1) or alternatively strong variability (4U 1820–30) in their X-ray count rate, or something in between (see, e.g., Figure 7.2 in Chapter 7).

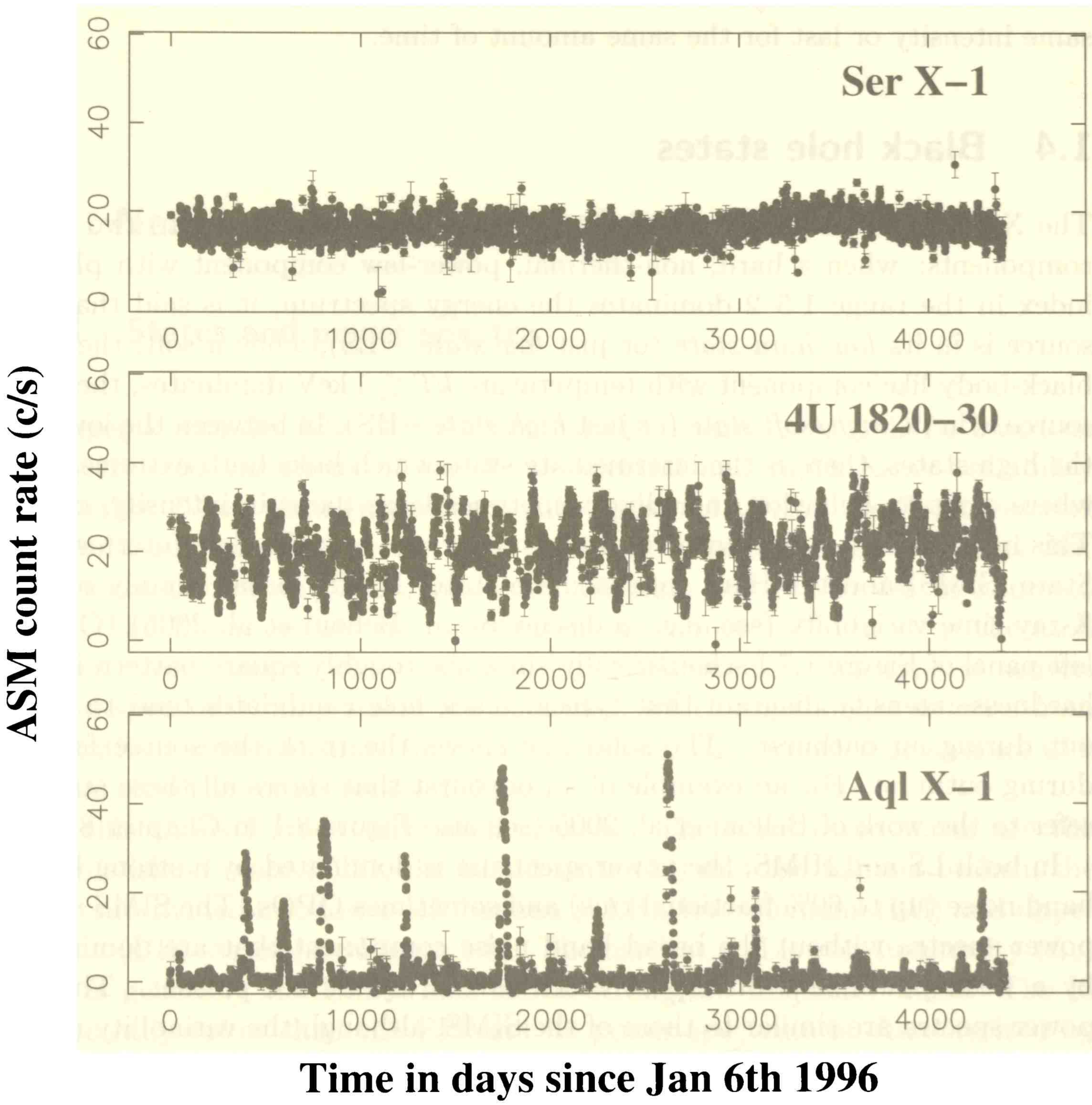

Figure 1.6: The long-term variability of three LMXBs as observed with the All Sky Monitor on board RXTE. Each point represents the 1-day average measurement of the count rate. The top panel shows a persistent source which has a roughly constant count rate (Serpens X-1), the middle panel shows a persistent source with a ~ 170 days quasi-periodic variability (4U 1820–30) and the bottom panel shows a transient source (Aql X-1).

In the case of transient sources, outburst are usually unpredictable, except in a few sources, in which it is possible to predict the beginning of the outbursts within a few tens of days. Not all outbursts from the same source reach the same intensity or last for the same amount of time.

1.4 Black hole states

The X-ray spectral properties of black holes can be classified into two main components: when a hard, non-thermal, power-law component with photon index in the range 1.5–2 dominates the energy spectrum, it is said that the source is in its *low/hard state* (or just *low state* – LS); when a soft, thermal, black-body like component with temperature $kT \lesssim 1\,\mathrm{keV}$ dominates, then the source is in its *high/soft state* (or just *high state* – HS). In between the low and the high states, there is the intermediate state which links both extremes and where complex behavior, including sometimes large flares in intensity, occur. This intermediate state can be usefully subdivided into the Soft Intermediate State (SIMS) and the Hard Intermediate state (HIMS) based mainly on the X-ray time variability (see, e.g., a discussion in Belloni et al. 2005). On the left panel of Figure 1.7 I schematically show the roughly square pattern in the hardness–intensity diagram that typical black hole candidates tend to trace out during an outburst. The solid line shows the track the source follows during outburst. For an example of an outburst that shows all these states I refer to the work of Belloni et al. 2005 (see also Figure 8.1 in Chapter 8).

In both LS and HIMS, the power spectrum is dominated by a strong broad band noise (up to 60% fractional rms) and sometimes QPOs. The SIMS shows power spectra without the broad band noise component that are dominated by a weak power law, on top of which several QPOs are present. The HS power spectra are similar to those of the SIMS, although the variability might be weaker and generally no QPOs are present. In all these cases, the broad and peaked features are found at low characteristic frequency ($<$ 100 Hz), however, sometimes weak high frequency QPOs (100–450 Hz) are also found in the HIMS and SIMS. On the right panel of Figure 1.7, I plot representative power spectra for the high state, soft and hard intermediate states and low state.

Of course, the behavior of black hole sources in the hardness–intensity diagram is not always as smooth and as clear as that shown in the left panel of Figure 1.7, nor are the power spectral components as clear as those shown in the right panel. For a general description of how the power spectral components vary as a function of source state I refer to the recent reviews by Homan & Belloni (2005) and van der Klis (2006). In Chapter 8 I study the black hole candidate XTE J1550–564 as it evolves during the 5 outbursts that have been detected with RXTE.

1.5 Neutron star phenomenology

1.5.1 States and power spectra

Hasinger & van der Klis (1989) classified the neutron star LMXBs based on the correlated variations of the X-ray spectral and rapid X-ray variability properties. They distinguished two sub-types of LMXBs, the Z sources and the atoll sources, whose names were inspired by the shapes of the tracks that they trace out in an X-ray color-color diagram on time scales of hours to days. The Z sources are the most luminous (above 10^{38} erg s^{-1}); the atoll sources cover a much wider range in luminosities. For each type of source, several spectral/timing states are identified, which are thought to arise from qualitatively different inner flow configurations (e.g. presence or absence of a corona, structure of accretion disk, jets).

In this thesis I study only atoll sources. The main three states are the extreme island state (EIS), the island state (IS) and the banana branch, the latter subdivided into lower-left banana (LLB), lower banana (LB) and upper banana (UB) states (see Figure 1.8). The hardest and lowest luminosity (L_x) state is generally the EIS, which shows strong low-frequency noise. The IS is spectrally softer than the EIS and its power spectrum is characterized by broad features and a dominant band-limited noise (BLN) component which becomes stronger and lower in characteristic frequency as the flux decreases and the spectrum gets harder at > 6 keV. In order of increasing L_x, I encounter the LLB, where the so called "twin kHz QPOs" are first observed, the LB, where dominant band limited noise at 10 Hz occurs and finally, the UB, where the (power law) very low frequency noise (VLFN) dominates at < 1 Hz. In the banana states, some of the broad features observed in the EIS and the IS become narrower (peaked) and occur at higher frequency. The twin kHz QPOs can be found in LLB (at frequencies in excess of 1000 Hz), only one is seen in the LB, and no kHz QPOs are detected in the UB. In Figure 1.8 I show a schematic color color diagram and representative power spectra for the EIS, IS, LLB and the UB states.

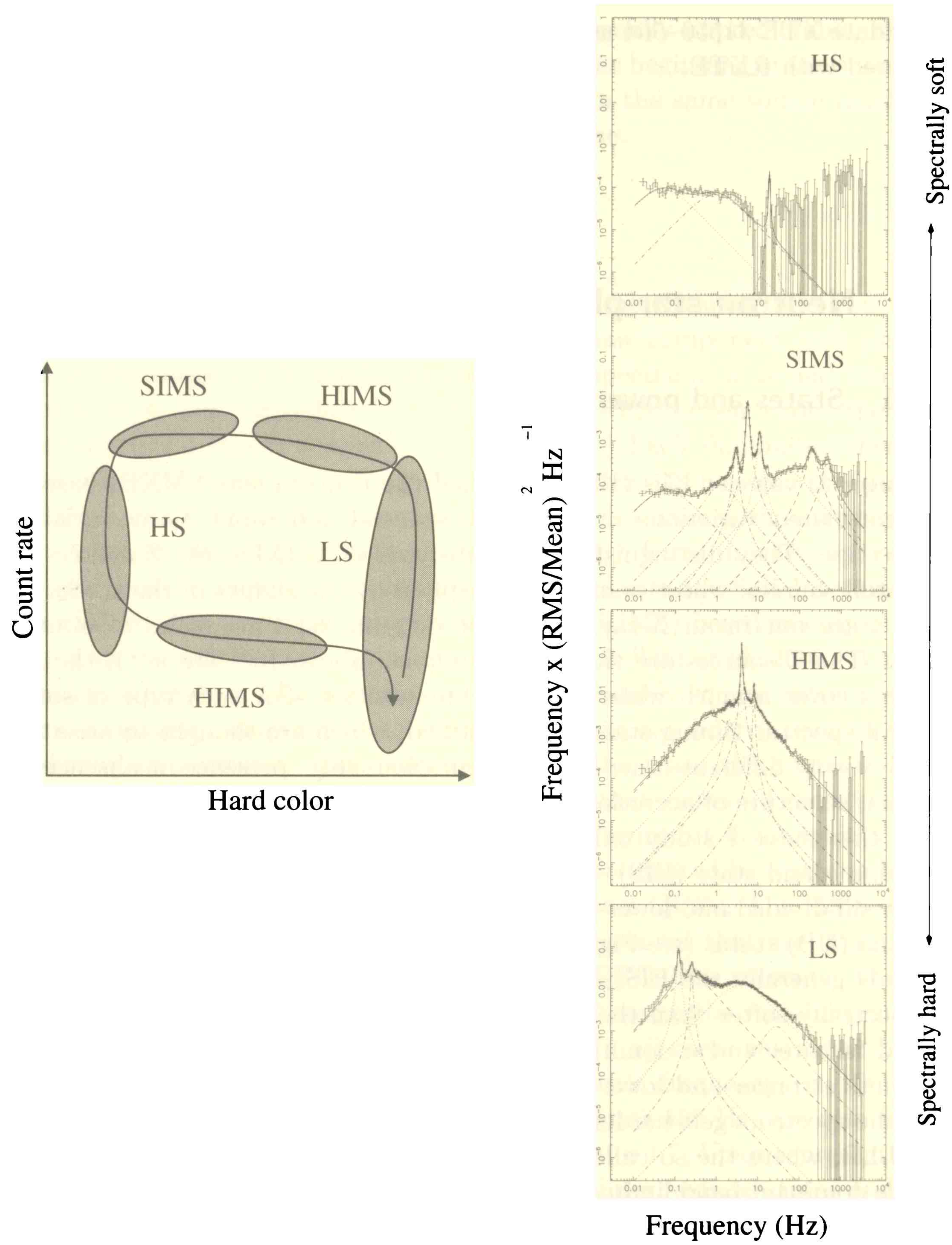

Figure 1.7: *Left:* Schematic hardness–intensity diagram for a typical black hole source outburst. The solid line shows the track the source follows during outburst (courtesy of M. Klein-Wolt). *Right:* Representative power spectra for black hole states (see also Chapter 8). The main states are the high state (HS), soft intermediate state (SIMS), hard intermediate state (HIMS) and the low state (LS).

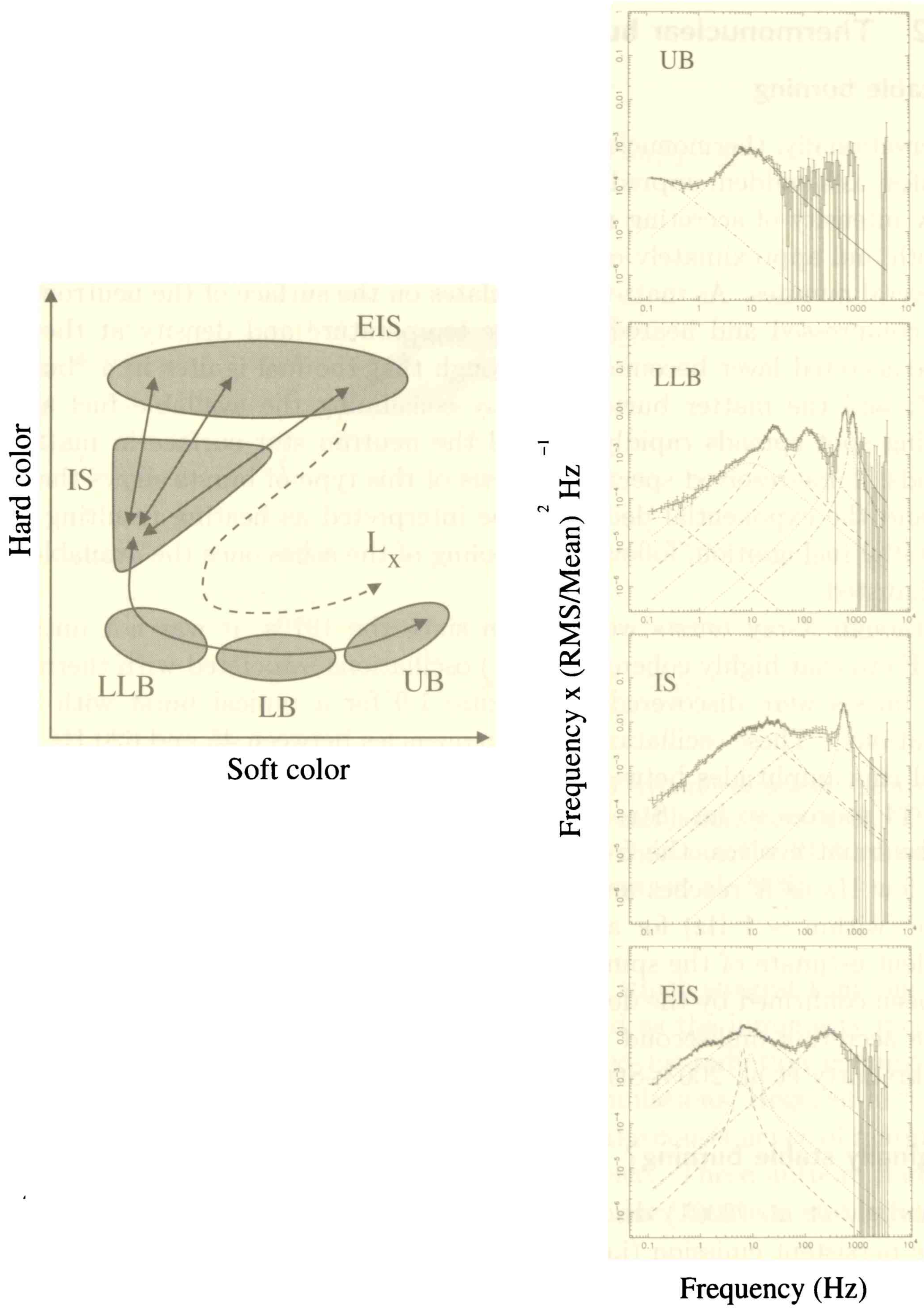

Figure 1.8: *Left:* Schematic color–color diagram for a typical atoll source. The solid line shows the track the source follows from state to state, and the dashed line indicates the direction in which the X-ray luminosity increases (courtesy of M. Klein-Wolt). The main states are the extreme island state (EIS), the island state (IS) and the banana branch, the latter subdivided into lower-left banana (LLB), lower banana (LB) and upper banana (UB) states. *Right:* Representative power spectra for the EIS, IS, LLB and the UB states.

1.5.2 Thermonuclear burning on the neutron star surface

Unstable burning

Observationally, thermonuclear X-ray bursts (also called Type-I X-ray bursts) manifest as a sudden, unpredictable and rapid (1 to 10 seconds) increase in the X-ray intensity of accreting neutron stars. The rise is generally followed by a smooth and approximately exponential decay which lasts from a few seconds to several minutes. As matter accumulates on the surface of the neutron star, it is compressed and heated until the temperature and density at the base of the accreted layer become large enough that the fuel ignites in a "burning spot", and the matter burns unstably consuming the available fuel as the burning spot spreads rapidly over all the neutron star surface in matter of seconds. Time-resolved spectral analysis of this type of bursts shows that the rise and the exponential decay can be interpreted as heating resulting from the initial fuel ignition, followed by cooling of the ashes once the available fuel is exhausted.

Although X-ray bursts were known since the 1970s, it was not until the RXTE era that highly coherent (burst) oscillations associated with thermonuclear bursts were discovered (see Figure 1.9 for a typical burst with burst oscillations). These oscillations have frequencies between 45 and 620 Hz, fractional rms amplitudes between 5 and 20% and have been detected in bursts from 14 sources so far (Strohmayer & Bildsten 2006; Galloway et al. 2006). As the burst evolves, the frequency of these oscillations generally increases by a few Hz as it reaches an asymptotic value, which has been found to be stable (within $\sim$ 1 Hz) for a given source. This asymptotic frequency is an excellent estimate of the spin frequency (within $\sim$ 1 Hz) for a given source as has been confirmed by the detection of burst oscillations at the spin frequency in the accreting millisecond pulsars SAX J1808.4–3658 and XTE J1814–338 (Chakrabarty et al. 2003; Strohmayer & Bildsten 2003).

Marginally stable burning?

Revnivtsev et al. (2001) discovered a new class of quasi-periodic oscillation in the persistent emission (i.e. not during Type-I bursts) from three neutron star X-ray binary sources. These new QPOs have frequencies in the milli-Hertz range, are usually seen before a Type-I X-ray burst but not immediately after, and their properties differ from those of the other QPOs found in neutron star systems (e.g., energy dependence, see also van der Klis 2006). Although Revnivtsev et al. (2001) could not discard an interpretation related to disk instabilities, they conclude that the mHz QPO is likely due to a special mode of nuclear burning on the neutron-star surface. This interpretation is strength-

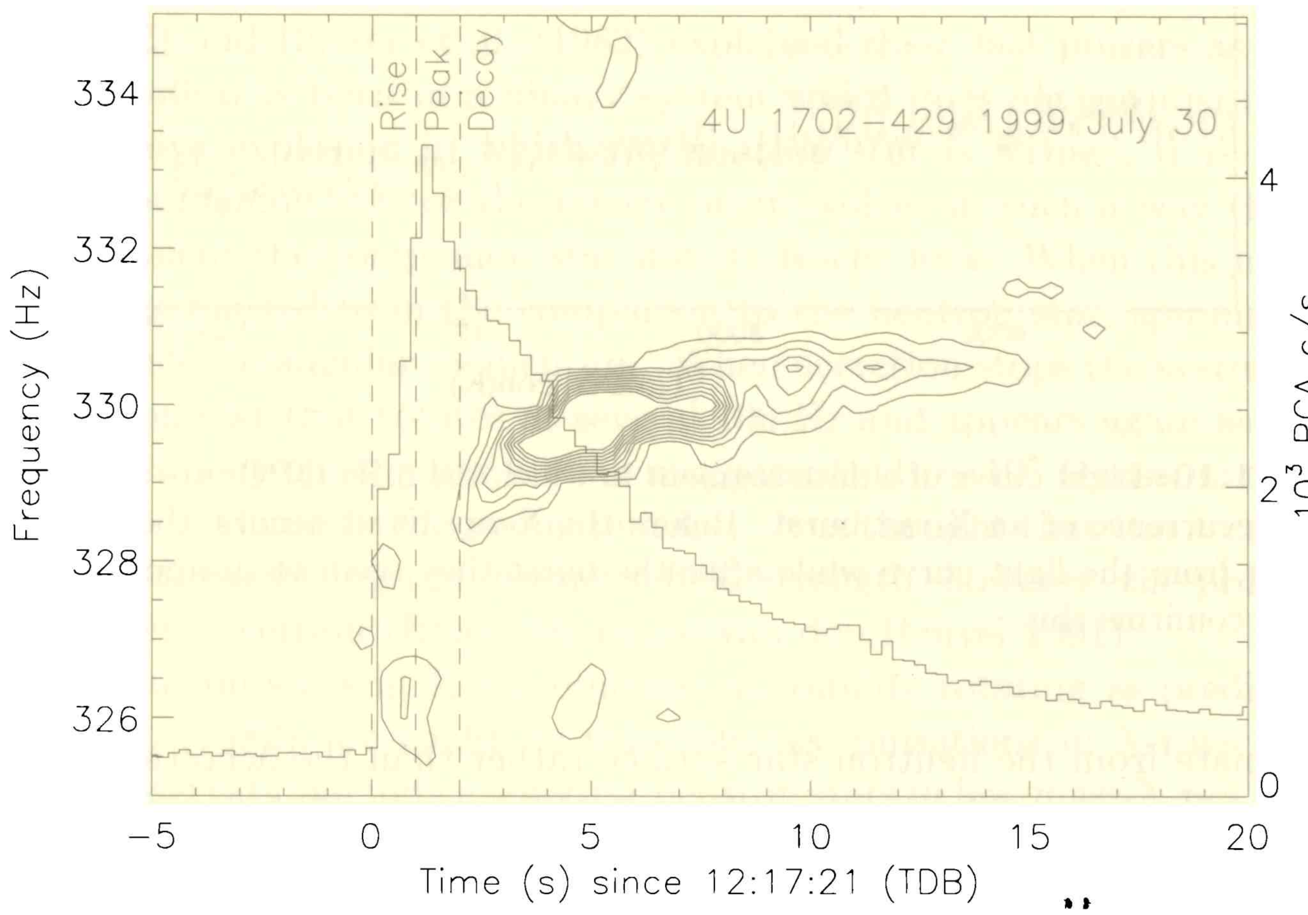

Figure 1.9: X-ray burst lightcurve (histogram) and dynamical power spectrum illustrating the typical frequency evolution of a burst oscillation (contours). The left axis marks the frequency of the oscillations and the right one the PCA count rate. This figure is courtesy of D. Galloway (see also Galloway et al. 2006).

ened by the results of Yu & van der Klis (2002), which suggest that the inner edge of the accretion disk slightly moves outward as the luminosity increases during each mHz cycle due to stresses generated by radiation coming from the neutron star surface. Based on numerical simulations, Heger et al. (2007) show that the mHz QPOs might be explained as the consequence of marginally stable nuclear burning on the neutron star surface. These authors find that the burning is oscillatory only close to the boundary between stable burning and unstable burning (i.e., Type-I X-ray bursts).

In Figure 1.10 I show a representative light curve where mHz oscillations are present before the occurrence of an X-ray burst and not after. These oscillations when present, can be seen directly in the light curve.

Confirming that these oscillations are related with a special mode of nuclear burning on the neutron–star surface is of great interest, as it would be the first time (except for the highly coherent pulsations in accreting millisecond pulsars) that a feature of the persistent X-ray variability has been identified

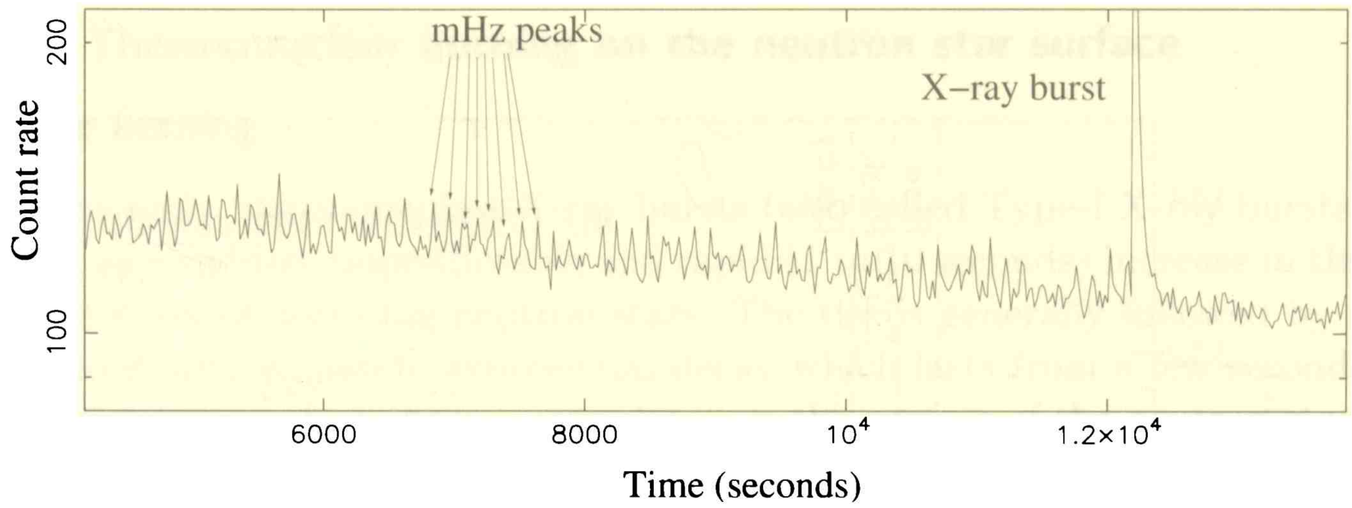

Figure 1.10: Light curve of a data segment in which the mHz QPOs are present prior to the occurrence of an X-ray burst. Before the X-ray burst occurs, the oscillations are clear from the light curve while after the burst they seem to disappear. Fourier analysis confirms this.

to originate from the neutron star surface rather than the accretion disk. To further investigate this, I am analyzing RXTE archival data of more than 40 neutron star binary systems to look for similar signals. In the cases in which mHz QPOs are present, I am studying their interactions with X-ray bursts. In Chapter 2 I present the first results, in which I show that the mHz QPO frequency constitutes the first identified observable that can be used to predict the occurrence of X-ray bursts. This result confirms that the mHz QPO phenomenon is intimately related with the processes that lead to a thermonuclear burst.

1.5.3 Millisecond pulsars

Radio pulsars are highly magnetized ($\gtrsim 10^8$ Gauss) rotating neutron stars which emit a collimated beam of radio waves. The youngest radio pulsars are observed to rotate rapidly, up to 100 times per second. This rapid rotation combined with the high magnetic field strength (10^{12-13} Gauss) of the neutron star produces beamed radio emission at the magnetic poles, and since the magnetic poles "are fixed" on the neutron star, the beams spin at the frequency of the neutron star (ν_s). After a radio pulsar is born it slows down as it loses energy until ν_s is so low (lower than a few tenths of Hz) that the pulsar mechanism is not able to produce detectable radio emission anymore and it is said that the pulsar has died. This process takes millions of years, depending on the initial spin frequency and magnetic field strength of the neutron star.

If it is true that new pulsars have frequencies not higher than $\sim$ 100 Hz, and that their spin frequency decreases with time, then how is it possible that there are radio pulsars with much higher spin frequencies than 100 Hz, the fastest now being 716 Hz? (Hessels et al. 2006). In the early 1980s, Alpar et al. (1982) and Backer et al. (1982) explained these fast pulsars as follows: if a radio pulsar is born in a binary system which does not get disrupted by the supernova explosion in which the neutron star is formed, it is possible that the companion star or the binary orbit evolves in such a way that at a certain moment the companion star fills its Roche lobe. When this happens, matter is exchanged from the companion to the neutron star, spinning it up by the transfer of angular momentum. When accretion stops the system is left with neutron star that rotates at several 100 Hz and appears again as a radio pulsar. This neutron star has a weak magnetic field ($\sim 10^8$ Gauss, in contrast to the 10^{12-13} Gauss in the young pulsars). It is thought that the accretion is responsible for reducing the magnetic field strength, however, the process for this is as yet uncertain (Bhattacharya & van den Heuvel 1991).

If the neutron stars in X-ray binaries are rapidly rotating as predicted by Alpar et al. (1982), we could, in principle, see pulsations in X-rays as well. The first observational indication that neutron stars in low-mass X-ray binaries rotate rapidly came in 1996 with the discovery of millisecond oscillations (with frequencies that usually show drifts) during thermonuclear X-ray bursts (see Section 1.5.2), but it was not until 1998 that the first accreting millisecond X-ray pulsar was discovered (Wijnands & van der Klis 1998a). Since then a total of 9 (and even 10 if we consider Aql X-1 as an accreting millisecond pulsar – see discussion in Chapter 3) have been found out of a sample of more than 150 neutron star LMXBs known up to date. These systems are known as Accreting Millisecond X-ray pulsars (AMXPs, also referred to as AMPs in the literature) and are thought to be accretion-powered; gas coming from the accretion disk couples to the star's magnetic field and gets channeled, forming "hot spots" perhaps at the magnetic poles, which can be seen in X-rays. These hot spots are fixed on the neutron star surface and therefore rotate with the spin frequency of the neutron star.

An important and not yet resolved issue is why most neutron star LMXBs do not show persistent pulsations in their X-ray emission. Several theoretical efforts have been made to explain this, the main question remaining whether the pulsation is hidden from the observer (e.g. there is a scattering medium that washes out the coherent beamed pulsations) or not produced at all (e.g., because the magnetic field is too weak to channel the accreting matter). So, given that pulsations were only seen from a few sources, in the literature (up to now) the neutron star systems were sub-classified into pulsating and non-pulsating ones. The recent discovery of HETE J1900.1–2455 showed that this classification might not cover all systems. This was the first AMXP which did not show persistent pulsations throughout the outburst, but only during the first ~ 2 months. Sudden increases in the amplitude of the pulsations were apparently triggered by thermonuclear X-ray bursts; the amplitude decreased steadily on timescales of days after the bursts (Galloway et al. 2007). This source was also different from the other AMXPs, as it has been in outburst for more than 2.5 years[1], while typical AMXP outbursts last for no more than a few weeks or months. This difference suggested that the accumulation of matter on the surface was burying the magnetic field (Galloway et al. 2007) and therefore extinguishing the pulsations. If the accumulation of matter is the key process that buries the magnetic field, then this result could explain why most of neutron star LMXBs do not show pulsations.

We are searching the full RXTE public archive data for coherent pulsations. In Chapters 3 & 4 I report on the discovery of episodes of intermittent coherent millisecond X-ray pulsations in two X-ray transients. These pulsations appear and disappear on timescales of hundreds of seconds and can be identified as occurring at the spin frequency of the respective sources. These short time scales cannot be explained by the burying scenario proposed for the intermittent AMXP HETE J1900.1–2455. Another important conclusion of our discoveries is that irrespective of the physical mechanisms behind the pulsations, it is now clear that a strict division between pulsating and non-pulsating neutron star sources cannot be made. It is possible that all sources pulsate occasionally, although the recurrence times could be very long.

[1] At the time of submitting the thesis to the printer, the source was still active.

1.6 Outline

In this thesis I present a study of different manifestations of accretion onto compact objects, studying periodic as well as aperiodic variability.

In Chapter 2 I report on the discovery of systematic frequency drifts in the frequency of the Millihertz QPOs. They constitute the first identified observable that can be used to predict the occurrence of X-ray bursts. Furthermore, our observational results confirm that the mHz QPO phenomenon is intimately related with the processes that lead to a thermonuclear bursts.

In Chapters 3 and 4 I report on the discovery of episodes of intermittent coherent millisecond X-ray pulsations at the spin frequency of the X-ray transients SAX J1748–2021 and Aql X-1. These findings provide new input for models: irrespective of the physical mechanisms behind the pulsations, it is now clear that there is not a strict division between pulsating and non-pulsating neutron star sources as it was thought before; it is possible that all sources pulsate occasionally although the recurrence times could be very long.

In Chapter 5 I report on the low-luminosity island state of the ultra-compact atoll source 4U 1820–30. I compare the frequencies of the variability components found in the power spectra with those in other atoll sources. These frequencies were previously found to follow a universal scheme of correlations; these correlations are frequency–shifted in the case of the variability measured in some accreting millisecond pulsars. Our results show that 4U 1820–30 is the first atoll source which shows no significant pulsations but has a significant shift in the frequency correlations compared with 3 other non-pulsating atoll sources.

In Chapter 6 I report on the time variability of the atoll source 4U 1636–53 in the banana state and, for the first time with RXTE, in the island state. I find that the so called "hectohertz QPO" shows a behavior different from that of other spectral components, indicating that the mechanism that sets its frequency differs from that for the other components, while the amplitude setting mechanism is common. I also show that a previously proposed interpretation of the narrow low-frequency QPO frequencies in different sources (in terms of harmonic mode switching) is not supported by our data, nor by some previous data on other sources and more importantly, that the frequency range that this QPO covers is found not to be related to source spin, angular momentum or luminosity.

In Chapter 7 I report on the X-ray source 1E 1724–3045 in the globular cluster Terzan 1. I study the flux transitions observed between February 2004 and October 2005 and conclude that they are due to changes in the accretion rate. I confirm the atoll nature of the source and report on the discovery of kHz QPOs.

Finally, in Chapter 8 I report on all 5 outbursts observed with RXTE from the black hole candidate XTE J1550–564. I investigate how the frequency, coherence and strength of each power spectral component evolve in time and as a function of spectral state and find that it is generally possible to follow the time evolution of the different power spectral components as they shift in frequency and vary in strength and coherence. Using this information I identify the different components and find frequency–frequency relations within the data of this source. I compare these relations with similar ones that I have used in Chapters 6 & 7.

2 Millihertz Oscillation Frequency Drift Predicts the Occurrence of Type I X-ray Bursts

D. Altamirano, M. van der Klis, R. Wijnands and A. Cumming

Astrophysical Journal Letters, 2008, 673, 35.

Abstract

Millihertz quasi-periodic oscillations (mHz QPOs) reported in three neutron-star low mass X-ray binaries have been suggested to be a mode of marginally stable nuclear burning on the neutron star surface. In this Letter, we show that close to the transition between the island and the banana state, 4U 1636–53 shows mHz QPOs whose frequency systematically decreases with time until the oscillations disappear and a Type I X-ray burst occurs. There is a strong correlation between the QPO frequency ν and the occurrence of X-ray bursts: when $\nu \gtrsim 9$ mHz no bursts occur, while $\nu \lesssim 9$ mHz does allow the occurrence of bursts. The mHz QPO frequency constitutes the first identified observable that can be used to predict the occurrence of X-ray bursts. If a systematic frequency drift occurs, then a burst happens within a few kilo-seconds after ν drops below 9 mHz. This observational result confirms that the mHz QPO phenomenon is intimately related with the processes that lead to a thermonuclear burst.

2.1 Introduction

Revnivtsev et al. (2001) discovered a new class of low frequency quasi-periodic oscillation (QPO) in three neutron star X-ray binary sources (Aql X-1, 4U 1608-52 and 4U 1636–53). This new QPO has frequencies between 7 and 9 $\times 10^{-3}$ Hz, i.e. it is in the milli-Hertz range, and its other properties also differ from those of the other QPOs found in the neutron star systems (e.g. energy dependence, see van der Klis 2006). Although Revnivtsev et al. (2001) could not discard an interpretation related with disk instabilities, they concluded that the mHz QPO is likely due to a special mode of nuclear burning on the neutron star surface. This interpretation was strengthened by the results of Yu & van der Klis (2002), who showed that the kHz QPO frequency is anti-correlated with the luminosity variations during the mHz oscillation, suggesting that the inner edge of the disk slightly moves outward as the luminosity increases during each mHz cycle due to stresses generated by radiation coming from the the neutron star surface. This is contrary to the correlation observed between X-ray luminosity (L_x) and kHz QPO frequency, where the inner disk edge is thought to move in, as the accretion rate and hence L_x, increases (van der Klis 2006, and references within).

The properties of the mHz QPOs as observed up to now can be summarized as follows: *(1)* the fractional rms amplitude strongly decreases with energy, from $\approx 2\%$ at 2.5 keV, down to an almost undetectable $< 0.2\%$ at ≈ 5 keV; *(2)* mHz QPOs occur only in a particular range of X-ray luminosity: $L_{2-20\ keV} \approx 5-11\times10^{36}$ erg/s; *(3)* the frequency of the mHz QPOs is between 7 and 9 mHz; *(4)* the mHz QPOs disappear with the occurrence of a type I X-ray burst; *(5)* as noted above, the kHz QPO frequency is approximately anti-correlated with the $2-5$ keV count rate variations that constitute the mHz oscillation.

Heger et al. (2007) suggested that the mHz QPOs could be explained as the consequence of marginally stable nuclear burning on the neutron star surface. They found an oscillatory mode of burning, with a period P_{osc} close to the geometric mean of the thermal[1] and accretion[2] timescales of the burning layer. For typical parameters, $P_{osc} \equiv \sqrt{t_{thermal} \cdot t_{accr}} \approx 2$ minutes, in accordance with the characteristic frequency of the mHz QPOs. The burning is oscillatory only close to the boundary between stable burning and unstable burning (in Type I X-ray bursts), explaining the observation that the mHz QPOs were seen within a narrow range of luminosities.

[1]The thermal timescale is defined as $t_{thermal} = c_p T/\epsilon$ where c_p, T and ϵ are the heat capacity at constant pressure , the temperature and the nuclear energy generation rate, respectively

[2]The accretion timescale is defined as $t_{accr} = y/\dot{m}$ where y and $\dot{m}$ are the column density of the burning layer and local accretion rate, respectively.

Two of the three sources in which Revnivtsev et al. (2001) found the mHz QPOs are transient atoll sources (Aql X-1 and 4U 1608–52) while the third one, 4U 1636–53, is a persistent atoll source (Hasinger & van der Klis 1989). The object of our current study, 4U 1636–53, has an orbital period of ≈ 3.8 hours (van Paradijs et al. 1990) and a companion star with a mass of $\approx 0.4\ M_{\odot}$ (assuming a NS of 1.4 $M_{\odot}$; Giles et al. 2002). 4U 1636–53 is an X-ray burst source (Hoffman et al. 1977) showing asymptotic burst oscillation frequencies of ≈ 581 Hz (Zhang et al. 1997; Strohmayer & Markwardt 2002). The aperiodic timing behavior of 4U 1636–53 has been studied with the EXOSAT Medium Energy instrument (Prins & van der Klis 1997) and with the Rossi X-ray Timing Explorer (RXTE, e.g. Wijnands et al. 1997; Di Salvo et al. 2003, and Chapter 6).

4U 1636-53 is a reference source for studying nuclear burning on the surface of a neutron star since it shows the full range of burst behavior: single and multi-peaked Type I X-ray bursts, superbursts, burst oscillations, photospheric radius expansion, regular and irregular burst sequences (e.g. Galloway et al. 2006) and mHz QPOs. As such, it is an ideal source to understand the relation between these different observational manifestations of nuclear burning.

Recently, Shih et al. (2005) reported that 4U 1636–53 has shown a significant decrease in its persistent L_x during the years 2000 and 2001. In Chapter 6 we show that during the low L_x period, 4U 1636–53 is observed in its (hard) island states. This provides an opportunity to study the mHz QPOs in harder and lower luminosity states than was possible up to now.

2.2 Data analysis & results

We used data from the RXTE Proportional Counter Array and the High Energy X-ray Timing Experiment (PCA and HEXTE, respectively; for instrument information see Jahoda et al. 2006; Gruber et al. 1996). Up to June, 2006, there were 338 public pointed observations. An observation covers 1 to 5 consecutive 90-min satellite orbits. Usually, an orbit contains between 1 and 5 ksec of useful data separated by 1–4 ksec data gaps; on rare occasions the visibility windows were such that RXTE continuously observed the source for up to 27 ksec. In total there were 649 gap-free data segments of length 0.3 to 27 ksec.

We produced energy spectra for each observation using Standard data modes and fitted them in the $2-25$ keV and $20-150$ keV bands for PCA and HEXTE, respectively. The interstellar absorption N_H was fixed at 3.75×10^{21} cm^{-2} (see Schulz 1999; Fiocchi et al. 2006). We used 1-sec resolution

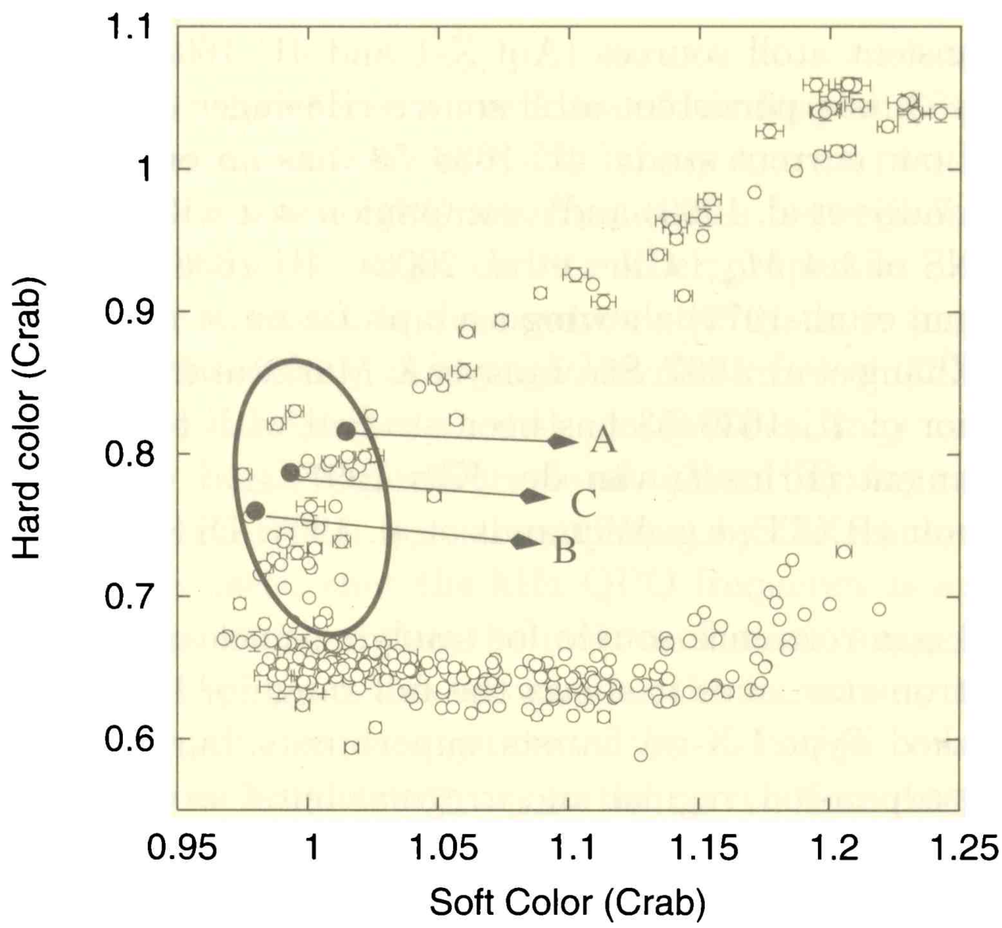

Figure 2.1: Color-color diagram as described in Chapter 6. Each data point represents the average of an observation (≈ 2 to ≈ 30 ksec). The ellipse marks the region in which mHz QPOs with decreasing frequency were found. The labels A, B and C correspond to those in Figure 2.3.

event mode PCA light curves in the $\approx 2 - 5$ keV range (where the mHz QPOs are strongest) and searched for periodicities in each of the 649 segments separately using Lomb-Scargle periodograms (Lomb 1976; Scargle 1982; Press et al. 1992). Segments in which one or more Type I X-ray bursts were detected were searched for periodicities before, in between, and after the bursts. We find that the oscillations in the $\approx 2-5$ keV range are evident from the light curves (see for example Figure 1.10 on page 16 of this manuscript, and figure 1 in Revnivtsev et al. 2001). The significance as estimated from our Lomb-Scargle periodograms (Press et al. 1992) confirm that the oscillations are all above the 3σ level. We estimated the uncertainties in the measured frequencies by fitting a sinusoid to 1000 sec data segments to minimize frequency-drift effects. The typical errors on the frequency are of the order of $2 - 6 \times 10^{-5}$ Hz (or $2 - 6 \times 10^{-2}$ mHz).

We detected mHz QPOs in 124 of the 649 segments. Most occur in segments with less than 4 ksec of useful data and sometimes the QPOs cover only part of a segment. Revnivtsev et al. (2001) reported the characteristics of the

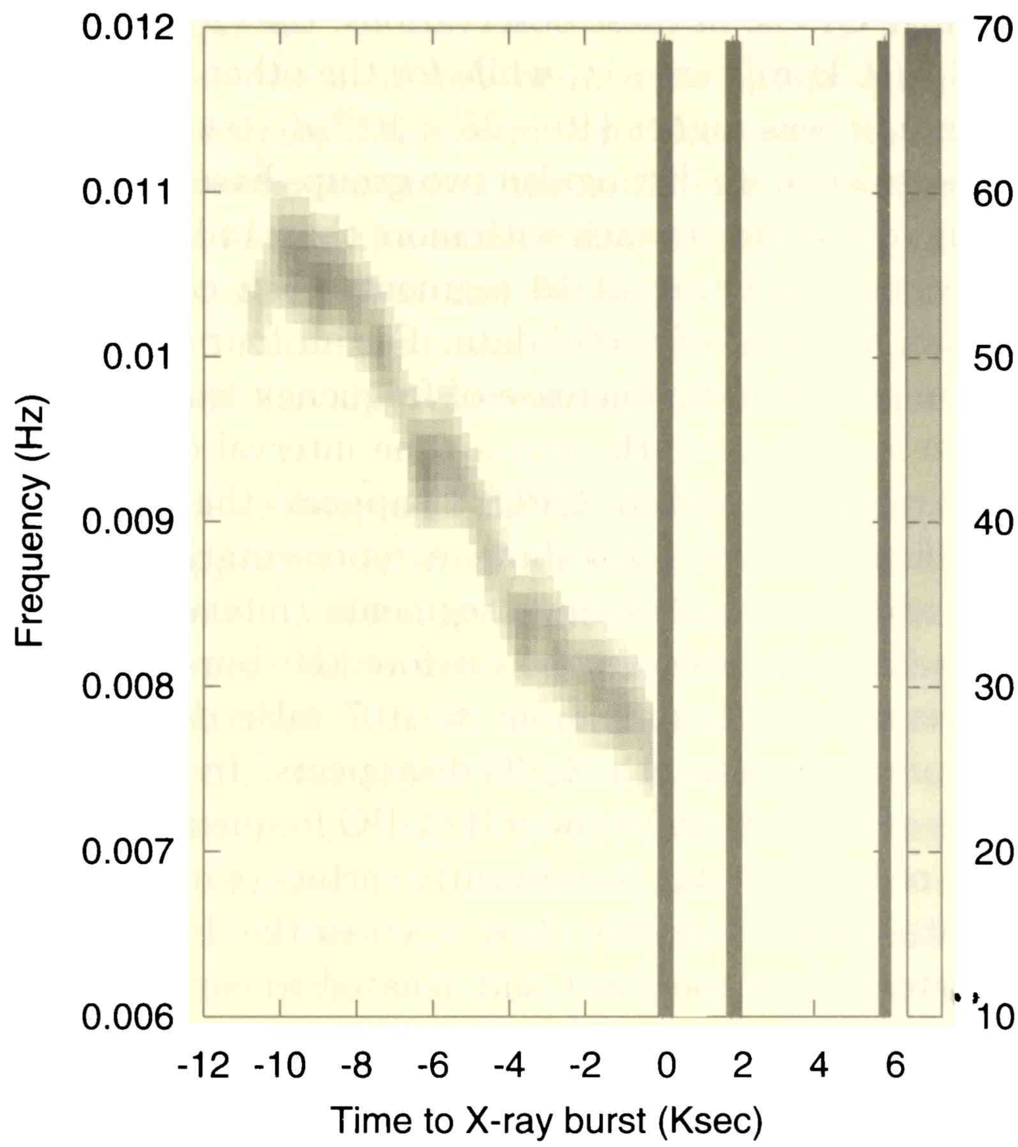

Figure 2.2: Dynamical power spectrum smoothed with a 750 seconds sliding window with steps of 200 seconds, showing the mHz QPOs during the last 12 ksec before the X-ray burst occurs. This sequence corresponds to case B in Figures 2.1 & 2.3 – ObsId: 60032-05-02-00. The three black vertical lines correspond to the times of occurrence of the X-ray bursts. For clarity, we plot only powers above 10 which correspond to $\gtrsim 2\sigma$ (single trial per 750 seconds window but normalized to the number of possible frequencies in the range 0–0.5 Hz).

mHz QPOs between March 1996 and February 1999. Using the X-ray colors averaged per observation as reported in Chapter 6, we find that their data sample the region at hard colors $\lesssim 0.7$ and soft colors $\gtrsim 1$ (see Figure 2.1), which represents the so called banana state (van der Klis 2006). Some of the later observations also sample the banana state. We re-analyzed all the data in this region of the color-color diagram and found results which are consistent with those reported by Revnivtsev et al. (2001): the frequency of the QPOs varies randomly between 6 and 9 mHz.

In the harder state close to the transition between the island and banana state and marked with the ellipse drawn in Figure 2.1, we found 22 segments with significant mHz QPOs; in these observations, the (2–150 keV) luminosity was $6 - 10 \times 10^{36}[d/(6\ \mathrm{kpc})]^2$ erg s^{-1}, while for the other cases, corresponding to the banana state, it was higher ($10 - 35 \times 10^{36}[d/(6\ \mathrm{kpc})]^2$ erg s^{-1}).

Among the 22 segments, we distinguish two groups based on segment length: the first consisting of 4 segments each with more than 14 ksec of uninterrupted data, and the second consisting of 18 segments each corresponding to one orbit with less than ≈ 4 ksec of useful data. For all four segments in the first group, we measure a systematic decrease of frequency from between 10.7 and 12.5 mHz down to less than 9 mHz over a time interval of 8 to 12 ksec, after which an X-ray burst occurs and the QPOs disappear (the QPOs become much less than 3σ significant). Figure 2.2 shows a representative dynamical power spectrum corresponding to one of these segments (interval B in Figure 2.3). The QPO is present $\approx$ 12 ksec seconds before the burst and its frequency systematically decreases with time from $\approx$ 10.7 mHz down to $\approx$ 7.6 mHz. Then the X-ray burst occurs and the QPO disappears. In the second group, 16 of the 18 segments of < 4 ksec show the mHz QPO frequency to decrease either within a segment, or between 2 or 3 consecutive orbits (with 2–4 ksec data gaps in between) at rates consistent with those seen in the 4 long segments. The two remaining segments are too short and isolated to constrain the frequency drift well.

To illustrate the interplay between this very systematic behavior of the mHz QPOs and our data structure, in Figure 2.3 we show a representative lightcurve. A, B and C mark three intervals in which the mHz QPOs were detected and that each terminate with an X-ray burst. As can be seen, we have data in which mHz QPOs are detected and followed through consecutive segments (case A), and data in which the oscillations are detected and disappear within one segment (cases B & C). Furthermore, we have data in which the oscillations are present from the start of the observation (case B) as well as data in which the mHz QPOs appear during an observation (case A & C).

Among our 22 segments, the frequency of the oscillations varies in the range $7 - 14.3$ mHz with directly observed onset frequencies between 10.7 and 14.3 mHz. Interpolating through gaps, the QPOs last for 7.5 to 16 ksec. Over such intervals, the frequency is always consistent with decreasing at average rates from 0.07 to 0.15 mHz ksec^{-1}, and the frequency had always dropped to $\lesssim 9$ mHz just before an X-ray burst (as estimated from the last 750 seconds before the burst). Interestingly, this last result applies to all cases in which we detect the mHz QPOs before an X-ray burst, including the cases that occur in the banana state: it seems that independent of the spectral state of the source, no X-ray burst will occur if the mHz QPOs are present at a frequency higher than $\approx$ 9 mHz (bursts do occur in both states that are not preceded by detectable mHz QPOs).

No relation between the 2–60 keV count rate and frequency was found: in two of the four long segments the count rate decreased about 10% during the time the mHz QPOs were present, while in the other two cases the count rate increased by approximately the same amount. No clear relation was found between frequency range covered and duration of the oscillation; perhaps this is related to the fact that, as shown in Figure 2.2, the frequency does not decrease smoothly but has short periods in which it is consistent with being constant.

When 4U 1636–53 is observed close to its island–banana state transition, the mHz QPOs disappear *only* when an X-ray burst occurs. However, this is not the case for the banana state, in which we found also observations in which the oscillations disappear below detectable levels without the occurrence of an X-ray burst. The interval of time required to again detect the oscillations after a burst occurred is variable. The two extreme cases are (i) observation 60032-01-06-000 where no mHz QPOs were detected during the $\approx$ 15 ksec of uninterrupted data following an X-ray burst and (ii) observation 40028-01-06-00, where mHz QPOs are detected again $\approx$ 6000 seconds after an X-ray burst occurred. We note that in the first case, the source was close to the transition between island and banana state while in the second case, the source was in the banana state. Nevertheless, no clear relation between this waiting time and the source state (island or banana state) was found. As bursts may be missed due to data gaps, a time interval of $\approx$ 1000 seconds between a (missed) X-ray burst and onset of the QPOs cannot in some cases be excluded (e.g. case A in Figure 2.3).

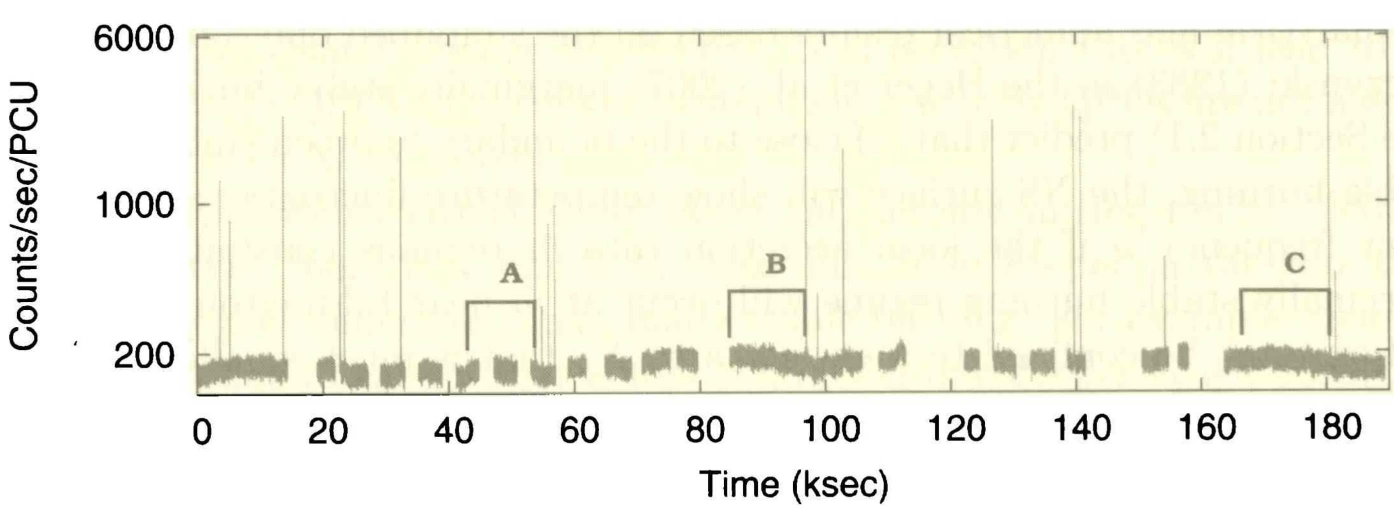

Figure 2.3: 2–60 keV PCA light curve of observations 60032-05-01,02,03 and 04. *A*, *B* and *C* indicate intervals in which the mHz QPOs are detected. In all three cases, the frequency of the mHz QPO decreases with time until the appearance of an X-ray burst.

2.3 Discussion

We have shown that close to the transition between the island and the banana state 4U 1636–53 exhibits mHz QPOs whose frequency systematically decreases with time until the oscillations disappear with the occurrence of a Type I X-ray burst. The mHz QPO frequency ν constitutes the first identified observable that can be used to predict the occurrence of X-ray bursts: when $\nu \gtrsim 9$ mHz no bursts occur, while $\nu \lesssim 9$ mHz does allow the occurrence of bursts. If a systematic frequency drift occurs, then a burst happens within a few kilo-seconds after ν drops below 9 mHz. This observational result confirms that the mHz QPO phenomenon is intimately related with the processes that lead to a thermonuclear burst.

The fact that the observation of a systematic frequency decrease with time implies the occurrence of a future X-ray burst, strongly suggests that the frequency of the mHz QPOs is related to the burning processes on the neutron star surface. One possibility is that the frequency of the QPO is somehow a measurement of the accumulation of fresh fuel on the neutron star surface which will be available for a future thermonuclear burst. To our knowledge, there has been only one attempt to theoretically explain the mHz QPOs phenomena (Heger et al. 2007). In this model the frequency of the QPO depends, among others, on the amount of available fresh fuel, on the local accretion rate and the composition of the material. It is beyond the scope of this Letter to perform numerical simulations as those reported by Heger et al. (2007). In the rest of this discussion we briefly compare these authors' model predictions with our observations and propose some more complex scenarios.

Analytical and numerical results based on the simplified one-zone model of Paczynski (1983) in the Heger et al. (2007) marginally stable burning model (see Section 2.1) predict that (i) close to the boundary between stable and unstable burning, the NS surface will show temperature fluctuations with constant frequency ν if the local accretion rate $\dot{m}$ remains constant; (ii) this marginally stable burning regime will occur at $\dot{m}$ near Eddington, hence accretion must be confined to a surface area S_A that is much smaller that the total area of the NS; (iii) ν correlates with $\dot{m}$ (see figure 4 in Heger et al. 2007) and (iv) thermonuclear bursts and mHz QPOs should not be observed at the same luminosity and therefore presumably at the same $\dot{m}$.

In this paper, we show that for constant luminosity the QPO frequency can systematically decrease in time and that instantaneously measured frequencies can be the same for different luminosities. We also show that mHz QPOs and thermonuclear bursts do in fact occur at the same luminosity and that both phenomena are clearly related. This means that we are dealing with a more complex scenario than that introduced by Heger et al. (2007).

The amount of time between the preceding X-ray burst and the onset of mHz QPOs is variable (> 6ksec) and apparently independent of source state. If the system is locally accreting at $\dot{m} \simeq \dot{m}_{Edd}$ and if none of the accreting fuel is burnt, only ≈ 1000 seconds are required to accrete a fuel layer of column depth y_f capable of undergoing marginally stable burning ($y_f \approx 10^8$ g cm^{-2} and $\dot{m} \approx 8 \cdot 10^4$ g cm^{-2} s^{-1} – see e.g. Heger et al. 2007). One possible explanation for the observed longer intervals between burst and onset of oscillations, is that a large fraction of the accreted fuel is burnt as it is accreted on the neutron star surface. Of course the burning fraction could vary in time, and this estimate is assuming that all the fuel was burnt during the last X-ray burst, which is not always true (Bildsten 1998). Interestingly, if this interpretation is correct and low partial burning fractions can occur, under certain conditions the mHz QPOs could appear in much less than a 1000 seconds after an X-ray burst.

The fact that the amount of time between the preceding X-ray burst and the onset of mHz QPOs is variable may be also an indication that not all the accreted fuel is burnt nor available to participate in the marginally stable burning. For example, accretion could occur onto an equatorial region occupying less than 10% of the surface area of the star (Heger et al. 2007). A possibility is that part of the fresh fuel burns stably at a rate $B(t)$ per unit area while the other part leaks away from this region at a rate $R(t)$. While the material accumulated at a rate $R(t)$ would serve as fuel for a thermonuclear burst, marginally stably burning of the matter on the equatorial belt is (in principle) still possible. Although such scenario cannot explain the frequency drifts we observe, it can explain why mHz QPO and X-ray bursts do occur at the same $\dot{m}$. If mHz QPOs can only occur at a certain local accretion rate $\dot{m}$ ($\simeq \dot{m}_{Edd}$), a small change in effective local accretion rate will lead to an absence of mHz QPOs. This might explain why the mHz QPOs are not always present between X-ray bursts.

Another possibility (which is not taken into account in Heger et al. (2007)'s model) is that there is a significant heat flux from deeper in the star that heats the region undergoing marginally stable burning. For example, changes in heat flux due to energy that is first conducted into deeper layers during an X-ray burst and then slowly outwards towards the surface might be possible. Such a change in the heat flux could affect the conditions of the burning layer (e.g. temperature or burning rate $B(t)$) and therefore could affect the characteristics of the burning processes on the neutron star surface.

Other aspects of the observations offer further challenges for theoretical models that explain burning processes on the neutron star surface as well those which explain atoll sources states. In particular, (i) why the systematic frequency drifts are observed close to the transition between the island and the banana state while the frequencies are approximately constant in the banana state. This may be another indication that the disk geometry of the system is changing during the state transition (see e.g. Gierliński & Done 2002); (ii) why in the transition between island and banana state the oscillations disappear *only* when an X-ray burst occurs, while in the banana state they can also disappear without an X-ray burst (see Section 2.2). Clearly, further theoretical work is needed. More observational work on the interactions between mHz QPOs and X-ray bursts is in progress and will provide further clues for theoretical models.

Acknowledgments: DA wants to thank A. Patruno, P. Cassella, P. Uttley, M. Linares for very helpful discussions. This work was supported by the "Nederlandse Onderzoekschool Voor Astronomie" (NOVA), i.e., the "Netherlands Research School for Astronomy", and it has made use of data obtained through the High Energy Astrophysics Science Archive Research Center Online Service, provided by the NASA/Goddard Space Flight Center. AC is grateful for support from NSERC, Le Fonds Québécois de la Recherche sur la Nature et les Technologies, the Canadian Institute for Advanced Research, and as an Alfred P. Sloan Research Fellow.

The most essential factor is persistence - the determination never to allow your energy or enthusiasm to be dampened by the discouragement that must inevitably come.

James Whitcomb Riley

3 Discovery of coherent millisecond X-ray pulsations in Aql X-1

P. Casella, D. Altamirano, A. Patruno, R. Wijnands, and M. van der Klis

Astrophysical Journal Letters, 2008, 674, 41

Abstract

We report the discovery of an episode of coherent millisecond X-ray pulsation in the neutron star low-mass X-ray binary Aql X-1. The episode lasts for slightly more than 150 seconds, during which the pulse frequency is consistent with being constant. No X-ray burst or other evidence of thermonuclear burning activity is seen in correspondence with the pulsation, which can thus be identified as occurring in the persistent emission. The pulsation frequency is 550.27 Hz, very close (0.5 Hz higher) to the maximum reported frequency from burst oscillations in this source. Hence we identify this frequency with the neutron star spin frequency. The pulsed fraction is strongly energy dependent, ranging from <1% at 3-5 keV to >10% at 16-30 keV. We discuss possible physical interpretations and their consequences for our understanding of the lack of pulsation in most neutron star low-mass X-ray binaries. If interpreted as accretion-powered pulsation, Aql X-1 might play a key role in understanding the differences between pulsating and non-pulsating sources.

3.1 Introduction

Accretion-powered millisecond X-ray pulsars (hereinafter AMXPs) had been predicted in the early 1980s as the progenitors of millisecond radio pulsars (Backer et al. 1982; Alpar et al. 1982). The first observational indication that neutron stars in low-mass X-ray binaries (LMXBs) rotate rapidly came in 1996 with the discovery of slightly drifting in frequency millisecond oscillations during thermonuclear X-ray bursts (for a review see Strohmayer & Bildsten 2006). However it was not until 1998 that the first AMXP was discovered (Wijnands & van der Klis 1998a). Since then, a total of eight AMXPs have been found out of the >150 LMXBs known up to date (Liu et al. 2007).

Since the theoretical prediction of the existence of AMXPs was made, the main issue remained to explain the lack of pulsation in the persistent X-ray emission of the majority of LMXBs. In recent decades many theoretical efforts have been made to explain this, the main question remaining whether the pulsation is hidden from the observer or not produced at all. At present, the scenarios most often considered are: [i] the magnetic field in non-pulsating LMXBs is too weak to allow channeling of the matter onto the magnetic poles; [ii] the magnetic field has comparable strength inside most LMXB neutron stars, but in the large majority of them it has been "buried" by accretion, resulting in a very low surface magnetic field (e.g. Cumming et al. 2001) which again is too weak to allow channeling of matter. After the accretion stops, the magnetic field eventually emerges from the neutron star surface and assumes its intrinsic value; [iii] pulsations *are* produced in all LMXBs, but in most of them they are attenuated by a surrounding scattering medium that washes out the coherent beamed pulsation (Brainerd & Lamb 1987; Kylafis & Klimis 1987; Titarchuk et al. 2002); [iv] the pulsations are attenuated by gravitational lensing from the neutron star (e.g. Meszaros et al. 1988).

From an observational point of view, since the discovery of the first AMXP efforts have been focused on finding differences between the sources showing pulsation and those that do not, in order to test different theoretical hypotheses. Possible observed differences so far are the orbital period (which is on average shorter in AMXPs than in other LMXBs, see e.g. Kaaret et al. 2006) and the time-averaged accretion rate (which is considered to be on average smaller in AMXPs than in other LMXBs, see e.g. Galloway 2006). However, although it is probable that orbital period and time-averaged accretion rate play an important role in the determination of AMXP properties, the reason for the lack of pulsation in most of LMXBs still has to be found.

The properties of the seventh discovered AMXP (HETE J1900.1-2455, Kaaret et al. 2006; Galloway et al. 2007) gave new insights on this issue. This source has a much higher inferred time-averaged accretion rate than in the other AMXPs. The pulsation became undetectable after two months from the beginning of the outburst, at strong variance with the other AMXPs in which pulsations were always detectable until the end of the outbursts. This has been interpreted as evidence for burying of the magnetic field by the accreted material during the outburst (Galloway et al. 2007).

Transient highly coherent pulsations were also observed in the neutron star system 4U 1636-53 (Strohmayer & Markwardt 2002) during an ~800 s interval. However, the pulsations were detected at the flux maximum of a superburst, hence they were likely nuclear-powered. This is different compared to the seven AMXP, where pulsations were interpreted in terms of an hot spot resulting from magnetic channeling of matter onto the neutron star surface.

We are searching the full Rossi X-ray Timing Explorer (RXTE) archive data for coherent pulsations (see also Chapter 4; Altamirano et al. 2008a). In this letter we report on the discovery of an episode of coherent millisecond X-ray pulsations in the neutron star binary Aql X-1. The LMXB recurrent X-ray transient Aql X-1 is an atoll source (Reig et al. 2000) which shows kHz quasi-periodic oscillations, X-ray bursts and burst oscillations (Zhang et al. 1998b). An orbital period of 18.95 hr was obtained by optical measurements (Chevalier & Ilovaisky 1991; Welsh et al. 2000). The presumed onset of the propeller effect (Illarionov & Sunyaev 1975; Stella et al. 1986) allowed Campana et al. (1998) to estimate a value for the magnetic field of $1-3\times10^{8}(\frac{D}{2.5kpc})$ G, consistent with the magnetic field expected (and later on measured) in AMXPs (see also Zhang et al. 1998a).

We analyzed RXTE archive data of Aql X-1 and found that the source showed coherent pulsation at a frequency near the neutron star spin frequency (as inferred from burst oscillations) in its persistent emission for 150 seconds during the peak of its 1998 outburst. The discovery of this pulsation episode may provide new insights on the issue of why some LMXBs pulse and some do not, after many years of debate.

3.2 Data Analysis

We analyzed the whole PCA public archive of Aql X-1, searching for coherent pulsation in its persistent emission. A total of 363 observations were analyzed. In addition to the two Standard Modes always present, the PCA data in different observations were obtained in two different high-time resolution modes (either Event Mode [125μs] or GoodXenon [$\sim 1\mu$s]); to all data we applied barycenter correction for Earth and satellite motion. For each observation we computed fast Fourier transforms from 128s data intervals (after filtering

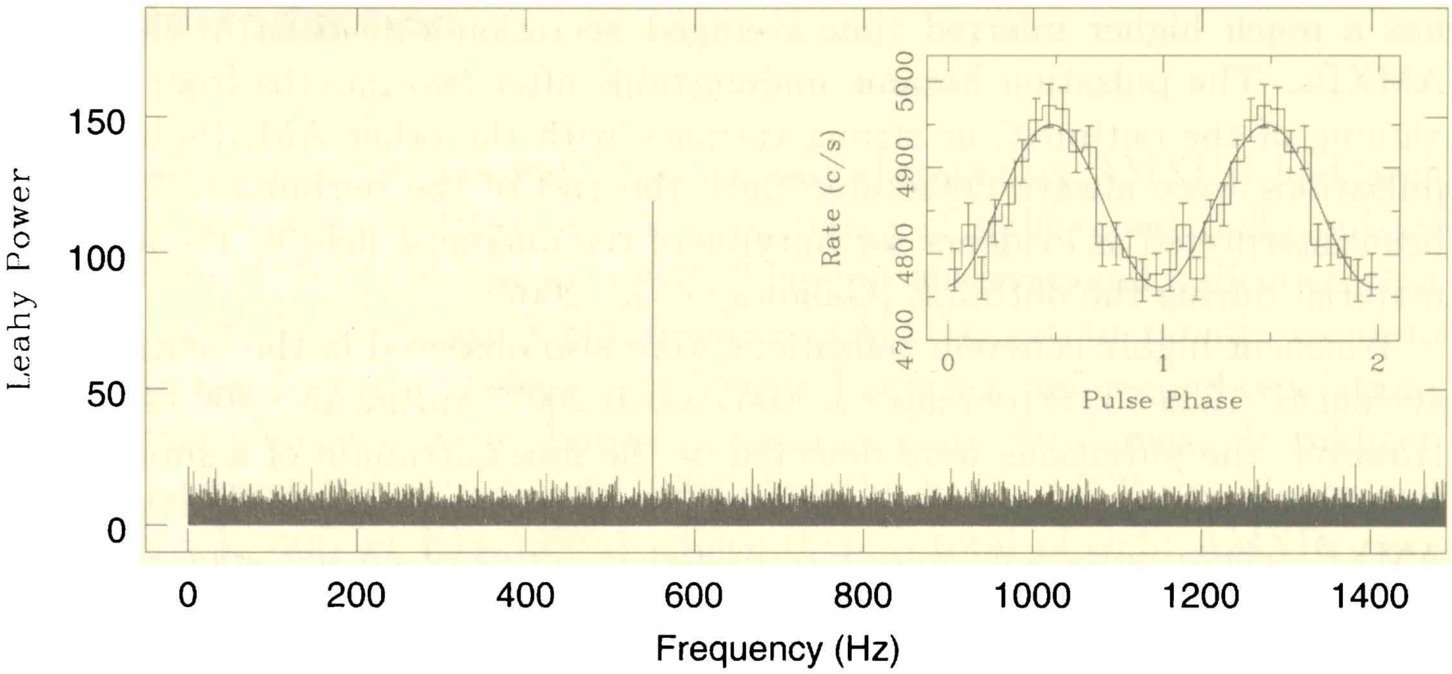

Figure 3.1: Power spectrum of the last 128s data interval of observation 30188-03-05-00 (see Figure 3.2). The power spectrum was obtained from the full bandpass event mode data. The frequency resolution is 1/128 Hz. The pulse is clearly visible at ~550 Hz. In the inset we plot the 2-60 keV light curve folded at the pulsation period. Two cycles are plotted for clarity. The solid line shows the best sinusoidal fit.

for the presence of X-ray bursts) and obtained power spectra with a Nyquist frequency of 4096 Hz and a frequency resolution of 1/128 Hz. We searched all power spectra for significant power at frequencies close to the expected pulse frequency (~550 Hz). Only one detection was found with a Leahy power of 120 (Leahy et al. 1983), corresponding to a single trial chance probability of 9×10^{-27} at a frequency of 550.27 Hz (see Figure 3.1).

The single trial significance of the pulsation is 11σ. Once we take into account the number of trials (i.e. the number of frequency bins times the number of 128 s power spectra we searched) the significance becomes 9σ (3×10^{-17} chance probability). Combined with its frequency being near that of the previously observed burst oscillations, we conclude that the pulsation is real and intrinsic to Aql X-1 and represents the spin of the neutron star in this source. A full description of the total data analysis is beyond the scope of this letter and will be the subject of a forthcoming publication. Here we focus on the detailed analysis performed of the single observation where pulsation was discovered.

The pulsation was detected at the end of a 1600-second long observation starting on 1998 March 10 at 22:28 UT (ObsId: 30188-03-05-00). All five proportional counter units were active during the whole observation, with a total 2-60 keV count rate varying between 4500 and 5500 counts/sec. During this observation high-time resolution data were available in Event Mode with

$125\mu s$ time resolution and 64 energy channels over the 2-60 keV instrument bandpass. The light curve of the observation is shown in the top panel of Figure 3.2.

The high power was detected in the last 128s interval of the observation. By using an epoch folding technique we obtain a period estimate of 1.8172746 ms. The folded profile was well modeled with a sinusoidal component with 1.9 ± 0.2 % amplitude (see inset of Figure 3.1). No second harmonic could be detected, with a 95% upper limit on the amplitude of 0.8 %. To study the evolution and the properties of the signal we extracted a light curve with maximum time resolution, divided it into 16-second segments and determined the pulsation amplitude and phase in each segment by an epoch folding technique (see Figure 3.2). The pulsation is detected for $\sim$ 150 seconds at the end of the observation; its amplitude gradually increases and then decreases again over these 150 seconds. To estimate the accuracy on our period measurement we performed a linear fit to the phases in the interval where pulsations are detected. Over this interval the phase is consistent with being constant. From a 3σ upper limit of 10^{-3} s^{-1} on the slope we derive a best period measurement of 1.817275(3) ms. The short duration of the pulsation did not allow us to obtain any useful upper limit on the frequency drift. From the number of cycles we were able to phase connect we can estimate the coherence of the pulsation as $Q \geq 8 \times 10^4$. No correction for the binary orbital motion was possible, given the small expected drift (< 2 mHz in 150 seconds) and the large uncertainty on the orbital phase ($\sim$80%, applying the orbital solution from Welsh et al. 2000).

In order to study the energy dependence of the pulsation we extracted light curves with maximum time resolution in different energy ranges and determined the pulsation amplitude and phase in each of them. In Figure 3.3 we show the amplitude vs. energy diagram. The pulsation shows a strong energy dependence, being not detected at low energies (with an upper limit on its amplitude of $\sim$1% below 5 keV) and strong at high energies.

3.3 Discussion

We discovered millisecond X-ray pulsations in the persistent X-ray emission of the LMXB Aql X-1. The pulsation is transient, present for only $\sim$150 seconds and has an average fractional amplitude (over the full 2-60 keV instrumental bandpass) of $\sim$2%, increasing up to >10% at energies above $\sim$16 keV. It appears and disappears gradually, on a time scale of a few tens of seconds, with a 3σ upper limit on its amplitude of 0.7% during the $\sim$128 seconds before its appearance.

This pulsating episode appears to be unique in the whole RXTE archive

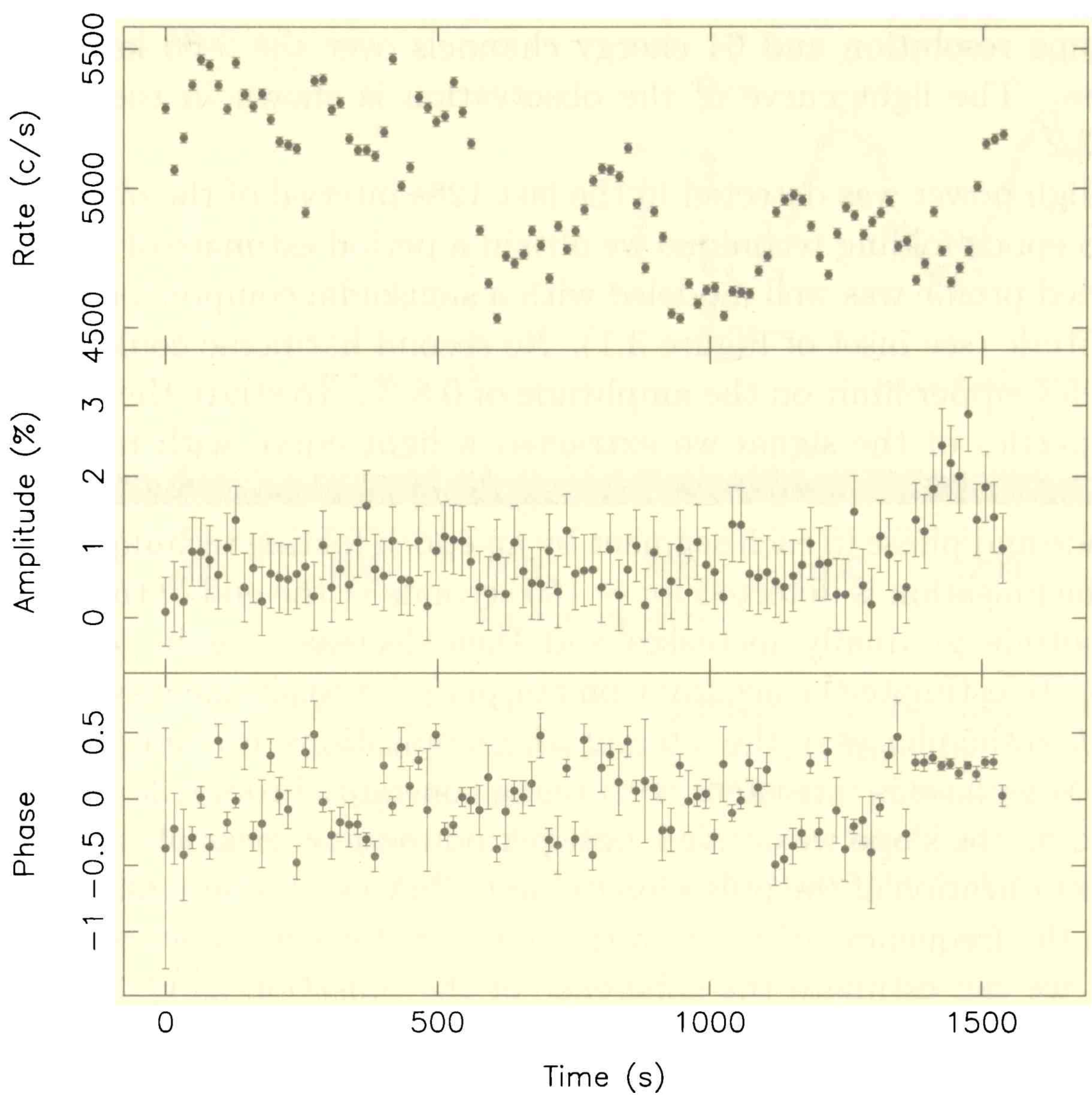

Figure 3.2: *Top panel*: 2-60 light curve with 16 seconds bin size. *Bottom panels*: Amplitude (*middle*) and phase (*bottom*) by epoch folding technique every 16 seconds, vs. time. Values of amplitude and phase between 0 and ~1400 s are consistent with those expected from Poissonian noise.

of Aql X-1 observations. In one third of the observations (corresponding to an exposure of 500 ks) the count rate is high enough to allow the detection (3σ, single trial) of a similar pulsating episode as the one we observed. Even considering only these data (instead of the total analyzed exposure of 1300 ks) we obtain a recurrence rate smaller than 3×10^{-4}. Such rarity in itself is extremely informative. Any physical interpretation must not only in fact explain the appearance of the pulsation, but also its extremely low occurrence rate.

The frequency of the pulsation is 550.27 Hz, ~0.53 Hz higher than the reported asymptotic frequencies for burst oscillations in this source (Zhang et al. 1998b). The light curve shows no evidence of an X-ray burst or other obvious feature within 1500 seconds before the appearance of the pulsation. Together with its high coherence, this leads us to conclude that the observed pulsation arises from a hot spot spinning with the neutron star. This makes Aql X-1 the millisecond X-ray pulsar with the longest orbital period and with the highest time-average accretion rate known at present.

The detection of this fast appearing pulsation in a LMXBs leads once again to the same question: is the pulsation in Aql X-1 usually hidden from the observer, by some scattering or screening medium that very rarely disappears (or strongly reduces its optical thickness) for ~150 seconds? Or is the pulsation usually absent, the episode we discovered being the result of an occasional and rare asymmetry on the neutron star surface?

In the following we analyze different possible scenarios.

3.3.1 Permanent pulsation

If a hot spot is normally present on the neutron star surface the question is what made it observable only for ~150 seconds. Different authors have argued against or in favor of the hypothesis that in non-pulsating sources the pulsation is washed out by some optically thick scattering media. The main issue is the value of the optical depth τ needed to attenuate the beamed oscillations. Psaltis & Chakrabarty (1999) discuss the apparent similarities between values of τ in pulsating and non-pulsating sources, and discard this hypothesis. Titarchuk et al. (2002) report on spectral fits giving other values of τ (for different sources), and conclude that the data *do* support this hypothesis. More recently, Göğüş et al. (2007) report on new, independent spectral fits and conclude that in non-pulsating LMXBs τ is not large enough to cause the pulsations to disappear (unless the electron temperature is very low, see also Titarchuk et al. 2007).

This issue appears to be difficult to resolve, mainly because of a substantial degeneracy between optical depth and electron temperature in the spectral fits. However, the pulsation episode in Aql X-1 now allows us to provide new insights into this issue. Even though due to their degeneracy the absolute values of spectral parameters can not be properly constrained, one would expect them to change when the pulsation appears. In particular, the appearance of the pulsation, if caused by a temporary (total or local) decrease of the optical depth of the scattering media, is expected to be accompanied by a decrease of the comptonization parameter, hence by a softening of the energy spectrum. However our spectral fits show that a two-component model (disk plus boundary layer) is sufficient to fit the data, without the need for any additional comptonized component. Moreover, neither spectral fitting nor analysis of hardness light curves show any evidence of spectral variability associated with the appearance of the pulsation. Furthermore, the similarities between the spectral properties of Aql X-1 and many other LMXBs would lead one to

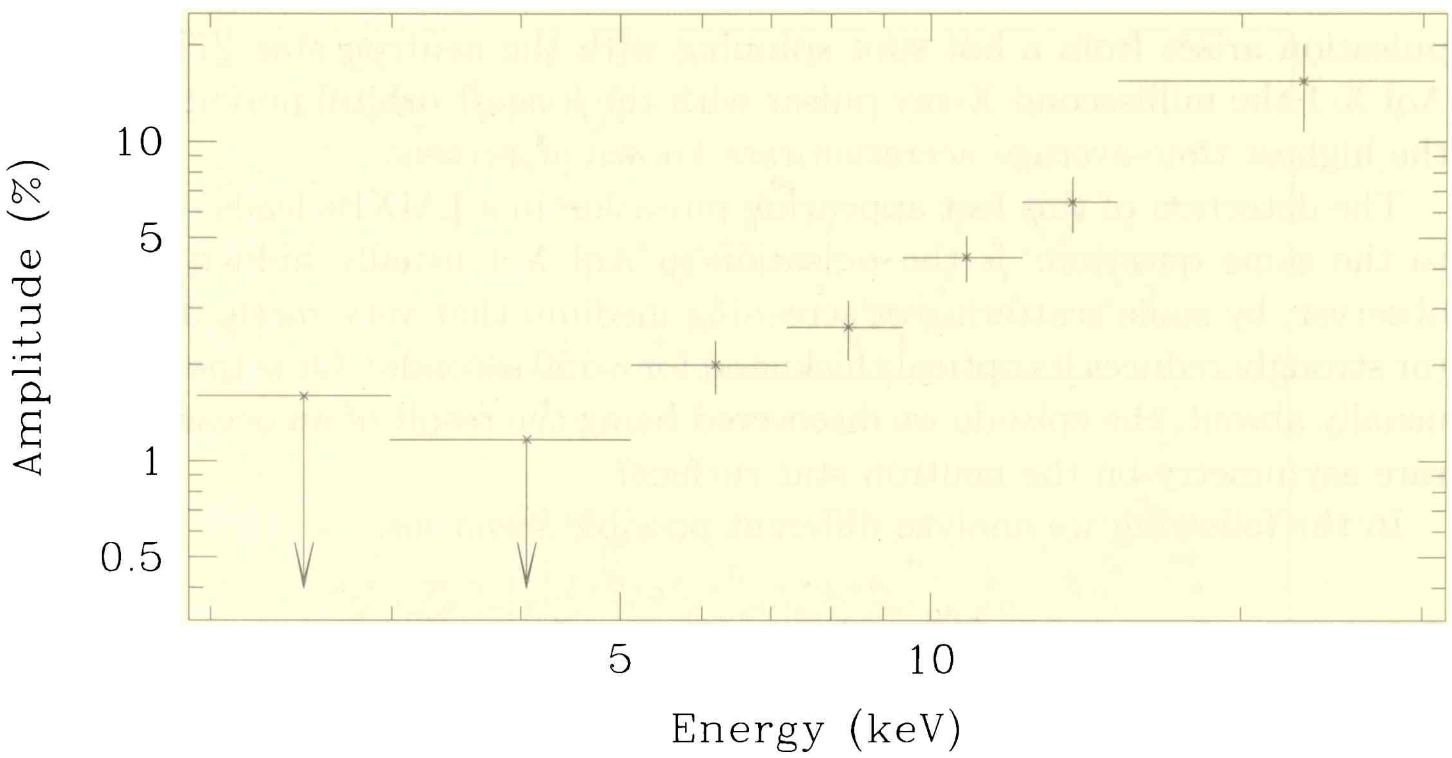

Figure 3.3: Amplitude of the pulsation as a function of energy. 1σ errors are shown.

expect similar episodes of pulsation in most of LMXBs. On the other hand, the very hard spectrum of the observed pulsation (see Figure 3.3) suggests that the beamed radiation is strongly comptonized (for a discussion on the expected energy dependence in the case of the screening scenario see Falanga & Titarchuk 2007).

An alternative could be to assume a non-isotropic screening medium: an occasional and rare hole in the medium or a reflecting cloud could have allowed the radiation from the hot spot to avoid the screening medium, thus becoming visible. Finally, the hot spot itself could have moved becoming temporally visible, either because of a different absorption through the line of sight or because of a change in the rotational of gravitational lensing geometry. We note that all these hypotheses could in principle be consistent with the observed gradual increase and decrease of the pulsation amplitude, but require very special and fine-tuned geometries.

Estimate of the magnetic field

Under the standard magnetic channeling hypothesis for creating the hot spot we can give an estimate of the magnetic field. The magnetic field must be strong enough to locally disrupt the disk flow. The pulsation episode happens when the source is in the soft state, close to the peak of the outburst. The 2-10 keV flux is $\sim 8.8 \times 10^{-9}$ erg s^{-1} cm^{-2} which corresponds, assuming a distance of 5 kpc (Jonker & Nelemans 2004) and a bolometric correction of 1.4 (Migliari & Fender 2006), to a bolometric luminosity of $\sim 3.7 \times 10^{37}$ erg s^{-1} $\sim 0.15 L_{Edd}$. Given the relatively high luminosity, by imposing that the radius at which this happens is larger than the neutron star radius we can derive a stringent lower limit on the magnetic dipole moment (Psaltis & Chakrabarty 1999) as $\mu \geq 0.47 \times 10^{26}$ G cm^3 which corresponds to a magnetic field of $\sim 10^8$ G at the pole.

This lower limit is consistent with the upper limit of $\sim 1.8 \times 10^9$ G obtained by Di Salvo & Burderi (2003) from the quiescent luminosity and with the estimate of $\sim 2 - 6 \times 10^8$ G obtained by Campana et al. (1998, assuming a corrected distance of 5 kpc instead of 2.5 kpc) from the reported onset of the propeller effect. Furthermore, our lower limit rules out the hypothesis of residual accretion onto the neutron star to explain the quiescent X-ray luminosity in Aql X-1, for which an upper limit for the magnetic field of $\sim 4 \times 10^7$ G had been derived (hypothesis a1 of Di Salvo & Burderi 2003).

3.3.2 Transient pulsation

The second possibility is that of a temporary asymmetry on the neutron star surface. Let us examine possible causes:

(I) Magnetic channeling: Accretion rate and magnetic field are the two key physical quantities playing a role in channeling of matter. A transient episode of channeling of matter could arise due to a temporary change in the accretion rate (although the X-ray flux, which is thought to be a good indicator of $\dot{M}$, does not show any variability correlated with the appearance of the pulsation) or a change in the accretion geometry. An alternative is the occurrence of some variability of the magnetic field. In the "burying" scenario timescales for the magnetic field to emerge are set by the Ohmic diffusion time and are at least of the order of 100-1000 yr (Cumming et al. 2001), obviously far larger than the few tens of seconds observed in Aql X-1. However a local temporary decrease of the Ohmic diffusion timescale could in principle let the magnetic field emerge. Possible causes could be a temporary local disruption of the screening currents, a star quake, or magnetic re-connections. Perhaps, a temporary local magnetic loop might form, somewhat similar to those observed in the solar corona, where hot coronal plasma "populates" different field lines. The magnetic field in this loop might be *locally* strong enough to disturb the flow of matter onto the neutron star surface. The resulting hot spot (not necessarily on the magnetic pole) could create the observed pulsation.

(II) Nuclear burning: The hot spot might be associated to a confined nuclear burning event. After its onset nuclear burning is expected to spread over the neutron star surface in a very short timescale. Hence one would not expect the resulting pulsation to last more than a few seconds. However the burst oscillations observed in many sources during the decay of X-ray bursts strongly challenge this simplified picture. Moreover, the discovery of a very coherent pulsation during a superburst in 4U 1636-53 (Strohmayer & Markwardt 2002) showed that long-lived, very coherent pulsations might arise due to nuclear burning. However the lack of any other X-ray signature of nuclear burning (such as an X-ray burst) associated with the pulsation in Aql X-1 strongly argues against this hypothesis.

(III) Surface wave: An asymmetry on the neutron star surface might result from an unstable surface mode, as the ones suggested to explain burst oscillations (see e.g. Piro & Bildsten 2004; Narayan & Cooper 2007). Since the amplitudes of surface modes have been predicted to increase with energy (Piro & Bildsten 2006), the hard energy dependence observed in Aql X-1, more similar to that of burst oscillations than that of accretion-powered pulsations, supports this possibility.

(IV) Other possibilities: The extreme rarity of this pulsation episode leads us to examine also more exotic physical explanations. Possible origins for a transient hot spot could be a self-luminous magnetic event on the neutron star surface, as magnetic re-connections or annihilations, or a sudden release of potential energy in the deep crust during a star quake.

Finally, we mention the possibility that some of the discussed instabilities could arise do to a collision with an external body (see e.g. Colgate & Petschek 1981). The fluence of the observed pulsation is $\sim 10^{35}$ergs, which corresponds to the free fall kinetic energy of a mass of $\sim$15 km^3 of iron. However, the observed gradual increase in the pulsation amplitude would be difficult to explain within this scenario. The probability to have such an impact is presumably extremely low. On the other hand, the observed event *is* very rare.

Whatever is the physical origin of the observed pulsations, their discovery implies the possible occurrence of transient pulsations in any of the *apparently* non-pulsating LMXBs (see, e.g., Chapter4).

Acknowledgments: The authors would like to thank A. Gurkan, G. Israel, and L. Stella for very useful comments and stimulating discussions. We also thank L. Bildsten and R. Cooper for pointing out the surface mode possibility.

Forecasting future events is often like searching for a black cat in an unlit room, that may not even be there.

Steve Davidson

4 Intermittent millisecond X-ray pulsations from the neutron-star X-ray transient SAX J1748.9–2021 in the globular cluster NGC 6440

D. Altamirano, P. Casella, A. Patruno, R. Wijnands and M. van der Klis

Astrophysical Journal Letters, 2008, 674, 45

Abstract

We report on intermittent X-ray pulsations with a frequency of 442.36 Hz from the neutron-star X-ray binary SAX J1748.9–2021 in the globular cluster NGC 6440. The pulsations were seen during both 2001 and 2005 outbursts of the source, but only intermittently, appearing and disappearing on timescales of hundreds of seconds. We find a suggestive relation between the occurrence of Type-I X-ray bursts and the appearance of the pulsations, but the relation is not strict. This behavior is very similar to that of the intermittent accreting millisecond X-ray pulsar HETE J1900.1–2455. The reason for the intermittence of the pulsations remains unclear. However it is now evident that a strict division between pulsating and non-pulsating does not exist. By studying the Doppler shift of the pulsation frequency we determine an orbit with a period of 8.7 hrs and an projected semi major axis of 0.39 lightsec. The companion star might be a main–sequence or a slightly evolved star with a mass of $\sim$1 $M_{\odot}$. Therefore, SAX J1748.9–2021 has a longer period and may have a more massive companion star than all the other accreting millisecond X-ray pulsars except for Aql X-1.

4.1 Introduction

Accreting millisecond pulsars (AMXPs) are transient low mass X-ray binaries (LMXBs) that show X-ray pulsations during their outbursts. A total of nine AMXPs out of 100 non-pulsating LMXBs have been found to date. The reason why only this small subgroup of binaries pulsates is still unknown. The first seven AMXPs discovered showed persistent X-ray pulsations throughout the outbursts. Recently Kaaret et al. (2006) discovered the AMXP HETE J1900.1–2455, which has remained active for more than 2.5 years[1] but showed pulsations only intermittently during the first $\sim$ 2 months of activity (Galloway et al. 2007). From the transient source Aql X-1 pulsations were detected (see Chapter 3) only for $\sim$ 150 sec out of the $\sim$ 1.5 Msec the source has (so far) been observed with the Rossi X-ray Time Explorer (RXTE).

Gavriil et al. (2006, 2007) recently reported on the detection of $\sim$ 442.3 Hz pulsations in an observation of the 2005 outburst of a transient source in the globular cluster (GC) NGC 6440. The pulsations followed a flux decay observed at the beginning of the observation and were reminiscent of those observed during superbursts; however, as Gavriil et al. (2007) suggest, they could also be a detection from a new intermittent accreting millisecond pulsar. Kaaret et al. (2003b) report a 409.7 Hz burst oscillation in an X-ray transient (SAX J1748.9–2021) located also in NGC 6440 and this GC harbors at least 24 X-ray sources (Pooley et al. 2002), so Gavriil et al. (2007) concluded that the burst oscillations and the pulsations were probably coming from different X-ray transients in the same GC.

The exact formation mechanisms behind the pulsations of these three sources remains unknown. The existence of intermittent pulsations with a small duty cycle implies that many other apparently non-pulsating LMXBs might be pulsating, bridging the gap between the small number of AMXPs and the large group of non-pulsating LMXBs.

We are performing a detailed analysis of all RXTE archival data of neutron-star LMXBs to search for transient pulsations in their X-ray flux (see also Chapter 3). In this Letter we present the results of our search on the three X-ray outbursts observed from the globular cluster NGC 6440.

[1] At the time of submitting this letter, the source is still active.

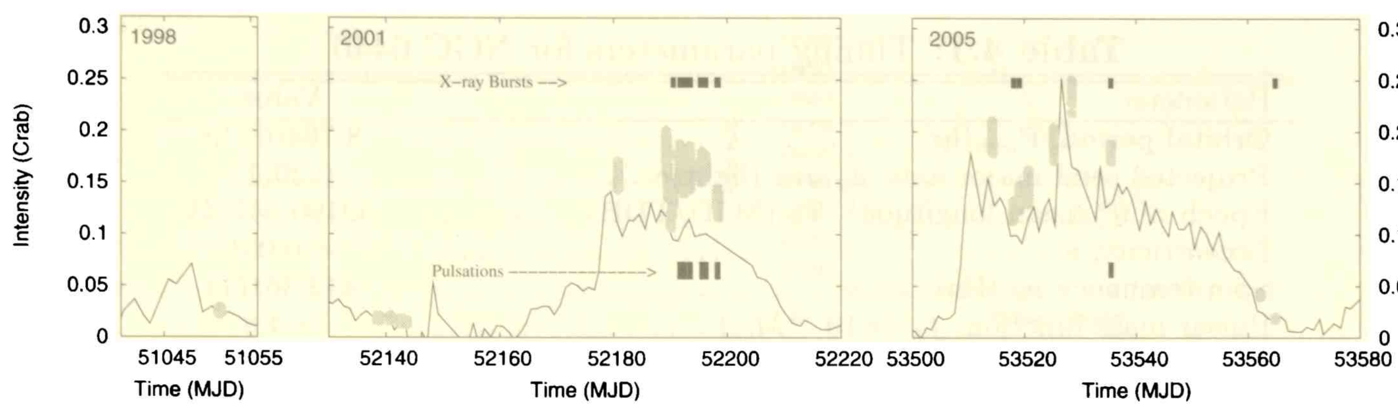

Figure 4.1: Intensity (2.0–16.0 keV) normalized by Crab vs. time of the three outbursts. Gray symbols show the 16-sec averaged intensity during the pointed PCA observations. The continuous line shows the ASM light curve. Black marks at the *top* mark the times of Type-I X-ray bursts. Black marks at the *bottom* mark the times when we detect significant pulsations. Years of the outburst is shown in each panel.

4.2 The neutron-star transient SAX J1748.9–2021 in NGC 6440

NGC 6440 is a GC at 8.5 ± 0.4 kpc (Ortolani et al. 1994). Bright X-ray outbursts from a LMXB were reported in 1971, 1998, 2001 and 2005 (Markert et al. 1975; in 't Zand et al. 1999; Verbunt et al. 2000; in't Zand et al. 2001; Markwardt & Swank 2005). in't Zand et al. (2001) from X-ray and optical observations concluded that the 1998 and 2001 outbursts were from the same object, which they designated SAX J1748.9–2021.

4.3 Observations, data analysis and results

We used data from the RXTE Proportional Counter Array (PCA, for instrument information see Jahoda et al. 2006). Up to July, 2007, there were 27 pointed observations of SAX J1748.9–2021, each covering 1 to 5 consecutive 90-min satellite orbits. Usually, an orbit contains between 1 and 5 ksec of useful data separated by 1–4 ksec data gaps due to Earth occultations and South Atlantic Anomaly passages. Adopting a source position ($\alpha = 17^h48^m52^s.163$, $\delta = -20^o21'32''.40$; J2000, Pooley et al. 2002) we converted the 2–60 keV photon arrival times to the Solar System barycenter with the FTOOL faxbary, which uses the JPL DE-200 ephemeris along with the spacecraft ephemeris and fine clock corrections to provide an absolute timing accuracy of 5-8 μs (Rots et al. 2004).

We performed a Fourier timing analysis using the high-time resolution data collected in the Event (E_125us_64M_0_1s) and the Good Xenon modes. Power

Table 4.1: Timing parameters for NGC 6440

Parameter	Value
Orbital period, P_{orb}(hr)	8.764(6) hr
Projected semi major axis, $a_x sini$ (lightsec.)	0.39(1)
Epoch of 0^o mean longitude[1], T_0 (MJD/TDB)	52190.047(4)
Eccentricity, e	< 0.001
Spin frequency ν_0 (Hz)	442.361(1)
Pulsar mass function, f_x ($\times 10^{-4} M_\odot$)	$\simeq 4.8$
Minimum companion mass, M_c ($M_\odot$)	$\gtrsim 0.1$

[1]The mean longitude at 0^o in a circular orbit corresponds to the ascending node of the orbit.

spectra were constructed using data segments of 128, 256 and 512 seconds and with a Nyquist frequency of 4096 Hz. No background or dead-time corrections were made prior to the calculation of the power spectra, but all reported rms amplitudes are background corrected; deadtime corrections are negligible.

4.3.1 Colors, light curves and states

From the Standard 2 data (Jahoda et al. 2006), we calculated colors and intensities with a time resolution of 16 seconds and normalized by Crab (see, e.g., see Chapters 5, 6, 7 & 8). The PCA observations sample three different outbursts (see Fig. 4.1). The color-color diagrams show a pattern (not plotted) typical for atoll sources. The power spectral fits confirm the identification of these states (see also Kaaret et al. 2003b). We looked for kHz QPOs, but found none.

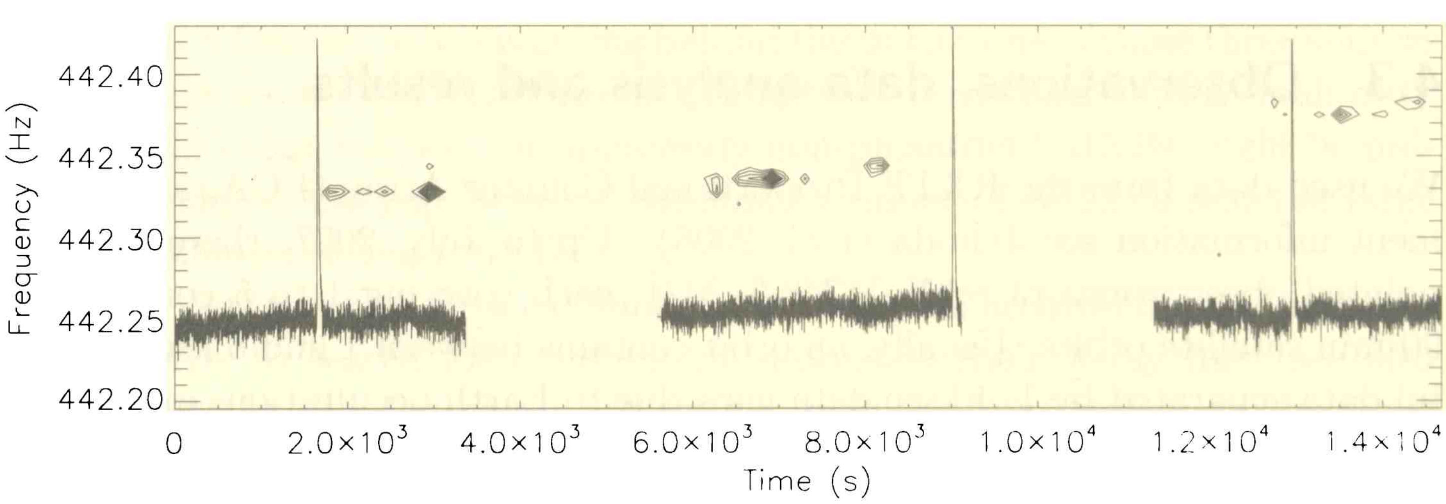

Figure 4.2: Dynamical power spectrum of observation 60035-02-03-00 showing intermittent pulsations (contours). In the light curve (line) three X-ray bursts are seen. The pulse frequency drifts due to orbital Doppler modulation. The lowest contour plotted corresponds to Leahy power 13 and the highest to 55. The contours were generated from power spectra for *non*-overlapping 128 sec intervals of data.

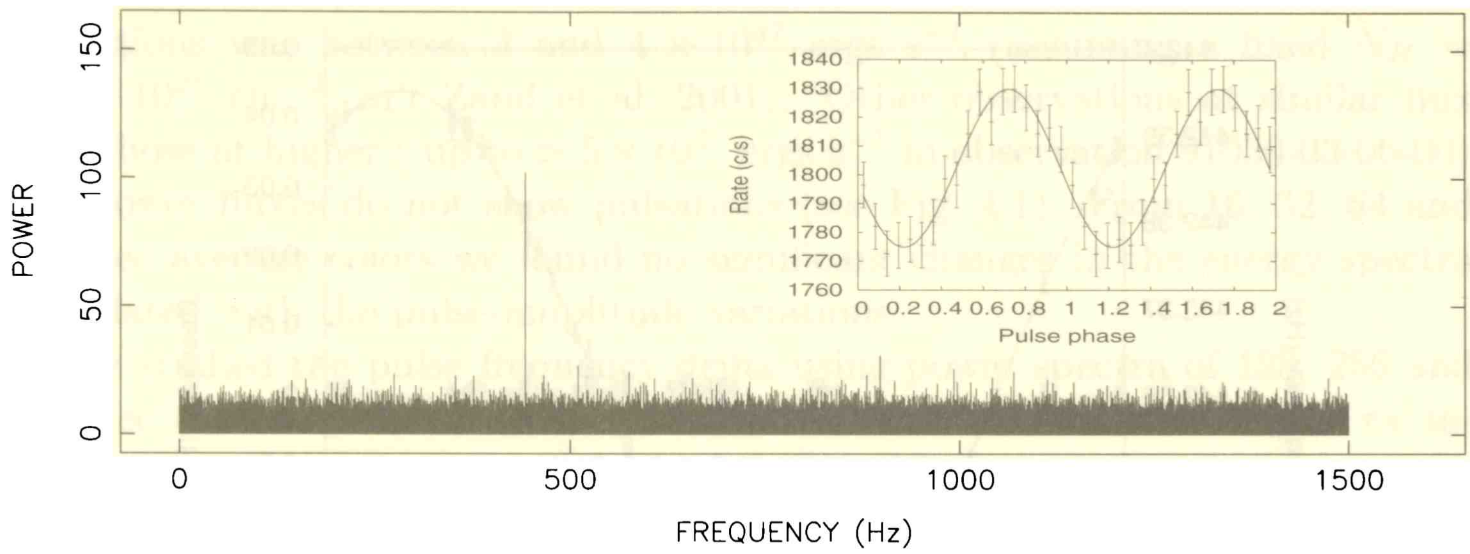

Figure 4.3: Leahy normalized (Leahy et al. 1983) power spectrum of 512 sec of data centered ~ 7 ksec after the start of this observation. Maximum Leahy power is 102, corresponding to a single-trial probability of $\sim 7 \cdot 10^{-23}$ given Poissonian statistics in the photon arrival times (van der Klis 1995a). Inset: The 2–60 keV light curve folded at the 2.26-ms period. Two cycles are plotted for clarity. The pulse profile is sinusoidal, with a 95% upper limit of 0.4% (rms) on the amplitude of the second harmonic.

No thermonuclear bursts were detected in the first outburst, sixteen during the second (Kaaret et al. 2003b; Galloway et al. 2006) and four during the third one. We searched for burst oscillations during all bursts in the 15–4000 Hz frequency range but found none. Kaaret et al. (2003b) reported a $\sim 4.4\sigma$ burst oscillation at ~ 409.7 Hz. We find these authors underestimated the number of trials by a factor of at least 180, as their estimate did not take into account the number of X-ray bursts analyzed and the fact that a sliding window was used to find the maximum power. Moreover, we also found that the distribution of powers is not exponential as these authors assumed. Taking into account these effects we estimate the significance for their detection to be $\lesssim 2.5\sigma$.

4.3.2 Pulsations

We inspected each power spectrum for significant features. We found several, at frequencies ~ 442.3 Hz in 7 observations: 60035-02-02-04/05/06, 60035-02-03-00/02/03 during the second outburst and 91050-03-07-00 during the third outburst (see also Gavriil et al. 2007, for a detailed analysis of this observation). in't Zand et al. (2001) concluded that the 1998 and 2001 outbursts from the LMXB in NGC 6440 were from the same source (Section 2). Since pulsations are detected in both the 2001 and 2005 outbursts, we can now conclude that these two outbursts are also from the same source. Hence, all outbursts

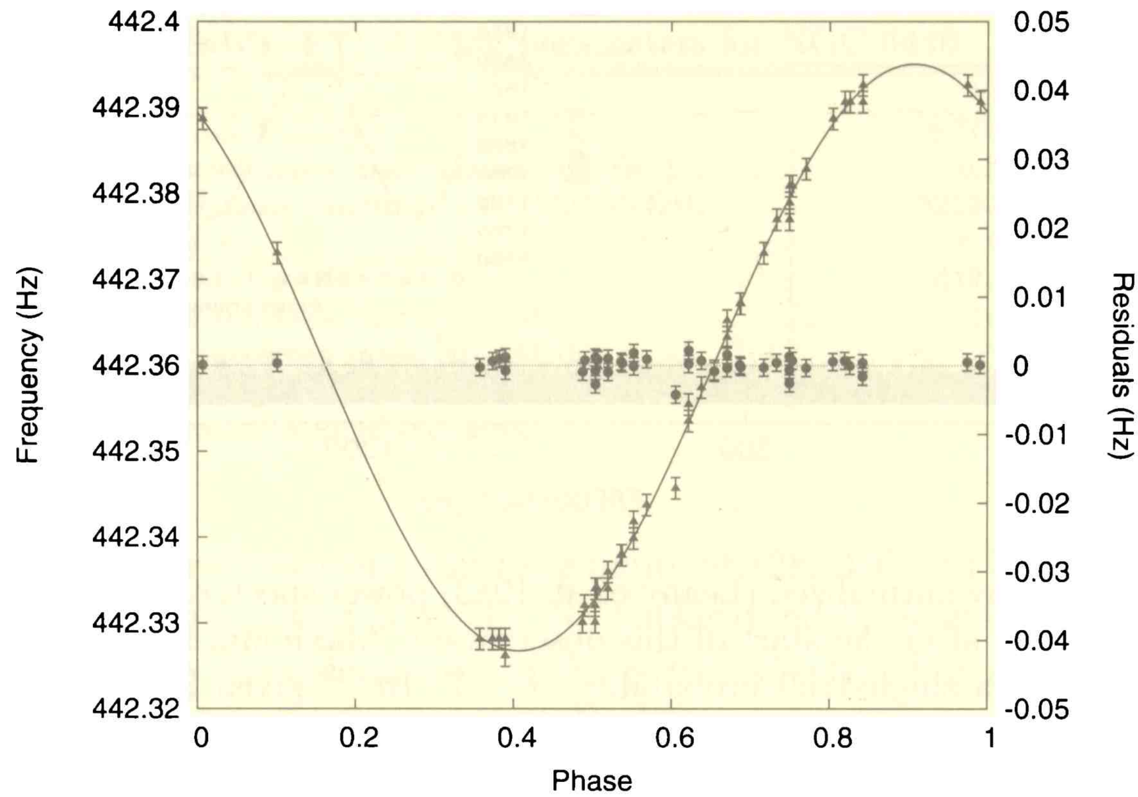

Figure 4.4: Pulse frequency as a function of orbital phase. The plot has been obtained by folding all data between the first and last pulse detection in 2001. Pulsations were detected during 6 of the 18 orbital cycles covered. Drawn curve is the best-fit orbital model, measured frequencies and post-fit residuals are shown. The residuals' r.m.s. is 1.2×10^{-3} Hz.

observed from NGC 6440 over the last decade are from SAX J1748.9–2021.

The pulsations are detected intermittently, appearing and disappearing on time scales of hundreds of seconds. The appearance of pulsations seems to be related to the occurrence of Type-I X-ray bursts, but the relation is not strict. The first two bursts were observed in an observation on October 8^{th} 2001; the first pulsations a day later. During the third outburst we detect four bursts; pulsations were only detected after the third one. We also detected pulsations with no preceding burst. The structure of our data does not allow us to tell if pulsations and/or other bursts occurred during data gaps. Figure 4.2 illustrates the relation between pulsations and bursts. The amplitude of the pulsations varies strongly between $\sim 2\%$ and (often) undetectable (0.3% rms amplitude upper limit at the 95% confidence level). Pulsations are seen right after the occurrence of the first and the third burst, but in the middle of the data pulsations are present without the detection of a preceding burst (although a burst could have happened just before the start of this data segment). In Figure 4.3 we show a power spectrum and corresponding 2–60 keV pulse profile (inset). In these data the pulsation is relatively hard; the rms amplitude increases with energy from $\sim 1\%$ at 3 keV to $\sim 3\%$ at 13 keV.

The 2–10 keV luminosity during the observations in which we detected pulsations was between 3 and 4 $\times$ 10^{37} ergs s^{-1} (assuming a fixed N_H = 8.2 $\times$ 10^{21} cm^{-2}; in't Zand et al. 2001). Other observations at similar flux and those at higher (up to $\simeq 5 \times 10^{37}$ ergs s^{-1} in observation 91050-03-06-00) and lower fluxes do not show pulsations (see Fig. 4.1). From 16, 32, 64 and 128 sec average colors we found no significant changes in the energy spectra correlated with the pulse-amplitude variations.

We studied the pulse frequency drifts using power spectra of 128, 256 and 512 sec data and find a clear 8.7 hours sinusoidal modulation which we interpret as due to Doppler shifts by binary orbital motion with that period. In order to obtain an orbital solution, we performed a χ^2 scan on the orbital parameters using the method described by Kirsch et al. (2004) and Papitto et al. (2005). Our best estimates are listed in Table 4.1. The combination of data gaps and intermittency of the pulsations yielded aliases, which are taken into account in the reported errors. In Figure 4.4 we plot the pulse frequency as a function of orbital phase.

4.4 Discussion

We have discovered intermittent pulsations from the neutron-star LMXB SAX J1748.9–2021. Pulsations appear and disappear on time scales of hundreds of seconds. Although we find a suggestive relation between the appearance of the pulsations and the occurrence of Type-I X-ray bursts (the pulsations appearing after a burst), the relation is not strict. We find bursts with no subsequent pulsations and pulsations with no preceding burst (although a burst could have occurred in the preceding data gaps). From the Doppler shifts on the pulsations we determine that the system is in a near-circular orbit with period of 8.7 hours and projected radius of 0.39 lightsec.

The stability of the pulsations (after correcting for the binary orbit) strongly suggests that the pulsation frequency reflects the neutron star spin frequency and that SAX J1748.9–2021 is an accreting millisecond X-ray pulsar. The characteristics of the pulsations are reminiscent of the those found in the AMXP HETE J1900.1–2455: in both sources the pulsations were only intermittently detected and a possible relation between burst occurrence and pulse amplitude exists. However, there are differences: in HETE J1900.1–2455 the pulsations were only seen during the first two months of the outburst and their amplitude decreased steadily on timescales of days after the bursts which might have caused them to reappear (Galloway et al. 2007). In SAX J1748.9–2021 we find the pulsations in the middle of the 2001 and 2005 outbursts and not in the beginning. Furthermore, the amplitude of the pulsations behaves erratically, switching between detection and non-detection on time scales of

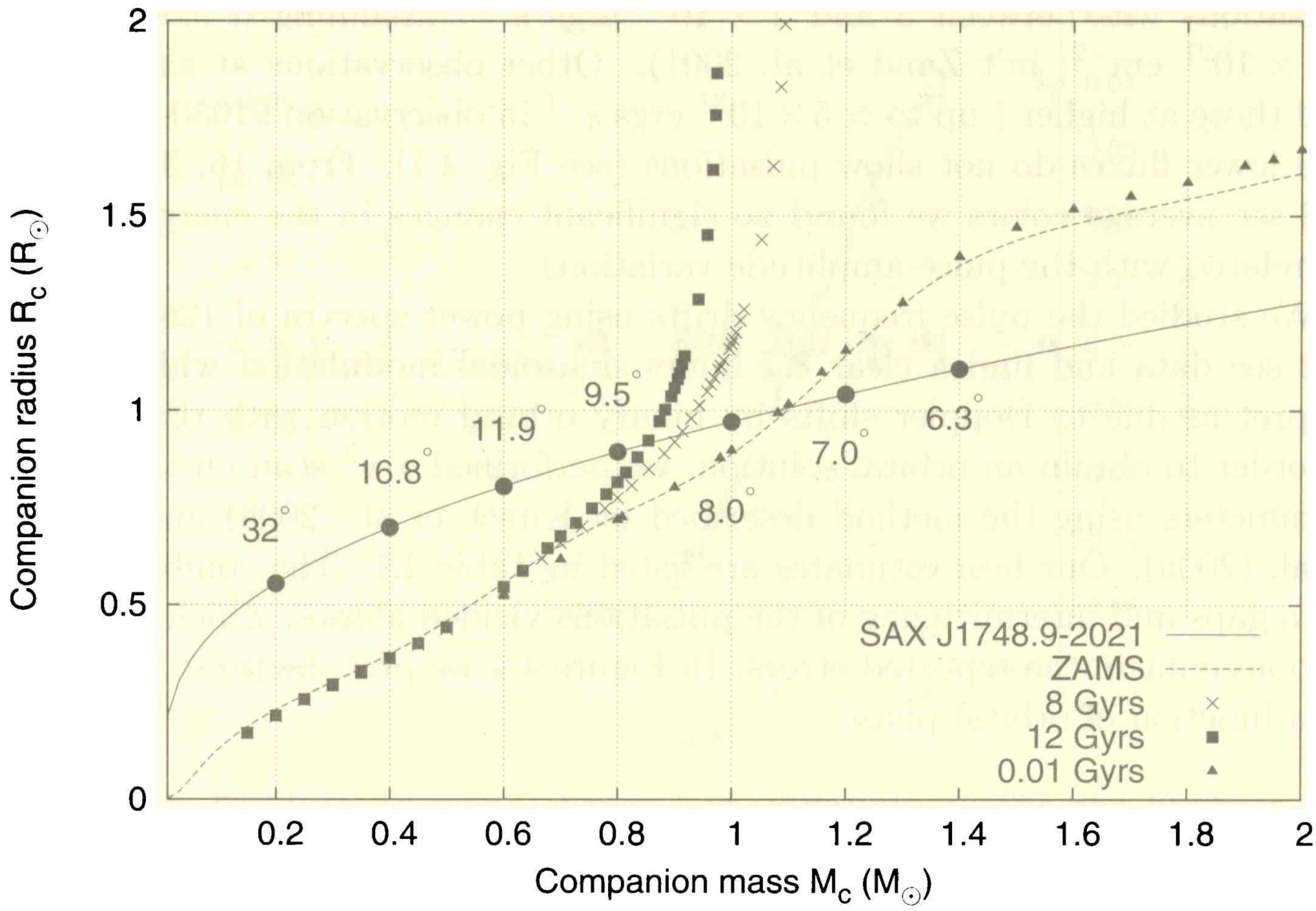

Figure 4.5: Mass–radius relationship for a Roche lobe-filling companion (continuous line), isochrones of 0.01, 8 and 12 Gyrs with solar metallicity (triangles, crosses and squares, respectively ; Girardi et al. 2000) and theoretical Zero-age main sequence (ZAMS, dashed line; Tout et al. 1996). Black circles mark the inclination of the system as estimated by the mass function of this system.

hundreds of seconds. Despite these differences, the behavior of the pulsations in both sources is so similar that we consider it likely that the same mechanism causes the intermittency of the pulsations in both.

A related system might be Aql X-1 in which a short-lived (~150 s) and very rare (duty cycle of 0.03%) episode of strong pulsations at the neutron-star spin frequency has been detected (Casella et al. 2008, see Chapter 3). In this source, no X-rays bursts were seen in the ~ 1400 s before the pulsations, making it unlikely that they were triggered by a burst. It is unclear if the pulsations in Aql X-1 were accretion–driven or due to unusual nuclear burning episodes; the same applies to SAX J1748.9–2021. The extreme rarity of the pulsations in Aql X-1 could indicate that the mechanism behind them is different from that responsible for the pulsations in HETE J1900.1–2455 and SAX J1748.9–2021. Nevertheless, irrespective of the mechanisms behind the pulsations in these three sources, it is clear that a strict division between pulsating and non-pulsating sources cannot be made anymore. It is possible that all sources pulsate occasionally although the recurrence times could be very long.

Assuming a constant dipolar magnetic field, following Psaltis & Chakrabarty (1999) (i.e., assuming a geometrically thin disk and neglecting inner disk wind mass loss, radiation drag and GR effects) we estimate the magnetic field to be $B \gtrsim 1.3 \times 10^8$ Gauss. This assumes a 10 km radius $1.4M_\odot$ neutron star and $\dot{M}_{max}$, the highest accretion rate at which pulses are detected, of 0.28 of the Eddington critical value as derived from the luminosity observed at the time using a bolometric flux correction of 1.4 (Migliari & Fender 2006). In the standard magnetic channeling scenario, the question remains of what causes the large variations in pulse amplitude.

Comparisons between HETE J1900.1–2455, SAX J1748.9–2021 and the other 7 AMSPs can provide clues to understand the pulse-strength variations. In SAX J1748.9–2021 and Aql X-1 the time scales on which the pulse amplitude can fluctuate are as short as $\sim 10^2$ s, too short for the properties of the neutron star core to change (Galloway et al. 2007). So, these changes must originate in the disk or the outer layers of the neutron star envelope. Galloway et al. (2007) suggested (for HETE J1900.1–2455) that the accumulation of matter on the surface burying the magnetic field (Cumming et al. 2001) plays a role. Our results show that this mechanism probably cannot work for SAX J1748.9–2021, as the pulsations are not seen in the beginning of the outbursts, but instead $\sim$ 3 weeks and $\sim$ 5 weeks after the start of the 2001 and 2005 outbursts, respectively, so after a considerable amount of matter has already accreted. Interestingly, we observe pulsations only around a mass accretion rate of $\simeq 2 \times 10^{-16}$ $M_\odot$/sec as inferred from the X-ray luminosity, not above or below, indicating that instantaneous mass accretion rate rather than total accreted mass is the important quantity.

In both HETE J1900.1–2455 and SAX J1748.9–2021 the pulsations seem to appear together with bursts although the exact connection is complex. This suggests that surface processes may affect the magnetic field. Hydrodynamic flows in the surface layer of the neutron star may screen the magnetic field (see review by Bhattacharya 2002, and references within); perhaps violent processes like bursts temporarily affect such flows, diminishing screening and enhancing the channeling.

Alternatively, variations in a scattering or screening medium may cause the pulse amplitude modulation (see e.g. discussions in Psaltis & Chakrabarty (1999), Titarchuk et al. (2002), Göğüş et al. 2007, Titarchuk et al. 2007, Chapter 3 and references within). For our results, the properties of such a medium should change on timescales of hundreds of seconds; note that we did not detect spectral changes associated with pulse strength modulation.

With an orbital period of $\sim$ 8.7 hours, this binary system is clearly not an ultra-compact binary as usually found in globular clusters and in fact, SAX J1748.9–2021 is the AMSP with the longest orbital period after Aql X-1, which has an orbital period of $\sim$ 19 hrs (Chevalier & Ilovaisky 1991; Welsh et al. 2000). The mass-radius relation for a low-mass Roche lobe-filling companion in a binary (Eggleton 1983) is $R_c = 0.24\ M_{NS}^{1/3}\ q^{2/3}\ (1+q)^{1/3}\ P_{hr}^{2/3}/[0.6\ q^{2/3} + \ell og(1+q^{1/3})]$, with P_{hr} the orbital period in hours, M_{NS} the mass of the neutron star, R_c radius of the companion and $q = M_c/M_{NS}$, the mass ratio. Given the mass function and the orbital period and assuming a $1.4M_{\odot}$ neutron star, we plot in Figure 4.5 the mass-radius relationship for the companion star. Given that the age of the Globular Cluster NGC 6440 is 10 ± 2 Gyrs (Santos & Piatti 2004) and its metallicity is approximately solar (Ortolani et al. 1994), in Figure 4.5 we also plot the isochrones for stars with ages of 8 and 12 Gyrs and solar metallicity. Stars with a $M_c < 0.85\,\mathrm{M}_{\odot}$ cannot fill the Roche lobe while stars with $M_c > 0.95\,\mathrm{M}_{\odot}$ would have a radius exceeding the Roche lobe. This would imply a donor star mass of $0.90 \pm 0.05M_{\odot}$. However, for masses of 0.95–1.1 $\mathrm{M}_{\odot}$, stars have evolved off the main sequence so binary mass transfer can have affected the radius of the donor star, which means we cannot firmly exclude masses of 0.95–1.1 $\mathrm{M}_{\odot}$. Therefore a more conservative mass range for the donor star is 0.85-1.1 $\mathrm{M}_{\odot}$. Intriguingly, this requires the inclination to be about 9^o, which has a $\lesssim 1\%$ a priori probability for an isotropic sample of binary inclinations. Of course, this estimate is assuming that SAX J1748.9–2021 is in a primordial binary. If a different evolutionary path took place (e.g. dynamical interactions), the mass of the companion might be much smaller (see e.g. van Zyl et al. 2004).

Acknowledgments: DA wants to thank Ben Stappers for very helpful discussions. This work was supported by the "Nederlandse Onderzoekschool Voor Astronomie" (NOVA), i.e., the "Netherlands Research School for Astronomy"

The true delight is in the finding out, rather than in the knowing.

Isaac Asimov

5 The Island state of the Atoll Source 4U 1820–30

Diego Altamirano, M. van der Klis, M. Méndez, S. Migliari, P.G. Jonker, A. Tiengo and W. Zhang

Astrophysical Journal, 2005, 633, 358

Abstract

We study the rapid X-ray time variability in all public data available from the *Rossi X-ray Timing Explorer's* Proportional Counter Array on the atoll source 4U 1820–30 in the low-luminosity island state. A total of $\sim$ 46 ks of data were used. We compare the frequencies of the variability components of 4U 1820–30 with those in other atolls sources. These frequencies were previously found to follow a universal scheme of correlations. We find that 4U 1820–30 shows correlations that are shifted by factors of 1.13 ± 0.01 and 1.21 ± 0.02 with respect to those in other atoll sources. These shifts are similar to, but smaller than the shift factor $\sim$ 1.45 previously reported for some accreting millisecond pulsars. Therefore, 4U 1820–30 is the first atoll source which shows no significant pulsations but has a significant shift in the frequency correlations compared with other 3 non-pulsating atoll sources.

5.1 Introduction

Accretion in neutron star low-mass X-ray binaries (LMXBs) can be studied through the spectral and timing properties of the associated X-ray emission. The Fourier power spectra of the X-ray flux of these systems, exhibit quasi-periodic oscillations (QPOs) as well as noise components between $\sim 1 \times 10^{-3}$ Hz and $\sim$ 1350 Hz. Most of these variability components are thought to be associated with processes in the accretion disk (for reviews and references see van der Klis 2000, 2004) but some of them may arise on the surface of the neutron star (see e.g. Revnivtsev et al. 2001; Strohmayer & Bildsten 2003). The timing properties at low frequencies ($\nu < 100$ Hz) as well as the spectral properties are the basis of the classification of these systems as either Z or atoll sources (Hasinger & van der Klis 1989). In recent literature, each variability component is designated L_i – L for 'Lorentzian', Belloni et al. (2002b) – where the index i indicates the component; the component's characteristic frequency is designated ν_i. For example, L_b is an often flat-topped broad band noise component at a low frequency ν_b, and L_u the upper kilohertz QPO with frequency ν_u (see van Straaten et al. 2003, for complete terminology).

The kilohertz QPOs are seen between a few hundred and $\sim$ 1350 Hz and when two of them are seen at the same time (twin kHz QPOs), the difference between their frequencies is constrained between $\sim$ 185 Hz and $\sim$ 400 Hz. In the 0.01-100 Hz range two to five band-limited noise, peaked-noise and QPO components are observed whose frequencies all correlate with one another and with that of the kilohertz QPOs (see van Straaten et al. 2005, and references within). An example is the WK correlation (after Wijnands et al. 1999), between the hump frequency ν_h and the break frequency ν_b. This relation may be fundamental in the understanding of the processes of accretion in LMXBs because, in atoll sources and black holes ν_b and ν_h correlate over 3 orders of magnitude (the Z sources have slightly higher ν_h). The existence of such correlations suggests that similar physical phenomena may be responsible for some of the QPOs and noise components found over wide ranges of frequency and coherence in Z, atoll and black hole sources.

van Straaten et al. (2005) found that the frequencies of the noise and QPO components of the accreting millisecond pulsar SAX J1808.4–3658 also correlate with ν_u, but, in a different way than those of the other atoll sources.

They interpreted the difference between the pulsar and the atoll sources as due to a shift in frequency of the upper kilohertz QPO and suggested that physical differences between these sources are most likely to affect the high frequency components. In SAX J1808.4-3658, the factors by which ν_u had to be multiplied to make the correlations coincide with those of the ordinary atoll sources were 1.420 ± 0.013 for ν_b, and 1.481 ± 0.013 for ν_h.

4U 1820–30 is a low-mass X-ray binary with an orbital period of only 11.4 minutes (Stella et al. 1987) and an X-ray burst source (Grindlay et al. 1976). It is located in the globular cluster NGC 6624 at a distance 7.6 ± 0.4 kpc (Kuulkers et al. 2003a). Radio emission has also been detected from the source (Geldzahler 1983; Migliari et al. 2004). 4U 1820–30 undergoes a regular ~ 176 day accretion cycle (Priedhorsky & Terrell 1984a), switching between high and low states differing by a factor $\sim$3 in luminosity (Strohmayer & Brown 2002). The ultra-compact nature of the system requires that the secondary is a low-mass helium dwarf (see e.g. Rappaport et al. 1987) so that the accreted material likely has a very low hydrogen abundance. Hasinger & van der Klis (1989) defined 4U 1820–30 as an atoll source and eight years later Smale et al. (1997) reported the discovery of kHz quasi-periodic oscillations. Zhang et al. (1998c) reported the result from a long-term monitoring data set obtained with the Rossi X-ray Timing Explorer. They observed kHz QPOs in both the lower banana and the island state (see van der Klis 2004, for nomenclature). They showed that the frequency of the kilohertz QPOs is correlated with the PCA count rate below a critical value (~ 2500 counts s^{-1} per 5 PCUs). Above this, the QPO frequencies remained constant while the count rate increased between ~ 2500 and ~ 3200 counts s^{-1} per 5 PCUs. Saturation of QPO frequency at high mass accretion rates is an expected signature of the marginally stable orbit (Miller et al. 1998; Kaaret et al. 1999); however, this is the only source reported to have shown this behavior, and to what extent count rate is a good indicator of accretion rate remains to be seen (see, e.g. the discussion of the issue in van der Klis 2001). Later, similar analysis were carried out, using instead of the count rate, (i) the energy flux, (ii) the X-ray spectral shape (Kaaret et al. 1999) and (iii) the parameter S_a (Bloser et al. 2000) which parameterizes atoll source location in the track of the color-color diagram. The same behavior as that observed by Zhang et al. (1998c) as a function of count rate was found, when the QPO frequency was plotted as a function of either of these three parameters. The saturation of QPO frequency was interpreted as strong additional evidence for the detection of the marginally stable orbit in the accretion disk of 4U 1820–30. However, since then Méndez (2002) has argued that the evidence of the saturation is not so compelling, especially when some instrumental corrections are taken into account. A general tendency for QPO frequency to saturate toward higher luminosity may be a feature of the same phenomenon that produces the parallel tracks in frequency-luminosity diagrams (van der Klis 2001).

In this paper, we report on the eight observations that are currently available of 4U 1820–30 in the island state. All previous works mentioned above included only one observation (20075-01-05-00) of the source in the island state, so the current analysis better allows us to constrain the power spectral components in the island state of 4U 1820–30 more accurately. We study the correlations between the characteristic frequencies of the various timing features, and compare these with those of four well-studied atoll sources, three low-luminosity bursters, one Z-source and one accreting millisecond pulsar. We show that the correlations between frequencies in 4U 1820–30 are shifted as found for SAX J1808.4–3658, but with a lower shift factor. We finally discuss whether the interpretation of a multiplicative shift of frequencies is the right explanation for the differences in frequency behavior between the millisecond accreting pulsar SAX J1808.4–3658 and the ordinary atoll sources.

5.2 Observations and data analysis

We used all public data available from the Rossi X-ray Timing Explorer's (RXTE) Proportional Counter Array (PCA; for instrument information see Zhang et al. 1993). There were 158 pointed observations in 9 programs (10074, 10075, 10076, 20075, 30053, 30057, 40017, 40019, 60030, 70030 and 70031). In our analysis, we use the 16-s time-resolution Standard 2 mode data to calculate X-ray colors. For each of the five PCA detectors (PCUs) we calculate a hard and a soft color defined as the count rate in the 9.7–16.0 keV band divided by the rate in the 6.0–9.7 keV band and the 3.5–6.0 keV rate divided by the 2.0–3.5 keV rate, respectively. For each detector we also calculate the intensity, defined as the count rate in the energy band 2.0–16 keV. To obtain the count rates in these exact energy ranges, we interpolate linearly between count rates in the PCU channels.We then subtract the background contribution in each band using the standard bright source background model for the PCA, version 2.1e [1]. No deadtime corrections were made as the effect of deadtime can be neglected for our purposes ($< 0.001\%$). We calculate the colors and intensity for each time interval of 16s. In order to correct for the gain changes as well as the differences in effective area between the PCUs themselves, we used the method introduced by Kuulkers et al. (1994): for each PCU we calculate, in the same manner as for 4U 1820–30, the colors of the Crab which can be supposed to be constant. We then average the 16s Crab colors and intensity for each PCU for each day. For each PCU we divide the 16s color and intensity values obtained for 4U 1820–30 by the corresponding Crab values that are closest in time but in the same RXTE gain epoch. The RXTE gain epoch changes with each new high voltage setting of the PCUs (Jahoda et al. 1996). After the Crab normalization is done, we average the colors and intensity over all

[1] PCA Digest at http://heasarc.gsfc.nasa.gov/ for details of the model

PCUs. Finally, we average the 16s colors per observation. Figure 5.1 shows the color-color diagram of the 158 different observations that we used for this analysis, and Figure 5.2 the corresponding hardness-intensity diagrams (soft and hard color vs. intensity).

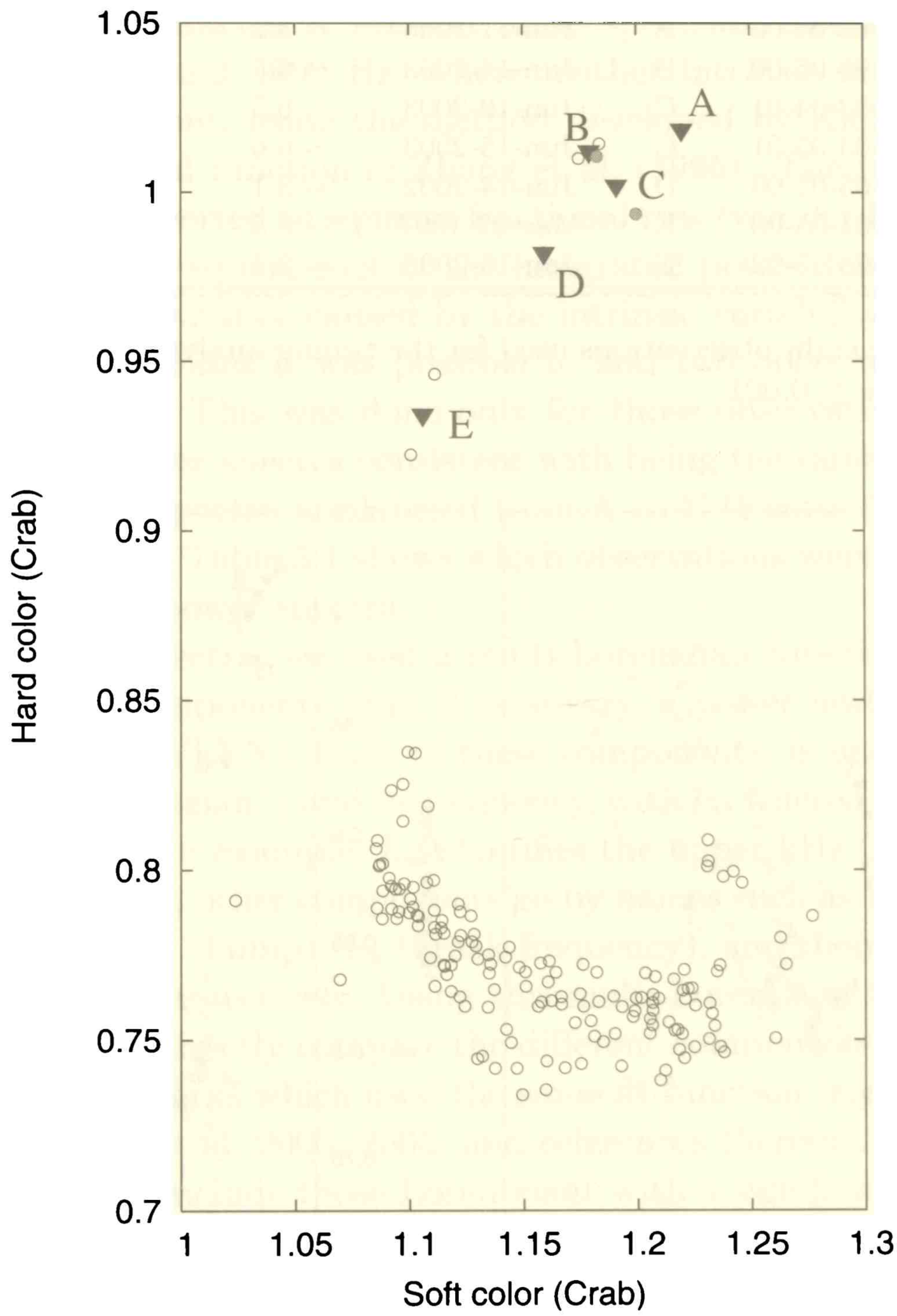

Figure 5.1: 4U 1820–30's hard color vs. soft color normalized to Crab colors as explained in Section 5.1. Each circle represents one of the 158 observations mentioned in Section 5.2. The triangles represent the average power spectra A to E. They correspond to one or two observations and are labeled in order of decreasing average hard color. For clarity, the two grey-filled circles represent the two observations averaged to get power spectrum C. The error bars are of the order of the size of the symbols.

We find 8 observations which are located in the island region of the color-

color diagram (hard colors greater than 0.9). These observations are the subject of this paper (see Table 5.1).

Hard Color	Observation ID	Label	Date of Observation	Duration (ks)	Number of PCUs on	Average (c/s/PCU)
1.018	40017-01-24-00	A	Jun-04-2003	~ 8.2	3	~ 268
1.010	70030-03-04-00	B	Jun-11-2003	~ 3.2	4	~ 281
1.014	70030-03-05-00	B	Jun-14-2003	~ 6.5	4	~ 308
0.993	70030-03-04-01	C	Jun-12-2003	~ 6.5	3	~ 283
1.010	70030-03-05-01	C	Jun-15-2003	~ 6.6	3	~ 358
0.982	70031-05-01-00	D	Jun-14-2002	~ 3.1	5	~ 297
0.922	20075-01-05-00	E	May-02-1997	~ 8.5	5	~ 354
0.946	70030-03-05-02	E	Jun-16-2003	~ 3.2	2	~ 421

Table 5.1: The eight observations used for the timing analysis. The statistical errors in hard color are $\lesssim 0.001$.

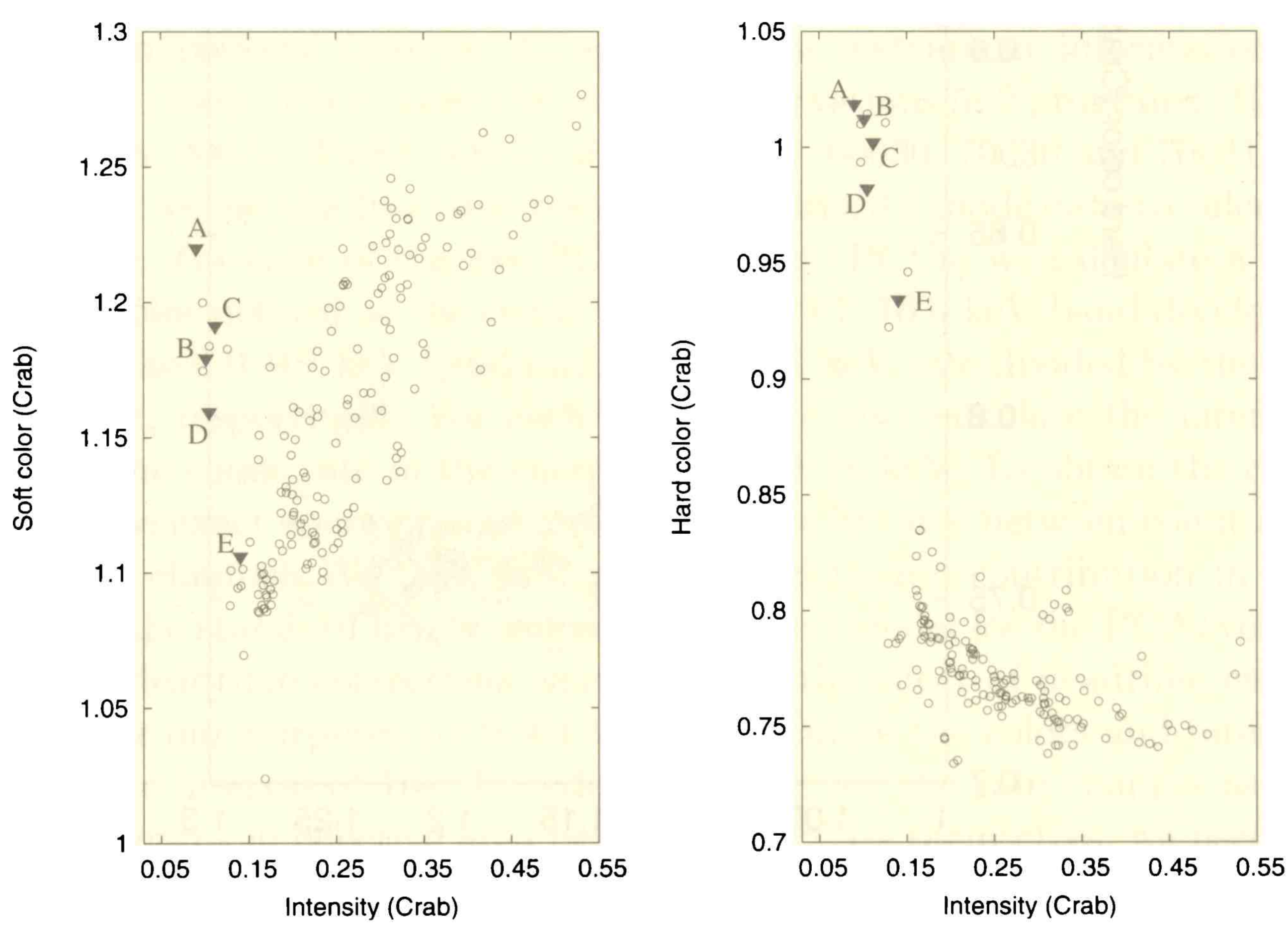

Figure 5.2: Soft color vs. intensity (left) and hard color vs. intensity (right) in Crab units as explained in Section 5.1. Symbols as in Figure 5.1. The error bars are of the order of the size of the symbols.

For the Fourier timing analysis of these 8 observations we used an $125\mu s$ time resolution Event mode (E_125us_64M_0_1s). Leahy-normalized power spectra were constructed using data segments of 128 seconds and 1/8192s time bins such that the lowest available frequency is $1/128 \approx 8 \times 10^{-3}$ Hz and the Nyquist frequency 4096 Hz. Detector drop-outs were removed but no background or deadtime corrections were performed prior to the calculation of the power spectra. We first averaged the power spectra per observation. We inspected the shape of the average power spectra at high frequency (> 2000 Hz) for unusual features in addition to the usual Poisson noise. None were found. We then subtracted a Poisson noise spectrum estimated from the power between 3000 and 4000 Hz, where neither intrinsic noise nor QPOs are known to be present, using the method developed by Klein-Wolt (2004) based on the analytical function of Zhang et al. (1995). The resulting power spectra were then converted to squared fractional rms (van der Klis 1995a). In this normalization the square root of the integrated power density is a direct measurement of the variance caused by the intrinsic variability in the source count rate. In three cases it was possible to add two observations together to improve statistics. This was done only for those observations which had similar colors and power spectra consistent with being the same within errors. The resulting power spectra are labeled from A to E (Figure 5.3) in order of decreasing hard color. Table 5.1 shows which observations were used to create each of the averaged power spectra.

To fit the power spectra, we used a multi-Lorentzian function: the sum of several Lorentzian components plus, if necessary, a power law to fit the very low frequency noise (VLFN). Each of these components, is usually described with an L_i (for 'Lorentzian') and its frequency, with ν_i, where i determines the type of component. For example, L_u identifies the upper kHz QPO and ν_u its frequency. By analogy, other components go by names such as L_ℓ (lower kHz), L_{hHz} (hectohertz), L_h (hump), L_b (break frequency), and their frequencies as ν_ℓ, ν_{hHz}, ν_h and ν_b, respectively. Using this multi-Lorentzian function makes it straightforward to directly compare the different components in 4U 1820–30 to those in previous works which used the same fit function (e.g., Belloni et al. 2002b; van Straaten et al. 2003, 2005, and references therein).

In the fits we only include those Lorentzians with a significance larger than 3σ based on the error in the power integrated from 0 to ∞. We give the results of the fits in terms of ν_{max} and Q, of which ν_{max} was introduced by Belloni et al. (2002b) as $\nu_{max} = \sqrt{\nu_0^2 + (\frac{FWHM}{2})^2} = \nu_0\sqrt{1 + \frac{1}{4Q^2}}$. For Q we use the standard definition $Q = \frac{\nu_0}{FWHM}$. FWHM is the full width at half maximum of the Lorentzian.

5.3 Results

Figures 5.1 and 5.2 show that in order A to E, the spectrum becomes softer, i.e. both hard and soft color decrease, while the spectrum is harder than in the banana branch and the intensity is approximately constant (see Figure 5.2). This is the expected behavior for an atoll source which is moving from the island to the lower left banana state in the color color diagram (van der Klis 2004).

In Figure 5.3, we show the average power spectra with their fits. Four to five Lorentzian components were needed for a good fit of power spectra A–D. Power spectrum E, whose colors are closest to the upper banana state, could be fitted with either six or seven Lorentzians. Both fits share six components whose frequencies are the same within errors; in the case of 7 Lorentzians, an extra component is present at $\nu_3 = 407.9 \pm 30.5$. This component is significant only at $\sim 2\sigma$ (single trial) level, and represents an $\sim 1.3\sigma$ improvement of the χ^2 of the fit according to an F-test. However, if this component, which is consistent with being the lower kilohertz QPO peak, is not included in the model, the fit becomes unstable unless the quality factor Q_{hHz} is fixed.

Table 5.2 gives the results of the fits to the power spectra and in Figure 5.4, we show the correlations of the characteristic frequencies ν_{max} of the power spectral components with the frequency of the upper kilohertz QPO ν_u. For power spectrum E, we always show the results for 7 Lorentzians.

As expected for the island state of an atoll source, ν_u is lower than $\sim$ 700 Hz (see e.g. van Straaten et al. 2003, 2005; van der Klis 2004) and increases monotonically from A to E with decreasing hard color. L_{hHz} is at similar frequencies as in the other atoll sources, between $\sim$ 100 and $\sim$ 200 Hz.

For L_b and L_h, a shift appears to exist between the correlations of 4U 1820–30 and those of the other atoll sources studied by van Straaten et al. (2005). To further investigate this, in Figures 5.5 and 5.6 we plot ν_b and ν_h respectively, versus ν_u. We use all the data used by van Straaten et al. (2005) for the atoll sources and the low luminosity bursters; however, of the millisecond pulsars, we only use data of SAX J1808.4–3658, which, in contrast to the others, has data points in the same frequency region as 4U 1820–30. As can be seen in Figures 5.5 and 5.6, our points for 4U 1820–30 are right in the important transition region around $\nu_u \sim 600$ Hz. On one hand for L_b (Figure 5.5), our points seem to link the SAX J1808.4–3658 data with those for the atoll sources with $\nu_u \gtrsim 600$ Hz. However, neither the frequency range covered by 4U 1820–30 nor SAX J1808.4–3658 is sufficient to draw the conclusion that the two different correlations below $\nu_u \sim 600$ Hz become the same correlation above $\nu_u \sim 600$ Hz, as the figure seems to suggest. On the other hand, as shown in Figure 5.6, in 4U 1820–30 the L_h points seem to lie between those of the atoll sources and those of SAX J1808.4–3658.

To determine the shift factors between the frequency correlations of 4U 1820–30 and those of the other atoll sources, and to be able to compare them

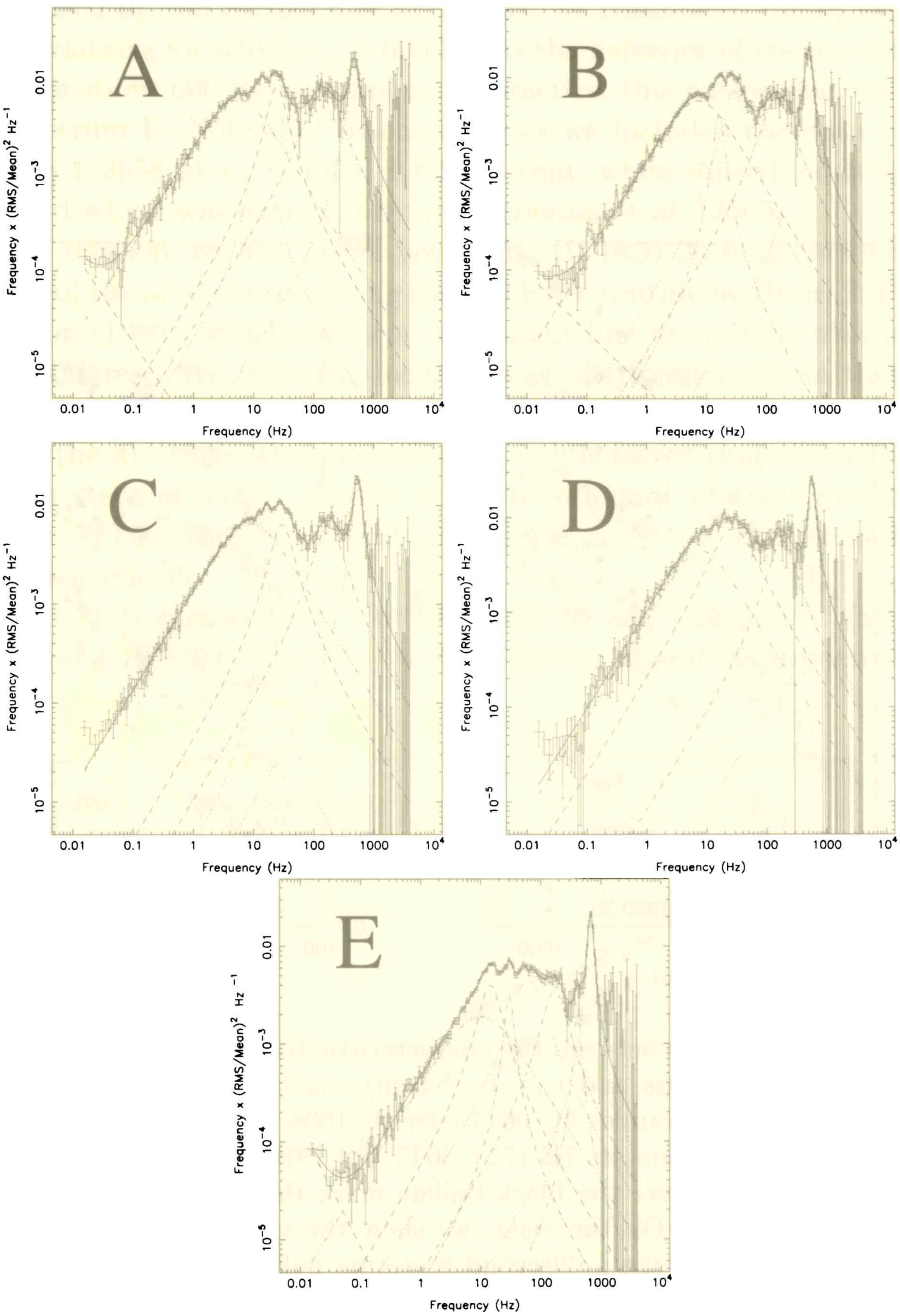

Figure 5.3: Power spectra and fit functions in the power spectral density times frequency representation for 4U 1820–30. Each plot corresponds to a different position in the color-color and color intensity diagrams (see Figures 5.1 and 5.2). The different lines mark the individual Lorentzian components of the fit. For a detailed identification, see Table 5.2, Figure 5.4 and Section 5.3.

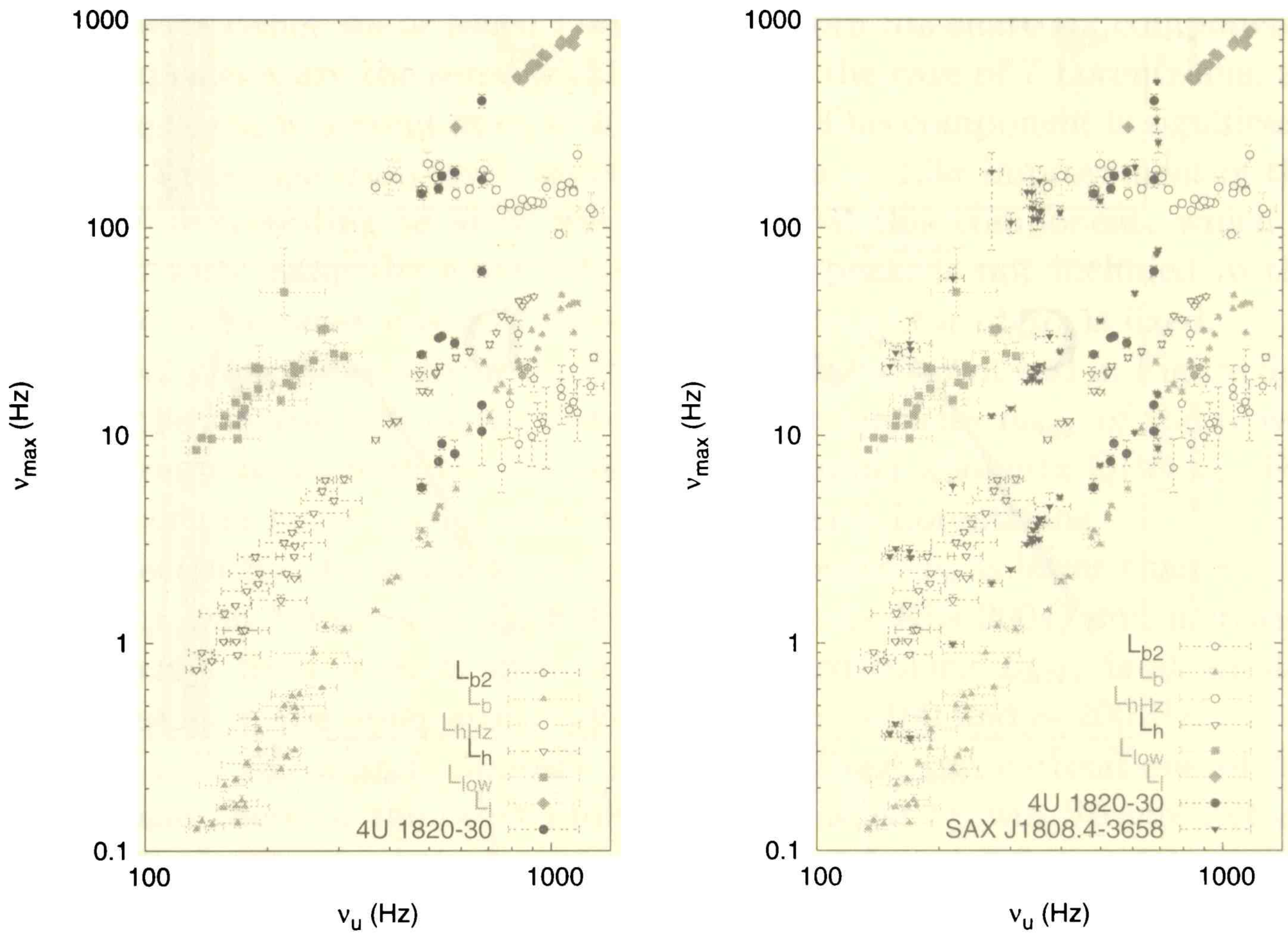

Figure 5.4: Correlations between the characteristic frequencies ν_{max} of the various power spectral components and ν_u. For clarity, on the *left* we plot the different components of the atoll sources 4U 0614+09, 4U 1608–52, 4U 1728–34 and Aql X-1 and the low luminosity bursters 1E 1724–3045, GS 1826–24 and SLX 1735–269 (van Straaten et al. 2005), where the black bullets mark the results for the island state features of 4U 1820–30. On the *right*, we show the same plot as on the left, but we include the results for the millisecond accreting pulsar SAX J1808.4–3658 (black triangles).

with the shift factors found for SAX J1808.4–3658, we followed the same procedure as used by van Straaten et al. (2005): we considered the ν_b vs. ν_u and ν_h vs. ν_u relations for which $\nu_u < 600$ Hz, as the behavior of the low-frequency components above 600 Hz is complex. In practice, this means that we exclude power spectrum E. Note that in our analysis we included the data point for SAX J1808.4–3658 at $\nu_u = 497.6 \pm 6.9$ Hz that, when shifted, ends up above 600 Hz, and which was excluded by van Straaten et al. (2005).

For each relation, we fit a power law to the 4U 1820–30 frequencies together with those of the atoll sources using the FITEXY routine by Brian P. Flannery & Vetterling (1989), which performs a straight line fit to data with errors in both coordinates. We took the logarithm of the frequencies so that fitting a power law becomes equivalent to fitting a straight line. Before fitting, we multiplied the 4U 1820–30 ν_u values with a shift factor that ran between 0.1 and 3 with steps of 0.001. The fit with the minimal χ^2 then gave the best shift factor. The errors in the shift factor use $\Delta\chi^2 = 1$, corresponding to a 68% confidence level.

The best shift factors in ν_u for 4U 1820–30 are 1.21 ± 0.02 ($\chi^2/dof = 19.4/18$) and 1.13 ± 0.01 ($\chi^2/dof = 45.3/18$) for ν_b and ν_h respectively.

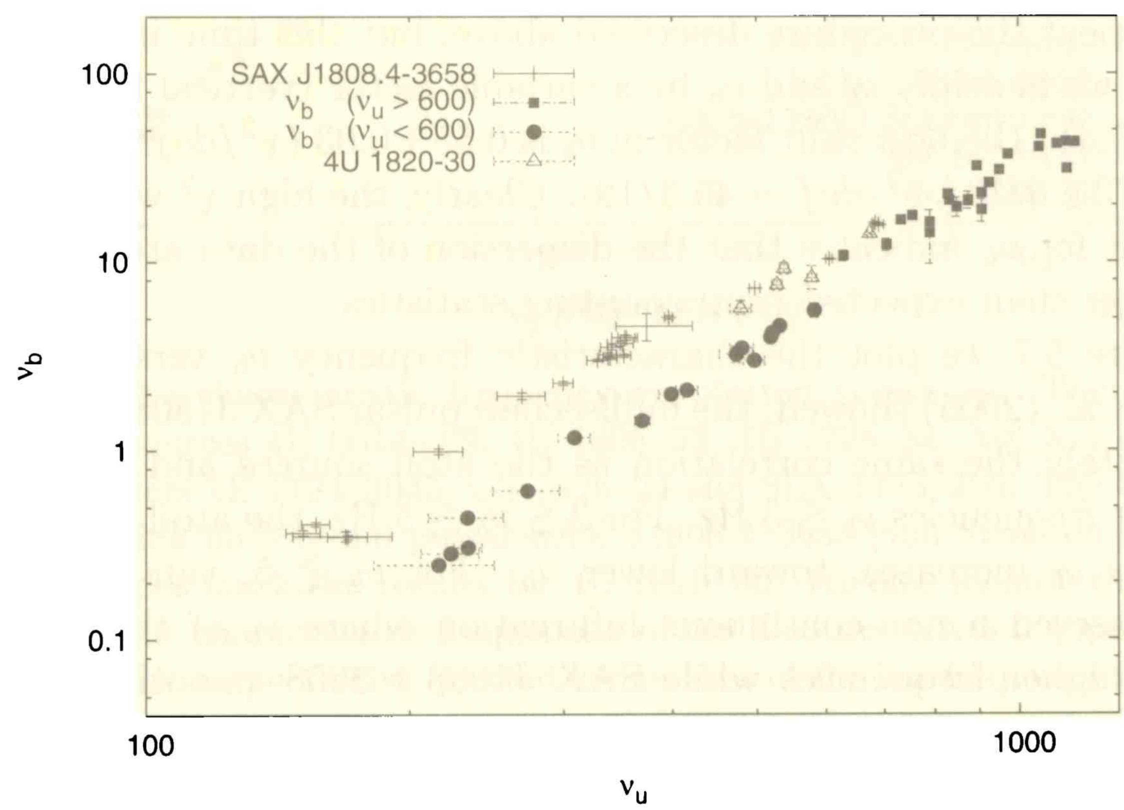

Figure 5.5: Correlation between the characteristic frequencies ν_b and ν_u. The black circles and the black squares mark the atoll sources 4U 0614+09, 4U 1608–52, 4U 1728–34 and Aql X-1 and the low luminosity bursters 1E 1724–3045, GS 1826–24 and SLX 1735–269 (van Straaten et al. 2005) for $\nu_u < 600$ Hz and $\nu_u > 600$ Hz, respectively. The open triangles mark the results for 4U 1820–30 and the crosses represent the results from van Straaten et al. (2005) for SAX J1808.4–3658.

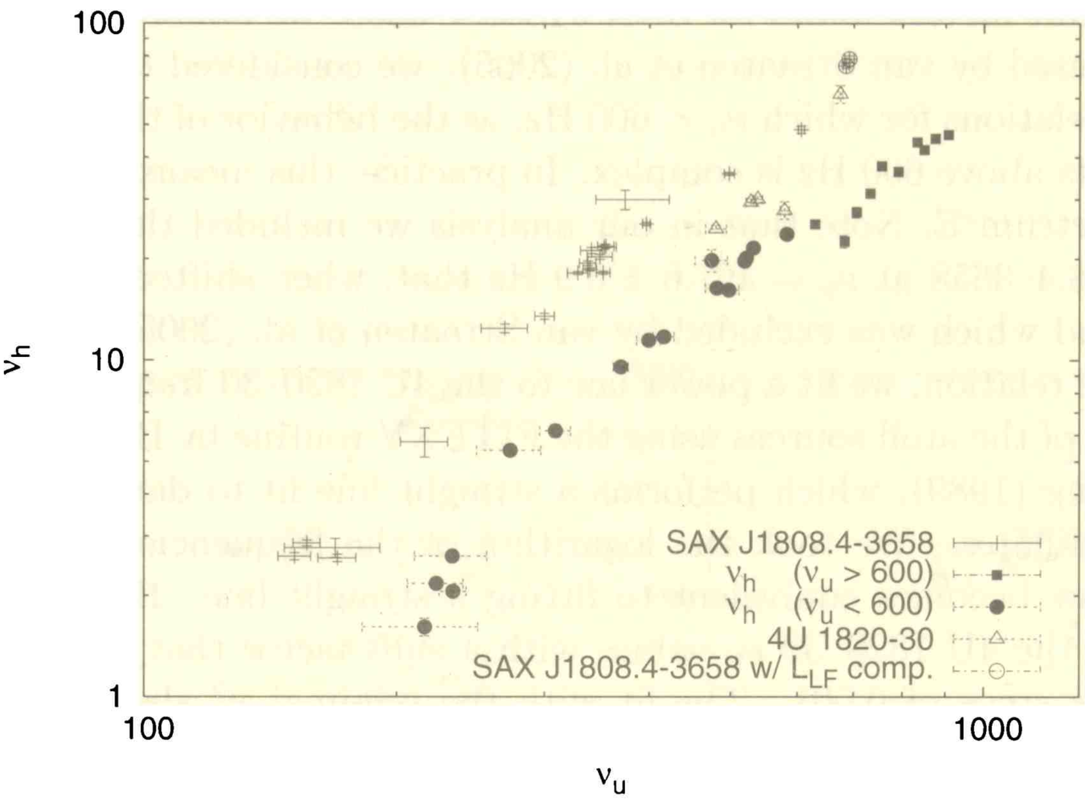

Figure 5.6: Correlation between the characteristic frequencies ν_h and ν_u. Symbols as in Figure 5.5. The two open circles represent the results for SAX J1808.4-3658 in which a L_{LF} component was also found (see van Straaten et al. 2005).

If we repeat the procedure described above, but this time instead of multiplying ν_u, we multiply ν_b and ν_h by a variable factor (vertical frequency shifts in Figure 5.4) , the best shift factor in ν_b is 0.55 ± 0.03 ($\chi^2/dof = 19.4/18$) and in ν_h is 0.73 ± 0.02 ($\chi^2/dof = 45.3/18$). Clearly, the high χ^2 when calculating the best fit for ν_h indicates that the dispersion of the data around the power law is larger than expected from counting statistics.

In Figure 5.7 we plot the characteristic frequency ν_h versus ν_b. As van Straaten et al. (2005) showed, the millisecond pulsar SAX J1808.4–3658 follows approximately the same correlation as the atoll sources and low luminosity bursters at frequencies $\nu_b \lesssim 3$ Hz. For $3 \lesssim \nu_b \lesssim 5$ Hz, the atoll sources slightly deviate, as ν_b increases, toward lower ν_h. For $\nu_b \gtrsim 5$, van Straaten et al. (2005) observed a non-continuous bifurcation where ν_b of the atoll sources jumps to higher frequencies while SAX J1808.4–3658 smoothly extends the correlation observed for $\nu_b \lesssim 3$ Hz. Our new data for 4U 1820–30, which are all at $\nu_b > 5$ Hz, seem to be in between these two correlations, apparently following the behavior of the atoll sources for $3 \lesssim \nu_b \lesssim 5$ Hz. However, the point for 4U 1820–30 at higher ν_b (and higher ν_h), falls in the correlation of SAX J1808.4–3658.

In Figure 5.7 we also show the frequency of the Horizontal Branch Oscillation (HBO) and its subharmonic versus that of the Low Frequency Noise (LFN) for the Z-source GX 5–1. The data of GX 5–1 was taken from van

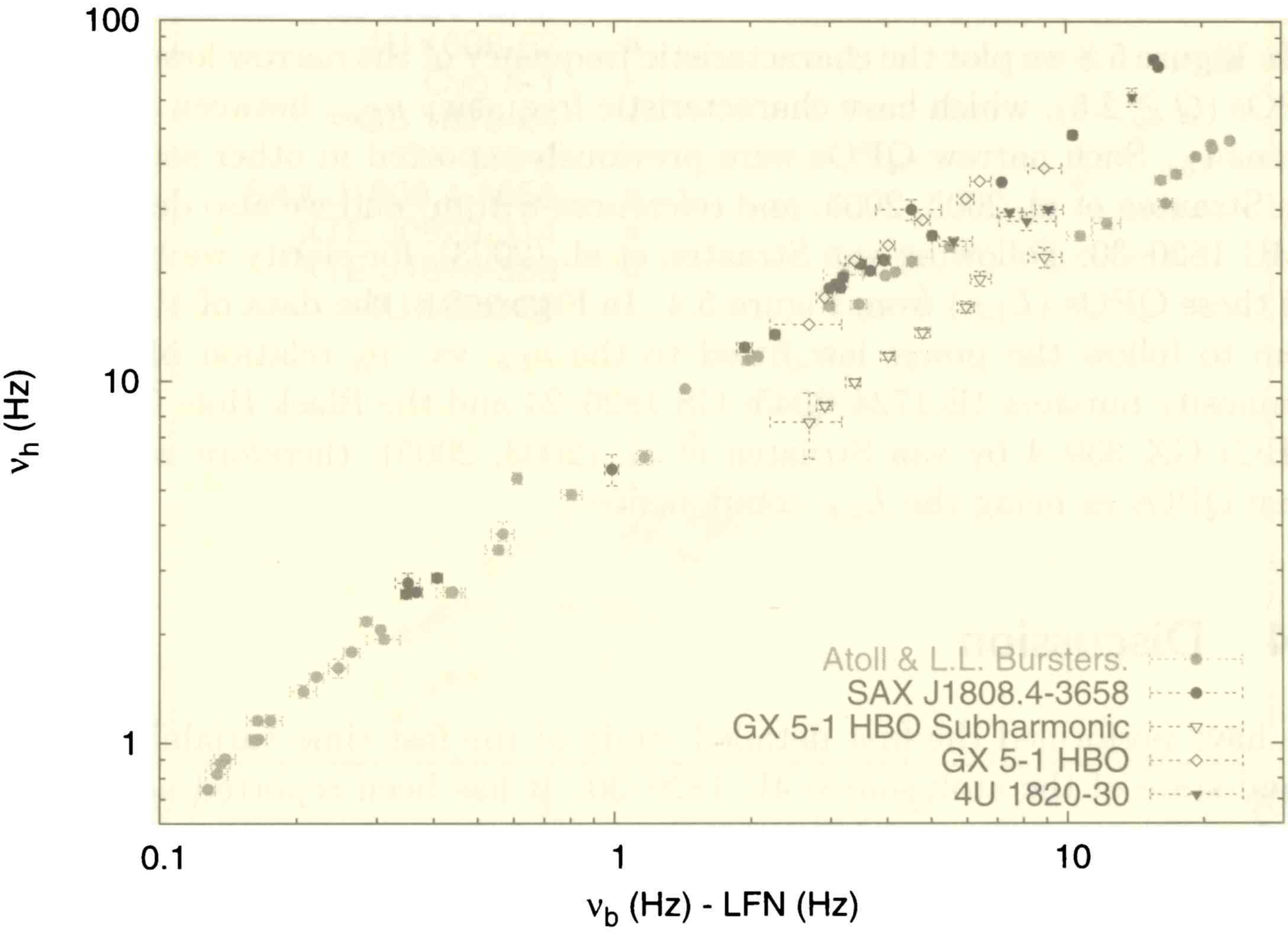

Figure 5.7: The characteristic frequency ν_h plotted versus ν_b. The grey circles mark the atoll sources 4U 0614+09, 4U 1608–52, 4U 1728–34, Aql X-1 and the low luminosity bursters 1E 1724–3045, GS 1826–24 and SLX 1735–269. The black circles mark the accreting millisecond pulsar SAX J1808.4–3658 (van Straaten et al. 2005). The filled triangles mark the results for 4U 1820–30. We also include the HBO and HBO subharmonic characteristic frequencies of the Z-source GX 5–1 (open diamonds and open triangles, respectively), plotted versus that of the low frequency noise (LFN) (van Straaten et al. 2003).

Straaten et al. (2003) (but see Jonker et al. 2002a, for original data). The HBO component of GX 5–1 follows the same correlation as SAX J1808.4–3658 but, as already noted by Wijnands et al. (1999), the HBO of Z-sources is slightly higher in this diagram than the L_h and L_{LF} components of atoll sources. The HBO subharmonic extends the correlation that is found for atoll sources and low luminosity bursters for $\nu_b \gtrsim 5$ Hz to lower frequencies, suggesting that the apparent bifurcation mentioned before could be associated with harmonic mode switching.

In Figure 5.8 we plot the characteristic frequency of the narrow low-frequency QPOs ($Q \gtrsim 2.5$), which have characteristic frequency ν_{max} between ν_b and ν_h, versus ν_h. Such narrow QPOs were previously reported in other sources (e.g. van Straaten et al. 2003, 2005, and references within) and we also detect them in 4U 1820–30. Following van Straaten et al. (2003), for clarity we have omitted these QPOs (L_{LF}) from Figure 5.4. In Figure 5.8, the data of 4U 1820–30 seem to follow the power law fitted to the ν_{LF} vs. ν_h relation of the low-luminosity bursters 1E 1724–3045, GS 1826–24 and the Black Hole Candidate (BHC) GX 339–4 by van Straaten et al. (2003, 2005); therefore we identify these QPOs as being the L_{LF} component.

5.4 Discussion

We have performed the first detailed study of the fast time variability in the island state of the atoll source 4U 1820–30. It has been reported before that the frequencies of the variability components of the atoll sources follow a universal scheme of correlations when plotted versus ν_u (van Straaten et al. 2003, and references within). In Figure 5.4 (left) we show that our data are in general agreement with this scheme. Van Straaten et al. (2005) showed that the accreting millisecond pulsar SAX J1808.4–3658 shows similar relations between its characteristic frequencies as the atoll sources do, but shifted (Figure 5.4 - right). This shift was interpreted to occur only between the characteristic frequencies of the low frequency components on one hand and ν_u (and ν_ℓ) on the other, where ν_u (and ν_ℓ) had to be multiplied by ~ 1.45 to make the correlations coincide. Figures 5.5 and 5.6 suggest that this could also be the case for 4U 1820–30. However, the shift factor for ν_u is 1.21 ± 0.02 and 1.13 ± 0.01 for L_b and L_h, respectively, giving an average of 1.17 ± 0.01 which is smaller than the values of 1.420 ± 0.013 and 1.481 ± 0.013, respectively, giving an average of 1.454 ± 0.009 (van Straaten et al. 2005). Similar shift factors as we find for 4U 1820–30 may in fact be present in other accreting millisecond pulsars and faint burst sources; for example in XTE J1751–305, van Straaten et al. (2005) found shift factors of 1.188 ± 0.045 and 1.112 ± 0.042

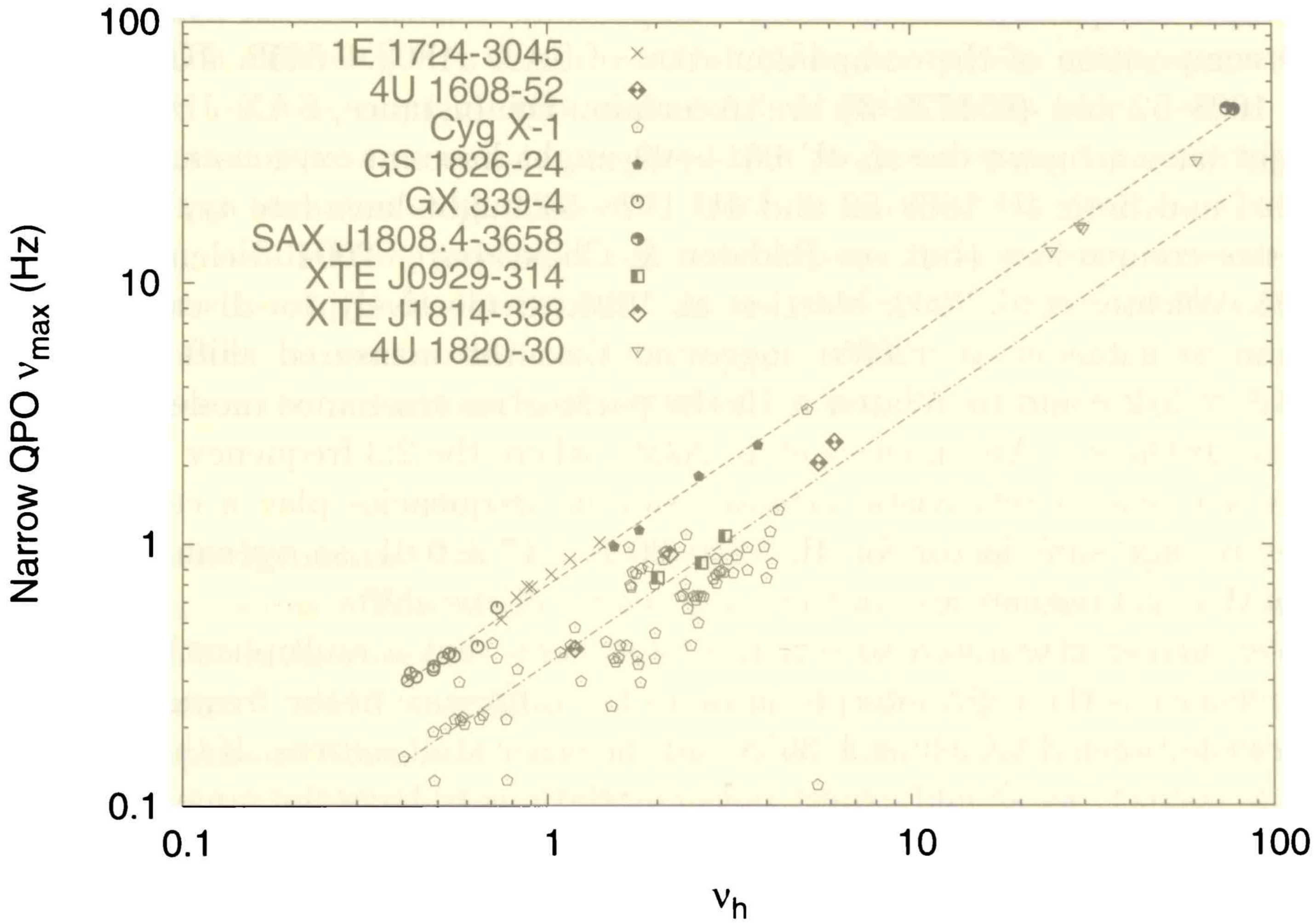

Figure 5.8: Characteristic frequencies ν_{LF} and $\nu_{LF/2}$ (see text) versus ν_h. The symbols are labeled in the plot, and represent the frequencies of the QPOs from the atoll source 4U 1608–52, the BHCs Cyg X–1 and GX 339–4, the low luminosity bursters 1E 1724–3045 and GS 1826–24 and the accreting millisecond pulsars XTE J0929–314, XTE J1814–338 and SAX J1808.4–3658 (van Straaten et al. 2003, 2005). The open triangles show the results for 4U 1820–30. The dashed line indicates a power law fit to the ν_{LF} vs. ν_h relation of the low-luminosity bursters 1E 1724–3045 and GS 1826–24, and the BHC GX 339–4. The dash-dotted line is a power law with a normalization half of that of the dashed line. The error bars are of the order of the size of the symbols.

for L_b and L_h, respectively. These results are consistent with our values, however, the results for XTE J1751–305 have larger errors. It is important to note that, XTE J1751–305 has a companion of 0.013-0.35 solar mass, suggesting a heated helium dwarf (Markwardt et al. 2002). Since 4U 1820–30 also has a low-mass helium dwarf, the similarity in frequency shifts might be related to the chemical composition of the material in the accreting disk. However, a simple "frequency shift–chemical composition" relation is not evident, since the composition of the companion stars of SAX J1808.4-3658, 4U 0614+09, 4U 1608–52 and 4U 1728–34 are uncertain. For instance, SAX J1808.4-3658 might have a brown dwarf, 4U 0614+09 might have an oxygen-carbon white dwarf and both 4U 1608–52 and 4U 1728–34 might have late type main sequence companions (but see Bildsten & Chakrabarty 2001; Nelemans et al. 2004; Wachter et al. 2002; Marti et al. 1998, respectively, for discussions).

van Straaten et al. (2005) suggested that the measured shift factors of $\sim 1.5 \equiv 3/2$ could be related with the parametric resonance models for kilohertz QPOs (e.g. Abramowicz et al. 2003), where the 2:3 frequency resonances between general relativistic orbital/epicyclic frequencies play a central role. The average shift factor for 4U 1820–30 is 1.17 ± 0.01, so we can reject the idea that 2:3 resonances are the (only) cause of the shifts.

We further attempted to test the hypothesis that a multiplicative shift of frequencies is the right interpretation of the difference in the frequency correlations between SAX J1808.4–3658 and the other atoll sources. If that hypothesis is correct, we should expect both correlations to have the same power law index within errors, and, the only significant difference between the correlations would arise from the normalization of each of the power laws. In order to quantify the differences, we performed two different fits where simultaneously a power law is fitted to the data of SAX J1808.4–3658, and another power law is fitted to the data of the atoll sources 4U 1608–52, 4U 0614+09 and 4U 1728–34. Then we compare the χ^2/dof of the fits. We only use data of the L_b components since L_h's behavior is more complex. If both power law indexes and normalizations are free parameters, the best fit gives a $\chi^2/dof = 60.2/30$. If we force both power laws to have the same index, but different normalizations, the best fit gives a $\chi^2/dof = 86.2/31$.

By comparing these results using an F-test, we find that the improvement of the fit when leaving all the parameters free as compared to forcing equal slopes is significant at the 3.4σ level. If the "shift" interpretation is correct, then the slopes of both correlations should be the same and then, we should not find a significant improvement of the fit. However, the fact that we are dealing with $\chi^2/dof \gtrsim 2$, reduces the statistical significance of our possible interpretations.

If we perform the same analysis between 4U 1820–30 and the atoll sources, we find χ_1^2/dof values of 19.4/16 and 19.6/17, i.e., no significant improvement of the fit. Therefore, in both cases the data are *not* inconsistent with the hypothesis that the differences between correlations are due to only a shift in ν_u (van Straaten et al. 2005).

As suggested by van Straaten et al. (2005), the simplest explanation for the shift between correlations, is that there is some physical difference between sources which affects ν_u. Up to now, such shifts had only been seen in accreting pulsars and only at high confidence in SAX J1808.4–3658, which led to the suggestion that the same source property that leads to strong pulsations also affects ν_u (van Straaten et al. 2005). 4U 1820–30 has no strong pulsations (Dib et al. 2005), invalidating any strict relation between these two characteristics. However, as the shifts in 4U 1820–30 are smaller than in SAX J1808.4-3658 and, as accidental circumstances such as an unfavorable viewing geometry could suppress the pulsations in 4U 1820–30, it is too early to reject this idea.

Acknowledgments: DA likes to thank M. Linares and R. Wijnands for helpful discussions. This work was supported by the "Nederlandse Onderzoekschool Voor Astronomie" (NOVA), i.e., the "Netherlands Research School for Astronomy", and it has made use of data obtained through the High Energy Astrophysics Science Archive Research Center Online Service, provided by the NASA/Goddard Space Flight Center.

ν_{max} (Hz)	Power spectrum A Q	rms (%)	comp.
479.73 ± 13.65	2.47 ± 0.52	9.90 ± 0.82	L_u
145.80 ± 11.15	0.58 ± 0.17	11.80 ± 0.83	L_{hHz}
24.56 ± 0.63	1.23 ± 0.18	9.80 ± 0.67	L_h
13.32 ± 0.41	2.15 ± 0.56	5.39 ± 0.84	L_{LF}
5.64 ± 0.48	0.09 ± 0.04	13.77 ± 0.47	L_b

ν_{max} (Hz)	Power spectrum B Q	rms (%)	comp.
527.99 ± 7.32	3.25 ± 0.41	9.46 ± 0.45	L_u
154.20 ± 8.80	0.72 ± 0.14	9.81 ± 0.53	L_{hHz}
29.48 ± 0.74	1.16 ± 0.14	9.15 ± 0.52	L_h
16.60 ± 0.35	2.50 ± 0.47	4.91 ± 0.60	L_{LF}
7.49 ± 0.48	0.10 ± 0.04	12.94 ± 0.35	L_b

ν_{max} (Hz)	Power spectrum C Q	rms (%)	comp.
537.98 ± 6.68	2.98 ± 0.34	9.61 ± 0.41	L_u
177.08 ± 7.90	0.82 ± 0.14	9.61 ± 0.47	L_{hHz}
30.06 ± 0.64	1.05 ± 0.13	8.83 ± 0.49	L_h
16.30 ± 0.28	3.66 ± 1.00	3.39 ± 0.52	L_{LF}
9.14 ± 0.66	0.04 ± 0.03	14.05 ± 0.40	L_b

ν_{max} (Hz)	Power spectrum D Q	rms (%)	comp.
578.98 ± 7.30	3.71 ± 0.47	10.14 ± 0.48	L_u
184.59 ± 12.70	0.86 ± 0.23	8.93 ± 0.75	L_{hHz}
27.86 ± 1.65	0.41 ± 0.11	12.73 ± 1.23	L_h
8.18 ± 1.19	0.15 ± 0.05	11.06 ± 1.18	L_b

ν_{max} (Hz)	Power spectrum E Q	rms (%)	comp.
675.01 ± 4.06	4.58 ± 0.41	8.54 ± 0.27	L_u
407.94 ± 30.54	$3.85^{+5.13}_{-1.82}$	2.81 ± 0.85	L_ℓ
170.37 ± 14.67	0.98 ± 0.42	6.65 ± 1.44	L_{hHz}
61.69 ± 3.69	0.77 ± 0.26	8.33 ± 1.27	L_h
29.61 ± 0.46	2.80 ± 0.53	4.00 ± 0.48	L_{LF}
14.41 ± 0.25	1.06 ± 0.25	6.89 ± 1.33	L_b
9.94 ± 3.77	0.00 ± 0.00	7.73 ± 1.77	L_{b2}^a

Power spectrum	Power laws Parameters PL index	rms (%)	Integration Interval (Hz)
A	1.9 ± 0.5	1.19 ± 0.15	0.01 – 0.08
B	1.6 ± 0.4	1.2 ± 0.1	0.01 – 0.06
E	2.22 ± 0.24	1.02 ± 0.53	0.01 – 0.08

Table 5.2: Characteristic frequencies ν_{max}, Q values ($\equiv \nu_0/FWHM$ – see Section 5.2), Integrated fractional rms (of the full PCA energy band) and identification (comp.) of the Lorentzians fitted for 4U 1820–30. The quoted errors in ν_{max}, Q and rms use $\Delta\chi^2 = 1.0$. ^{a}: Lorentzian with $\sim 2.7\sigma$ significance.

6 X-ray time variability across the atoll source states of 4U 1636–53

D. Altamirano, M. van der Klis, M. Méndez, P.G. Jonker, M. Klein-Wolt and W.H.G. Lewin

Astrophysical Journal, 2006, Submitted

Abstract

We have studied the rapid X-ray time variability in 149 pointed observations with the *Rossi X-ray Timing Explorer* (RXTE)'s Proportional Counter Array of the atoll source 4U 1636–53 in the banana state and, for the first time with RXTE, in the island state. We compare the frequencies of the variability components of 4U 1636–53 with those in other atoll and Z-sources and find that 4U 1636–53 follows the universal scheme of correlations previously found for other atoll sources at (sometimes much) lower luminosities. The hectohertz QPO shows behavior indicating that the mechanism that sets its frequency differs from that for the other components, while the amplitude setting mechanism is common. A previously proposed interpretation of the narrow low-frequency QPO frequencies in different sources in terms of harmonic mode switching is not supported by our data, nor by some previous data on other sources and the frequency range that this QPO covers is found not to be related to spin, angular momentum or luminosity.

6.1 Introduction

Low-mass X-ray binaries (LMXBs) can be divided into systems containing a black hole candidate (BHC) and those containing a neutron star (NS). The accretion process onto these compact objects can be studied through the timing properties of the associated X-ray emission (see, e.g., van der Klis 2006, for a review). Hasinger & van der Klis (1989) classified the NS LMXBs based on the correlated variations of the X-ray spectral and rapid X-ray variability properties. They distinguished two sub-types of NS LMXBs, the Z sources and the atoll sources, whose names were inspired by the shapes of the tracks that they trace out in an X-ray color-color diagram on time scales of hours to days. The Z sources are the most luminous; the atoll sources cover a much wider range in luminosities (e.g. , Ford et al. 2000, and references therein). For each type of source, several spectral/timing states are identified which are thought to arise from qualitatively different inner flow configurations. In the case of atoll sources, the main three states are the extreme island state (EIS), the island state (IS) and the banana branch, the latter subdivided into lower-left banana (LLB), lower banana (LB) and upper banana (UB) states. Each state is characterized by a unique combination of color color diagram and timing behavior. The EIS and the IS occupy the spectrally harder parts of the color color diagram (CD) corresponding to lower X-ray luminosity (L_x). The different patterns they show in the CD are traced out in days to weeks. The hardest and lowest L_x state is generally the *EIS*, which shows strong low-frequency flat-topped noise. The *IS* is spectrally softer than the *EIS*. Its power spectrum is characterized by broad features and a dominant band-limited noise (BLN) component which becomes stronger and lower in characteristic frequency as the flux decreases and the > 6 keV spectrum gets harder. In order of increasing L_x we encounter the *LLB*, where the twin kHz QPOs are first observed, the *LB*, where dominant 10-Hz BLN occurs and finally, the *UB*, where the < 1 Hz (power law) very low frequency noise (VLFN) dominates. In the banana states, some of the broad features observed in the EIS and the IS become narrower (peaked) and occur at higher frequency. The twin kHz QPOs can be found in *LLB* at frequencies in excess of 1000 Hz, only one is seen in the *LB*, and no kHz QPOs are detected in the *UB* (see reviews by Hasinger & van der Klis 1989; van der Klis 2000, 2004, 2006, for detailed descriptions of the different states. See also Figure 1.8 on page 13 for a Schematic color–color diagram and representative power spectra of a typical atoll source.).

4U 1636–53 is an atoll source (Hasinger & van der Klis 1989) which has an orbital period of ~ 3.8 hours (van Paradijs et al. 1990) and a companion star with a mass of $\sim 0.4\ M_\odot$ (assuming a NS of $\sim 1.4\ M_\odot$, see Giles et al. 2002, for a discussion). It was first observed as a strong continuous X-ray source (Norma X-1) with Copernicus (Willmore et al. 1974) and Uhuru (Giacconi et al. 1974). 4U 1636–53 is an X-ray burst source (Hoffman et al. 1977) which shows asymptotic burst oscillation frequencies of $\sim$ 581 Hz (see e.g. Zhang et al. 1997; Giles et al. 2002). This is probably the approximate spin frequency; although Miller (1999) presented evidence that these oscillations might actually be the second harmonic of a neutron star spin frequency of $\sim$ 290 Hz, this was not confirmed in further work by Strohmayer (2001a). Prins & van der Klis (1997) studied the aperiodic timing behavior of 4U 1636–53 with the EXOSAT Medium Energy instrument up to frequencies of $\sim$ 100 Hz both in the island and the banana state. Wijnands et al. (1997), using observations with RXTE, discovered two simultaneous quasi-periodic oscillations (QPOs) near 900 Hz and 1176 Hz when the source was in the banana state. The frequency difference $\Delta\nu$ between the two kHz QPO peaks is nearly equal to half the burst oscillation frequency, similar to what has been observed in other sources with burst oscillations or pulsation frequency > 400 Hz. To the extent that this implies $\Delta\nu \sim \nu_{spin}/2$, this is inconsistent with spin-orbit beat-frequency models (Wijnands et al. 2003) for the kHz QPOs such as proposed by Miller et al. (1998). Other complications for beat frequency models include the fact that $\Delta\nu$ is neither constant (e.g. in Sco X-1, van der Klis et al. 1997) nor exactly equal to half the burst oscillation frequency. Generally, $\Delta\nu$ decreases as the kHz QPO frequency increases, and in 4U 1636–53, observations have shown $\Delta\nu$ at frequencies lower as well as higher than half the burst oscillation frequency (Méndez et al. 1998a; Jonker et al. 2002a).

van Straaten et al. (2002, 2003) compared the timing properties of the atoll sources 4U 0614+09, 4U 1608–52 and 4U 1728–34 and conclude that the frequencies of the variability components in these sources follow the same pattern of correlations. Di Salvo et al. (2003), based on five detections of kHz QPOs in 4U 1636–53 in the banana state was able to show that at least in that state the source might fit in with that same scheme of correlations. The detailed investigation of 4U 1636–53 is important because it is one of the most luminous atoll sources (Ford et al. 2000) that shows the full complement of island (this paper) and banana states and that also shares other timing features with often less luminous atoll sources. For example, Revnivtsev et al. (2001) found a new class of low frequency QPOs in the mHz range which they suggested to be associated with nuclear burning in 4U 1636–53 and 4U 1608–52 (see also Chapter 2). Méndez (2000) and Méndez et al. (2001) compared the relations between kHz QPOs and inferred mass accretion rate in 4U 1728–34, 4U 1608–52, Aql X-1 and 4U 1636–53, and showed that the dependence of the frequency of one of the kHz QPOs upon X-ray intensity is complex, but similar among sources. Jonker et al. (2000a) discovered a third kHz QPO in 4U 1608–52, 4U 1728–34, and 4U 1636–53 which is likely an upper sideband to the lower kHz QPO. Recently, Jonker et al. (2005) found in 4U 1636–53 an additional (fourth) kHz QPO, likely the corresponding lower sideband.

In this paper, we present new results for low frequency noise with characteristic frequencies 1 – 100 Hz and QPOs in the range 100 – 1260 Hz, for the first time including RXTE observations of the island state of this source. These results better constrain the timing behavior in the various states of 4U 1636–53. We compare our results mainly with those of the atoll sources 4U 0614+09, 4U 1608–52 and 4U 1728–34 and find that the frequency of the hectohertz component may not be constant as previously stated, but may have a sinusoidal like modulation within its range from $\sim$ 100 to $\sim$ 250 Hz. Our results also suggest that the mechanism that sets the frequency of the hHz QPOs differs from that for the other components, while the amplitude setting mechanism is common. Finally, we demonstrate that it is not possible to clearly distinguish between two harmonics of the low-frequency QPO L_{LF} across different sources, as was previously thought (van Straaten et al. 2003).

6.2 Observations and data analysis

We use data from the Rossi X-ray Timing Explorer (RXTE) Proportional Counter Array (PCA; for instrument information see Zhang et al. 1993). There were 149 pointed observations in the four data sets we used (60032-01, 60032-05, 70036-01, 80425-01 & 90409-01), each consisting of a fraction of one to several entire satellite orbits, for $\sim$ 1 to $\sim$ 26 ksec of useful data per observation. We use the 16-s time-resolution Standard 2 mode data to calculate X-ray colors as described in Chapter 5. Hard and soft color are defined as the 9.7–16.0 keV / 6.0–9.7 keV and 3.5–6.0 keV / 2.0–3.5 keV count rate ratio, respectively, and intensity as the 2.0–16.0 keV count rate. Type I X-ray bursts were removed, background was subtracted and deadtime corrections were made. In order to correct for the gain changes as well as the differences in effective area between the PCUs themselves, we normalize our colors by the corresponding Crab color values (see Kuulkers et al. 1994; van Straaten et al. 2003) that are closest in time but in the same RXTE gain epoch, i.e., with the same high voltage setting of the PCUs (Jahoda et al. 2006). In Table 6.2 we show for reference the all-epoch averaged colors for Crab Nebula. All active PCUs were used to calculate the colors in 4U 1636–53 except for observation 60032-01-01-02, where due to a PCU3 malfunction we only used PCUs 0 and 2. Figure 6.1 shows the color-color diagram of the 149 different observations that we used for this analysis, and Figure 6.2 the corresponding hardness-intensity diagrams (soft and hard color vs. intensity).

For the Fourier timing analysis we used data from the $\sim 125\mu s$ (1/8192 s) time resolution Event mode E_125us_64M_0_1s. First, we used a 2 second-binned light curve in order to detect and remove data drop-outs and X-ray bursts (these data were also excluded from the rest of the analysis). Leahy-normalized power spectra were constructed using data segments of 128 seconds and 1/8192s time bins such that the lowest available frequency is $1/128 \approx 8 \times 10^{-3}$ Hz and the Nyquist frequency 4096 Hz. No background or deadtime corrections were made prior to the calculation of the power spectra. We first averaged the power spectra per observation. We inspected the shape of the average power spectra at high frequency ($>$ 2000 Hz) for unusual features in addition to the usual Poisson noise. None were found. We then subtracted a Poisson noise spectrum estimated from the power between 3000 and 4000 Hz, where neither intrinsic noise nor QPOs are known to be present, using the method developed by Klein-Wolt (2004) based on the analytical function of Zhang et al. (1995). The resulting power spectra were converted to squared fractional rms (van der Klis 1995a). In this normalization the square root of the integrated power density equals the variance of the intrinsic variability in the source count rate. In order to improve the statistics, observations were averaged together if they described the same source state. Since it is known from previous work on similar sources that the position of the source in the color-color diagram generally is well correlated to its spectral/timing state (see e.g. van der Klis 2006, and references within), we first grouped observations with similar colors. Within each group, we then compared the shape of each average power spectrum with all of the other ones to create subgroups in which all power spectra had a dependence of power on frequency that was identical within errors. So, narrow features had to be at the same frequency for average power spectra to be added together. The resulting data selections are labeled interval A to N (see Table 6.1 for details on which observations were used for each interval and their colors). A disadvantage of this method is that we can loose information about narrow features moving on time scales shorter than an observation, such as the lower kilohertz QPO (see e.g. Berger et al. 1996; Di Salvo et al. 2003). The "shift and add" method (Méndez et al. 1998b), to some extent might be able to compensate for this; we explore in the Appendix this issue. Our method is the best suited one to study the behavior of the broad features such as typically seen in low mass X-ray binaries' power spectra (e.g. van Straaten et al. 2002, 2003, 2005; Altamirano et al. 2005; Linares et al. 2005). For these broad components, which are the main aim of this paper, the gain in signal to noise due to this averaging process outweighs a minor additional broadening due to frequency variations.

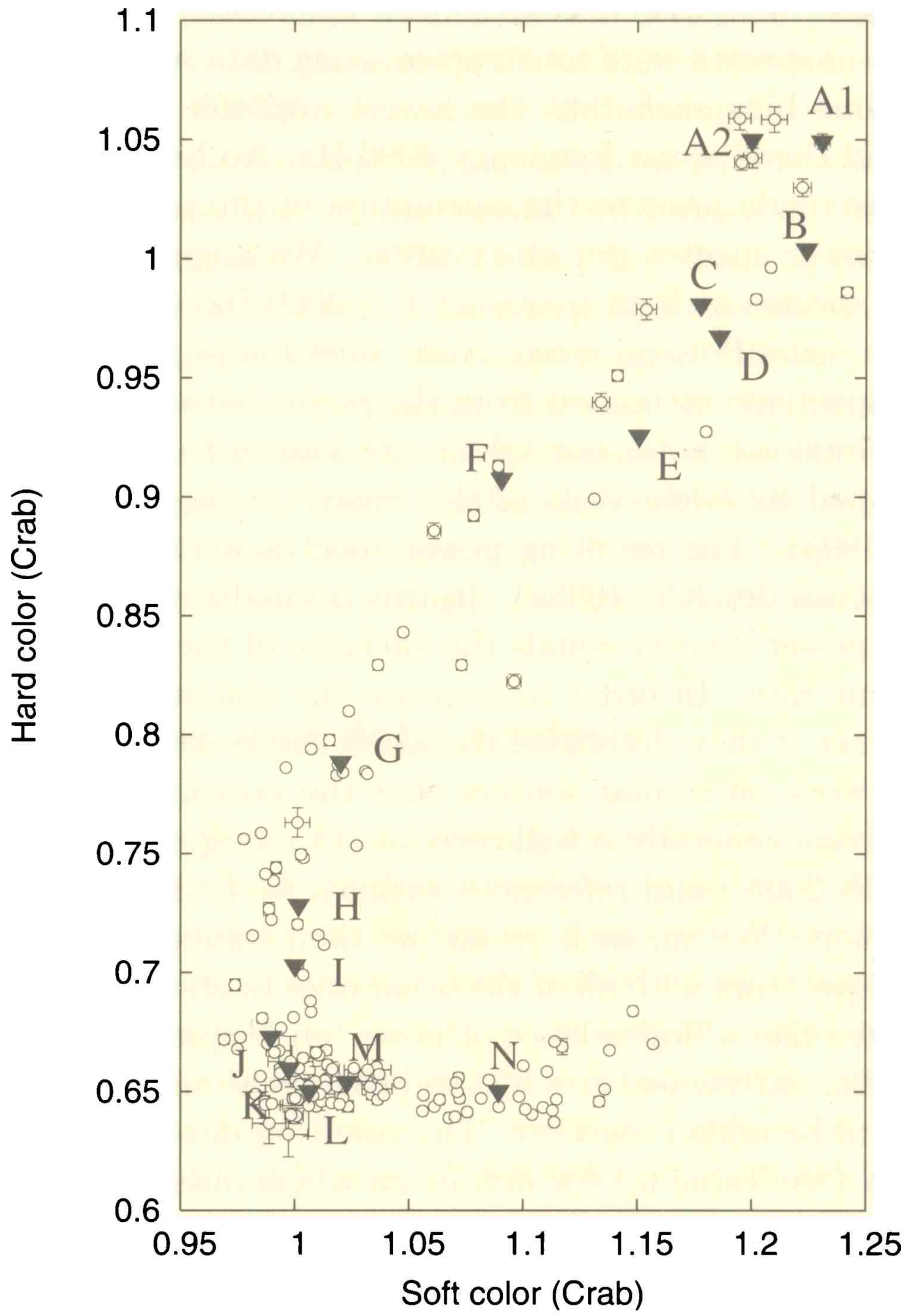

Figure 6.1: Hard color versus soft color normalized to the Crab Nebula as explained in Section 6.1. Each circle represents the average soft/hard color of one of the observations used for this paper. The filled triangles mark averages of 1 to 32 observations and are labeled with letters, in order from (A) the island state, Lower Left Banana (J) to the Lower banana (N).

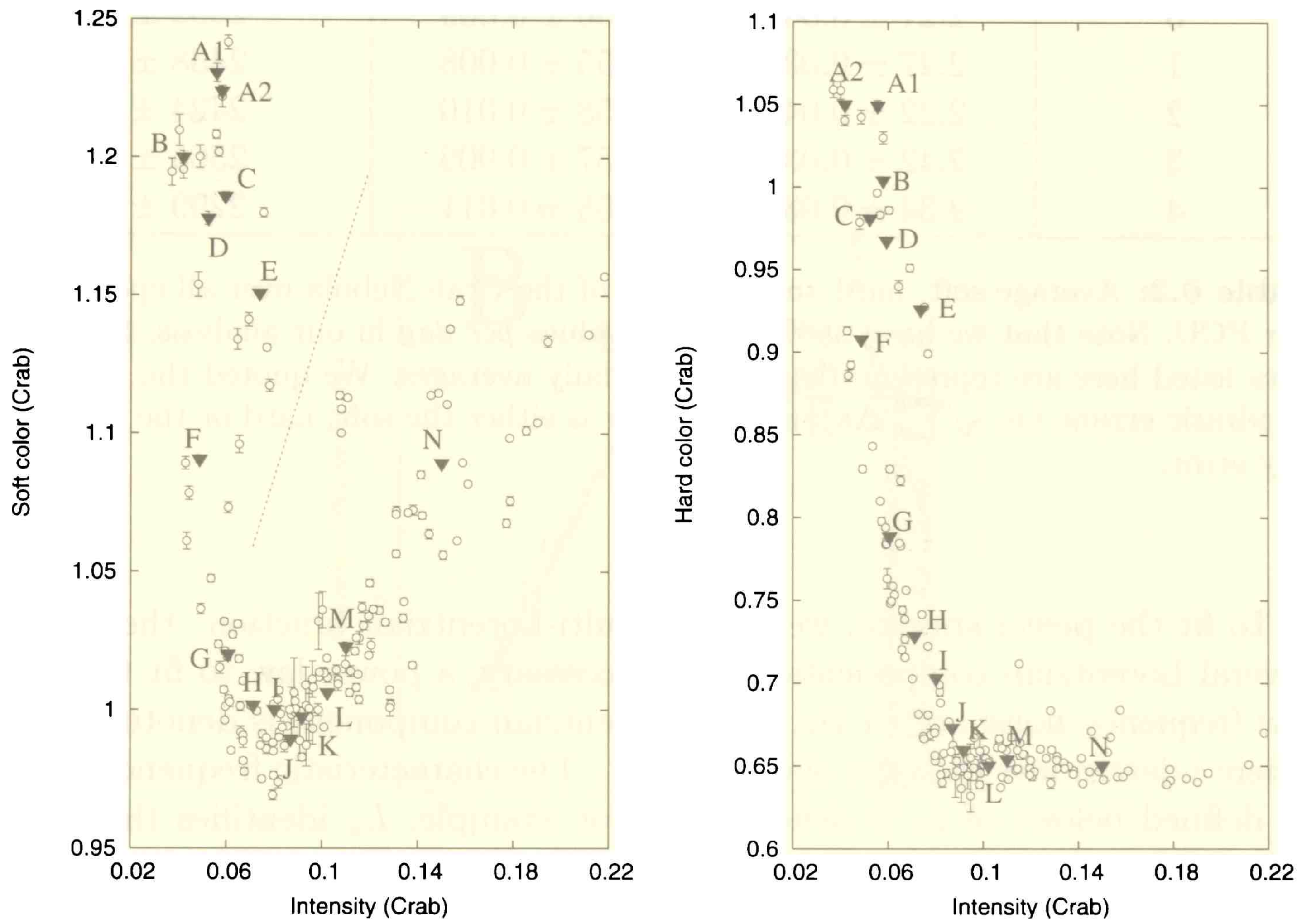

Figure 6.2: Soft color vs. intensity (left) and hard color vs. intensity (right) in units of the Crab Nebula as explained in Section 6.1. Symbols as in Figure 6.1. For clarity, the dashed line separates the observations corresponding to the IS (left), from the observations corresponding to the BS (right).

Interval A1			
Observation	Soft color (Crab)	Hard color (Crab)	Intensity (Crab)
80425-01-04-01	1.2306 ± 0.0034	1.0493 ± 0.0032	0.0557 ± 0.0001
Interval A2			
80425-01-03-00	1.2097 ± 0.0056	1.0585 ± 0.0053	0.0400 ± 0.0001
90409-01-01-00	1.1945 ± 0.0049	1.0590 ± 0.0049	0.0370 ± 0.0001
90409-01-01-01	1.1954 ± 0.0032	1.0403 ± 0.0031	0.0418 ± 0.0001
90409-01-02-00	1.2002 ± 0.0040	1.0424 ± 0.0042	0.0487 ± 0.0001

Table 6.1: Observations used for the timing analysis. The colors and intensity are normalized to Crab (see Section 6.2). The complete table can be obtained digitally from ApJ.

PCU Number	Crab's soft color	Crab's hard color	Crab's intensity (c/s)
0	2.21 ± 0.04	0.56 ± 0.009	2552 ± 21
1	2.27 ± 0.03	0.55 ± 0.008	2438 ± 21
2	2.22 ± 0.04	0.58 ± 0.010	2424 ± 20
3	2.42 ± 0.03	0.57 ± 0.009	2365 ± 20
4	2.34 ± 0.03	0.58 ± 0.011	2299 ± 21

Table 6.2: Average soft, hard and intensity of the Crab Nebula over all epochs and per PCU. Note that we have used averaged values *per day* in our analysis; the numbers listed here are representative for those daily averages. We quoted the averaged quadratic errors, i.e. $\sqrt{\sum_i^n \Delta\kappa_i^2/n}$, where $\Delta\kappa$ is either the soft, hard or the intensity day error.

To fit the power spectra, we used a multi-Lorentzian function: the sum of several Lorentzian components plus, if necessary, a power law to fit the very low frequency noise at $\lesssim 1$ Hz. Each Lorentzian component is denoted as L_i, where i determines the type of component. The characteristic frequency (ν_{max} as defined below) of L_i is denoted ν_i. For example, L_u identifies the upper kHz QPO and ν_u its characteristic frequency. By analogy, other components have names such as L_ℓ (lower kHz), L_{hHz} (hectohertz), L_h (hump), L_b (break frequency), and their frequencies are ν_ℓ, ν_{hHz}, ν_h and ν_b, respectively. For reference, in Figure 6.3 we show two representative power spectra in which we labeled the different components. Using this multi-Lorentzian function makes it straightforward to directly compare the different components in 4U 1636–53 to those in previous works which used the same fit function (e.g., Belloni et al. 2002b; van Straaten et al. 2002, 2003, 2005; Altamirano et al. 2005, Chapter 5 and references therein).

We only include those Lorentzians in the fits whose single trial significance exceeds 3σ based on the negative error bar in the power integrated from 0 to ∞. We give the frequency of the Lorentzians in terms of characteristic frequency ν_{max} as introduced by Belloni et al. (2002b): $\nu_{max} = \sqrt{\nu_0^2 + (FWHM/2)^2} = \nu_0\sqrt{1 + 1/4Q^2}$. For the quality factor Q we use the standard definition $Q = \nu_0/FWHM$. FWHM is the full width at half maximum and ν_0 the centroid frequency of the Lorentzian. Note that Q values in excess of ~ 3 will generally be affected by smearing in an analysis such as ours. Such values are commonly seen in L_{LF}, L_ℓ and L_u. In Section 6.3 we indicate in which cases this could have occurred.

We only report the results for $\nu_{max} \gtrsim 1$ Hz. 4U 1636–53 is one of three atoll sources which are known to show millihertz QPOs which affect the power law behavior of the noise at $\lesssim 1$ Hz (Revnivtsev et al. 2001). For the study of

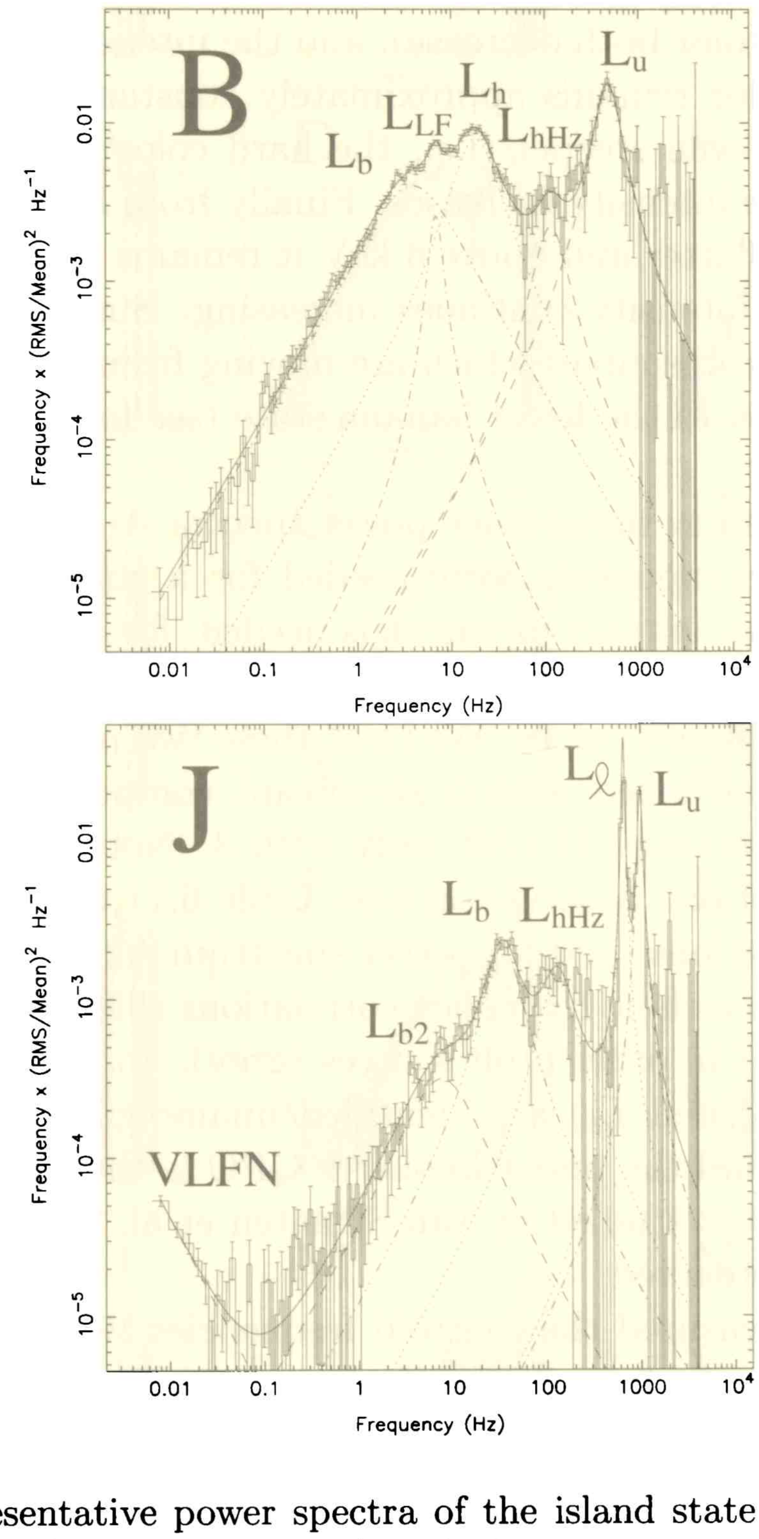

Figure 6.3: Representative power spectra of the island state (above - interval B) and the banana state (below - interval J) with their components.

these QPOs, see Chapter 2.

6.3 Results

Figures 6.1 and 6.2 show that in order A to H, the spectrum becomes softer (i.e. hard and soft color both decrease), and the intensity changes little. From H to L the soft color remains approximately constant but above 6 keV the spectrum becomes even steeper (i.e., the hard color decreases further) and, from interval G, the intensity increases. Finally from L to N, below 6 keV the spectrum becomes flatter and above 6 keV it remains approximately constant in slope, while the intensity continues increasing. Similar behavior has been observed in other atoll sources which are moving from the island to the lower left banana and then to the lower banana state (see for example van Straaten et al. 2003).

In Figure 6.4 we show the average power spectra $A-N$ with their fits. Two to five Lorentzian components were needed for a good fit, except in power spectrum I, where an extra component is needed, for a total of six. Table 6.5 gives the fit results. Power spectra A1 and A2 have the same ν_u within errors, and only slightly different colors. We treat these two power spectra separately because A1 could be fitted with 5 significant components and A2, as well as the combined spectrum A1+A2, only with 3. Note, that power spectrum A1 is the average of one observation (see Table 6.1) which was performed in between the observations used for power spectrum A2. In Figure 6.5 we show our measured characteristic frequency correlations (black) together with those previously measured in other atoll sources (grey). In intervals H–L, the twin kilohertz QPOs (L_u and L_ℓ) are identified unambiguously. The correlation between the lower and the upper kilohertz QPO is the same as that found in the other atoll sources studied by van Straaten et al. (2003). For intervals M and N, only L_u is observed.

We separately measured the centroid frequencies ν_0 of the kHz QPOs (see Table 6.3). The centroid frequency difference $\Delta\nu$ varied between 274.6$\pm$5.7 Hz (in interval K) and 316.4 $\pm$ 5.7 Hz (interval I). These values are between the extremes found by Jonker et al. (2002a) ($\Delta\nu$ = 330 $\pm$ 9 Hz) and Di Salvo et al. (2003) ($\Delta\nu = 242 \pm 4$ Hz). Note that those authors used much shorter time intervals to detect the kHz QPOs and hence were more sensitive to short lived extreme cases. Our average power spectra contain those data which is necessary to detect the broad components well, and hence our measured $\Delta\nu$'s occur at intermediate values, which is when the kHz QPOs are strongest (see e.g. Méndez et al. 2001). So our method averages out the extreme cases. In power spectrum N, L_u reaches the highest centroid frequency found among

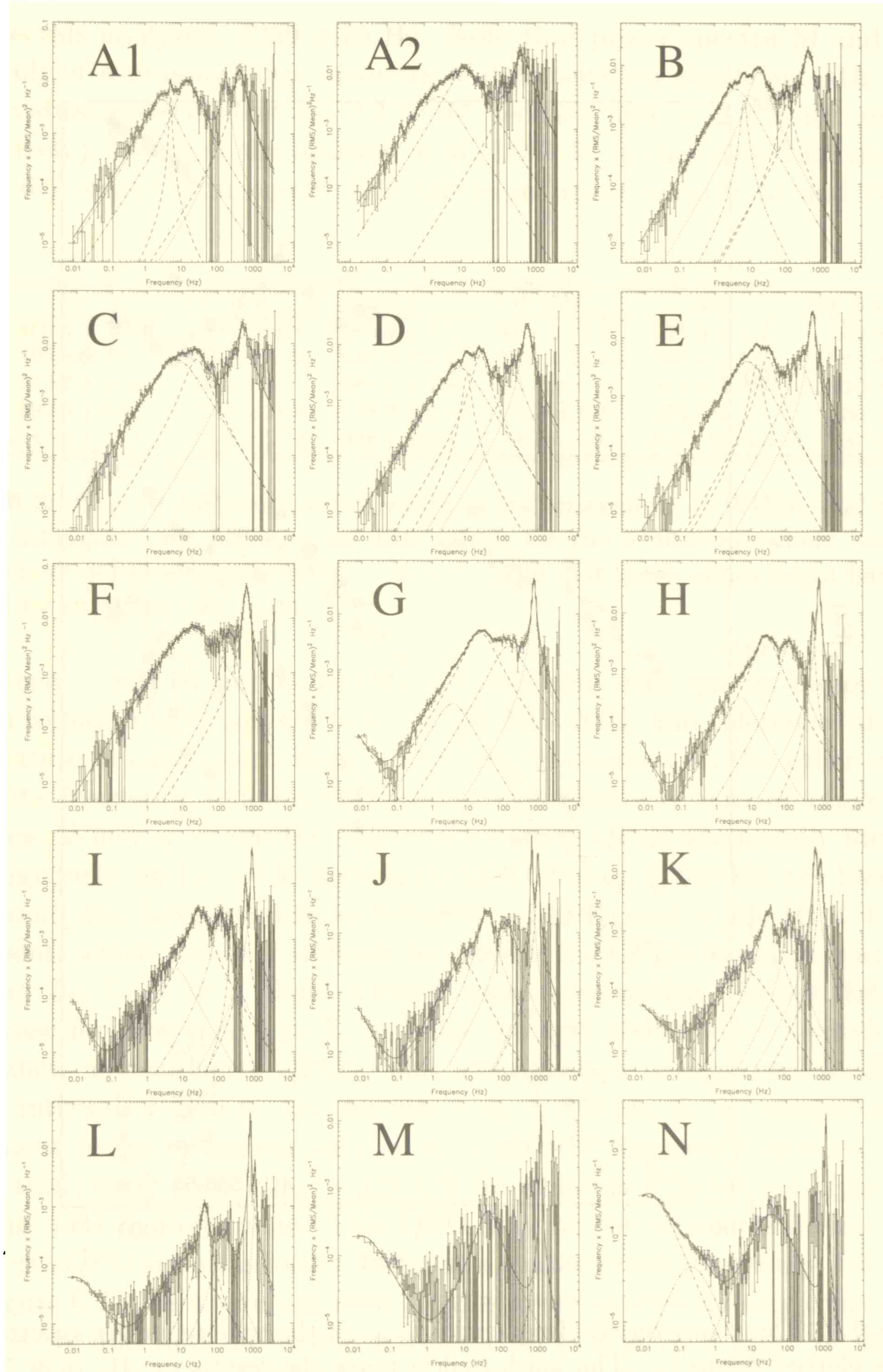

Figure 6.4: Power spectra and fit functions in the power spectral density times frequency representation. Each plot corresponds to a different region in the color-color and color-intensity diagrams (see Figures 6.1 and 6.2). The curves mark the individual Lorentzian components of the fit. For a detailed identification, see Table 6.5 and Figure 6.5.

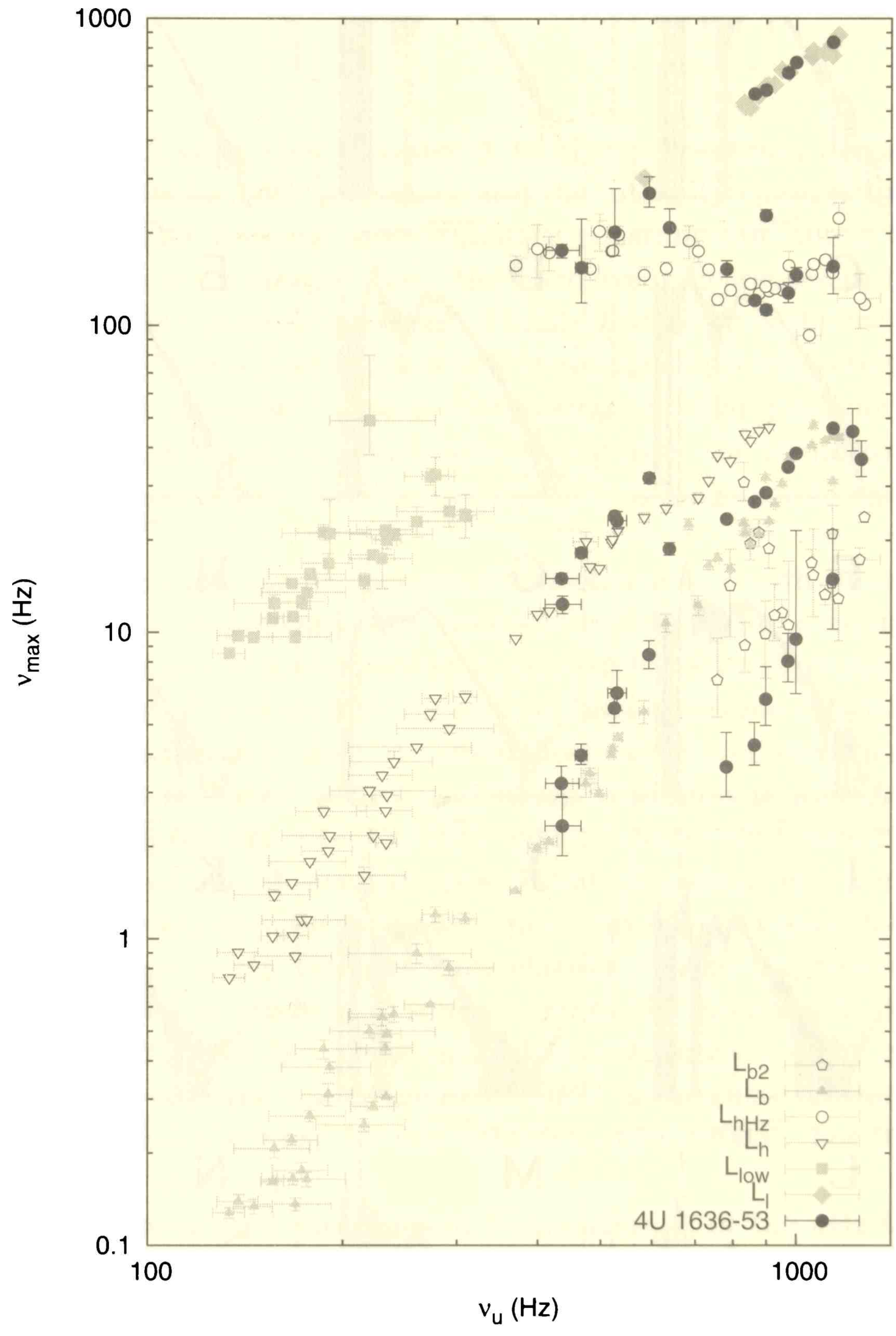

Figure 6.5: The characteristic frequencies ν_{max} of the various power spectral components plotted versus ν_u. The black bullets mark the results for 4U 1636 53. The other symbols mark the atoll sources 4U 0614+09, 4U 1728 34 (van Straaten et al. 2002), 4U 1608 52 (van Straaten et al. 2003), and Aql X-1 (Reig et al. 2004) and the low luminosity bursters 1E 1724 3045, GS 1826 24 and SLX 1735 269 (van Straaten et al. 2005, but also see Belloni et al. 2002b).

the intervals analyzed, 1259 ± 10 Hz. Note that power spectra M and N are the result of averaging large amounts of data with no significant kHz QPOs in individual observations ($\sim 2.2 \times 10^4$ seconds and $\sim 2.5 \times 10^5$ seconds, respectively), based on the position of 4U 1636–53 in the color-color diagram. Figure 6.6 displays the upper kHz QPOs in power spectra M and N more clearly.

Int.	ν_{u0}	$FWHM^*_{\nu_{u0}}$	$\nu_{\ell 0}$	$FWHM^*_{\nu_{\ell 0}}$	$\Delta\nu_0$	Ratio $\nu_{u0}/\nu_{\ell 0}$
H	860.4 ± 1.7	136.2 ± 4.8	565.4 ± 5.1	90.4 ± 12.3	295.0 ± 5.4	1.52 ± 0.01
I	896.8 ± 2.6	115.8 ± 6.3	580.4 ± 5.1	77.2 ± 12.5	316.4 ± 5.7	1.54 ± 0.01
J	972.1 ± 3.5	98.0 ± 8.7	661.1 ± 1.8	73.8 ± 4.1	311.0 ± 3.9	1.470 ± 0.006
K	992.9 ± 6.6	177.4 ± 16.9	718.3 ± 2.4	121.5 ± 6.3	274.6 ± 5.7	1.38 ± 0.01
L	1147.2 ± 16.6	123.4 ± 27.8	836.1 ± 0.7	64.1 ± 1.9	311.1 ± 16.6	1.37 ± 0.02

Table 6.3: Central frequencies, full width at half maximum (FWHM) and the frequency difference $\Delta\nu_0$ between the kHz QPOs for the 5 intervals where both kHz QPOs where detected significantly ($> 3\sigma$). *: Note that these values might have been affected by smearing (see text) .

Between ~ 100 Hz and ~ 200 Hz, a Lorentzian with quality factor $Q \sim 1$ is often found in atoll sources (see van der Klis 2004, and references therein). This feature is called hectohertz QPO and, in contrast to the other components, its frequency remains confined to this relatively narrow range as ν_u increases. When $\nu_u \gtrsim 800$ Hz, the twin kilohertz QPOs are usually identified unambiguously, and so is the hectohertz QPO. For $\nu_u \lesssim 600$ Hz, the lower kHz QPO could also have frequencies between ~ 100 Hz and ~ 300 Hz if it would be present, which makes it difficult to classify the QPOs found in that range as either L_ℓ, L_{hHz} or a blend without more information. In our data, this is the case for intervals A to E; in Table 6.5 and hereafter we identify those Lorentzians as hectohertz QPOs. This identification is supported by the fact that in intervals F and G, i.e., for $600 < \nu_u < 800$ Hz, L_ℓ is undetected; this component seems to appear only at $\nu_u > 800$ Hz. Interval I shows a $\sim 3.1\sigma$ (single trial) peak with $\nu_{max} = 229 \pm 9$ Hz which is a factor $\sim$2 higher than the usual hHz in that range. This QPO may be the second harmonic of the hectohertz QPO simultaneously found at a characteristic frequency 113 ± 4 Hz (see Figure 6.7). As a result of refitting the power spectrum using centroid frequencies, we find that the second harmonic QPO is at $\nu_0 = 228 \pm 10$ Hz while the first harmonic hHz QPO is at $\nu_0 = 107 \pm 5$ Hz for a ratio of 2.13 ± 0.13, consistent with 2.

Figure 6.5 shows that also L_h and L_b lie on the correlations previously observed in other sources. However, our results show that ν_b may anti-correlate with ν_u at $\nu_u \gtrsim 1100$ Hz. This result has already been observed in Z sources, however for atoll sources this behavior has not been observed with certainty

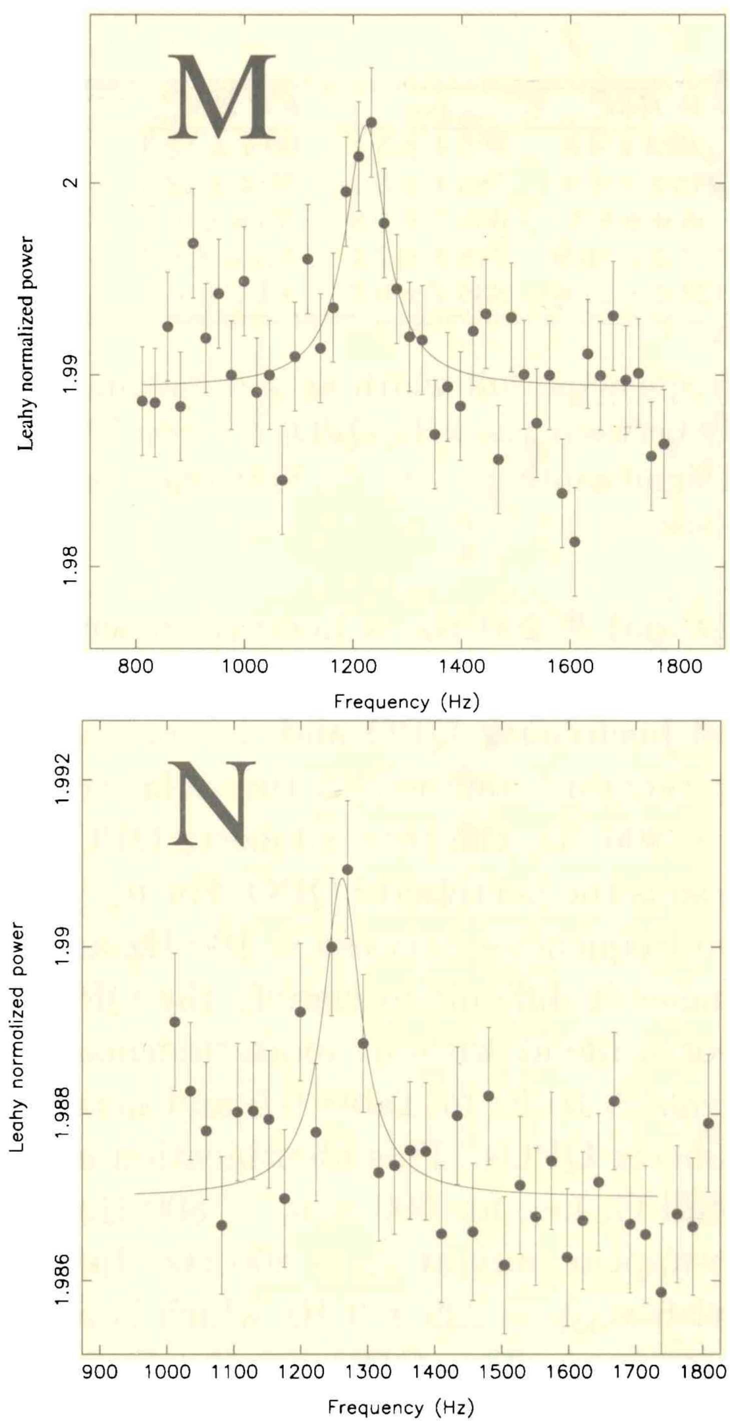

Figure 6.6: kHz QPOs of intervals M and N, respectively. These are Leahy normalized power spectra with no Poisson noise subtraction.

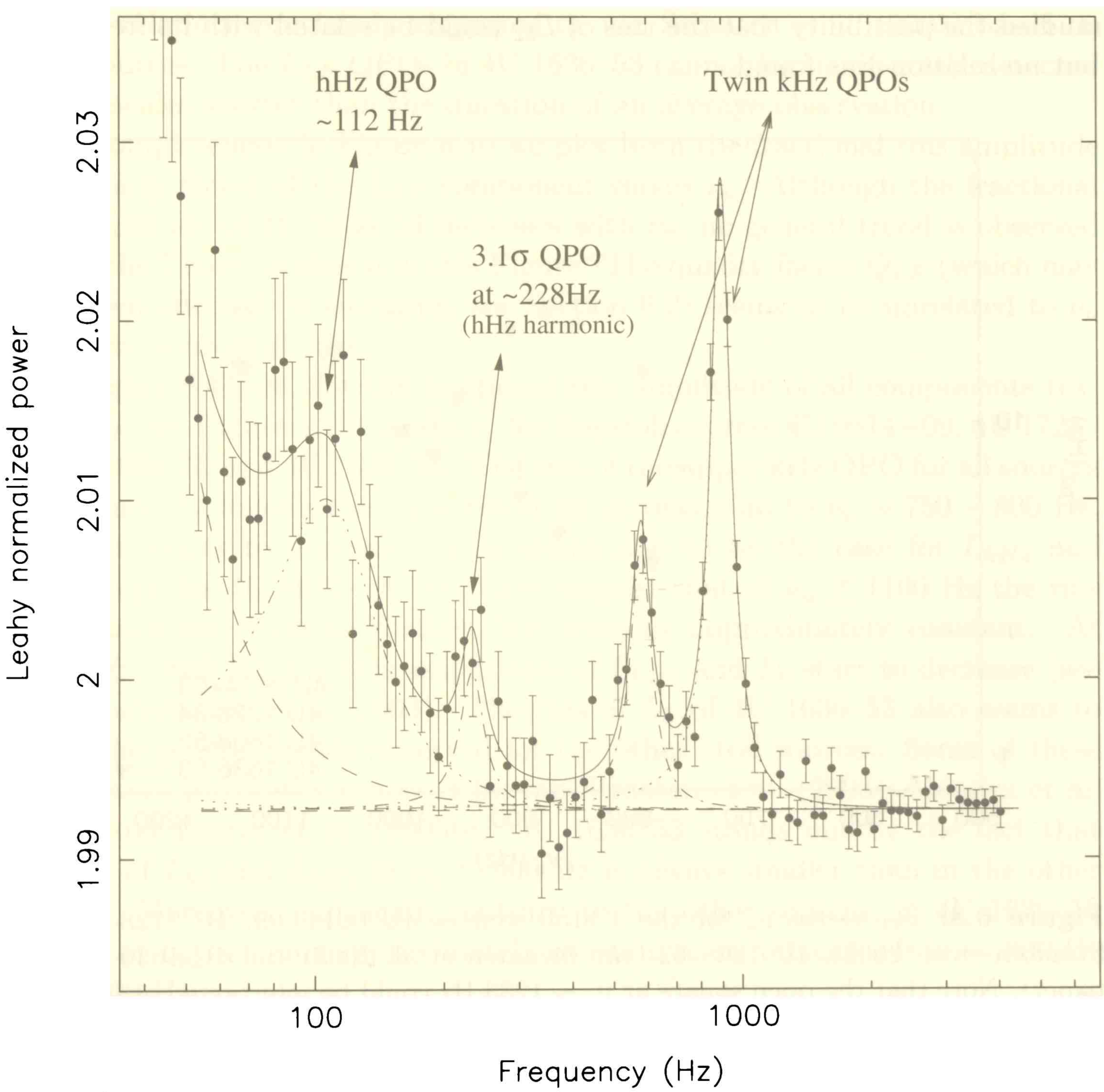

Figure 6.7: Part of the power spectrum of interval I, showing the twin kHz QPOs, the hHz QPO and its possible harmonic. This is a Leahy normalized power spectrum with no Poisson noise subtraction.

(see Section 6.4). L_{b2} seems to have lower frequencies than in other atoll sources. To further investigate this, in Figure 6.8 we plot ν_{b2} versus ν_u with different symbols for each of the 4 atoll sources for which this component has been measured. Clearly, the range in which L_{b2} has been found for similar ν_u is rather large (up to nearly a decade), particularly at $\nu_u < 1000$ Hz. We also studied the possibility that the rms of L_{b2} could be related with its frequency, but no relation was found.

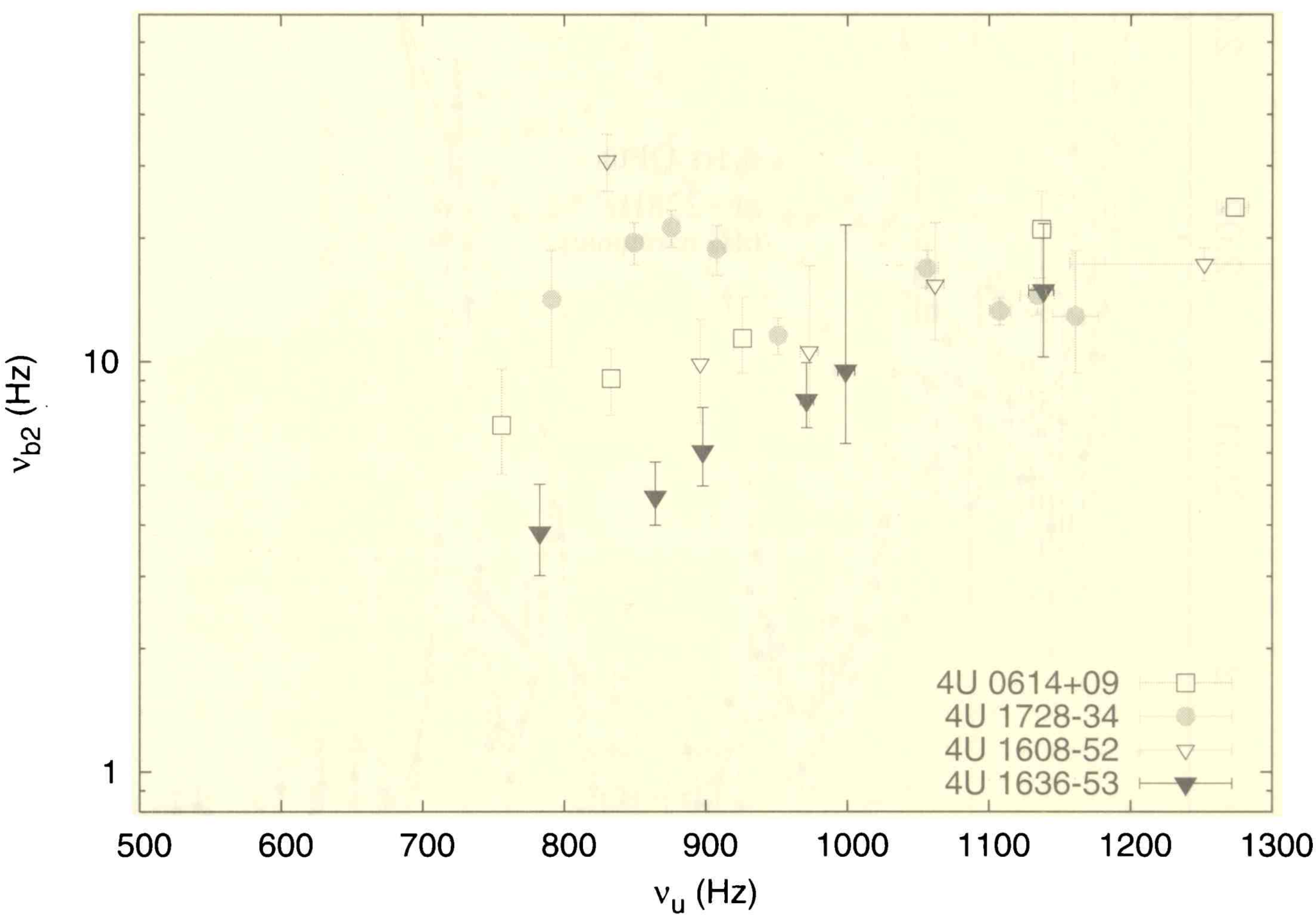

Figure 6.8: ν_{b2} versus ν_u for the 4 atoll sources 4U 0614+09, 4U 1728–34 (van Straaten et al. 2002), 4U 1608–52 (van Straaten et al. 2003) and 4U 1636–53 (this paper). Note that the open square at $\nu_u \sim 1233$ Hz could be interpreted as either L_b or L_{b2} (van Straaten et al. 2002).

Intervals A, B, D and E show a narrow QPO with a characteristic frequency between ν_b and ν_h (see Table 6.5). For other neutron stars such narrow QPOs were previously reported by Yoshida et al. (1993) in 4U 1608–52, by Belloni et al. (2002b) in the low luminosity bursters 1E 1724–3045 and GS 1826–24, by van Straaten et al. (2002) in 4U 0614+09, 4U 1728–34, by van Straaten et al. (2003) in 4U 1608-52, by Altamirano et al. (2005) in 4U 1820–30 (see also Chapter 5), by van Straaten et al. (2005) in the accreting millisecond pulsars (AMXP) XTE J0929–314, XTE J1814–338 and SAX J1808.4–3658 and by Linares et al. (2005) in XTE J1807–294. Similar features were also seen in the BHCs Cyg X-1 by Pottschmidt et al. (2003) and GX 339–4 by Belloni et al. (2002b, but also see van Straaten et al. 2003). Following van Straaten et al. (2003), for clarity we have omitted these QPOs (L_{LF}) from Figure 6.5. In Figure 6.9 we plot their characteristic frequencies vs. ν_h. The results for 4U 1636–53 are in the range of, but seem to follow a different relation than, the two relations previously suggested by van Straaten et al. (2003) based on other sources. The L_{LF} QPOs in 4U 1636–53 cannot be significantly detected on timescales shorter than the duration of an average observation.

For completeness, in Figure 6.10 we plot both the fractional rms amplitude and quality factor of the L_{LF} component versus ν_u. Although the fractional rms amplitude of 4U 1636–53 increases with ν_u, no general trend is observed among the 7 sources shown in this Figure. The quality factor Q_{LF} (which may have been affected by smearing, see Section 6.2) seems to be unrelated to ν_u for all the sources shown.

In Figure 6.11 we plot the fractional rms amplitude of all components (except L_{LF}, see Figure 6.10) versus ν_u for the atoll sources 4U 0614+09, 4U 1728–34, 4U 1608–52 and 4U 1636–53. The rms of the upper kHz QPO for all sources approximately follows the same trend: it increases up to $\nu_u \sim 750 - 800$ Hz, and then starts to decrease. This seems also to be the case for L_{hHz} and L_b. Except for 4U 0614+09, the data suggest that at $\nu_u \gtrsim 1100$ Hz the rms of L_u does not decrease further, but remains approximately constant. At $\nu_u \sim 750 - 800$ Hz, the rms amplitudes of L_{hHz} and L_b start to decrease (see also van Straaten et al. 2003). The rms of L_h of 4U 1636–53 also seems to follow the general trends observed for the other atoll sources. Some of these results were previously reported by van Straaten et al. (2003), Méndez et al. (2001) and Barret et al. (2005b). 4U 1636–53 stands out by the fact that the rms of L_{b2} and L_{hHz} at $\nu_u \lesssim 900$ Hz is always smaller than in the other sources. Moreover, and again contrary to the other sources, in 4U 1636–53 the rms of L_{b2} remains approximately constant as ν_u increases from ~ 800 Hz to ~ 1200 Hz.

In Figure 6.12 we plot the quality factors Q_u, Q_ℓ and Q_{hHz} versus ν_u. As noted in Section 6.2, the Q values of L_ℓ, and to a lesser extent, L_u, have likely been affected by smearing. The Q values of the other components are not plotted since they are usually broad. The data on 4U 1636–53 are in general agreement with what was found using similar methods on the other sources (van Straaten et al. 2002). Q_u increases monotonically with ν_u until $\nu_u \sim 900 - 1000$ Hz. At this frequency, Q_u seems to decrease for all sources, to immediately increase again as ν_u increases. Q_ℓ shows a rather random behavior due to smearing (see Di Salvo et al. 2003 and Barret et al. 2005b,a for Q_ℓ measurements less affected by smearing); we display this quantity in

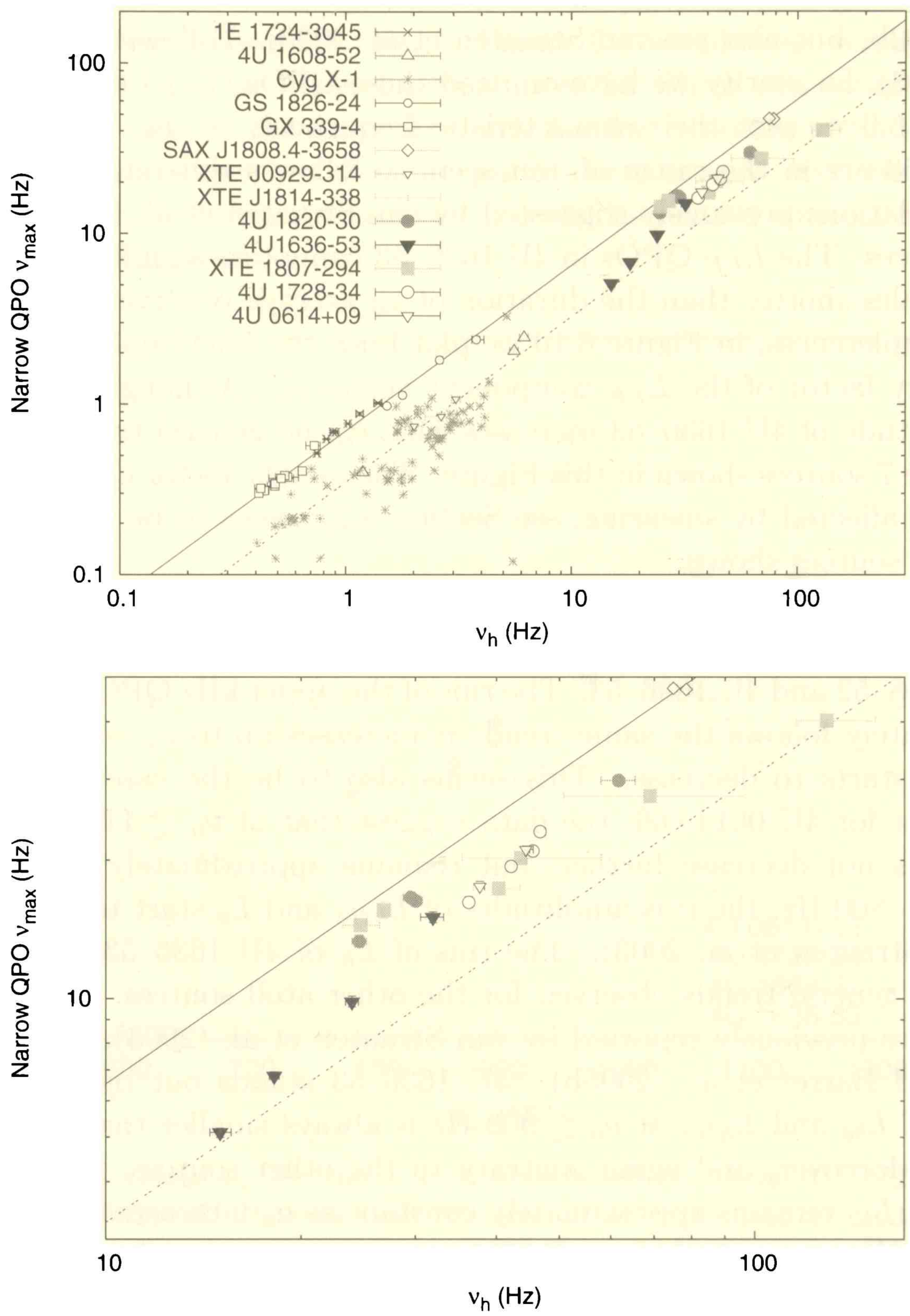

Figure 6.9: *(Above)* Characteristic frequencies ν_{LF} and $\nu_{LF/2}$ (see text) versus ν_h . The symbols are labeled in the plot, and represent the frequencies of the QPOs in the atoll sources 4U 1728–34, 4U 0614+09, 4U 1608–52, 4U 1820–30, the BHCs Cyg X-1 and GX 339–4, the low luminosity bursters 1E 1724–3045 and GS 1826–24 and the accreting millisecond pulsars XTE J0929–314, XTE J1814–338 and SAX J1808.4–3658 (van Straaten et al. 2003, 2005; Altamirano et al. 2005). The filled triangles show the results for 4U 1636–53. The drawn line indicates a power-law fit to the ν_{LF} vs. ν_h relation of the low-luminosity bursters 1E 1724–3045 and GS 1826–24, and the BHC GX 339–4. The dashed line is a power law with a normalization half of that of the drawn line. *(Bottom)* A zoom of the high frequency region.

Figure 6.12 for comparison to previous works using the same method.

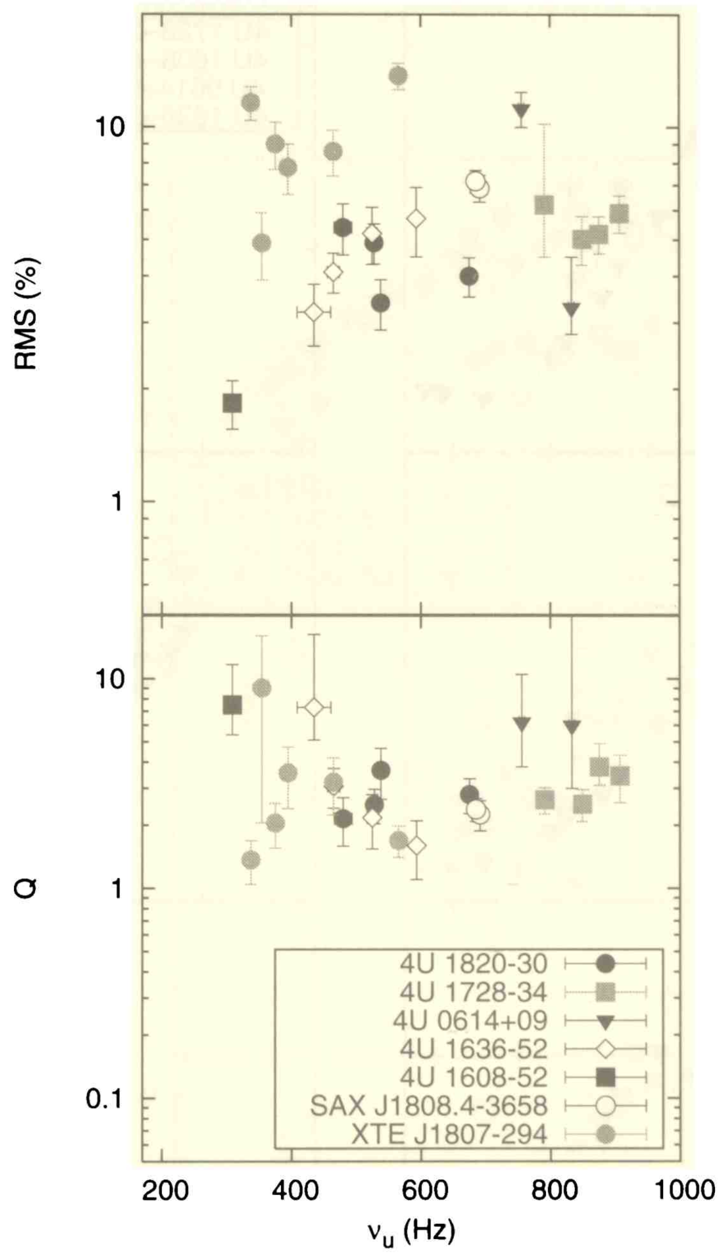

Figure 6.10: L_{LF}'s rms (*above*) and Q (*below*) versus ν_u for 7 atoll sources. The symbols are labeled are the same in both plots. The scatter of the points are likely due to the averaging method (see text).

Q_{hHz} shows a complicated behavior. To further investigate this behavior, we first re-binned the Q_{hHz} data by a factor 3 and fitted a straight line. The best fit gives $\chi^2/dof = 93/12 \sim 7.7$. Since the data appears to show two bumps separated by a minimum creating a roughly sinusoidal pattern, we also tried to fit a straight line plus a sine wave. The best fit has a $\chi^2/dof = 16.9/9 \sim 1.8$ which gives a 3.4σ improvement of the fit based on an F-test. The results of this fit are listed in Table 6.4. In Figure 6.5 it can be seen that ν_{hHz} appears to display a similar pattern. Fitting the relation of ν_{hHz} versus ν_u with only a straight line gives a $\chi^2/dof = 156/12 = 13$ while a straight line plus a sine gives a $\chi^2/dof = 28.4/9 \sim 3.15$, once again, we find a 3.4σ improvement of

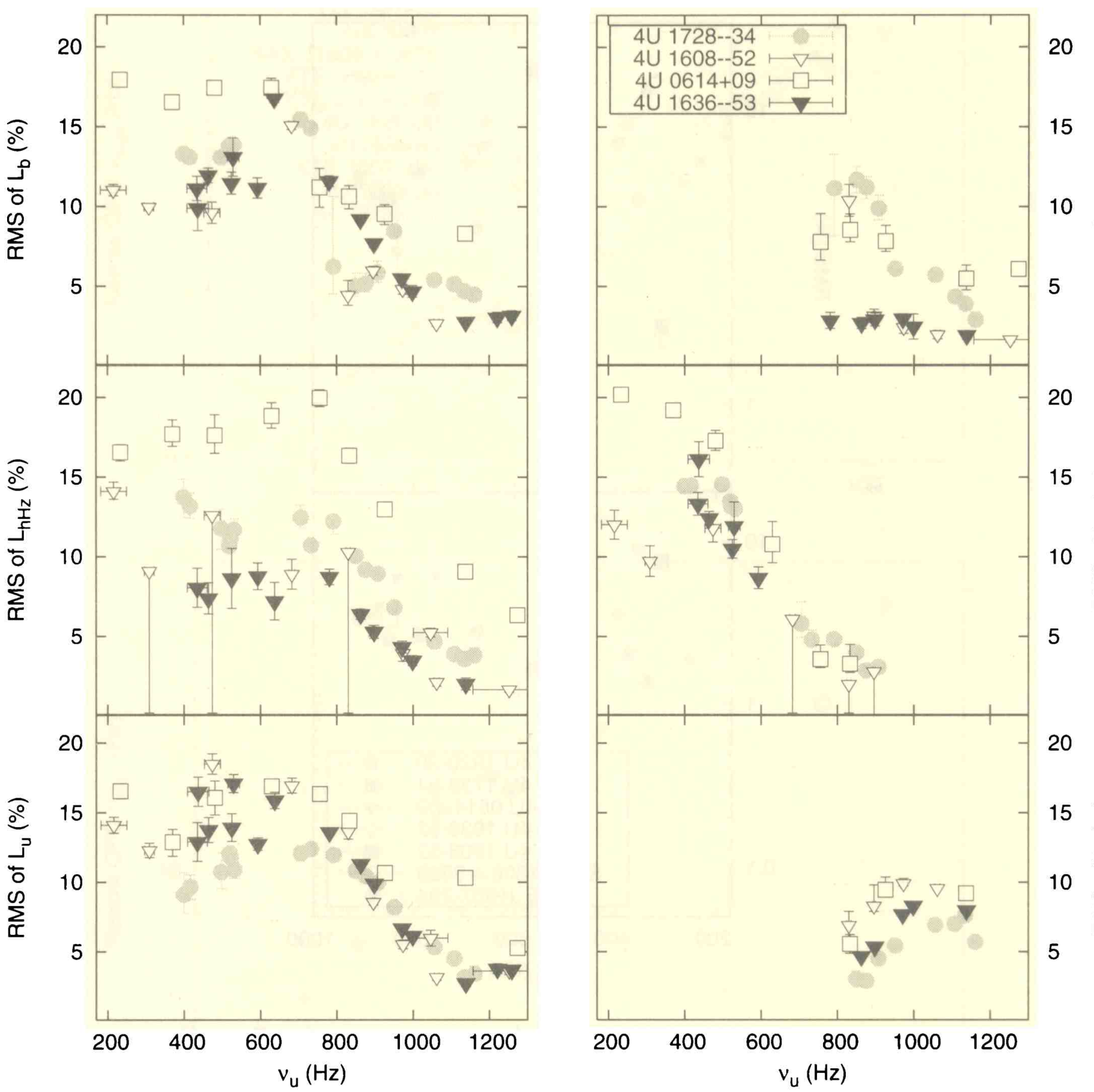

Figure 6.11: The fractional rms amplitude of all components (except L_{LF}) plotted versus ν_u. The symbols are labeled in the plot. The data for 4U 1728–34, 4U 1608–52 and 4U 0614+09 were taken from van Straaten et al. (2005). Note that for L_{hHz} and L_h of 4U 1608–52, the 3 triangles with vertical error bars which intersect the abscissa represent 95% confidence upper limits (see van Straaten et al. (2003) for a discussion). Also note that we exclude the 3 points in the rms_ℓ versus ν_u plot which were identified as L_{low} by van Straaten et al. (2003).

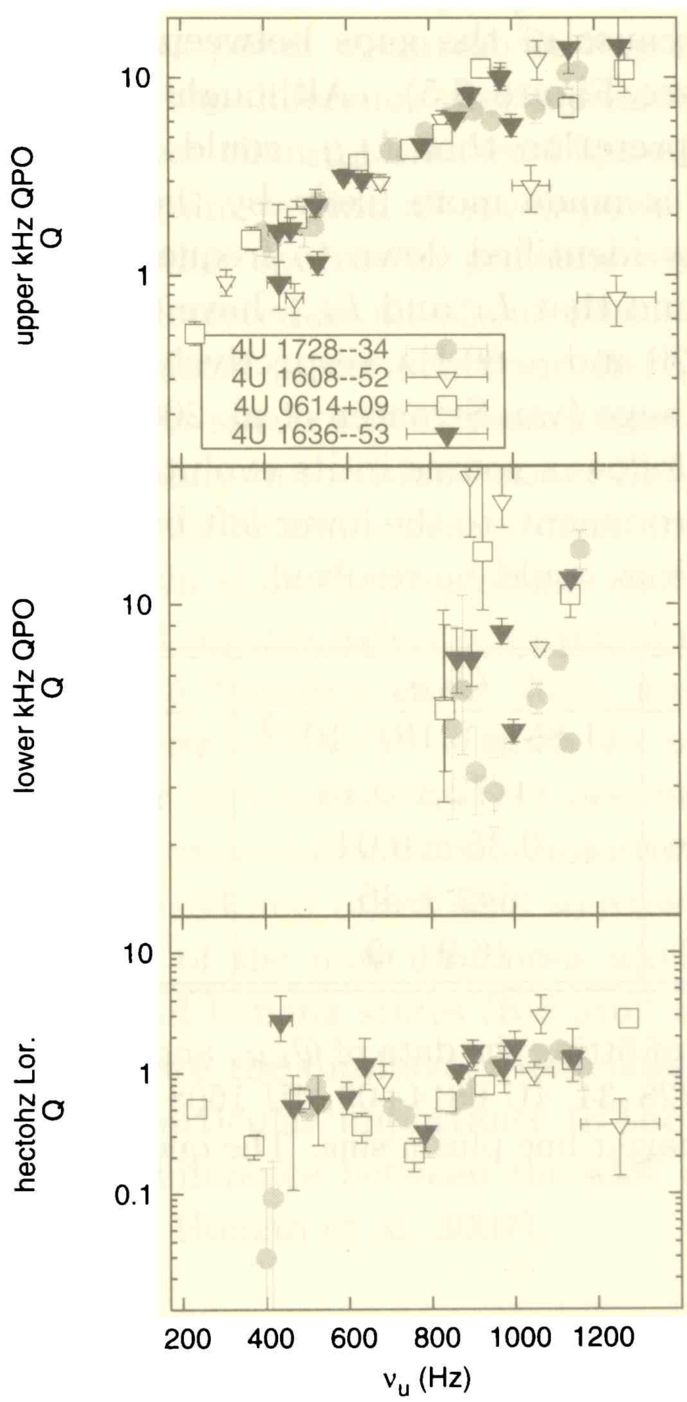

Figure 6.12: Quality factor Q of L_u, L_ℓ and L_{hHz} versus ν_u. Symbols are the same as in Figure 6.11. Note that the results for the quality factor are probably affected by the averaging method (see Sections 6.1, 6.3 and the Appendix).

the fit based on an F-test. The results of this fit are also given in Table 6.4.

With the present data it is difficult to distinguish if this is the behavior of L_{hHz} alone, or is due to blending with other components which are not strong and coherent enough to be observed separately on short time scales and are lost in the averaging of the power spectra. This, as well as other ambiguities (see discussion about the identification of $L_{\ell ow}$ in van Straaten et al. 2003), arise because of the gaps between the ν_{ℓ}, $\nu_{\ell ow}$, ν_h and ν_{hHz} versus ν_u relations (see Figure 6.5). Although we are not able to explain those gaps, the interpretation that L_{hHz} could be affected by the presence of other components is made more likely by the fact that L_{ℓ} in Z sources can be unambiguously identified down to frequencies of $\sim$ 150 Hz (see e.g. Jonker et al. 2002b) and that L_h and $L_{\ell ow}$ have sometimes been observed at frequencies up to $\sim$ 120 and $\sim$ 60 Hz, respectively, i.e., in both cases reaching the hectohertz QPO range (van Straaten et al. 2005, Linares et al. 2005). If it would be possible to follow a source in its evolution from the extreme island states where $L_{\ell ow}$ is prominent, to the lower left banana where L_{ℓ} is seen, then some of these ambiguities could be resolved.

	Q_{hHz}	$\nu_{hHz}(Hz)$
Slope	$(1.85 \pm 0.19) \cdot 10^{-3}$	$(-6.3 \pm 1.3) \cdot 10^{-2}$
Constant	-0.72 ± 0.14	203 ± 12
Amplitude	0.35 ± 0.04	23.9 ± 2.2
Period	542 ± 46	602 ± 35
χ^2/dof	16.9 / 9	28.4 / 9

Table 6.4: The results of fitting the data of Q_{hHz} and ν_{hHz} versus that of ν_u for the four atoll sources 4U 1728–34, 4U 0614+09, 4U 1608–52 and 4U 1636–53. We used the combination of a straight line plus a sine. The quoted errors use $\Delta\chi^2 = 1.0$.

6.4 Discussion

In this paper, we report a detailed study of the time variability of the atoll source 4U 1636–53 using RXTE that includes, for the first time, observations of this source in the (low-luminosity) island state. We divided the data into 15 intervals, A to N, based on the position of the source in the color diagram. Based on the fact that, (i) intervals A1, B, D and E show a narrow QPO with a characteristic frequency between ν_b and ν_h which was previously seen in other atoll sources when they were in their island state (e.g. van Straaten et al. 2002, and Chapter 5); (ii) intervals A1, A2, B, D, E and F do not show either L_{ℓ} or power-law VLFN at frequencies lower than 0.5 Hz, which would be expected to be present in the banana state (Hasinger & van der Klis 1989; van der Klis 2004, 2006); (iii) the intensity of the source starts to increase from interval G (see Figure 6.2) and (iv) intervals A1 to F occupy the hardest loci in the color diagram (see Figures 6.5 and 6.2), we conclude that intervals A1 to F show the source in the island state, representing the first RXTE observations of 4U 1636–53 in this state. Interval G may represent the transition between the IS and the LLB since its power spectrum is very similar to that of the first five intervals, but with the difference that a weak (~ 1.2 % rms) VLFN is present at a frequency lower than 0.1 Hz (see Figure 6.5).

Along the color color diagram we find all seven power spectral components that were already seen in other sources in previous works (see van der Klis 2004, for a review): L_u is detected in all of our power spectra, L_ℓ is unambiguously detected starting from power spectrum H ($\nu_u \sim 800$ Hz), L_{hHz} is observed in 11 out of 15 power spectra at frequencies between 100 and 270 Hz, L_h and L_{LF} are detected mainly in the island state, L_b is always observed and finally L_{b2} is detected when L_b becomes peaked from interval G.

Previous works have shown that the frequencies of the variability components observed in other atoll sources follow a universal scheme of correlations when plotted versus ν_u (van Straaten et al. 2003, and references therein). We have found that the noise and QPO frequencies of the time variability of 4U 1636–53 follow similar correlations as well (see Section 6.3) confirming the predictive value of this universal scheme. However, we also found some differences between 4U 1636–53 and other atoll sources which we discuss below. As 4U 1636–53 is one of the most luminous atoll sources showing the full complement of island and banana states (full atoll track), the object is of interest in order to investigate the luminosity dependence of spectral/timing state behavior. This is of particular importance to the ongoing effort to understand the origin of the difference between the atoll sources and the more luminous Z sources (see e.g. Homan et al. 2007).

6.4.1 The broad components in 4U 1636–53 and Z-source LFN

As can be clearly seen in Figure 6.8, where we show ν_{b2} versus ν_u, the behavior of the L_{b2} component differs significantly between sources. For 4U 1636–53 and 4U 0614+09, ν_{b2} increases with ν_u, while this is not seen for 4U 1608–52 and 4U 1728–34. This frequency behavior is different from that observed for all other components (see Section 6.3), which instead is very consistent between sources, even for the case of the hHz QPO, which has not been seen to correlate with other components (see van der Klis 2004, for a review). This unusual, somewhat erratic behavior of L_{b2} may be related to the fact that it is usually detected as a relatively weak wing to a much stronger L_b, so that small deviations in the time-averaged shape of L_b have a large effect on L_{b2}.

In order to investigate the relation of L_{b2} to the well-known low frequency noise (LFN) which occurs in the same frequency range in Z sources, in Figure 6.13 we plot the results for 4U 1636–53 together with those for the LFN in the Z sources (Hasinger & van der Klis 1989) GX 17+2 (Homan et al. 2002), Cyg X-2 (Kuznetsov 2002), GX 340+0 (Jonker et al. 2000a) and GX 5–1 (Jonker et al. 2002b). Note that the broad-band noise in these Z sources was not fitted with a zero-centered Lorentzian but with a cutoff power law or a smooth broken power law. We used the results of the conversion from power laws to zero-centered Lorentzians done by van Straaten et al. (2003). Previous works (e.g. Psaltis & Chakrabarty 1999; van Straaten et al. 2003) compared the time variability of Z sources with that of atoll sources and tried to associate variability components among these sources. Based on frequency-frequency plots, only the kHz QPOs and the horizontal branch oscillations (HBO) found in the Z sources can be unambiguously identified with atoll source components, the latter with L_h. van Straaten et al. (2003) suggested that the LFN might be identified with L_{b2} and noted that (like in the case of L_{b2}) the characteristic frequency of the LFN, when plotted versus ν_u, does not follow exactly the same relations between Z sources. By comparing the different frequency patterns in Figure 6.13, we find that the behavior of the LFN component of GX 17+2, and that of L_{b2} of 4U 1636–53 are similar, which might indicate that the physical mechanism involved is the same. Perhaps this is related to the fact that 4U 1636–53 is a relatively luminous atoll source (see Ford et al. 2000) while GX 17+2 may be a relatively low luminosity Z-source (Homan et al. 2002). Hence, 4U 1636–53 might be relatively close in L_x to GX 17+2 and differ more in L_x from the other two sources introduced above. Note that the time variability of GX 17+2 is different from that of the other Z sources plotted in Figure 6.13. For instance, the characteristic frequency of its LFN is rather low and it appears as a peak, it shows a flaring branch oscillation (FBO) and the harmonic of the HBO is relatively strong, whereas the other Z sources plotted show a flat LFN, no FBO and a weak harmonic to the HBO (Jonker et al. 2002b). As previously noted by Kuulkers et al. (1997), these properties set GX 17+2 apart from the 'Cyg-like' Z sources GX 5–1, GX 340+0 and Cyg X-2 and, associate it with the 'Sco-like' Z sources Sco X-1 and GX 349+2, not plotted in Figure 6.13 because no systematic study of the of the LFN and QPO behavior of these sources in terms of ν_{max} is available as yet.

We further investigated the frequency similarities between 4U 1636–53 and GX 17+2 by plotting our results for the two sources. No clear component associations were found. GX 17+2 is the only Z source that had shown an

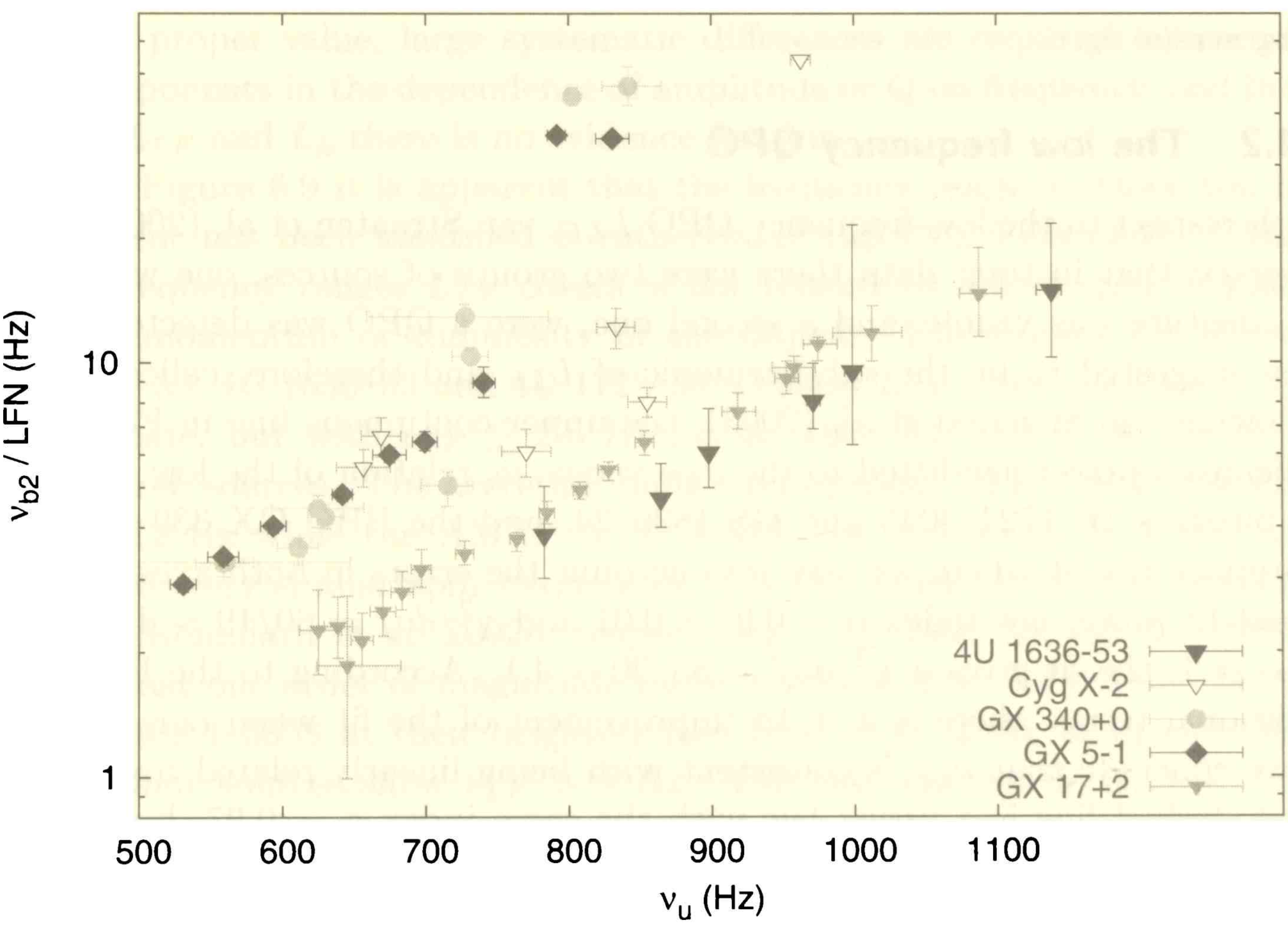

Figure 6.13: ν_{b2} versus ν_u for the atoll source 4U 1636–53 (this paper) and the characteristic frequencies of the low-frequency noise (LFN) versus ν_u for the Z sources GX 17+2 (Homan et al. 2002), Cyg X-2 (Kuznetsov 2002), GX 340+0 (Jonker et al. 2000a) and GX 5–1 (Jonker et al. 2002a) – see text and van Straaten et al. (2003) for details. (see also Figure 6.8)

anti-correlation between the frequency of one of its components (HBO) and the kHz QPOs at high $\nu_u \gtrsim 1050$ Hz (Homan et al. 2002). A similar effect was seen in the atoll source 4U 0614+09 between ν_b and ν_u (van Straaten et al. 2002). As can be seen in Figure 6.5, a similar decrease of ν_b with ν_u at high frequency may occur in 4U 1636–53. However, the error bars on ν_b are rather large in the relevant range, and the data are still consistent with ν_b being constant at $\nu_u \gtrsim 1100$ Hz, and marginally, even with a further increase in frequency. It is interesting to note, that while 4U 0614+09 has a much lower L_x than 4U 1636–53, both sources apparently show this same turnover in ν_b versus ν_u.

6.4.2 The low frequency QPO

With respect to the low-frequency QPO L_{LF}, van Straaten et al. (2003, 2005) observed that in their data there were two groups of sources, one where the L_{LF} feature was visible, and a second one, were a QPO was detected which they suggested to be the sub-harmonic of L_{LF} and therefore, called $L_{LF/2}$. Following van Straaten et al. (2003), the upper continuous line in Figure 6.9 indicates a power law fitted to the ν_{LF} versus ν_h relation of the low luminosity bursters 1E 1724–3045 and GS 1826–24, and the BHC GX 339–4. If we reproduce the fit where we take into account the errors in both axes, we find a best fit power-law index $\alpha = 0.97 \pm 0.01$ and $\chi^2/dof = 80/19 \sim 4.2$. If we fix $\alpha = 1$, the fit gives a $\chi^2/dof = 83/20 \sim 4.1$. According to the F-test for additional terms, there is a $< 1\sigma$ improvement of the fit when α is set free, so we conclude that ν_{LF} is consistent with being linearly related to ν_h. The lower dashed line is a power law with the same index $\alpha = 0.97$, but with a normalization half of that of the dashed line.

As can be seen in Figure 6.9, in 4U 1636–53 the L_{LF} component does not follow either of the two power-law fits. If we fit the points for 4U 1636–53, we find that the power-law index is $\alpha_2 = 1.40 \pm 0.09$ ($\chi^2/dof = 0.14/2$), significantly different from that of the other sources. Given the above, it is probably incorrect to think that the difference in the ν_{LF} vs. ν_h relation between GX 339–4, GS 1826–24 and 1724–3045 on one hand and 4U 1608–52, Cyg X-1 and XTE J0929-314 on the other is associated with harmonic mode switching (van Straaten et al. 2003). This conclusion is supported by the work of Linares et al. (2005) who also found a different correlation ($\alpha = 0.58 \pm 0.06$, see also Figure 6.9) in XTE 1807–294 over a much wider range of frequencies than we obtained for 4U 1636–53, by the high χ^2/dof for the $\nu_{LF} - \nu_h$ fit on the data of the low luminosity bursters 1E 1724–3045, GS 1826–24, and the BHC GX 339–4 (see previous paragraph), by the fact that if we use the centroid frequencies instead of ν_{max}, the relations worsen (see van Straaten et al. 2003), and by the fact that the points for 4U 1728–38 (van Straaten et al. 2002) fall in between the two power laws, (solid and dashed line in Figure 6.9). Nevertheless it is interesting that the data for 4U 0614+09, 4U 1728–34, 4U 1636–53, 4U 1820–30, 4U 1608–52 XTE 1807–294, SAX J1808.4–3658, XTE J1814–338 and XTE J0929–314 all fall on, or in between, the two previously defined power laws, i.e., follow a single relation to within a factor of ~ 2. We note that all the ν_{LF} values discussed here could in principle have been affected by smearing in the averaging process discussed in Section 6.2. However, for smearing to shift a frequency-frequency point away from its proper value, large systematic differences are required between the two components in the dependence of amplitude or Q on frequency, and in the case of L_{LF} and L_h there is no evidence for this.

From Figure 6.9 it is apparent that the frequency range in which the L_{LF} component has been identified is rather large (up to 2.5 decades). Clearly, which frequency ranges L_{LF} covers is not related to source spin frequency, angular momentum or luminosity of the object. The sources 4U 1608–52, 4U 1820–30, 4U 1636–53 and 4U 1728–34 all show L_{LF} when they are in their island state, but with $\nu_{LF} \lesssim 2.6$ Hz for 4U 1608–52, and $\gtrsim 30$ Hz for the other three sources. The accreting millisecond pulsar XTE J1807–294 shows $\nu_{LF} \gtrsim 12$ Hz while the AMXP XTE J0929–314 shows $\nu_{LF} \lesssim 1$ Hz, while both have very similar spin frequencies (191 Hz, Markwardt et al. 2003 and 185 Hz, Remillard et al. 2002b, respectively). 4U 1820–30 and 4U 1636–53 are at least one order of magnitude more luminous than XTE 1807–294 and SAX J1808.4–3658 at their brightest (see Ford et al. 2000; Wijnands 2005), but all four sources show $\nu_{LF} > 5$ Hz. The only systematic feature in the LF QPO frequencies is that while frequencies up to 50 Hz are seen in neutron stars, black holes have not been reported to exceed 3.2 Hz, nor did atoll sources in the EIS exceed 2.6 Hz. So, BHCs and NS in the extreme island state are similar in this respect; (this may be related to an overall similarity in power spectral shape for such sources in these states that was noted before; see, e.g., Psaltis & Chakrabarty 1999; Nowak 2000; Belloni et al. 2002b; van Straaten et al. 2002).

6.4.3 The X-ray luminosity dependence of rms

It has been suggested that an anti-correlation may exist between the average X-ray luminosity of different sources and the rms amplitude of their power spectral components (see discussion in Jonker et al. 2001; van Straaten et al. 2002, 2003, and references therein). From Figure 6.11 we find differences in kHz QPO rms amplitudes of no more than a factor 2 between sources which differ in average luminosity by a factor up to 10, except for one point of

4U 0614+09 at $\nu_u \sim 1140$ Hz, where the rms of the upper kHz QPOs is a factor ~ 7 higher than that of the other atoll sources. Méndez et al. (2001), Jonker et al. (2001) and van Straaten et al. (2002) have already noted that the data are inconsistent with a model in which the absolute amplitudes of the kHz QPOs are the same among sources, and the decrease in rms with luminosity between sources is only caused by an additional source of X-rays unrelated to the kHz QPOs.

From Figure 6.11 it can also be seen that the largest rms amplitude differences are found in the hHz QPOs. For this component we can define three groups: (1) 4U 0614+09, which has the strongest rms_{hHz} ; (2) 4U 1636–53, which has the weakest rms_{hHz} ; and (3) 4U 1728–34 and 4U 1608–52, which have rms_{hHz} between those of (1) and (2). From figure 1 in Ford et al. (2000), it can be seen that 4U 0614+09 is the faintest X-ray source of our sample, while 4U 1636–53 is the brightest. 4U 1728–34 and 4U 1608–52 show luminosities between the first two. This clear X-ray luminosity–rms anti-correlation for L_{hHz} may be suggested, but not as clear, in the other components (see also Figure 6.10).

The fact that the rms of L_{hHz} starts to decrease at the same ν_u as that of L_u and L_b, while ν_{hHz} does not correlate with ν_u as all other frequencies do, suggests that the frequency setting mechanism is different for L_{hHz} compared with the other components, while the amplitude setting mechanism is common. As pointed out in Section 6.3, the drop in rms in L_u, L_{hHz} and L_b starts at ν_u between 700 and 800 Hz. For the case of 4U 1636–53 shown here, this corresponds to interval G. The power spectrum of this interval may represent the transition between the island and the banana state, when the geometric configuration of the system is thought to change (e.g. Jonker et al. 2000b; Gierliński & Done 2002). For example, the appearance of a puffed-up disk could smear out the variability coming from the inner region where the oscillations are produced.

6.4.4 The nature of the hectohertz QPOs

While our results indicate that the characteristic frequency of the hHz QPO may oscillate as a function of ν_u, ν_{hHz} remains constrained to a limited range of frequencies (100–250 Hz) for 4U 1636–53 and for the other sources used in Figure 6.5. A similar result has been reported for ν_{hHz} in several other atoll sources such as in MXB 1730–335 (Migliari et al. 2005), 4U 1820–30 (Chapter 5) and in the atoll source and millisecond accreting pulsar SAX J1808.4–3658 (Wijnands & van der Klis 1998b; van Straaten et al. 2005). Interestingly, the presence of L_{hHz} has not been confirmed for Z-sources (van der Klis 2006), possibly due to the intrinsic differences between atoll and Z-sources such as luminosity.

van Straaten et al. (2002) have suggested a link between the $\lesssim$ 100 Hz QPOs reported by Nowak (2000) in the black holes Cyg X-1 and GX 339–34 and L_{hHz}. van Straaten et al. (2002) also suggested that L_{hHz} could be related to the $\sim$ 67 Hz QPO in the black hole GRS 1915+105 (Morgan et al. 1997) and the $\sim$ 300 Hz QPO in the BHC GRO J1655–40 (Remillard et al. 1999b) which also have stable frequencies. Fragile et al. (2001) made a tentative identification of the $\sim$ 9 Hz QPO in the BHC GRO J1655–40 (Remillard et al. 1999b) with the orbital frequency at the Bardeen-Petterson (B–P) transition radius (Bardeen & Petterson 1975) and suggested the same identification for L_{hHz} in neutron star systems. In this scenario, the orbital frequency at the radius where a warped disk is forced to the equatorial plane by the Bardeen–Petterson effect can produce a quasi-periodic signal (see Fragile et al. 2001, for an schematic illustration of the scenario).

Attempts have been made to theoretically estimate the B–P transition radius from accretion disks models in terms of the angular momentum and the mass of the compact object (e.g. Bardeen & Petterson 1975; Ivanov & Illarionov 1997; Hatchett et al. 1981; Nelson & Papaloizou 2000). Fragile et al. (2001) propose a parameterization involving a scaling parameter A, which according to them lies in the range $10 \lesssim A \lesssim 300$. These authors write the B–P radius as $R_{BP} = A \cdot a_\star^{2/3} \cdot R_{GR}$, where $a_\star = Jc/GM^2$ is the dimensionless specific angular momentum (J and M are the angular momentum and the mass the compact object, respectively) and R_{GR} is GM/c^2. The Keplerian orbital frequency associated with the B–P transition radius can be written as $\nu_{kep,BP} = c^3 \cdot (2\pi G)^{-1} \cdot (Ma_\star A^{3/2})^{-1}$. If we assume that the atoll sources plotted in Figure 6.5 all have masses between 1.4 and $2M_\odot$, that $0.3 < a_\star < 0.7$ (see e.g. Salgado et al. 1994; Cook et al. 1994, and references within) and that the central frequency of the hHz QPOs is between $\sim$ 100 and $\sim$ 250 Hz, we can constrain the scaling factor A for these source to be between $\sim$ 20 and $\sim$ 84. If A only depends on the accretion disk (i.e. does not depend on the central object), this can be used to constrain the frequency range in which we expect to observe $\nu_{kep,BP}$ in black holes. For example, the black hole BHC GRO J1655–40, whose mass is estimated from optical investigations as $M = 6.7 \pm 1.2M_\odot$ (Orosz & Bailyn 1997; Shahbaz et al. 1999) and whose specific angular momentum $a_\star$ can be estimated to be between 0.5 and 0.95 (Cui et al. 1998; Fragile et al. 2001), would have $\nu_{kep,BP}$ between $\sim$ 5.6 and $\sim$ 108 Hz, which would exclude the 300 Hz QPO observed in GRO J1655–40 but would be consistent with the the 9 Hz QPO as proposed by Fragile et al. (2001). To allow $\sim$ 300 Hz, a lower black hole angular momentum $a_\star$ ($\lesssim 0.22$ for A between 20 and 84) would be required.

6.5 Summary

- Our observations of 4U 1636–53, including the first RXTE island state data of the source, show timing behavior remarkably similar to that seen in other atoll NS-LMXBs. We observe all components previously identified in those sources, and find their frequencies to follow the relations previously observed. This is a striking result, since the sources compared in this work were observed at intrinsic luminosities different by more than an order of magnitude.

- The previously proposed interpretation of the QPO frequencies ν_{LF} and $\nu_{LF/2}$ in different sources in terms of harmonic mode switching is not supported by our data on 4U 1636–53, nor by data previously reported for other sources. However, these frequencies still follow a single relation to within a factor of 2 for all sources.

- The low frequency QPO L_{LF} is seen in black holes and in accreting millisecond pulsars as well as in non-pulsing neutron stars at frequencies between $\sim$ 0.1 and $\sim$ 50 Hz. The frequency range that L_{LF} covers in a given source is not related to spin frequency, angular momentum or luminosity of the object.

- The rms and frequency behavior of the hectohertz QPO suggest that the mechanism that sets its frequency differs from that for the other components, while the amplitude setting mechanism is common. Furthermore, the hHz QPO shows a clear X-ray luminosity-rms anti-correlation between sources.

Acknowledgments: DA wants to thank S. van Straaten for all his help in the analysis of these data. DA also wants to thank R. Wijnands and C. Fragile for very helpful comments and discussions and J. Homan for comments on an earlier version of this manuscript. This work was supported by the "Nederlandse Onderzoekschool Voor Astronomie" (NOVA), i.e., the "Netherlands Research School for Astronomy", and it has made use of data obtained through the High Energy Astrophysics Science Archive Research Center Online Service, provided by the NASA/Goddard Space Flight Center.

6.6 Appendix

In this Appendix we further discuss other possible approaches to analyze the characteristics of complex power spectra such as generally found in neutron star low-mass X-ray binaries.

In the ideal case, we would have data with enough statistics to be able to follow the evolution of the parameters of all observable components in the power spectra on sufficiently short time scales to be sensitive to the smallest meaningful variations. Unfortunately, this is not the case for the present data and meaningful variations are averaged out in our data. These variations can sometimes be recovered by the use of alternative methods. For example, with the "shift and add" method introduced by Méndez et al. (1998b), it has been possible to better constrain some of the characteristics of the kHz QPOs in several sources than without this method (e.g. Méndez et al. 1998b; Barret et al. 2005a). A disadvantage of the method is that it distorts the power spectrum at the lowest and highest frequencies covered.

We investigated if this method could also be used for our purpose. However, in our experiments with this we encountered several complications. From the observational point of view, in order to use this method we require a sharp power spectral feature that can be accurately traced in time. There are two possibilities for such features: the lower kHz QPO L_ℓ and the low-frequency Lorentzian L_{LF}. While the lower kHz QPO is usually superimposed on well-modeled Poisson noise, tracing L_{LF} is complicated by the fact that it is superimposed on strong variable broad band noise (see van der Klis 2006, and references within). More importantly, while L_ℓ can be traced on sufficiently short time scales ($\lesssim$ 64sec) for the intrinsic changes in the characteristics of the power spectrum to be minimal, typically an entire observation is required for detecting L_{LF} at sufficient signal to noise. In practice this means that we can only use the shift and add method with L_ℓ, which constrains us to only that relatively limited part of the data where L_ℓ is actually detected (see Figure 6.5). We note that L_{LF} and L_ℓ are not simultaneously detected in our data set.

We analyzed all the datasets described in Section 6.2 and found that $\sim$ 15% ($\sim$ 0.17 Msec) of our data have traceable lower kHz QPOs. Most of that time the lower kHz QPOs are detected at frequencies between 700 and 850 Hz (the full range was 600–900 Hz).

In order to use the shift and add method we must adopt a relation between the frequency of the component we wish to shift on (here the lower kHz QPO) and the frequency of the component we wish to detect (here the low frequency QPOs/noise). For example, in their original work Méndez et al. (1998b) supposed that the difference between the lower and the upper kHz QPO frequency remained constant when both peaks move. The study of the characteristics of the low frequency QPOs/noise using the shift and add method is complicated by the fact that we have imprecise information about their relation with the lower kHz QPOs: a constant frequency difference certainly does not apply even to narrow ranges in shift frequency. The aim of this paper as well as the aim of the papers cited below is to present observational results that help constrain those relations.

As van Straaten et al. (2002, 2003) showed, the frequencies of all components except those of the hHz QPOs are correlated in a similar way between sources (see Figure 6.5). However, van Straaten et al. (2005) and Linares et al. (2005) also showed that those correlations are shifted in pulsating sources and as shown in Chapter 5, even non-pulsating systems might show frequency shifts. Additionally, the results of van Straaten et al. (2002, 2003, 2005), Linares et al. (2005) and Altamirano et al. (2005) show that although the frequency relations between the different components are well fitted with a power law, the index and normalization of the power law are different for each relation and may also depend on frequency range.

In order to quantify the problem described above, we studied observation 60032-01-05-00 using power spectra of 64-sec data segments at 2 Hz frequency resolution. This is a very good observation for our purpose since: (i) it has $\sim$ 27 ksec of uninterrupted data; (ii) the lower kHz QPO is strong enough to be significantly detected within 64 seconds for the entire 27 ksec; (iii) the lower kHz QPO frequency drifts between $\sim$ 700 and $\sim$ 860 Hz and (iv) the power spectrum can be fitted with 4 Lorentzians: 2 for the kHz QPOs, one for L_b (at 40 ± 4 Hz) and one for L_{b2} (at 20 ± 12 Hz; 2.9σ).

We first analyzed the power spectrum obtained by aligning the L_ℓ components. We found that L_b and L_{b2} had blended into a broad component at $\sim$ 100 Hz. This result was expected, as a drift of 160 Hz in ν_ℓ does not imply a drift of the same magnitude in the frequencies of the low ν components. We then tried to align the power spectra by predicting the position of the low-frequency components from ν_ℓ using a different power law relation for each component as reported by van Straaten et al. (2005) for L_b and $\nu_{b2} = e^{-24\pm8} \cdot \nu_u^{+3.8\pm1.3}$ for L_{b2} (the relation for L_{b2} is based on our data for 4U 1636–53; given the large errors in our data, the χ^2/dof for the power law fit was 0.26) . The results depended on which power law we used: no significant changes in the resulting power spectrum were found when trying to align L_{b2}, while the power of both components was smeared out producing a blend when we tried to align L_b. This was clearly the effect of the difference in power law indices and normalizations between components. As the frequency relations we used are between ν_u and the frequencies of the other components, we had to assume a relation between ν_ℓ and ν_u in order to predict the frequency variations. We variously assumed $\Delta\nu = \nu_u - \nu_\ell = 280$, 300 & 350 Hz and obtained similar results in each case. We also predicted $\Delta\nu$ by fitting a line to the $\Delta\nu$ vs. ν_ℓ data reported by Jonker et al. (2002a) in the range $720 \lesssim \nu_\ell \lesssim 900$ Hz. Again, the results of the power-spectral fits were the same within errors as those of the previous experiments.

We repeated the last exercise (using the power law relations) also for all 0.17 Msec of ν_ℓ useful data and for L_{b2}, L_b and L_h (we use the power law relation as reported by van Straaten et al. 2005 for L_h). We again found that our results were dependent on the power law used and not significantly better defined than the average power spectra obtained when all 0.17 Msec of data were averaged together without shift.

In another experiment we calculated 4 average power spectra including all 0.17 Msec of useful data by selecting only those 64-second segments which had ν_ℓ between 650–700, 700–750, 750–800, and 800–850 Hz respectively, and averaging these selected power spectra without shifting. In all cases we detect both kHz QPOs, a power law VLFN and L_b. As expected from the results shown in Figure 6.5, ν_b is correlated with the frequency of both kHz QPOs. The measured frequencies are all consistent within errors with those reported on Figure 6.5 and Table 6.5. The lack of statistics in each average power spectrum did not allow us to well constrain the power spectral parameters of other components.

Finally, we fitted a line to the relation between ν_{LF} and ν_h defined by the 4-points visible in Figure 6.9. We used the ν_{LF} we find in all four power spectra (A1, B, D and E) to predict ν_h and shift and add these four power spectra together. Again, we find that the blend of components (this time between L_b and L_h) and the distortion of the power spectra at low frequencies prevented us to better estimate the L_h parameters.

So, neither the shift and add method nor selecting data on ν_ℓ in 64-sec segments (i.e. much shorter than an observation) in our data provides an advantage in measuring the broad low frequency components better. Therefore, in this paper we decided to the straightforward method described in Section 6.2.

	ν_{max} (Hz)	Q	RMS (%)	ID
Interval A1	434.8 ± 26.1	1.6 ± 0.5	12.9 ± 1.4	L_u
	175.9 ± 8.9	2.7 ± 1.3	8.06 ± 1.23	L_{hHz}
	15.0 ± 0.6	0.7 ± 0.1	13.3 ± 0.7	L_h
	5.1 ± 0.1	$7.3^{+9.0}_{-2.2}$	3.2 ± 0.6	L_{LF}
	3.2 ± 0.4	0.33 ± 0.07	11.1 ± 0.7	L_b
Interval A2	436.4 ± 28.2	0.92 ± 0.24	16.5 ± 1.05	L_u
	12.3 ± 0.8	0.27 ± 0.11	16.1 ± 1.1	L_h
	2.34 ± 0.52	0.14 ± 0.09	9.9 ± 1.4	L_b
Interval B	464.9 ± 9.4	1.7 ± 0.2	13.8 ± 0.9	L_u
	$154.7^{+68.8}_{-36.6}$	0.53 ± 0.42	7.4 ± 1.8	L_{hHz}
	18.2 ± 0.3	0.75 ± 0.06	12.4 ± 0.4	L_h
	6.83 ± 0.11	3.07 ± 0.66	4.1 ± 0.5	L_{LF}
	4.03 ± 0.31	0.19 ± 0.03	11.9 ± 0.4	L_b
Interval C	529.3 ± 15.4	1.1 ± 0.1	17.1 ± 0.6	L_u
	23.1 ± 1.6	0.47 ± 0.15	11.9 ± 1.5	L_h
	6.38 ± 1.01	0.09 ± 0.05	13.1 ± 1.2	L_b
Interval D	524.7 ± 8.0	2.2 ± 0.4	13.9 ± 1.0	L_u
	$201.7^{+78.0}_{-32.5}$	0.58 ± 0.35	8.6 ± 1.9	L_{hHz}
	23.9 ± 0.5	0.99 ± 0.13	10.5 ± 0.6	L_h
	9.8 ± 0.3	2.17 ± 0.63	5.2 ± 0.9	L_{LF}
	5.6 ± 0.7	0.15 ± 0.04	11.4 ± 0.7	L_b
Interval E	593.1 ± 4.3	3.1 ± 0.2	12.7 ± 0.4	L_u
	270.3 ± 31.7	0.63 ± 0.20	8.7 ± 0.8	L_{hHz}
	31.2 ± 1.3	0.89 ± 0.15	8.7 ± 0.7	L_h
	15.04 ± 0.41	1.6 ± 0.5	5.7 ± 1.2	L_{LF}
	8.5 ± 0.9	0.22 ± 0.03	11.2 ± 0.6	L_b
Interval F	637.2 ± 7.9	3.06 ± 0.32	15.9 ± 0.6	L_u
	208.7 ± 30.1	1.2 ± 0.6	7.2 ± 1.2	L_{hHz}
	18.7 ± 0.9	0.02 ± 0.04	16.9 ± 0.2	L_b
Interval G	780.01 ± 1.78	4.5 ± 0.1	13.6 ± 0.1	L_u
	152.7 ± 10.4	0.32 ± 0.11	8.7 ± 0.49	L_{hHz}
	23.4 ± 0.5	0.34 ± 0.03	11.6 ± 0.3	L_b
	3.8 ± 0.9	0.20 ± 0.11	2.8 ± 0.5	L_{b2}
Interval H	862.8 ± 1.8	6.2 ± 0.2	11.4 ± 0.1	L_u
	568.3 ± 4.6	7.06 ± 1.22	4.6 ± 0.2	L_ℓ
	120.6 ± 3.6	1.03 ± 0.14	6.4 ± 0.3	L_{hHz}
	26.6 ± 0.5	0.57 ± 0.04	9.2 ± 0.2	L_b
	4.3 ± 0.7	0.35 ± 0.11	2.7 ± 0.3	L_{b2}
Interval I	897.9 ± 2.1	8.2 ± 0.5	9.9 ± 0.2	L_u
	585.5 ± 5.3	7.6 ± 1.1	5.3 ± 0.3	L_ℓ
	228.81 ± 9.05	$5.6^{+5.6}_{-1.9}$	2.6 ± 0.5	L^h_{hHz}
	112.68 ± 4.34	1.51 ± 0.33	5.29 ± 0.41	L_{hHz}
	28.6 ± 0.6	0.80 ± 0.09	7.72 ± 0.28	L_b
	6.06 ± 1.41	0.32 ± 0.14	2.93 ± 0.41	L_{b2}
Interval J	971.1 ± 4.7	9.9 ± 1.1	6.7 ± 0.2	L_u
	666.2 ± 2.1	8.7 ± 0.5	7.7 ± 0.2	L_ℓ
	127.9 ± 9.6	1.1 ± 0.3	4.3 ± 0.4	L_{hHz}
	34.6 ± 0.8	1.1 ± 0.1	5.5 ± 0.2	L_b
	8.07 ± 1.56	0.34 ± 0.14	2.99 ± 0.31	L_{b2}
Interval K	998.18 ± 7.94	5.76 ± 0.74	6.14 ± 0.23	L_u
	728.04 ± 2.63	5.3 ± 0.3	8.3 ± 0.2	L_ℓ
	148.2 ± 8.1	1.6 ± 0.5	3.4 ± 0.3	L_{hHz}
	38.8 ± 0.9	1.2 ± 0.2	4.69 ± 0.37	L_b
	$9.5^{+12}_{-3.2}$	0.07 ± 0.35	2.48 ± 0.79	L_{b2}
Interval L	1138.37 ± 9.02	$14.08^{+9.80}_{-3.66}$	2.7 ± 0.3	L_u
	837.5 ± 1.0	11.4 ± 0.4	7.9 ± 0.09	L_ℓ
	156.1 ± 33.6	1.3 ± 0.5	2.03 ± 0.38	L_{hHz}
	46.4 ± 0.9	2.4 ± 0.4	2.8 ± 0.2	L_b
	14.9 ± 5.8	0.00 ± 0.00	1.9 ± 0.3	L_{b2}
Interval M	1220.5 ± 11.2	16.6 ± 6.5	3.71 ± 0.34	L_u
	44.2 ± 7.2	0.56 ± 0.28	3.1 ± 0.3	L_b
Interval N	1259.1 ± 9.9	$14.4^{+34.7}_{-5.4}$	1.8 ± 0.2	L_u
	36.7 ± 4.9	0.05 ± 0.13	2.37 ± 0.11	L_b

Table 6.5: Characteristic frequencies ν_{max}, Q values ($\nu_{max} \equiv \nu_{central}/FWHM$), fractional rms (in the full PCA energy band) and component identification (ID) of the Lorentzians fitted for 4U 1636–53. The quoted errors use $\Delta\chi^2 = 1.0$. Where only one error is quoted, it is the straight average between the positive and the negative error. Note that the results for the quality factor of both L_ℓ and L_{LF} components are affected by our averaging method (see Sections 6.1, 6.3 and the Appendix).

7 Discovery of kilohertz quasi-periodic oscillations and state transitions in the low-mass X-ray binary 1E 1724–3045 (Terzan 2)

D. Altamirano, M. van der Klis, M. Méndez, R. Wijnands, C. Markwardt and J. Swank

Astrophysical Journal, 2007, Submitted

Abstract

We have studied the rapid X-ray time variability in 99 pointed observations with the *Rossi X-ray Timing Explorer* (RXTE)'s Proportional Counter Array of the low-mass X-ray binary 1E 1724–3045 which includes, for the first time, observations of this source in its island and banana states, confirming the atoll nature of this source. We report the discovery of kilohertz quasi-periodic oscillations (kHz QPOs). Although we have 5 detections of the lower kHz QPO and one detection of the upper kHz QPO, in none of the observations we detect both QPOs simultaneously. By comparing the dependence of the rms amplitude with energy of kHz QPOs in different atoll sources, we conclude that this information cannot be use to unambiguously identify the kilohertz QPOs as was previously thought. We find that Terzan 2 in its different states shows timing behavior similar to that seen in other neutron-star low mass X-ray binaries (LMXBs). We studied the flux transitions observed between February 2004 and October 2005 and conclude that they are due to changes in the accretion rate.

7.1 Introduction

Low-mass X-ray binaries (LMXBs) can be divided into systems containing a black hole candidate (BHC) and those containing a neutron star (NS). The accretion process onto these compact objects can be studied through the timing properties of the associated X-ray emission (see, e.g., van der Klis 2006, for a review). Hasinger & van der Klis (1989) classified the NS LMXBs based on the correlated variations of the X-ray spectral and rapid X-ray variability properties. They distinguished two sub-types of NS LMXBs, the Z sources and the atoll sources, whose names were inspired by the shapes of the tracks that these sources trace out in an X-ray color-color diagram (CD) on time scales of hours to days. The Z sources are the most luminous, but the atoll sources are more numerous and cover a much wider range in luminosities (e.g. Ford et al. 2000, and references within). For each type of source, several spectral/timing states are identified which are thought to arise from qualitatively different inner flow configurations (van der Klis 2006). In the case of atoll sources, the three main states are the extreme island state (EIS), the island state (IS) and the banana branch, the latter subdivided into lower-left banana (LLB), lower banana (LB) and upper banana (UB) states. The EIS and the IS occupy the spectrally harder parts of the color color diagram and correspond to lower levels of X-ray luminosity (L_x). The associated patterns in the CD are traced out in hours to weeks. The hardest and lowest L_x state is the EIS, which shows strong (up to 50% rms amplitude, see Linares et al. 2007, and references within) low-frequency flat-topped noise also known as band-limited noise (BLN). The IS is spectrally softer and has higher X-ray luminosity than the EIS. Its power spectra are characterized by broad features and a dominant BLN component which becomes weaker and generally higher in characteristic frequency as the flux increases and the > 6 keV spectrum gets softer. In order of increasing L_x we then encounter the LLB, where twin kHz QPOs are generally first observed, the LB, where 10-Hz BLN is still dominant and finally, the UB, where the < 1 Hz (power law) very low frequency noise (VLFN) dominates. In the banana states, some of the broad features observed in the EIS and the IS become narrower (peaked) and occur at higher frequency. In particular, the twin kHz QPOs can be found in the LLB at frequencies higher than 1000 Hz, only one kHz QPO can be generally found in the LB, and neither of them is detected in the UB (see reviews by van der Klis 2000, 2004, 2006, for detailed descriptions of the different states. See also Figure 1.8 on page 13 for a Schematic color–color diagram and representative power spectra of a typical atoll source).

A small number of weak NS LMXBs (usually burst sources and often referred to as 'weak' or 'faint bursters') resemble atoll sources in the EIS, but in the absence of state transitions this identification has been tentative (see for example Barret et al. 2000b; van der Klis 2006). An important clue is provided by the correlations between the component frequencies (and strengths - see e.g. van Straaten et al. 2002, 2003; Altamirano et al. 2006 and Chapters 5, 6 & 8) which helps to identify components across sources. For example, van Straaten et al. (2002, 2003) compared the timing properties of the atoll sources 4U 0614+09, 4U 1608–52 and 4U 1728–34 (see also Chapter 6, for similar results when the atoll source 4U 1636–53 was included in the sample) and conclude that the frequencies of the variability components in these sources follow the same pattern of correlations when plotted versus the frequency of the upper kHz QPO (ν_u). van Straaten et al. (2003) also showed that low luminosity systems extend the frequency correlations observed for the atoll sources. This last result gave further clues in the link between the atoll and the low luminosity sources.

Psaltis et al. (1999) found an approximate frequency correlation involving a low-frequency QPO, the lower kHz QPO frequency and two broad noise components interpreted as low-frequency versions of these features. This correlation spans nearly three decades in frequency, where the Z and bright atoll sources populate the $> 100\,$Hz range and black holes and weak NS systems the $< 10\,$Hz range. As already noted by Psaltis et al. (1999), because the correlation combines features from different sources which show either peaked or broad components with relatively little overlap, the data are suggestive but not conclusive with respect to the existence of a single correlation covering this wide frequency range (van der Klis 2006).

The low-luminosity neutron star systems can play a crucial role in clearing up this issue. Observations of different source states in such a system could connect the < 10 and > 100 Hz regions mentioned above by direct observation of a transition in a single source. In the case of the pattern of correlations reported by van Straaten et al. (2003), low luminosity NS systems extend the frequency correlations observed for ordinary atoll sources down to ~ 100 Hz. Unfortunately, the low luminosity NS systems are usually observed in only one state (EIS), which makes it difficult to properly link these sources to the atoll sources. However, some of these objects show rare excursions to higher luminosity levels which might correspond to other states. The occurrence of these excursions are usually unpredictable. Therefore, in practice it was not possible until now to check on the frequency behavior of the different variability components as such a source enters higher luminosity states.

1E 1724–3045 is a classic low luminosity LMXB; a persistent Low-Mass X-ray binary located in the globular cluster Terzan 2 (Grindlay et al. 1980) which is a metal-rich globular cluster of the galactic bulge. Its distance is estimated to be between 5.2 to 7.7 kpc (Ortolani et al. 1997). These values are consistent with that derived from a type I X-ray burst that showed photospheric expansion (see Grindlay et al. 1980, but also see Kuulkers et al. 2003a; Galloway et al. 2006). The type I X-ray bursts observed from this source also indicate that the compact object is a weakly magnetized neutron star (Swank et al. 1977; Grindlay et al. 1980). Emelyanov et al. (2002) have shown, using ~ 30 years of data from several X-ray satellites, that the luminosity of Terzan 2 increased until reaching a peak in 1997, after which it started to decrease. They suggest that the evolution of the donor star or the influence of a third star could be the cause of this behavior. Olive et al. (1998) and Barret et al. (2000a) have shown that during earlier observations of Terzan 2 its X-ray variability at frequencies $\gtrsim 0.1$ Hz resembled that of black hole candidates. This state was tentatively identified as the extreme island state for atoll sources. Until now, no kilohertz quasi-periodic oscillations have been reported for this source, which was attributed to the fact that the source was always observed in a single intensity state (Barret et al. 2000b).

Monitoring observations by the All Sky Monitor aboard the Rossi X-ray Timing Explorer showed that the source was weakly variable in X-rays (less than about a factor of 3 on a few day time scale for the first 8 years of the monitoring). However, recently Markwardt & Swank (2004) reported (using PCA monitoring observations of the galactic bulge - Swank & Markwardt 2001) that during February 2004, 1E 1724–3045 flared up from its relatively steady ~ 20 mCrab to ~ 66 mCrab (2–10 keV). In this paper we report a complete study of the timing variability of the source. For simplicity, and since only one bright X-ray source is detected in the globular cluster (see Section 7.4.1), in the rest of this report we will refer to 1E 1724–3045 as Terzan 2.

7.2 Observations and data analysis

7.2.1 Light curves and color diagrams

We use data from the Rossi X-ray Timing Explorer (RXTE) Proportional Counter Array (PCA; for instrument information see Zhang et al. 1993; Jahoda et al. 2006). There were 534 slew observations until October 30^{th} 2006, which are part of the PCA monitoring observations of the galactic bulge (Swank & Markwardt 2001) and which were performed typically every 3 days. These observations were only used to study the long-term L_x behavior of the source.

There were also 99 pointed observations in the nine data sets we used (10090-01, 20170-05, 30057-03, 50060-05, 60034-02, 80105-10, 80138-06, 90058-06 &

91050-07), containing ~ 0.8 to ~ 26 ksec of useful data per observation. We use the 16-s time-resolution Standard 2 mode data to calculate X-ray colors. Hard and soft color are defined as the 9.7–16.0 keV / 6.0–9.7 keV and 3.5–6.0 keV / 2.0–3.5 keV count rate ratio, respectively, and intensity as the 2.0–16.0 keV count rate. The energy-channel conversion was done using the pca_e2c_e05v02 table provided by the RXTE Team[1]. Channels were linearly interpolated to approximate these precise energy limits. X-ray type I bursts were removed, background was subtracted and deadtime corrections were made. In order to correct for the gain changes as well as the differences in effective area between the PCUs themselves, we normalized our colors by the corresponding Crab Nebula color values; (see Kuulkers et al. 1994; van Straaten et al. 2003, see table 2 in Chapter 6 for average colors of the Crab Nebula per PCU) that are closest in time but in the same RXTE gain epoch, i.e., with the same high voltage setting of the PCUs (Jahoda et al. 2006).

7.2.2 Fourier timing analysis and fitting models.

For the Fourier timing analysis we used either the Good Xenon or the Event modes E_125us_64M_0_1s or E_16us_64M_0_8s data. Leahy-normalized power spectra were constructed using data segments of 128 seconds and 1/8192 s time bins such that the lowest available frequency is $1/128 \approx 8 \times 10^{-3}$ Hz and the Nyquist frequency 4096 Hz. No background or deadtime corrections were performed prior to the calculation of the power spectra. We first averaged the power spectra *per observation.* We inspected the shape of the average power spectra at high frequency ($>$ 2000 Hz) for unusual features in addition to the usual Poisson noise. None were found. We then subtracted a Poisson noise spectrum estimated from the power between 3000 and 4000 Hz, using the method developed by Klein-Wolt (2004) based on the analytical function of Zhang et al. (1995). In this frequency range, neither intrinsic noise nor QPOs are expected based on what we observe in other sources. The resulting power spectra were converted to squared fractional rms (van der Klis 1995a). In this normalization the power at each Fourier frequency is an estimate of power density such that the square root of the integrated power density equals the fractional rms amplitude of the intrinsic variability in the source count rate in the frequency range integrated over.

In order to study the behavior of the low-frequency components usually found in the power spectra of neutron star LMXBs, we needed to improve the statistics. We therefore averaged observations which were close in time and had both similar colors and power spectra (see e.g. van Straaten et al.

[1]see http://heasarc.gsfc.nasa.gov/docs/xte/pca_news.html

2002, 2003, 2005; Altamirano et al. 2005, 2006, and references within – see also Appendix in Chapter 6 for a discussion on other possible methods). The resulting data selections are labeled from A to R (ordered mainly in time – see Table 7.3 for details on which observations were used for each interval and their colors). Their corresponding average power spectra are displayed in Figure 7.1.

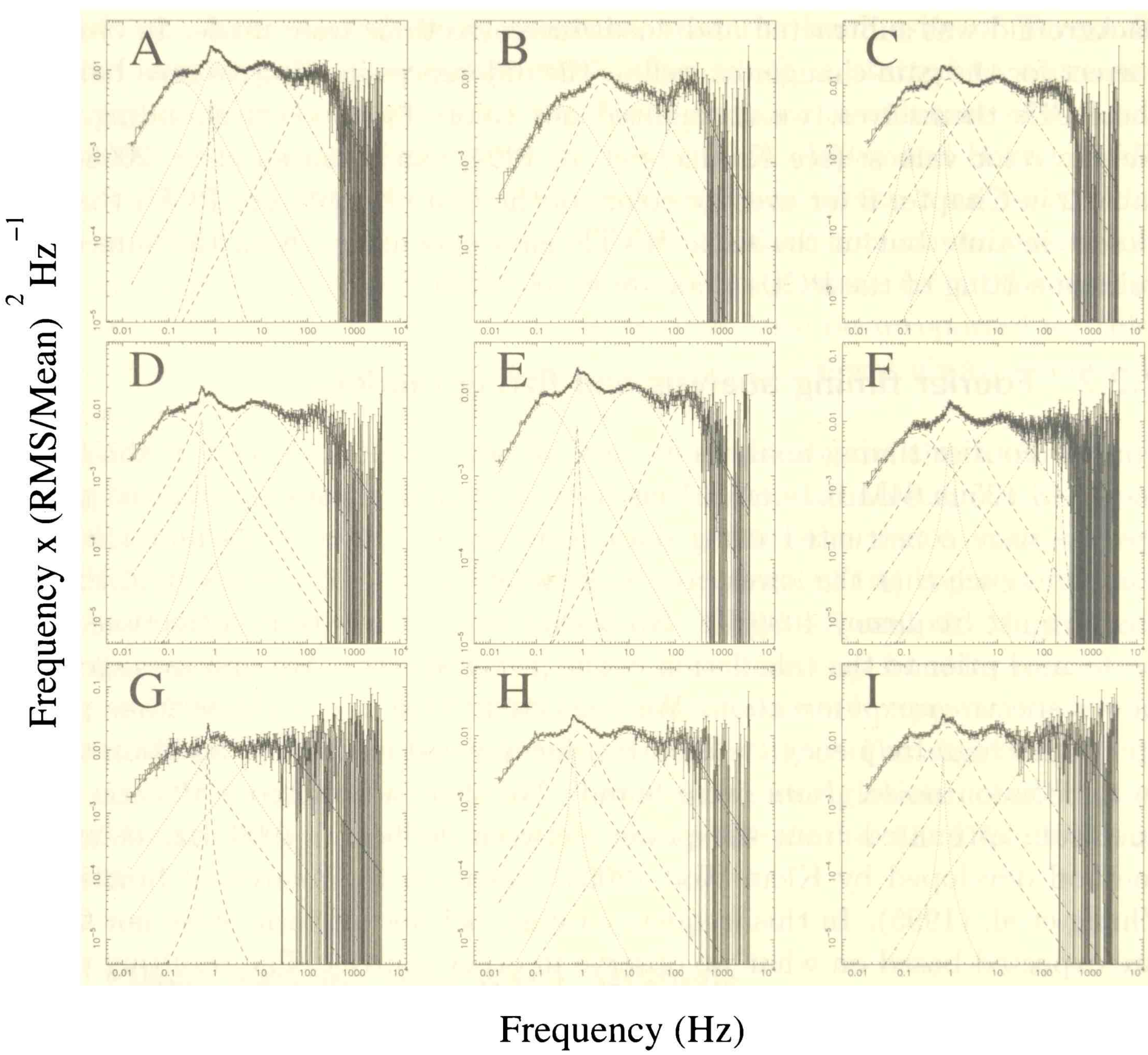

Figure 7.1: Power spectra and fit functions in the power spectral density times frequency representation. Each plot corresponds to a different region in the color-color and color-intensity diagrams (see Figures 7.4 and 7.2). The curves mark the individual Lorentzian components of the fit. For a detailed identification, see Table 7.4 and Figure 7.7.

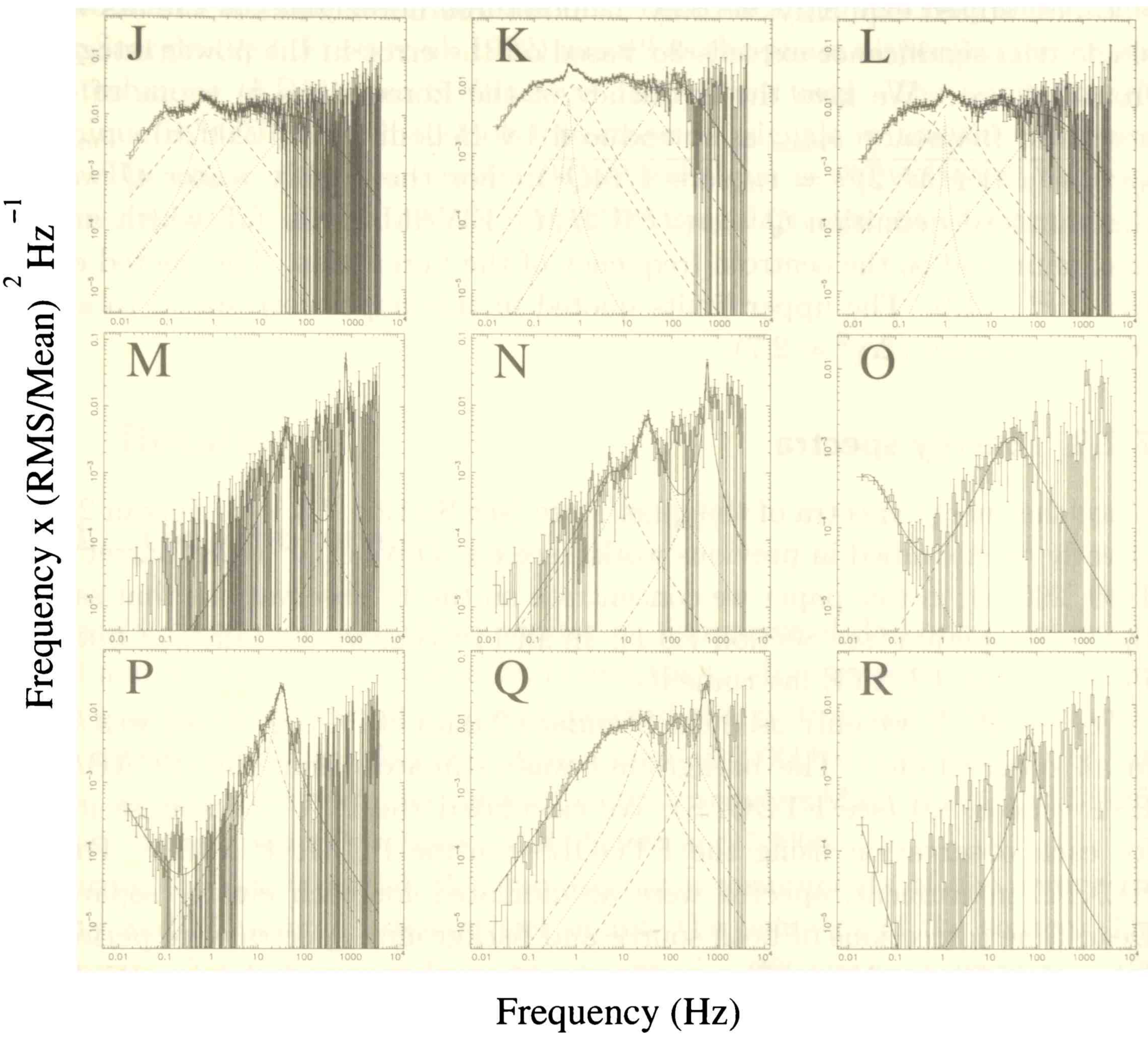

Figure 7.1 continued.

To fit the power spectra, we used a multi-Lorentzian function: the sum of several Lorentzian components plus, if necessary, a power law to fit the very low frequency noise (VLFN - see van der Klis 2006 for a review). Each Lorentzian component is denoted as L_i, where i determines the type of component. The characteristic frequency (ν_{max} as defined below) of L_i is denoted ν_i. For example, L_u identifies the upper kHz QPO and ν_u its characteristic frequency. By analogy, other components go by names such as L_ℓ (lower kHz), L_{hHz} (hectohertz), L_h (hump), L_b (break frequency), and their frequencies as ν_ℓ, ν_{hHz}, ν_h and ν_b, respectively. Using this multi-Lorentzian function makes it straightforward to directly compare the characteristics of the different components observed in Terzan 2 to those in previous works which used the same fit function (e.g., Belloni et al. 2002b; van Straaten et al. 2003, 2005; Altamirano et al. 2005, 2006, and references therein).

Unless stated explicitly, we only include those Lorentzians in the fits whose single trial significance exceeds 3σ based on the error in the power integrated from 0 to ∞. We give the frequency of the Lorentzians in terms of characteristic frequency ν_{max} as introduced by Belloni et al. (2002b): $\nu_{max} = \sqrt{\nu_0^2 + (FWHM/2)^2} = \nu_0\sqrt{1 + 1/(4Q^2)}$. For the quality factor Q we use the standard definition $Q = \nu_0/FWHM$. FWHM is the full width at half maximum and ν_0 the centroid frequency of the Lorentzian. The quoted errors use $\Delta\chi^2 = 1.0$. The upper limits quoted in this paper correspond to a 95% confidence level ($\Delta\chi^2 = 2.7$).

7.2.3 Energy spectra

Since the energy spectra of the quiet state (see Section 7.3.1) of Terzan 2 have already been studied in previous works (see e.g. Olive et al. 1998; Barret et al. 1999, 2000a), in this paper we concentrate on the 14 observations that sample the flaring period (see Section 7.3.1). In all 14 cases, we used data of both the PCA and the HEXTE instruments.

For the PCA, we only used the Standard 2 data of PCU 2, which was active in all observations. The background was estimated using the PCABACKEST version 6.0 (see FTOOLS). We calculated the PCU 2 response matrix for each observation using the FTOOLS routine PCARSP V10.1. For the HEXTE instrument, spectra were accumulated for each cluster separately. Dead time corrections of both source and background spectra were performed using HXTDEAD V6.0. The response matrices were created using HXTRSP V3.1. For both PCA and HEXTE, we filtered out data recorded during, and up to 30 minutes after passage through the South Atlantic Anomaly (SAA). We only use data when the pointing offset from the source was less than 0.02 degrees and the elevation of the source respect to the Earth was greater than 10 degrees. We did not perform any energy selection prior to the extraction of the spectra. Finally, we fitted the energy spectra using XSPEC V11.3.2i.

7.2.4 Search for long term periodicities

Recently, Wen et al. (2006) have performed a systematic search for periodicities in the light curves of 458 sources using data from the RXTE All Sky Monitor (ASM). Terzan 2 was not included in their analysis, probably due to the fact that the ASM source average count rate is low: 2.05±0.01 count/s (the average of the errors – $1/n\sum err_i$ – is 0.8 count/s).

Since the PCA galactic bulge monitoring (Swank & Markwardt 2001) has observed the source for more than 8 years, and the lowest detected source count rate was 170 ± 5 counts/sec, this new data set provides useful information to search for long term modulations. Lomb-Scargle periodograms (Lomb 1976; Scargle 1982; Press et al. 1992) as well as the phase dispersion minimization technique (PDM - see Stellingwerf 1978) were used. The Lomb-Scargle technique is ideally suited to look for sinusoidal signals in unevenly sampled data. The phase dispersion minimization technique is well suited to the case of non-sinusoidal time variation covered by irregularly spaced observations.

7.3 Results

7.3.1 The light curve

Figure 7.2 shows both the PCA monitoring lightcurve of the source (see upper panel and Swank & Markwardt 2001) and the Crab normalized intensity (see lower panel and Section 7.2.1) of each pointed observation versus time (in units of modified Julian date MJD = Julian Date$-$2400000.5). In the rest of this paper, we will refer as "quiet period" to that between MJD 51214 and 52945, and as "flaring period" between MJD 52945 and 53666.

During the quiet period, 333 monitoring measurements of the source intensity and 85 pointed observations sample the behavior of the source. The count rate slowly decreases from an average of $\sim$ 300, to an average of $\sim$ 190 counts/s/5PCU at an average rate of -0.059 ± 0.002 count/s/day. In the flaring period, 7 flares sampled with 201 monitoring observations were detected with the galactic bulge scan. 14 pointed observations partially sampled parts of 4 of these flares. In Table 7.2 we list approximate dates at which the flux transitions occurred, the flare durations and the maximum count rates detected with the PCA. As mentioned in Section 7.2.4, the monitoring is done approximately once every three days; additional gaps in the data are present due to visibility windows. As of course we do not have details of flares that may have occurred during these gaps, the information in Table 7.2 is only approximate. In Figure 7.3 we show the intensity of the source during the flaring period. We label the different flares F1, F2, F3, F4, F5, F6 and F7 in order of time of occurrence.

We detected three Type I X-ray bursts. One was during the quiet-state observation 10090-01-01-021 and two during the flaring-state observations 80138-06-06-00 and 90058-06-02-00. A detailed study of these X-ray bursts as well as a comparison to bursts observed in other sources can be found in Galloway et al. (2006).

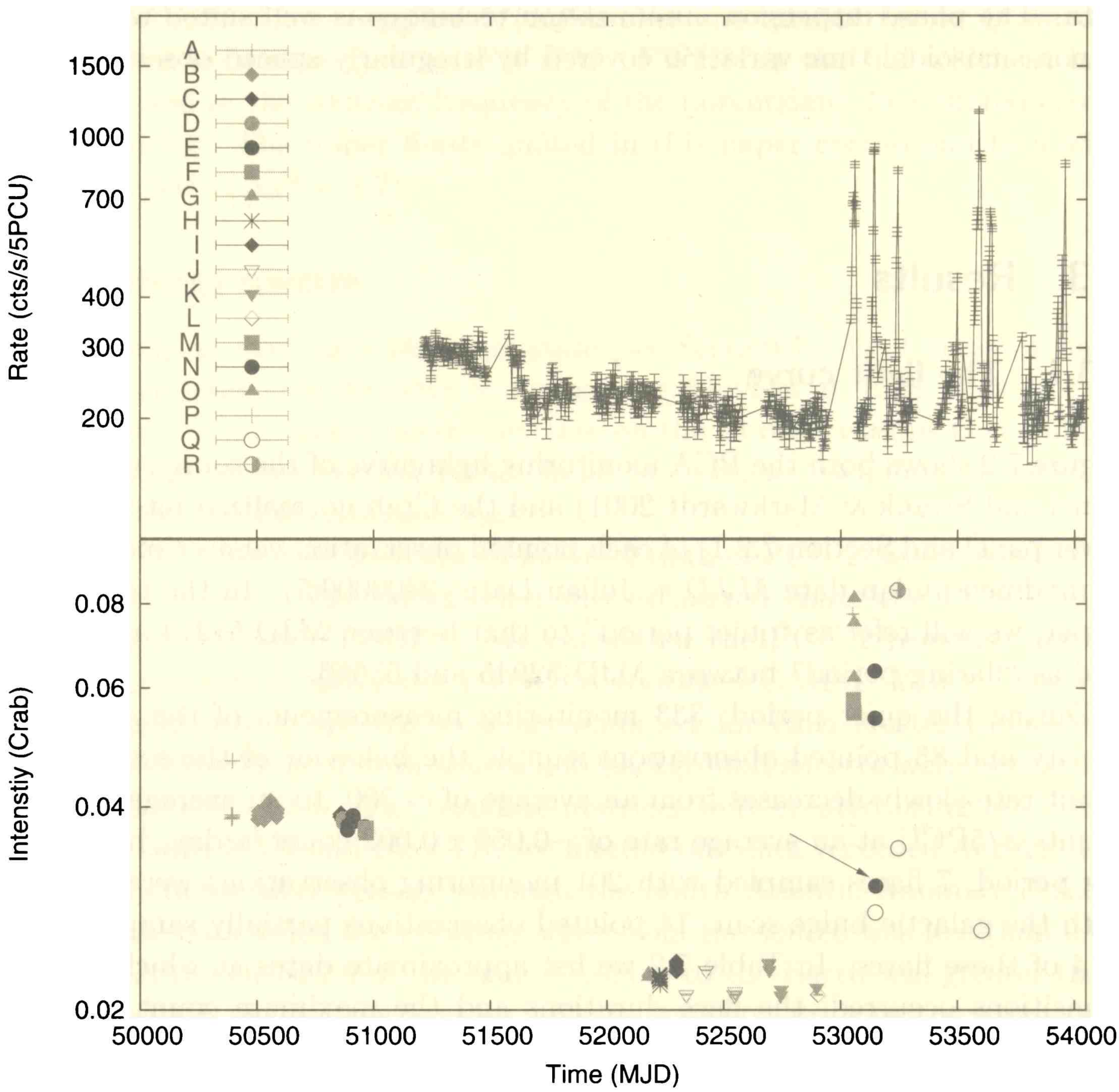

Figure 7.2: *Above:* PCA count rate obtained from the monitoring observations of Terzan 2 (Monitoring observation of the galactic bulge - see Swank & Markwardt 2001). These data was used for the study of the long-term variability (see Sections 7.2.4 & 7.3.8). *Below:* Terzan 2 intensity (Crab normalized - see Section 7.2) versus time of all pointed observations. These observations were used for the study of the 0.1–1200 Hz X-ray variability (see Sections 7.2.2, 7.3.4 & 7.3.3) except for the observation 90058-06-04-00, which is marked with an arrow (see Section 7.3). The modified Julian date is defined as $MJD =$ Julian Date-2400000.5.

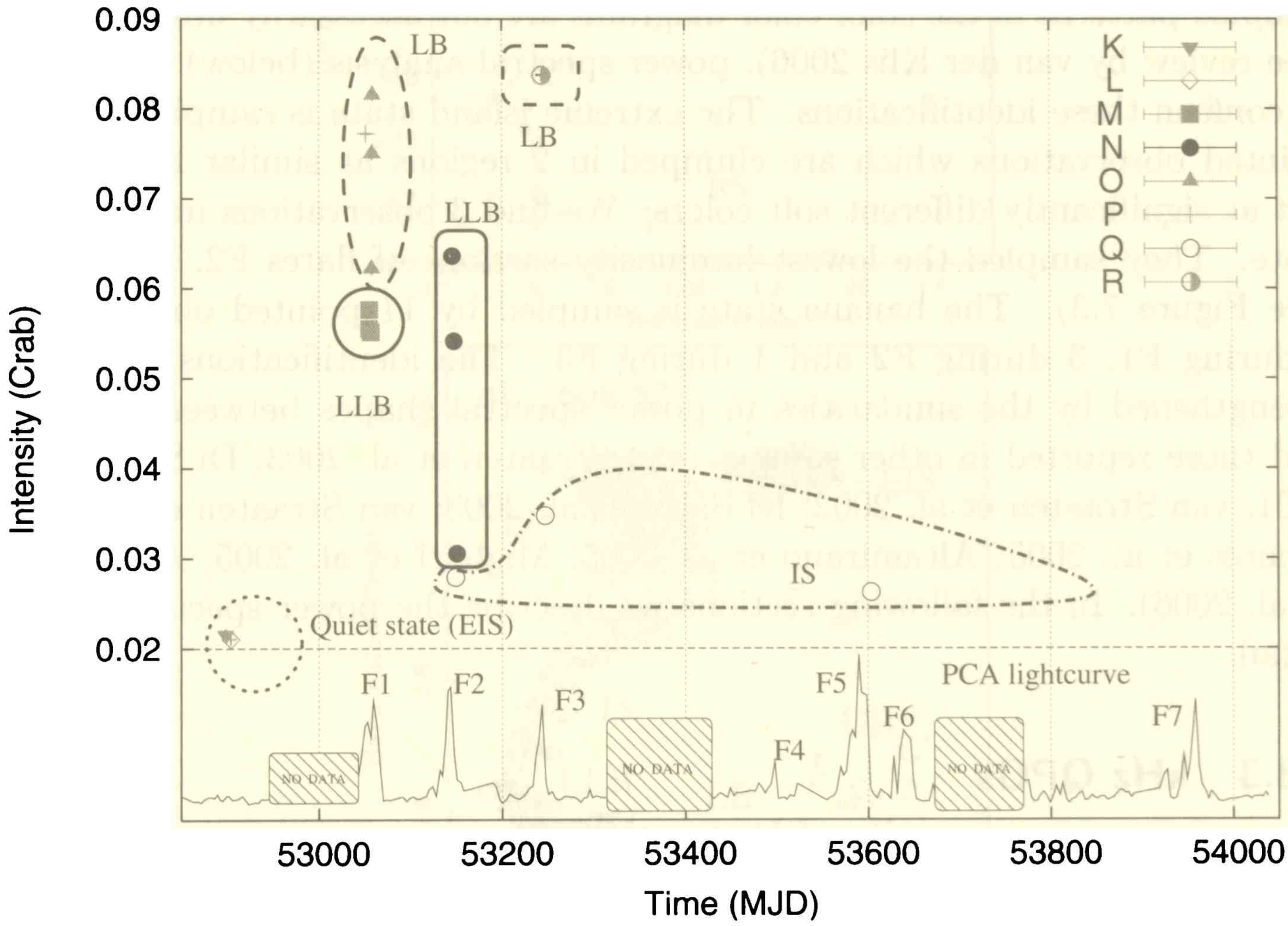

Figure 7.3: *Above:* Intensity in units of the Crab Nebula of the observations which were performed during the flare state. The different states are labeled (see Section 7.3.2). *Below:* Intensity versus time showing the seven flares. The data are the same as those of Figure 7.2.

7.3.2 Color diagrams; identification of states

Figure 7.4 (top) shows the color-color diagram of the 99 pointed observations. For comparison, we also include the color-color diagram of the atoll source 4U 1608–52, which has been observed in all extreme island, island and banana states (Figure 7.4, bottom). The similarity in shape suggests that Terzan 2 underwent state transitions during observations of the flares. Based on Figure 7.4 we can identify the probable extreme island, island and banana state with the hardest, intermediate and softest colors, respectively. Since partially sampled patterns in the color color diagrams are not necessarily unambiguous, (see review by van der Klis 2006), power spectral analysis (below) is required to confirm these identifications. The extreme island state is sampled with 85 pointed observations which are clumped in 2 regions at similar hard colors but at significantly different soft colors. We find 3 observations in the island state. They sampled the lowest luminosity sections of flares F2, F3 and F5 (see Figure 7.3). The banana state is sampled by 11 pointed observations: 7 during F1, 3 during F2 and 1 during F3. The identifications above are strengthened by the similarities in power spectral shapes between Terzan 2 and those reported in other sources (van Straaten et al. 2003; Di Salvo et al. 2001; van Straaten et al. 2002; Di Salvo et al. 2003; van Straaten et al. 2005; Linares et al. 2005; Altamirano et al. 2005; Migliari et al. 2005; Altamirano et al. 2006). In the following sections we describe the power spectra in more detail.

7.3.3 kHz QPOs

We searched each averaged observation's power spectrum for the presence of significant kHz QPOs at frequencies $\gtrsim$ 400 Hz. As reported in other works (Barret et al. 1999; Belloni et al. 2002b), during the quiet period the power spectra of single averaged observations show significant power up to $\sim$ 300 Hz which is fitted with broad ($Q \lesssim 0.5$) Lorentzians plus if necessary, one sharp Lorentzian to account for L_{LF}. During the flaring period, we found that several observations show power excess above 400 Hz. For each observation we fitted the averaged power spectra between 400 and 2000 Hz with a model consisting of one Lorentzian and a constant to take into account the QPO and Poisson noise, respectively. In 5 of the 14 observations that sample the flaring period, we detect significant QPOs, with single trial significances up to 6.5σ. In Table 7.1 we present the results of our fits and information on these observations. As can be seen, the first three observations were performed during the rise of the first flare while the fourth and fifth observations where done during the decay of the second flare (see Figure 7.3). As can be seen in

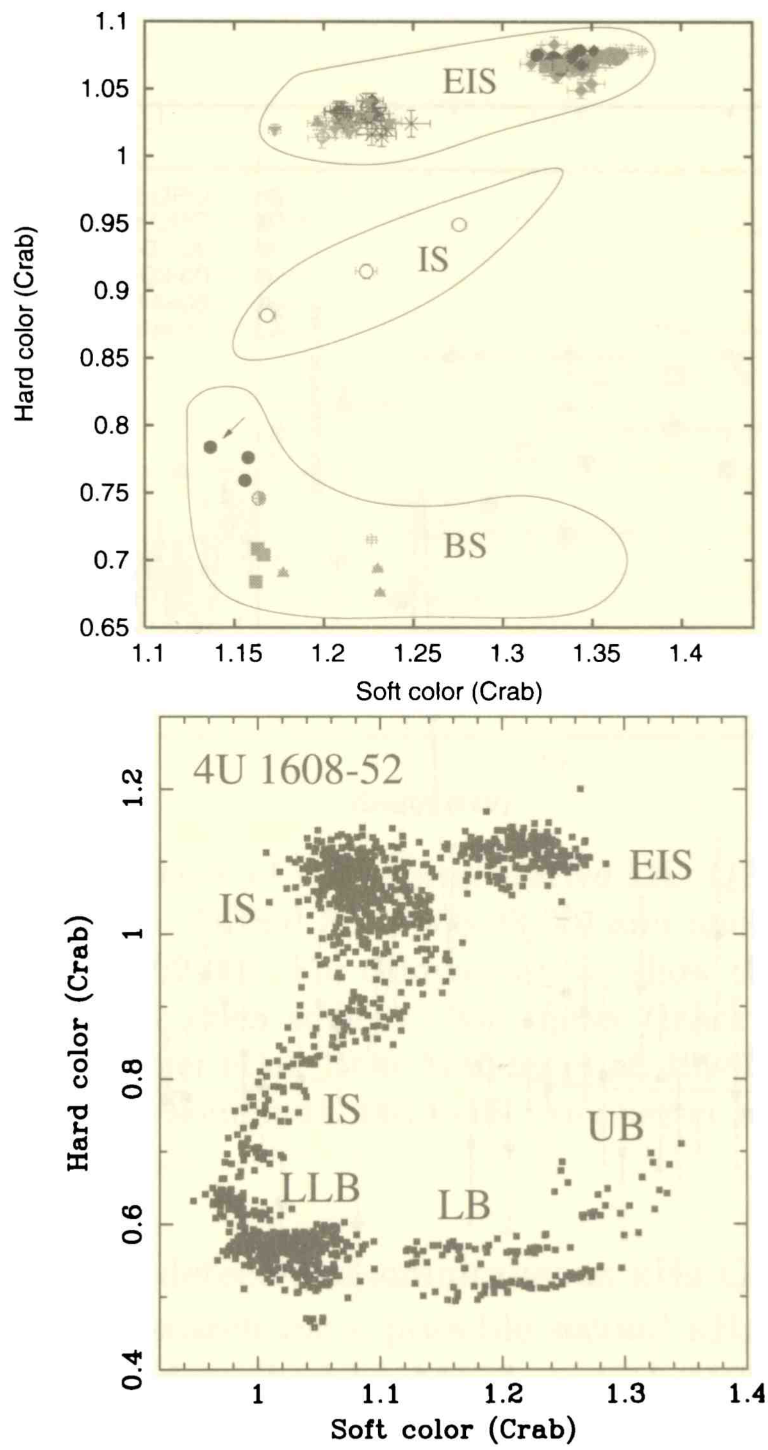

Figure 7.4: *Top:* Hard color versus soft color normalized to Crab as explained in Section 7.2. Different symbols represent the selections used for averaging the power spectra as explained in Section 7.2 and shown in Figure 7.1 (see Figure 7.2 for symbols). The arrow marks observation 90058-06-04-00, which was excluded from interval N (see Section 7.3). *Bottom:* Hard color versus soft color normalized to Crab for the NS source 4U 1608–52. This source has been observed in all expected atoll states: extreme island state (EIS), island state (IS), lower left banana (LLB), lower banana (LB) and upper banana (UB). The similarity between both figures suggest that Terzan 2 has been observed in similar states as 4U 1608–52.

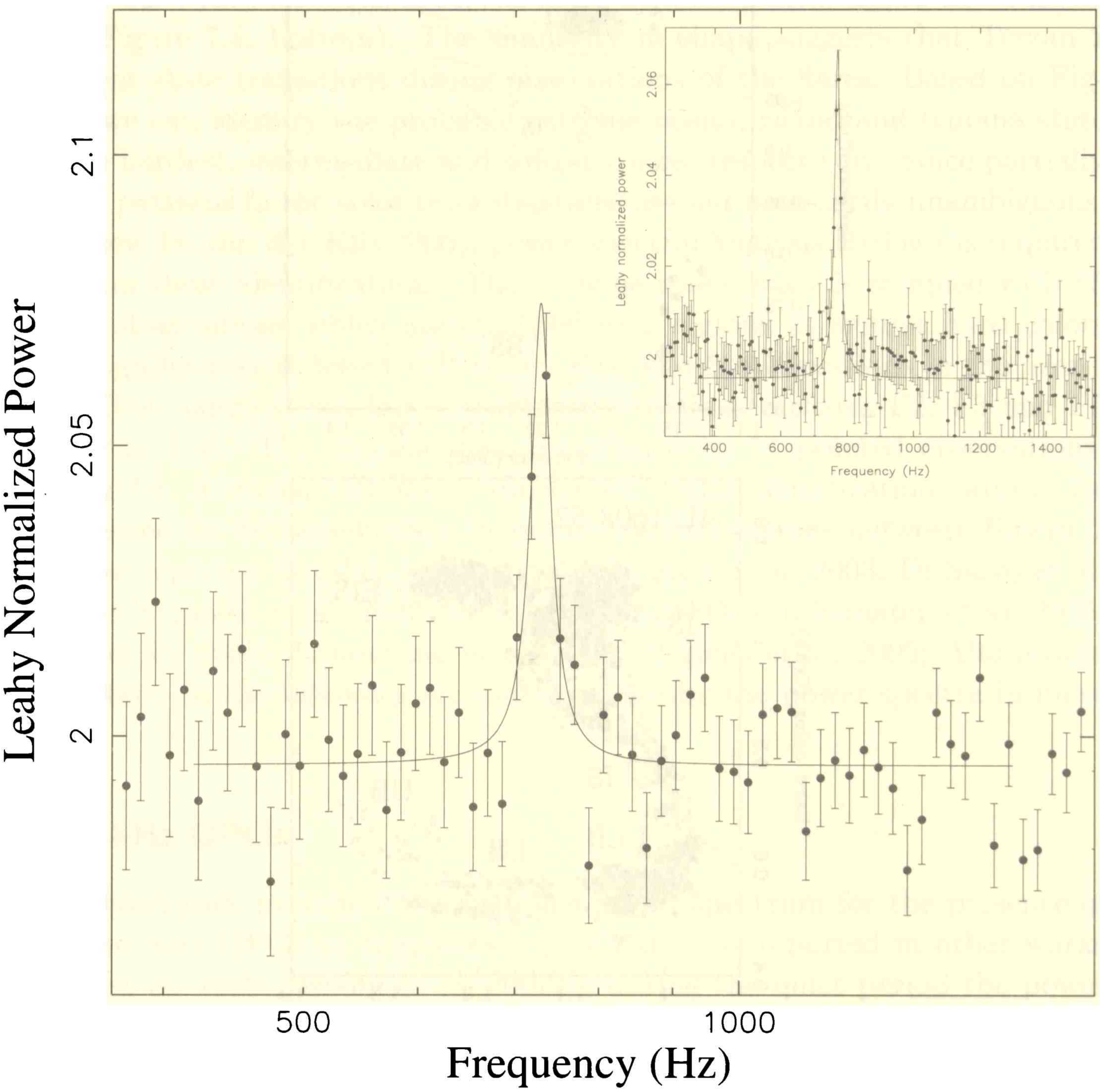

Figure 7.5: Fit to the kHz QPO in observation 80138-06-02-00. In the subplot on the top-right of the figure, we show the fit to the data after using the shift-and-add method on all 5 observations reported in Table 7.1 where the main peak was set to the arbitrary frequency $\nu = 770$ Hz (see Section 7.3.3). No significant detections of a second kHz QPO were found.

Table 7.1, there are significant frequency variations. Unfortunately, due to the sparse coverage of the flares and the fact that we cannot detect the QPO on shorter time scales than an observation, no further conclusions are possible.

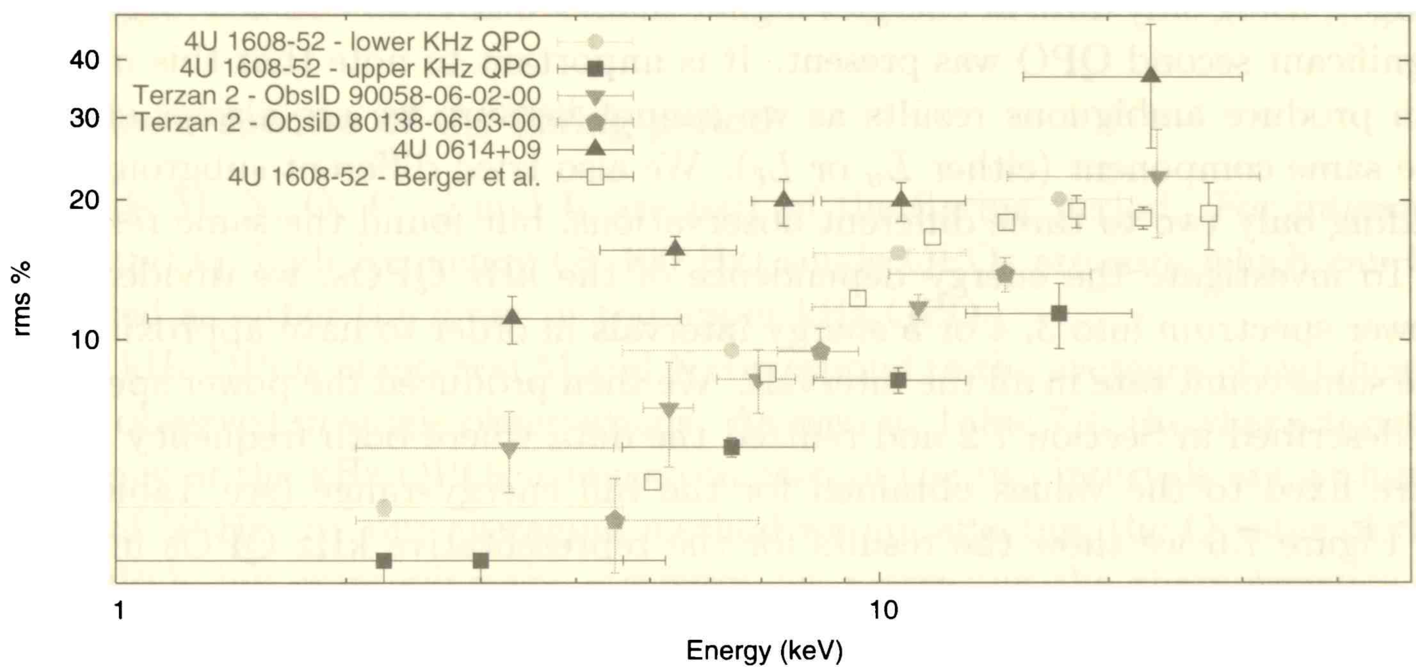

Figure 7.6: Energy dependence of two representative kHz QPOs of Terzan 2. One in flare F1 (grey pentagons – OBSid 80138-06-03-00) and another in flare F2 (grey triangles – OBSid 90058-06-02-00). For comparison we show the energy dependence of both lower (grey circles & open squares) and upper (black squares) peak of the atoll source 4U 1608–52 (Berger et al. 1996; Méndez et al. 1998b) and the upper peak (black triangles) of the atoll source 4U 0614+09 (Méndez et al. 1997; van Straaten et al. 2000).

We do not significantly detect two simultaneous kHz QPOs in any of the 5 observations. In order to search for a possible second kHz QPO, we used the shift–and–add method as described by Méndez et al. (1998b). We first tried to trace the detected kilohertz QPO using a dynamical power spectrum (e.g. see figure 2 in Berger et al. 1996) to visualize the time evolution of the QPO frequency, but the signal was too weak to be detected on timescales shorter than thė averaged observation. Therefore, for each observation we used the fitted averaged frequency (see Table 7.1) to shift each kilohertz QPO to the arbitrary frequency of 770 Hz. Next, the shifted, aligned, power spectra were averaged. The average power spectrum was finally fitted in the range 300–2048 Hz so as to exclude the edges, which are distorted due to the shifting method. To fit the averaged power spectrum, we used a function consisting of a Lorentzian and a constant to fit the QPO and the Poisson noise, respectively. We studied the residuals of the fit, but no significant power excess was present apart from the 770 Hz feature. In Figure 7.5 we show the fitted kHz QPO for observation 80138-06-02-00 (no shift and add was applied) and the shifted-and-added kHz QPO detected with the method mentioned above. Since it is known that the kHz QPOs become stronger at higher energies (e.g. Berger et al. 1996; Méndez et al. 1998a; van der Klis 2000, and references within), we repeated the analysis described above (which was performed on the full PCA energy range), using only data at energies higher than $\sim$ 6 keV or $\sim$ 10 keV. Again, no significant second QPO was present. It is important to note that this method can produce ambiguous results as we cannot be sure we are always shifting the same component (either L_u or L_ℓ). We also tried different subgroups, i.e. adding only two to three different observations, but found the same results.

To investigate the energy dependence of the kHz QPOs, we divided each power spectrum into 3, 4 or 5 energy intervals in order to have approximately the same count rate in all the intervals. We then produced the power spectrum as described in Section 7.2 and refitted the data where both frequency and Q were fixed to the values obtained for the full energy range (see Table 7.1). In Figure 7.6 we show the results for the representative kHz QPOs in flares F1 and F2 (observations 80138-06-03-00 and 90058-06-02-00, respectively). Similarly to what is observed in other sources, the fractional rms amplitude of the kHz QPOs increases with energy. The data show that there is no significant difference in the energy dependence of the kHz QPO at $\sim$ 599 Hz with that at $\sim$ 772 Hz.

7.3.4 Averaged power spectrum

The power spectra of the quiet period

Intervals A to L are all part of the quiet segment. 4 to 6 components were needed to fit all the power spectra of this group, where 11 out of the 12 power spectra showed significant broad components at $\sim$ 150, $\sim$ 10, $\sim$ 1 and at $\sim$ 0.2 Hz. Interval G is the exception where the broad component at $\sim$ 150 Hz was not significantly detected (8.5% rms-amplitude upper limit). A QPO ($Q \gtrsim 2$) at $\sim$ 0.8 Hz was also significantly detected in 11 out of 12 power spectra, interval B being the exception (1.4% rms-amplitude upper limit). Finally, an extra component (L_{vl}) at frequency $\nu_{vl} \sim 0.1$ Hz was detected only in interval C.

Similar power spectra have been reported in the extreme island state of the neutron star atoll sources 4U 0614+09, 4U 1728–34 (van Straaten et al. 2002), XTE J1118+480, SLX 1735–269 (Belloni et al. 2002b) and 4U 1608–52 (van Straaten et al. 2003). Olive et al. (1998) and Belloni et al. (2002b) analyzed an early subset of the data we present in this work. Our results are consistent with the frequencies reported in those works. Following van Straaten et al. (2002), Belloni et al. (2002b) and van Straaten et al. (2003), we identify the components as L_u, $L_{\ell ow}$, L_h, L_{LF} and L_b, where $\nu_u \sim 150$ Hz, $\nu_{\ell ow} \sim 10$ Hz, $\nu_h \sim 1$ Hz, $\nu_{LF} \sim 0.8$ Hz and $\nu_b \sim 0.1$ Hz, respectively. These identifications are strengthened by the correlations shown in Figure 7.7, in which we plot the characteristic frequency of all components versus that of ν_u for several atoll sources (see Section 7.3.6); clearly, we observe the same components as seen in the EIS in other atoll sources.

The power spectra of the flaring period

Intervals M, N, O, P, Q and R are part of the flaring period. For intervals M, N and Q, high frequency ($\gtrsim$ 400 Hz) single QPOs are seen which can be identified as either the lower or the upper kHz QPO.

The kHz QPOs in interval M and N correspond to the averages of significant QPOs observed in single observations. As seen in Table 7.1, the characteristic frequency of the kHz QPOs averaged in each of the two intervals are within a range of 50 Hz. By our averaging method we are affecting the Q value of the kHz QPOs but improving the statistics for measuring the characteristics of the features at lower frequencies (see Appendix in Chapter 6 for a discussion on this issue).

Interval Q is an average of three single observations (see Table 7.3) that individually do not show significant QPOs ($Q > 2$) at high frequencies although low-Q power excess can be measured. L_h in interval Q is only 2.6σ significant (single trial) but required for a stable fit.

Interval O shows a broad component at 30.5 ± 6.3 Hz and a 3.3% rms low-frequency noise. In this case, the very low frequency noise was fitted with a broad Lorentzian because a power law gave an unstable fit. The excess of power at $\nu \gtrsim 1000$ Hz is less than 3σ significant. Interval P shows a power spectrum with a power-law low frequency noise, and two Lorentzian components at frequencies 15.5 ± 1.6 and 30.5 ± 6.3 Hz (see Figure 7.1). In this case the high $\chi^2/dof = 218/163$ reveals that the Lorentzians do not satisfactorily fit the data. As can be seen in Figure 7.1, there is a steep decay of the power above $\nu \sim 35$ Hz and power excess at ~ 70 Hz. A fit with three Lorentzians becomes unstable. To further investigate this, we refitted the power spectrum using instead two Gaussians and one power law to fit the power at $\nu \lesssim 40$ Hz, and one Lorentzian to fit the possible extra component at ~ 70 Hz. The steeper Gaussian function better fits the steep power decay than the Lorentzians. In this fit, with three more free parameters, we obtain a $\chi^2/dof = 188/160$, and the Lorentzian at 69.1 ± 2.6 Hz becomes 3.4σ single-trial significant. This power spectrum is very similar to those reported by Migliari et al. (2004) and Migliari et al. (2005) for the atoll sources 4U 1820–30 and Ser X-1, respectively. Besides the similarity in shape of the power

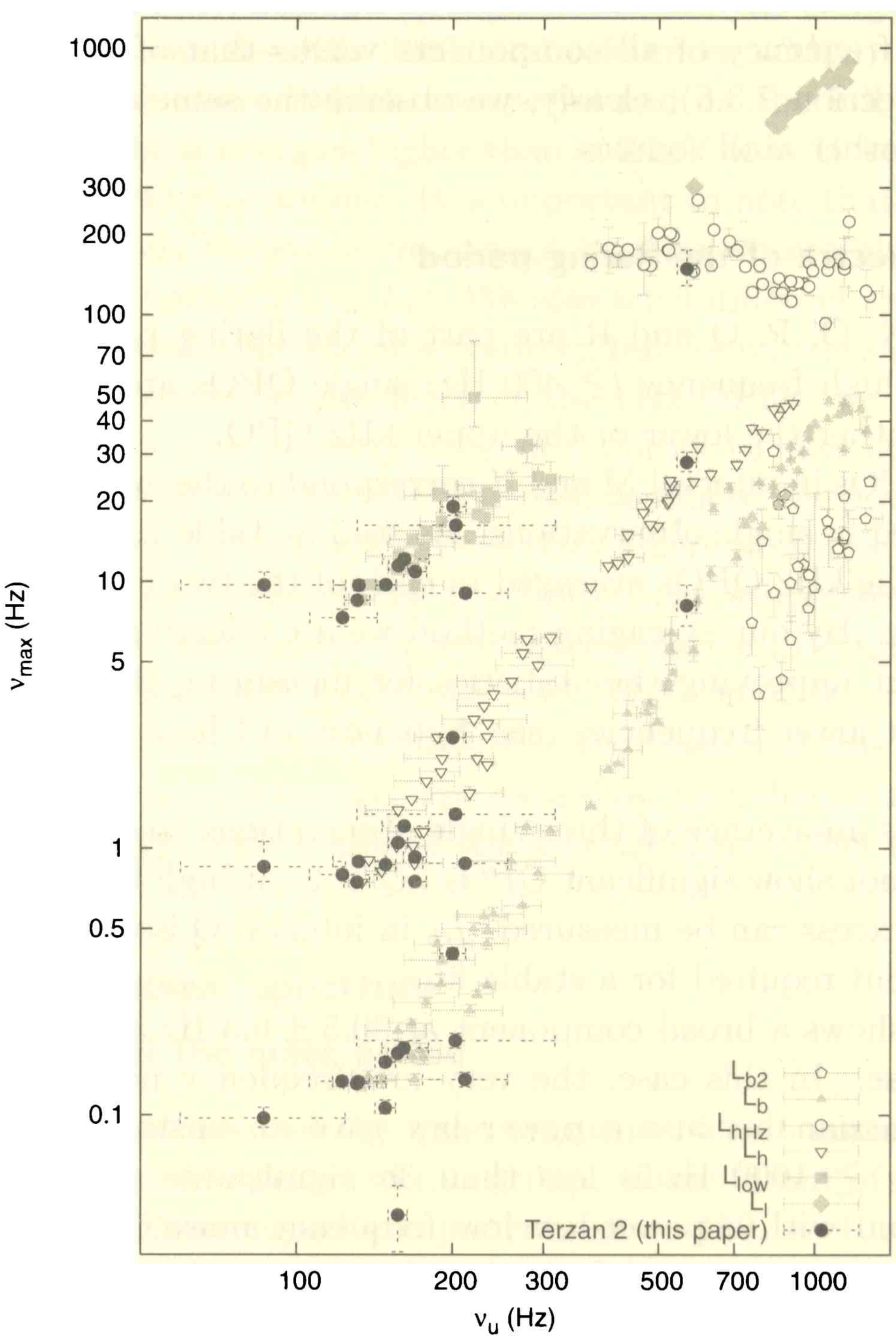

Figure 7.7: The characteristic frequencies ν_{max} of the various power spectral components plotted versus ν_u. The grey symbols mark the atoll sources 4U 0614+09, 4U 1728–34 (van Straaten et al. 2002), 4U 1608–52 (van Straaten et al. 2003), Aql X-1 (Reig et al. 2004) and 4U 1636–53 (Altamirano et al. 2006) and the low luminosity bursters Terzan 2 (previous results), GS 1826–24 and SLX 1735–269 (van Straaten et al. 2005, but also see Belloni et al. 2002b). The black bullets mark our results for Terzan 2. Note that we only plot the results for Intervals A-L and Q. In Intervals M and N we detect L_ℓ (see Sections 7.3.3 & 7.4.2) and for intervals O, P and R no kHz QPOs were detected (see Section 7.3.4).

spectrum, it is interesting to note that in both cases these authors found a best fit with components at similar frequencies to the ones we observe in Terzan 2 and which they interpreted as ν_b, ν_h and ν_{hHz}. This coincidence suggests that the sources were in very similar states. To our knowledge, no systematic study of this state has been reported as yet.

Interval R consists of only one observation (90058-06-05-00) of $\sim$ 1.4 ksec of data. In addition to a power law with index $\alpha = 3.1 \pm 0.7$, we detect one Lorentzian at 68.5 ± 7.2 Hz. Its frequency is rather high if we compare it with the other power spectra presented in this paper and even when compared with results in other sources (see Figure 7.7). This result might be due to blending of components due to the low statistics present in this power spectrum.

From the 99 pointed observations, only observation 90058-06-04-00 was not included in any of the averages described above. The averaged colors of this observation are very similar to those of Interval N (observations 90058-06-01-00, 90058-06-02-00) but the power spectrum does not show a significant QPO at $\simeq$ 560 Hz and can be fitted with a single Lorentzian at $\nu_{max} = 23.6 \pm 3.3$ Hz, $Q = 0.5 \pm 0.2$ and rms= $13.2 \pm 0.9\%$. The residuals of the fit show excess power at $\simeq$ 800 Hz but no significant kHz QPO. Although the colors of observation 90058-06-04-00 are different from those of interval N, the power spectrum may be similar. Because of the color difference we refrained from averaging 90058-06-04-00 into interval N.

7.3.5 Integrated power

In order to study the rms amplitude dependence on color and intensity, we calculated the average integral power per observation between 0.1 and 1000 Hz. In Figure 7.8 we show the 0.01–1000 Hz averaged rms amplitude (%), of each of the 99 observations, versus its average hard color. The observations which sample the island and banana state correlate with the averaged hard color. This type of correlation has been already observed in black hole candidates and neutron star systems (see e.g. Homan et al. 2001). At colors harder than 1.0, there are two clumps (grey squares in Figure 7.8) which can also be seen in the color-color diagram (Figure 7.4). They both correspond to observations of the extreme island state (quiet state) of the source. As we show in Figure 7.1, the power spectral shape remains approximately the same with time. However, for a given hard color, the total rms amplitude can change up to $\simeq$ 30%. No correlation with time, intensity or soft color was found and these changes are seen within a small range in intensity (less than 4 mCrab). Similar results are also observed when the rms amplitude is calculated in the 0.01–300 Hz range.

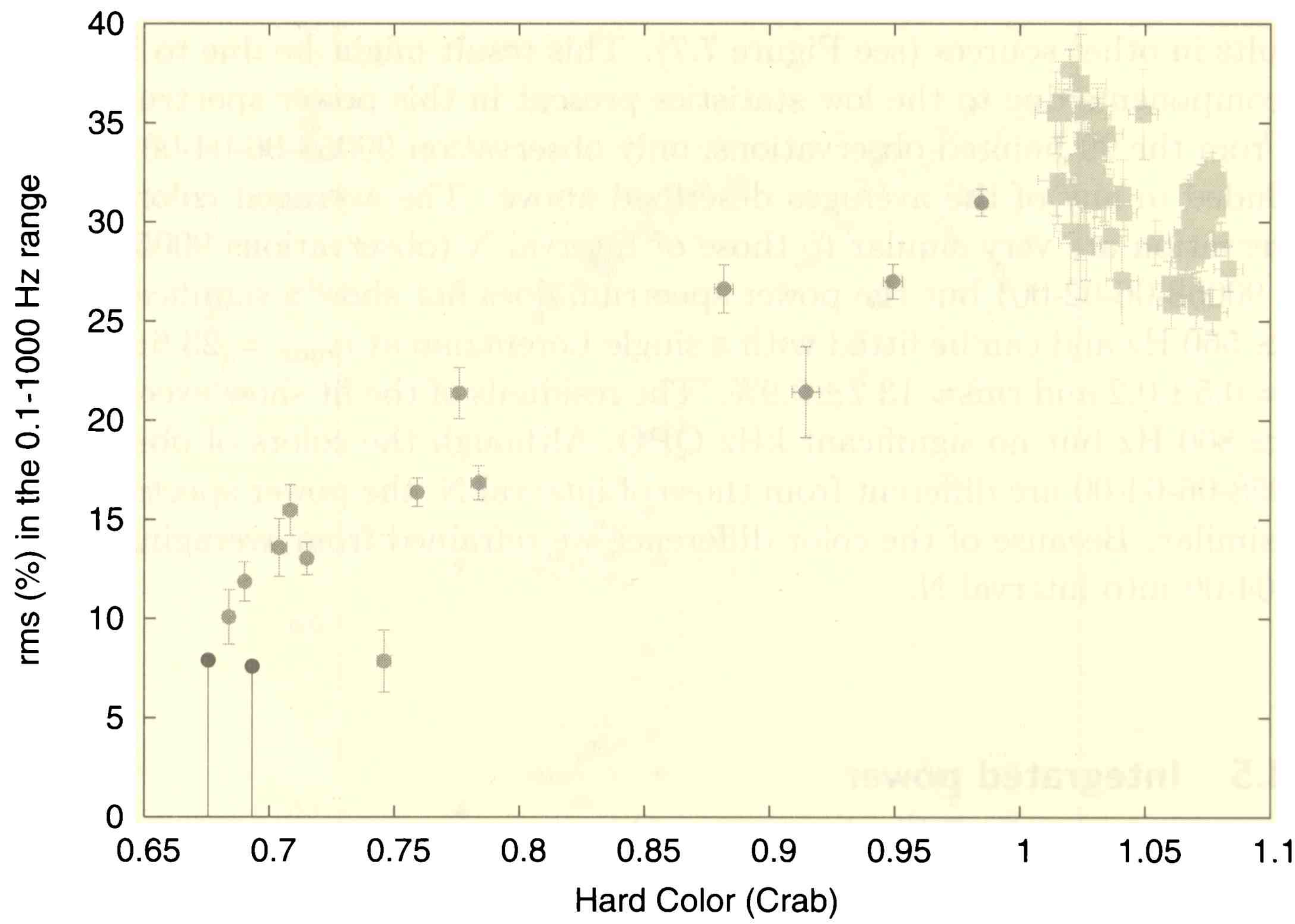

Figure 7.8: Fractional rms (%) amplitude versus hard color normalized to the Crab Nebula as explained in Section 7.2. The light-grey squares represent the data of the "quiet" state while the dark-grey circles represent the data for the "flare" state. The black circles represent the upper limit ($\Delta\chi^2 = 2.7$) for the observations 80138-06-05-00 and 80138-06-06-00 which also partially sampled the flare states.

7.3.6 Comparing Terzan 2 with other LMXBs

The flaring period

In Figure 7.9 we plot the frequency correlations between L_{LF} and L_ℓ reported by Psaltis et al. (1999) and updated by Belloni et al. (2002b). In Figure 7.7 we plot the characteristic frequency of all components versus that of ν_u for the atoll sources 4U 0614+09, 4U 1728–34, 4U 1608–52, 4U 1636–53 and Aql X-1 and the two low luminosity bursters GS 1826–24 and SLX 1735–269 (van Straaten et al. 2002, 2003; Reig et al. 2004; Altamirano et al. 2006). Using these correlations to identify the highest frequencies we observe (in intervals M, N & Q) as either ν_u or ν_ℓ presents a problem. Both interpretations give consistent results since the correlations observed are complex when $\nu_u \gtrsim$ 600 Hz (van Straaten et al. 2005).

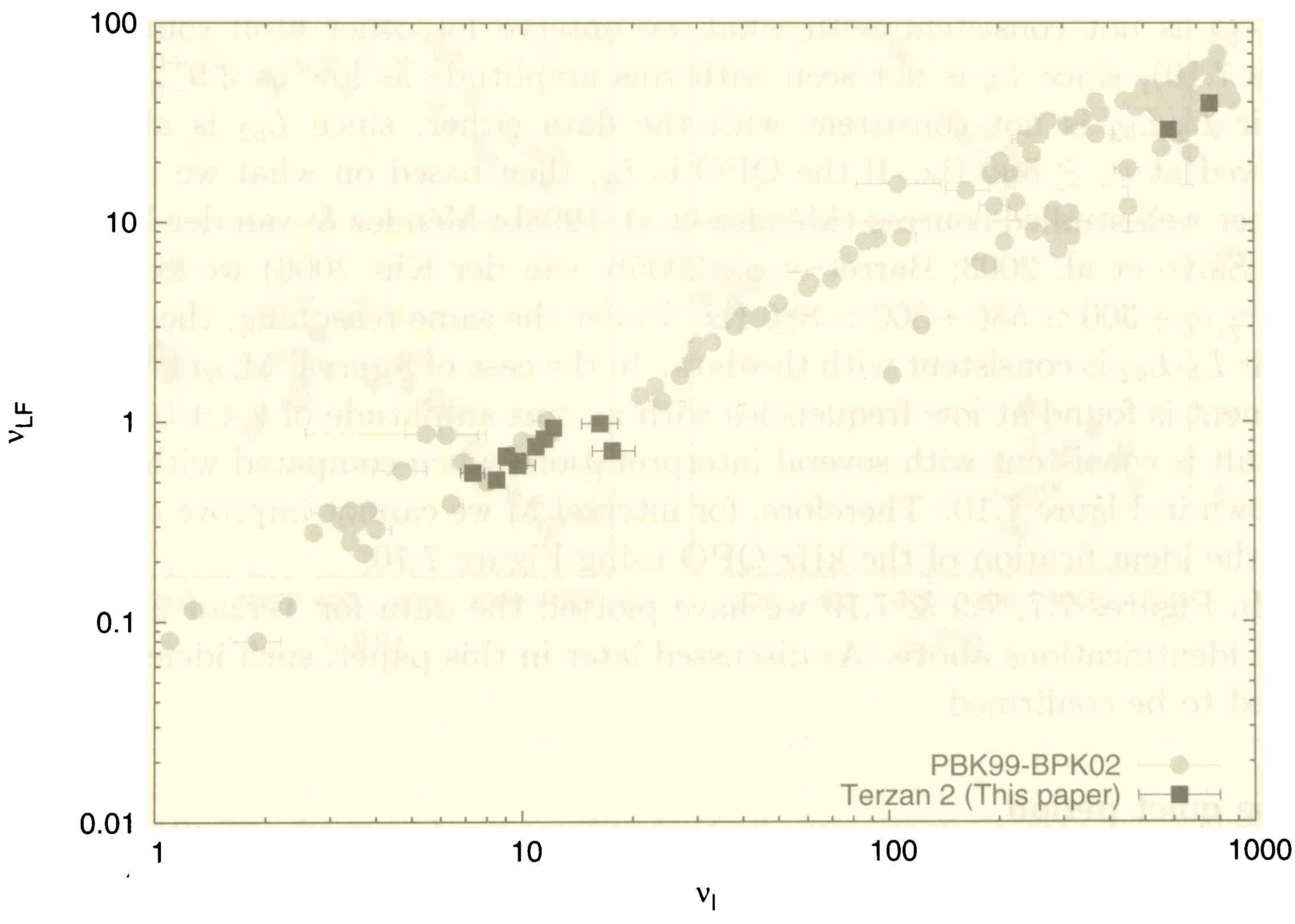

Figure 7.9: PBK relation after Psaltis et al. (PBK99 - 1999) and Belloni et al. (BPK02 - 2002b). The black squares at $\nu_{LF} < 10$ Hz represent the data of Intervals A and C–L while the black squares at $\nu_{LF} > 20$ Hz represent the data of Intervals M and N. In Interval B we do not detect L_{LF} and in intervals Q–R we do not detect L_ℓ.

In recent work, Barret et al. (2005a,b,c) have systematically studied the variation of the frequency, rms amplitude and the quality factor Q of the lower and upper kHz QPOs in the low-mass X-ray binaries 4U 1636–536, 4U 1608–

52 and 4U 1735–44. Although Q depends on the frequency of the component, these authors show that Q_ℓ is always above ~ 30, while Q_u is generally below ~ 25. By comparing our results for the kHz QPOs with those of Barret et al. (2005a,b,c), we find that the 5 QPOs listed in Table 7.1 (and averaged in intervals M and N) are relatively high-Q and hence consistent with being L_ℓ, but also still consistent with being L_u. The quality factor of the kHz QPO found in interval Q is low (2.4 ± 0.6) and hence this kHz QPO is probably L_u.

In Figure 7.10 we plot the fractional rms amplitude of all components (except L_{LF}) versus ν_u for the 4 atoll sources 4U 0614+09, 4U 1728–34, 4U 1608–52, 4U 1636–53. With respect to the kHz QPO identification, the interpretation that we found L_ℓ in interval N is strengthened by the rms amplitudes of the two low-frequency components found in the averaged power spectrum. If the QPO we observe is not L_ℓ but L_u, then the low frequency QPO pairs can be identified as either L_h-L_b or L_b-L_{b2}. For $\nu_u = 586.1 \pm 6.6$, the pair L_h-L_b is not consistent with what we observe for other atoll sources (Figure 7.10), since L_b is not seen with rms amplitude as low as $3.9^{+0.8}_{-0.5}\%$. The pair L_b-L_{b2} is not consistent with the data either, since L_{b2} is always observed at $\nu_u \gtrsim 800$ Hz. If the QPO is L_ℓ, then based on what we observe in other well-studied sources (Méndez et al. 1998b; Méndez & van der Klis 1999; Di Salvo et al. 2003; Barret et al. 2005b; van der Klis 2006) we expect that $\nu_u \simeq \nu_\ell + 300 \simeq 586 + 300 \simeq 886$ Hz. Under the same reasoning, then only the pair L_b-L_{b2} is consistent with the data. In the case of interval M, only one component is found at low frequencies with an rms amplitude of $6.4 \pm 0.6\%$. This result is consistent with several interpretations when compared with the data shown in Figure 7.10. Therefore, for interval M we cannot improve confidence in the identification of the kHz QPO using Figure 7.10.

In Figures 7.7, 7.9 & 7.10 we have plotted the data for Terzan 2 based on the identifications above. As discussed later in this paper, such identifications need to be confirmed.

The quiet period

In Figure 7.10 we show that the rms amplitude of L_u, $L_{\ell ow}$, L_h and L_b in Terzan 2 approximately follow the trend observed for other sources. Since Psaltis et al. (1999) interprets $L_{\ell ow}$ and L_ℓ as the same component in different source states, in Figure 7.10 we plot the data for both components together. Of course, in Figure 7.10 and Figure 7.7 as well, there is the well-known gap between these two components. Regarding lower frequency components, the point inside the circle represents our result for L_{vl} in interval C, which is the weakest component found in the EIS of Terzan 2. We plotted our results with those for L_{b2}. This component might be related with the VLFN Lorentzian

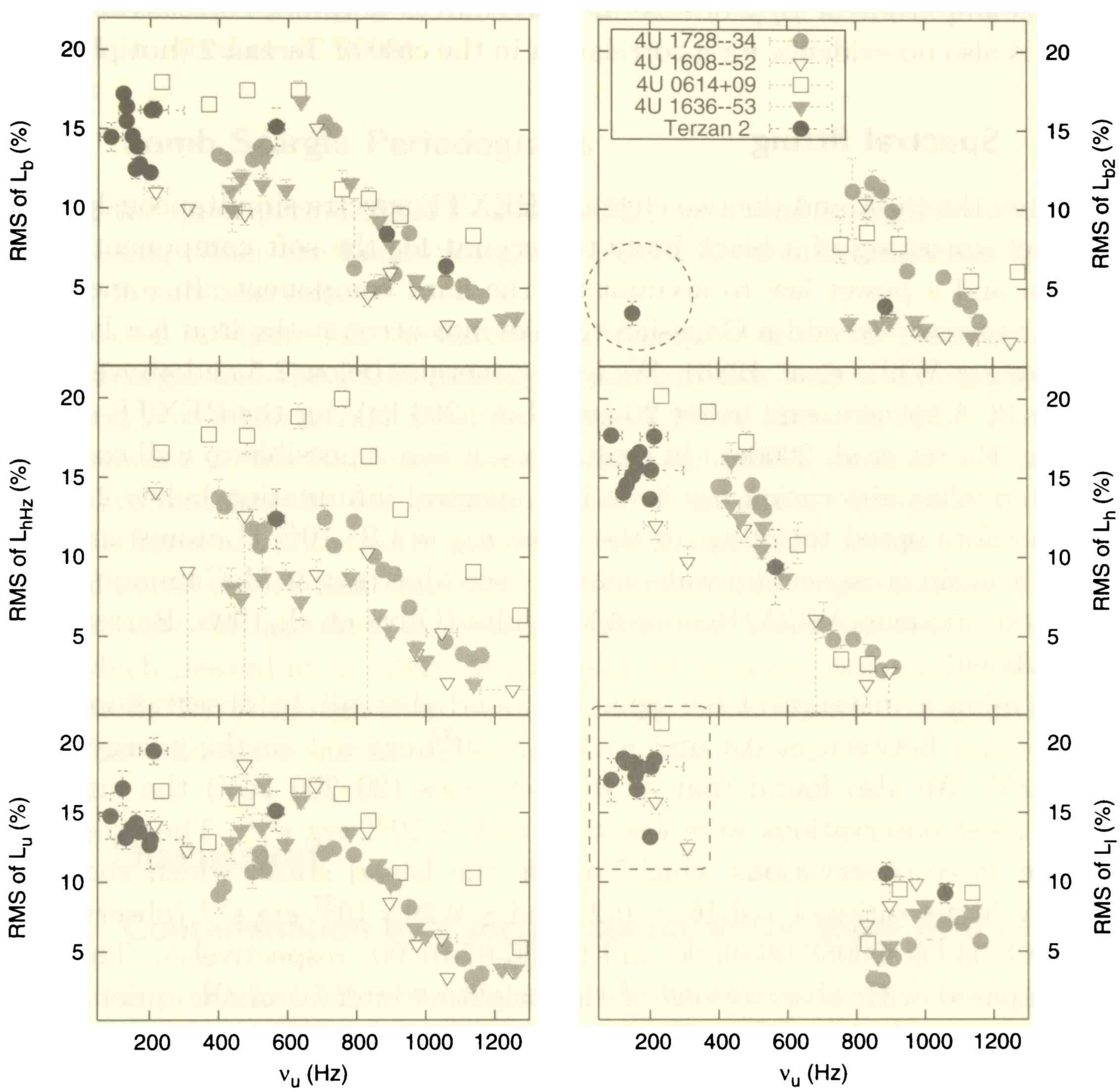

Figure 7.10: The fractional rms amplitude of all components (except L_{LF}) plotted versus ν_u. The symbols are labeled in the plot. The data for 4U 1728–34, 4U 1608–52 and 4U 0614+09 were taken from van Straaten et al. (2005). The data for 4U 1636–53 were taken from Altamirano et al. (2006). Note that for L_{hHz} and L_h of 4U 1608–52, the 3 triangles with vertical error bars which intersect the abscissa represent 95% confidence upper limits (see van Straaten et al. (2003) for a discussion). The points inside the circle represent our results for L_{vl} while the points inside the square represent results for L_{low} (see Section 7.4 for a discussion). Note that as mentioned in Section 7.3.6, the points for intervals M and N (ν_u > 800 Hz) were plotted under the assumption that $\nu_u = \nu_\ell + 300$ Hz.

(see Schnerr et al. 2003; Reerink et al. 2005). In Chapter 6 we showed that the rms amplitude of L_{LF} of several atoll sources does not correlate with ν_u. There is also no evidence for a correlation in the case of Terzan 2 (not plotted).

7.3.7 Spectral fitting

We fitted the PCA and the two cluster's HEXTE spectra simultaneously using a model consisting of a black body to account for the soft component of the spectra and a power law to account for the hard component. In some cases, it was necessary to add a Gaussian to take into account the iron Kα line (6.4 keV, see e.g. White et al. 1986). We ignore energies below 2.5 and above 25keV for the PCA spectra, and below 20 and above 200 keV for the HEXTE spectra (see e.g. Barret et al. 2000a). In most cases, it is not possible to well constrain the interstellar absorption n_H if we lack spectral information below 2.5 keV. We therefore opted to fix n_H to the value $n_H = 1.2 \cdot 10^{22}$ H atoms cm^{-2} (in the Wisconsin cross section wabs model – see Morrison & McCammon 1983) based on previous ASCA/BeppoSAX results (Olive et al. 1998; Barret et al. 1999, 2000a).

Assuming a distance of 6.6 kpc, we found that all 14 observations have luminosities between $\sim$ 0.4 and $\sim$ 1.35 $\times$ 10^{37} erg s^{-1} in the energy range 2–20 keV. We also found that at high energies (20–200 keV) the luminosities of most observations were less than 0.09 $\times$ 10^{37} erg s^{-1}. The exceptions are the three observations which sample the island state, which show 20–200 keV luminosities of $\sim$ 0.16, $\sim$ 0.23 and $\sim 0.29 \times 10^{37}$ erg s^{-1} (observations 90058-06-03-00, 90058-06-06-00 and 91050-07-01-00, respectively). This may be compared with observations of the brightest interval of the quiet period of Terzan 2, which have averaged luminosities $L_{1-20keV}$ = 0.81 $\times$ 10^{37} erg s^{-1} and $L_{20-200keV}$ = 0.48 $\times$ 10^{37} erg s^{-1} (Barret et al. 2000a). Clearly, in between the flares the luminosity can drop to similarly low values as in the quiet period. This is consistent with the lightcurve we show in Figure 7.2. We note that the observations studied by Barret et al. (2000a) correspond to MJDs 50391 – 50395 (November 4-8, 1996) and sample the brightest part of the quiet period of this source observed with RXTE (see Figure 7.2).

We are particularly interested in the luminosity at which the kHz QPOs are detected in Terzan 2 compared with other sources. Ford et al. (2000) have measured simultaneously the properties of the energy spectra and the frequencies of the kHz QPOs in 15 low-mass X-ray binaries covering a wide range of X-ray luminosities. The observations of intervals M and N (see Table 7.2) have average luminosities $L_{2-50keV}/L_{Edd}$ between 0.025 and 0.04 (where L_{Edd} = 2.5 $\times$ 10^{38} erg s^{-1}). The three observations that sample the island state (interval Q) have average luminosity $L_{2-50keV}/L_{Edd} \simeq 0.02$. This means that during the flares, Terzan 2 shows kHz QPOs at similar luminosities to the atoll sources Aql X-1, 4U 1608–52, 4U 1702–42 and 4U 1728–34 (see figure 1 in Ford et al. 2000).

7.3.8 Lomb Scargle Periodograms

During the quiet period (51214–52945 MJD), we found no significant periodicities using either the Lomb-Scargle or the PDM techniques in the full data set nor in sub-intervals.

As shown in Figure 7.2, the flares seem to occur every $\sim 60-100$ days. Both Lomb-Scargle and the PDM techniques confirm this with a significant signal of period $P = 90.55 \pm 2.06$ days. In Figure 7.11 we show the PCA lightcurve (top) versus a 20-bin 90.55 days period folded lightcurve (bottom). The folded lightcurve matches the occurrence of most of the flares. However, it is clear that the flares are not strictly periodic. For example, F3 seems to occur later and F6 occur earlier than expected. Furthermore, it is not possible to say if F7 is an early or late flare, or even a blend of two flares (we observed a small flare which peaked at $\simeq$ 53926 MJD, followed by a big one which peaked at $\simeq$ 53958 MJD). Although there are gaps in the data, Figure 7.11 suggests that some flares do not occur at all (see arrow in this figure).

7.4 Discussion

7.4.1 Contamination by a second source in the same field of view?

As shown in Figure 7.2, the luminosity of the source slowly decreases with time during the quiet period 51214–52945 MJD. Although the rms amplitude changes up to 30% (see Figure 7.8), the X-ray timing characteristics are very similar (see Interval A to L in Figure 7.1). During the 53000–53700 MJD period, the source shows flares which show different X-ray timing characteristics consistent with the island and banana states observed in other atoll sources (see e.g. van Straaten et al. 2003, 2005; Belloni et al. 2002b; Altamirano et al. 2005, 2006). A possible mechanism of the observed flux variations in Terzan 2 could be the emergence of a second X-ray source in this globular cluster unresolved by the 1° (FWHM) field of view of the PCA. If two sources are observed simultaneously with RXTE, then we would expect to see power spectra which are a combination of the intrinsic time variability of both sources.

To further investigate this, we compared the absolute rms amplitude that we observe both in the quiet and flaring states. Observation 80105-10-01-00 is the last observation performed during the quiet period from which we measured an average source countrate of $\sim$ 200 counts / second. The integrated power

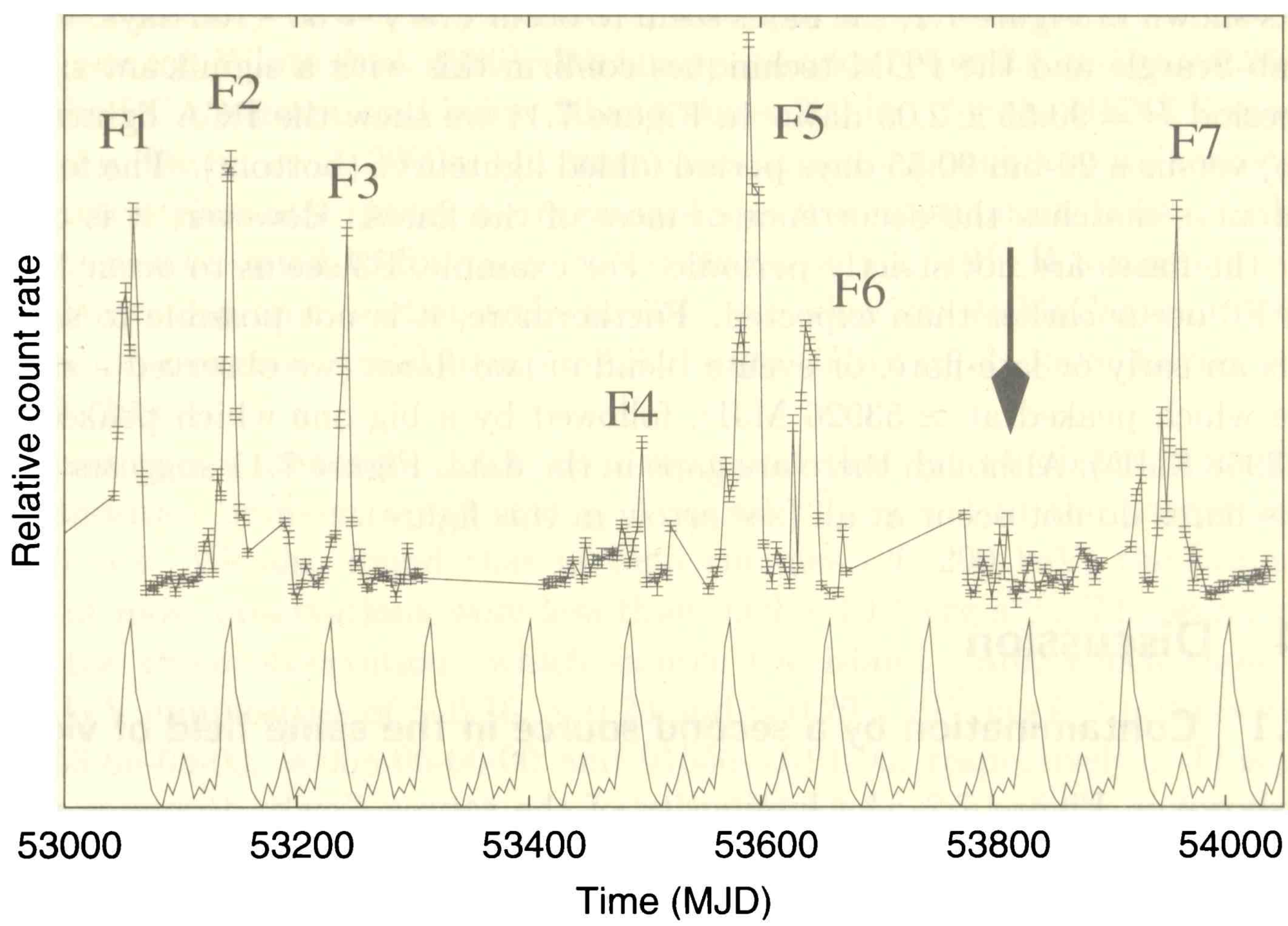

Figure 7.11: The PCA monitoring observation lightcurve of Terzan 2 in the time interval 53013–54050 MJD (*above*) versus a series of folded light curves with period of 90.55 days (*below*). The black arrow shows the position of a possible missed flare (see Section 7.4.3

between $7.8 \cdot 10^{-3}$ and 1 Hz is $(3.4 \pm 2)10^{-2}$, which corresponds to a fractional rms amplitude of $\sim 18 \pm 0.6\%$, i.e. an absolute rms amplitude of 36 ± 1 counts/second.

Observation 80138-06-01-00 is the first observation performed during the flaring state. Its average countrate is ~ 740 counts / second and the absolute rms amplitude in the 0.0078−1 Hz range is 21.4±4.4 counts/second (2.9±0.6% fractional rms amplitude). Clearly, the absolute rms amplitudes are different when comparing quiet and flaring periods. If we repeat the analysis using the second RXTE observation during the flaring state (80138-06-02-00), the discrepancy is higher. This observation has an average source countrate of ~ 405 counts/second and the upper limit for the absolute rms amplitude in the $7.810^{-3} - 1$ Hz frequency range is 5 counts/second.

Given the characteristics of the power spectra, flares cannot be explained by assuming that another source has emerged, unless Terzan 2 turned off at the same time that the other X-ray source turned on, which is unlikely. Therefore, we conclude that the flux transitions are intrinsic to the only low mass X-ray binary detected in the globular cluster Terzan 2: 1E 1724–30 (Revnivtsev et al. 2002).

7.4.2 The kilohertz QPOs, different states and their transitions

The results presented in this paper show that the low luminosity source 1E 1724 3045 in the globular cluster Terzan 2 can be identified as an atoll source. This is the first time a source previously classified as weak burst source showed other states than those of the extreme island state, confirming previous suggestions that these sources are atoll sources. We have identified the new states as the island and banana states based on comparisons between color color diagrams of different sources and the characteristics of the power spectra. We have detected at least one of the the kHz QPOs, and as explained in Sections 7.3.4 and 7.3.3, in 5 cases we may be detecting the lower kHz QPO (intervals M and N – see also Table 7.1) and in one case the upper one (interval Q). No simultaneous twin kHz QPOs were detected within any of the 14 observations that sample the flares. Future observations of flares will allow us to confirm these identifications and might allow us to detect both kHz QPOs simultaneously.

We found that the frequencies of the various components in the power spectra of Terzan 2 followed previously reported relations (Figures 7.7 and 7.9). Terzan 2 is a particularly important source in the context of these frequency correlations because it is one of the few neutron star sources that has been demonstrated to show power spectral features that reach frequencies as low as $\simeq 0.1$ Hz, which is uncommon for neutron star low mass X-ray binaries, but not for black holes. Our results demonstrate that in each of the flares, Terzan 2 undergoes flux transitions that, if directly observed, would probably allow us to resolve current ambiguities in the identification of components, such as the case of $L_{\ell ow}$ component in atoll sources. This component is interpreted by some authors as a broad lower kHz QPO at very low frequencies (see Psaltis et al. 1999; Nowak 2000; Belloni et al. 2002b) which becomes peaked at higher frequencies, while other authors interpret L_{ℓ} and $L_{\ell ow}$ as different components (see e.g. discussion in van Straaten et al. 2003). Another example is the identification of the upper kHz QPO at low frequencies. van Straaten et al. (2003) have suggested that the broad component observed at $\simeq$ 150 Hz in the EIS of atoll sources becomes the peaked upper kHz QPO L_u. These authors based their interpretation on the frequency correlations shown in Figure 7.7. Nevertheless, as van Straaten et al. (2003) argue, these identifications should be taken as tentative. One way to confirm the link between them would be to observe the gradual transformation from one to another one.

During the time between flares, the source shows intensities similar to those measured before the quasi-periodic flares started. Unfortunately there are no observations during those intervals, but we expect that then Terzan 2 shows X-ray variability similar to that reported in intervals A–L. If this is the case, the state transition between the extreme island state and the island state should be observable in observations at the beginning or at the end of each flare. Given the relatively gradual and predictable transitions, Terzan 2 becomes the best source known up to now to study these important transitions.

7.4.3 On the ~ 90 days flare recurrence

The long-term quasi-periodic signals observed in some LMXBs X-ray lightcurves are generally associated with the possible precession period of a tilted accretion disk or alternatively long term periodic variations in the accretion rate or periodic outbursts of X-ray transients. Some examples are the $\simeq$ 35 cycle in Her X-1 which is thought to be caused by a varying obscuration of the neutron star by a tilted-twisted precessing accretion disc; the $\simeq$ 170 days accretion cycle of the atoll source 4U 1820–30, (Priedhorsky & Terrell 1984a; Simon 2003); the 122-125 day cycle in the outbursts of the recurrent transient Aql X-1 (Priedhorsky & Terrell 1984b; Kitamoto et al. 1993). Understanding the mechanisms that trigger the long-term variability associated with variations in the accretion rate of LMXBs can allow us to better predict, within each source, when the state transitions occur. This is useful because these transitions are usually fast and therefore difficult to observe.

The power spectra of our observations of Terzan 2 during the flaring confirm that the source undergoes EIS-IS-LLB-LB-UB state transitions, as observed in other neutron star atoll systems (and not as seen for Z-sources, see reviews by van der Klis 2004, 2006, and references within). As the source increased in X-ray luminosity, we found that the components in the power spectra increased in frequency which is consistent with the interpretation that the accretion disk is moving inwards toward the compact object. Therefore, the flaring with average 90 days period is most probably an accretion cycle. We note that the modulation of the light-curve could be related to the orbital period of the system or set by the precession of a tilted disk. However, the mechanisms involved in those interpretations are very unlikely to affect the frequency of the kHz QPOs.

If the flares are explained as an accretion cycle, then it is puzzling why the source underwent a smooth decrease of L_x for $\simeq$ 8 years before it started to show the flares. Terzan 2 may not be the only source that shows this kind of behavior. For example, KS 1731–260 is a low-luminosity burster that has shown a high L_x phase, during which Revnivtsev & Sunyaev (2003) reported a possible $\simeq$ 38 days period, and a low L_x phase, during which much stronger variability was observed (which was described as red noise). After its low L_x phase, KS 1731–260 has turned into quiescence (Wijnands et al. 2002b,a). In Figure 7.12 we show the bulge scan light curve of the source during the low L_x phase. At MJD $\sim$ 51550 the source reached very low intensities, then flared up again for $\gtrsim$ 250 days to finally turn into quiescence. The low luminosities are confirmed by the ASM light curve (not plotted). Recently, Shih et al. (2005) reported that the persistent atoll source 4U 1636–53 has also shown a period of high L_x followed by a period of low L_x. During high L_x, no long-term periodicity was found, but a highly significant $\simeq$ 46 days period was observed after its L_x decline.

These similar patterns of behavior might point towards a common mechanism, which then must be unaffected by the intrinsic differences between these sources.

For example, while Terzan 2 remained with approximately constant luminosity in its extreme island state for $\simeq$ 8 years before showing long term periodicities, 4U 1636–53 and KS 1731–260 were observed with variable luminosity and in different states, including the banana state in which the kHz QPOs were found (see e.g. Wijnands et al. 1997 and Shih et al. 2005 for 4U 1636–53 and Wijnands & van der Klis 1997 and Revnivtsev & Sunyaev 2003 for KS 1731–260). While Terzan 2 reached a maximum luminosity of $L_x/L_{Edd} \simeq 0.02$ during one of the flares, 4U 1636–53 shows similar luminosities only at its lowest L_x levels (while it has reached $L_x/L_{Edd} \gtrsim 0.15$ – see Altamirano et al. 2006). Further differences may be related to whether these systems are normal or ultra-compact binaries. While 4U 1636–53 is not

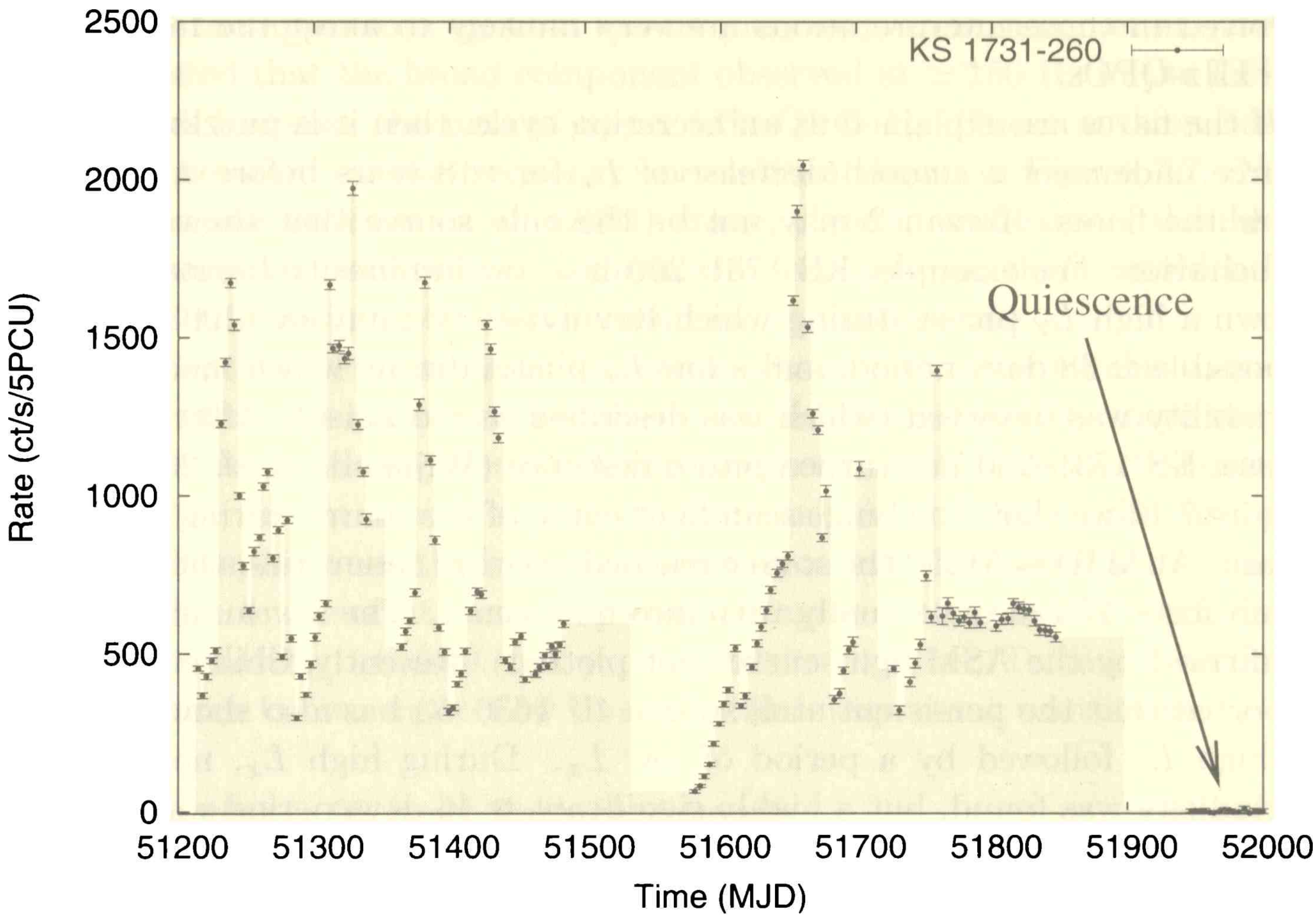

Figure 7.12: The PCA monitoring observation lightcurve of the atoll source KS 1731–260 during part of its low L_x period. Unfortunately, there are no PCA monitoring observations of the source before to MJD 51200. Clearly, the source flares up similarly to Terzan 2 before it turns into quiescence. Interestingly, the data at MJD $\sim$ 51550 shows that the source had a period of very low intensity, followed by a flaring up that lasted for $\sim$ 250 days before the source finally turned into quiescence.

ultra-compact (see below), in't Zand et al. (2007) has recently proposed that Terzan 2 may be classified as ultra-compact based on measurements of its persistent flux, long burst recurrence times and the hard X-ray spectra. If the luminosity behavior of these sources is related, the differences outlined above suggest that the mechanism that triggers the modulation of the light curve at low L_x may not depend on the accretion history, the luminosity of the source or even whether the system is ultra-compact or not. The modulation period may depend on these factors.

Unfortunately, we cannot compare the orbital periods and the companions of the three systems, as these are only known for 4U 1636–53 ($\sim$ 3.8 hours and $\simeq$ 0.4 $M_\odot$). Nevertheless, with the present data it is already possible to exclude some mechanisms. For example, mass transfer feedback induced by X-ray irradiation (Osaki 1985) is unlikely. In this model, X-ray radiation from the compact object heats the companion star surface, causing enhancement of the mass accretion rate in a runaway instability. However, in Osaki's scenario, it is not clear how the system could remember the phase of the cycle if one of the flares is missed or if the size of the flares differs much. Flares F4 and F5 in Terzan 2, independently of the other two sources, may already raise an objection to this model. Although we miss part of F4 due to a gap in the data, Figure 7.2 shows that F4 was quite short (less than 9 days), while F5 was the longest ($\lesssim$ 36 days) and strongest flare.

Shih et al. (2005) have suggested that the atoll source 4U 1636–53 may turn into quiescence after its low L_x period, as was observed for KS 1731–260. Such an observation for 4U 1636–53 as well as for Terzan 2 would give credibility to the link between these sources. To our knowledge, there is no model which predicts such behavior.

7.4.4 Energy dependence as a tool for kHz QPO identification

Homan & van der Klis (2000) discovered a single 695 Hz QPO in the low mass X-ray binary EXO 0748–676 and identified this QPO as the lower kHz QPO. These authors based their identification on the fact that at that time: (i) from the 11 kilohertz QPO pairs found in atoll sources, eight had ranges of lower peak frequencies that include 695 Hz, which was the case for only three of the upper peaks and (ii) the upper peaks in atoll sources generally had Q lower than $\sim$ 14, while their QPO had Q$\gtrsim$ 38, value more common for lower peaks. While from Figure 7.7 it can be seen that (i) is not valid anymore, since the upper kHz QPOs have been detected down to 300–400 Hz (and possibly down to $\lesssim$ 100 Hz – see Section 7.3.4), at these low frequencies L_u is usually much broader than they observed, which confirms their identification (see Section 7.3.6 and Barret et al. 2005a,b,c).

Homan & van der Klis (2000) also based their identification on the comparison of the energy dependence of the QPO with that of the two kilohertz peaks in 4U 1608–52, which have rather different energy dependences (Berger et al. 1996; Méndez et al. 1998b; Méndez et al. 2001). Similarly, Méndez et al. (2001) use the same method to strengthen the identification of the single kHz QPO observed in the atoll source Aql X-1. To further investigate if this method could be used to identify the sharp kHz QPOs we report in Section 7.3.3, in Figure 7.6 we compare the energy dependence of the kHz QPOs in 4U 1608–52 (Berger et al. 1996; Méndez et al. 1998b; Méndez et al. 2001) and 4U 0614+09 (Méndez et al. 1997) with that of Terzan 2. The data for Terzan 2 seem to fall in between those for L_ℓ and L_u of 4U 1608–52 but shows a completely different behavior than the data of 4U 0614+09. The fact that the rms amplitude of the upper kHz QPO in 4U 0614+09 and 4U 1608–52 are significantly different (by up to a factor of 3) and that the data for Terzan 2 fall in between those of L_ℓ and L_u in 4U 1608–52 show that the method does not lead to unambiguous results. Mean source luminosity, instantaneous luminosity and instantaneous QPO frequency may all affect QPO energy dependence in addition to QPO type.

7.5 Summary

(I) We presented a detailed study of the time variability of the atoll source 1E 1724–3045 (Terzan 2) which includes, for the first time, observations of this source in its island and banana states confirming the atoll nature of this source. We find that the different states of Terzan 2 show timing behavior similar to that seen in other NS-LMXBs. Our results for the extreme island state are consistent with those previously reported in Belloni et al. (2002b) and van Straaten et al. (2003).

(II) We report the discovery of kilohertz quasi-periodic oscillations (kHz QPOs). Although we do not detect two kHz QPOs simultaneously nor significant variability above 800 Hz, the detection of the lower and the upper kHz QPOs at different epochs and the power excess found at high frequencies (such as the case in intervals O or observation 90058-06-04-00) suggest that simultaneous twin kHz phenomena as well as significant variability up to $\sim$ 1100 Hz (or more) is probable.

(III) By comparing the dependence of the rms amplitude with energy of kHz QPOs in the atoll sources 4U 1608–52, 4U 0614+09 and Terzan 2, we show that this dependence appears to differ between sources and therefore cannot be used to unambiguously identify the kilohertz QPOs in either L_u or L_ℓ, as previously thought.

(IV) We studied the flux transitions or flares observed since February 2004 and from the source state changes observed we conclude that they are due to aperiodic changes in the accretion rate.

(V) State transitions between the extreme island state and the island state should be observable in observations at the beginning or at the end of each flare. Given the relatively gradual and predictable transitions, Terzan 2 becomes the best source known upto now to study such transitions.

Acknowledgments: This work was supported by the "Nederlandse Onderzoekschool Voor Astronomie" (NOVA), i.e., the "Netherlands Research School for Astronomy"

MJD	ObsId	Used in interval	ν_0 (Hz)	FWHM	Q	rms (%)	Sig.	c/s (5PCU)
53054.94	80138-06-02-00	M	731 ± 3	33.2 ± 7.3	22.1 ± 4.8	10.4 ± 0.8	6.5σ	~ 665
53055.00	80138-06-02-01	M	764 ± 2	14.3 ± 5.2	53.4 ± 19.4	6.9 ± 0.8	4.3σ	~ 690
53056.69	80138-06-03-00	M	772 ± 1	15.1 ± 4.2	51.1 ± 14.2	7.1 ± 0.6	5.6σ	~ 660
53145.57	90058-06-01-00	N	559 ± 2	17.3 ± 6.9	32.3 ± 12.8	6.6 ± 0.7	4.7σ	~ 765
53147.21	90058-06-02-00	N	599 ± 1	20.3 ± 4.8	29.5 ± 6.9	7.4 ± 0.5	6.6σ	~ 610

Table 7.1: Fit results for the 5 averaged observations showing significant kHz QPOs.

Time interval (MJD)	Duration (days)	Maximum Count Rate (cts/s/5PCU)	Flare label	N^o. of pointed obs. sampling the flare
$\sim$ 53038 – 53071	33	$\sim$ 850	F1	7
$\sim$ 53127 – 53155	28	$\sim$ 950	F2	4
$\sim$ 53233 – 53250	17	$\sim$ 830	F3	2
$\sim$ 53493 – 53502	9	$\sim$ 450	F4	0
$\sim$ 53566 – 53602	36	$\sim$ 1150	F5	1
$\sim$ 53631 – 53651	20	$\sim$ 650	F6	0
$\sim$ 53934 – 53972	38	$\sim$ 865	F7	0

Table 7.2: Data on the 6 flares observed until MJD 53667. See Section 7.3 for details. (The modified Julian date is defined as $MJD =$ Julian Date$-$2400000.5).

Interval A			
Observation	Soft color (Crab)	Hard color (Crab)	Intensity (Crab)
10090-01-01-000	1.3615 ± 0.0017	1.0760 ± 0.0013	0.0389 ± 0.0001
10090-01-01-001	1.3508 ± 0.0019	1.0761 ± 0.0014	0.0384 ± 0.0001
10090-01-01-00	1.3619 ± 0.0019	1.0757 ± 0.0015	0.0384 ± 0.0001
10090-01-01-020	1.3783 ± 0.0021	1.0781 ± 0.0016	0.0386 ± 0.0001
10090-01-01-021	1.4435 ± 0.0019	0.9846 ± 0.0013	0.0468 ± 0.0001
10090-01-01-022	1.3638 ± 0.0017	1.0788 ± 0.0013	0.0387 ± 0.0001
10090-01-01-02	1.3723 ± 0.0039	1.0801 ± 0.0029	0.0389 ± 0.0001
Interval B			
20170-05-01-00	1.3501 ± 0.0075	1.0660 ± 0.0058	0.0383 ± 0.0001
20170-05-02-00	1.3440 ± 0.0077	1.0492 ± 0.0059	0.0384 ± 0.0001
20170-05-03-00	1.3498 ± 0.0076	1.0541 ± 0.0058	0.0389 ± 0.0001
20170-05-04-00	1.3449 ± 0.0073	1.0632 ± 0.0056	0.0394 ± 0.0001
20170-05-05-00	1.3492 ± 0.0071	1.0703 ± 0.0055	0.0398 ± 0.0001
20170-05-06-00	1.3392 ± 0.0072	1.0650 ± 0.0056	0.0394 ± 0.0001
20170-05-07-00	1.3465 ± 0.0072	1.0726 ± 0.0055	0.0393 ± 0.0001
20170-05-08-00	1.3295 ± 0.0071	1.0605 ± 0.0056	0.0382 ± 0.0001
20170-05-09-00	1.3398 ± 0.0070	1.0704 ± 0.0054	0.0389 ± 0.0001
20170-05-10-00	1.3163 ± 0.0064	1.0687 ± 0.0051	0.0387 ± 0.0001
20170-05-11-00	1.3601 ± 0.0071	1.0714 ± 0.0054	0.0400 ± 0.0001
20170-05-12-00	1.3365 ± 0.0074	1.0747 ± 0.0058	0.0399 ± 0.0001
20170-05-13-00	1.3532 ± 0.0070	1.0721 ± 0.0053	0.0409 ± 0.0001
20170-05-14-00	1.3215 ± 0.0076	1.0768 ± 0.0061	0.0407 ± 0.0001
20170-05-15-00	1.3417 ± 0.0070	1.0658 ± 0.0054	0.0394 ± 0.0001
20170-05-16-00	1.3398 ± 0.0081	1.0669 ± 0.0062	0.0398 ± 0.0001
20170-05-17-00	1.3290 ± 0.0072	1.0832 ± 0.0057	0.0386 ± 0.0001
20170-05-18-00	1.3318 ± 0.0086	1.0682 ± 0.0067	0.0392 ± 0.0001
20170-05-19-00	1.3336 ± 0.0068	1.0667 ± 0.0053	0.0395 ± 0.0001
20170-05-20-00	1.3309 ± 0.0069	1.0599 ± 0.0054	0.0397 ± 0.0001

Table 7.3: Observations used for the timing analysis. The colors and intensity are corrected by dead time and normalized to the Crab Nebula (see Section 7.2). The complete table can be obtained digitally from ApJ.

Characteristic Frequency (Hz)	Q	rms (%)	Component ID
	Interval A		
156.9 ± 6.6	0.25 ± 0.06	13.9 ± 0.4	L_u
11.5 ± 0.2	0.04 ± 0.03	17.6 ± 0.3	L_{low}
1.05 ± 0.01	0.47 ± 0.02	16.3 ± 0.3	L_h
0.820 ± 0.006	5.76 ± 0.87	3.3 ± 0.3	L_{LF}
0.171 ± 0.005	0.32 ± 0.06	12.4 ± 0.6	L_b
	Interval B		
200.1 ± 11.6	0.55 ± 0.09	12.6 ± 0.5	L_u
19.1 ± 1.5	$--$	13.2 ± 0.2	L_{low}
2.59 ± 0.05	0.40 ± 0.04	13.6 ± 0.4	L_h
0.40 ± 0.02	$--$	12.2 ± 0.2	L_b
	Interval C		
148.4 ± 6.8	0.27 ± 0.05	13.8 ± 0.3	L_u
9.7 ± 0.1	$--$	18.6 ± 0.1	L_{low}
0.86 ± 0.01	0.55 ± 0.02	15.1 ± 0.3	L_h
0.633 ± 0.007	6.2 ± 1.2	3.1 ± 0.3	L_{LF}
0.158 ± 0.006	$--$	14.5 ± 0.3	L_b
0.106 ± 0.006	1.94 ± 1.02	$3.4^{+0.8}_{-0.5}$	L_{vl}
	Interval D		
130.8 ± 7.4	0.21 ± 0.07	13.1 ± 0.3	L_u
8.5 ± 0.20	$--$	18.5 ± 0.1	L_{low}
0.74 ± 0.01	0.53 ± 0.03	14.5 ± 0.3	L_h
0.512 ± 0.004	6.5 ± 0.9	3.9 ± 0.2	L_{LF}
0.131 ± 0.005	$--$	15.4 ± 0.2	L_b
	Interval E		
169.2 ± 8.6	0.31 ± 0.07	13.6 ± 0.4	L_u
10.8 ± 0.2	0.01 ± 0.04	18.2 ± 0.3	L_{low}
0.92 ± 0.01	0.45 ± 0.03	16.6 ± 0.3	L_h
0.750 ± 0.006	7.8 ± 1.8	2.8 ± 0.2	L_{LF}
0.144 ± 0.004	0.34 ± 0.07	12.7 ± 0.6	L_b
	Interval F		
216.1 ± 2.2	17.9 ± 8.4	3.1 ± 0.5	$***$
161.4 ± 17.0	0.14 ± 0.13	14.2 ± 0.8	L_u
12.1 ± 0.5	0.10 ± 0.07	16.6 ± 0.6	L_{low}
1.21 ± 0.04	0.44 ± 0.04	15.6 ± 0.5	L_h
0.93 ± 0.01	3.5 ± 0.9	4.4 ± 0.6	L_{LF}
0.179 ± 0.009	0.09 ± 0.04	13.8 ± 0.3	L_b
	Interval G		
17.5 ± 2.4	$--$	19.6 ± 0.5	L_{low}
1.17 ± 0.07	0.3 ± 0.1	16.4 ± 1.1	L_h
0.716 ± 0.008	$11.2^{24.5}_{3.6}$	4.1 ± 0.6	L_{LF}
0.152 ± 0.016	$--$	16.4 ± 0.7	L_b
	Interval H		
131.7 ± 15.8	0.3 ± 0.1	13.2 ± 0.8	L_u
9.6 ± 0.4	$--$	18.5 ± 0.2	L_{low}
0.892 ± 0.026	0.47 ± 0.04	14.5 ± 0.4	L_h
0.634 ± 0.006	4.6 ± 0.8	4.5 ± 0.4	L_{LF}
0.133 ± 0.005	$--$	16.3 ± 0.2	L_b
	Interval I		
211.7 ± 40.3	$--$	19.4 ± 0.9	L_u
9.05 ± 0.39	0.17 ± 0.07	18.8 ± 0.6	L_{low}
0.87 ± 0.02	0.47 ± 0.06	17.6 ± 0.7	L_h
0.67 ± 0.01	8.2 ± 3.3	3.2 ± 0.4	L_{LF}
0.136 ± 0.009	0.13 ± 0.05	16.2 ± 0.5	L_b
	Interval J		
86.4 ± 32.8	$--$	14.7 ± 1.6	L_u
9.71 ± 1.07	0.19 ± 0.13	17.3 ± 1.5	L_{low}

Continued on next page

Characteristic Frequency (Hz)	Q	rms (%)	Component ID
0.8 ± 0.1	$--$	17.6 ± 1.6	L_h
0.60 ± 0.02	1.5 ± 0.4	$8.8^{+2.2}_{-1.2}$	L_{LF}
0.097 ± 0.008	0.27 ± 0.08	14.4 ± 0.9	L_b
	Interval K		
122.5 ± 18.6	0.04 ± 0.3	16.7 ± 1.2	L_u
7.3 ± 0.5	$--$	18.8 ± 0.4	L_{low}
0.79 ± 0.03	0.54 ± 0.06	14.0 ± 0.6	L_h
0.556 ± 0.006	5.1 ± 1.5	4.3 ± 0.5	L_{LF}
0.134 ± 0.006	$--$	17.2 ± 0.3	L_b
	Interval L		
202.7 ± 94.6	$--$	13.04 ± 2.08	L_u
16.3 ± 1.8	$--$	18.3 ± 0.6	L_{low}
1.34 ± 0.05	0.48 ± 0.07	15.5 ± 0.6	L_h
0.98 ± 0.01	10.06 ± 8.60	$3.3^{+0.6}_{-0.5}$	L_{LF}
0.19 ± 0.01	$--$	16.1 ± 0.4	L_b
	Interval M		
758.9 ± 4.8	12.2^{+12}_{-4}	9.1 ± 0.7	L_ℓ
39.4 ± 2.5	1.3 ± 0.6	6.4 ± 0.6	L_b
	Interval N		
586.1 ± 6.6	5.5 ± 1.24	10.6 ± 0.8	L_ℓ
29.1 ± 1.1	1.1 ± 0.2	8.4 ± 0.5	L_b
4.9 ± 1.6	0.47 ± 0.3	$3.9^{+0.8}_{-0.5}$	L_{b2}
	Interval O		
30.5 ± 6.3	0.28 ± 0.17	5.8 ± 0.4	$***$
0.025 ± 0.002	0.3 ± 0.1	3.3 ± 0.1	$***$
	Interval P		
30.9 ± 0.4	2.02 ± 0.21	12.6 ± 0.6	$***$
15.5 ± 1.6	1.005 ± 0.156	7.9 ± 0.9	$***$
	Interval Q		
565.0 ± 24.5	2.4 ± 0.6	15.10 ± 1.44	L_u
148.7 ± 23.3	0.7 ± 0.4	12.4 ± 1.8	L_{hHz}
28.02 ± 2.37	1.06 ± 0.56	$9.4^{+2.7}_{-1.8}$	L_h^{**}
8.1 ± 1.4	0.10 ± 0.08	15.1 ± 1.2	L_b
	Interval R		
68.5 ± 7.2	1.8 ± 1.1	5.5 ± 0.9	$***$

Table 7.4: Characteristic frequencies ν_{max}, Q values ($\nu_{max} \equiv \nu_{central}/FWHM$), fractional rms (in the full PCA energy band) and component identification (ID) of the Lorentzians fitted for Terzan 2. The quoted errors use $\Delta\chi^2 = 1.0$. Where only one error is quoted, it is the straight average between the positive and the negative error. "$--$": Broad Lorentzians whose quality factor was fixed to 0.
**: This component is not 3σ significant. However, without this component the fit becomes unstable (see Section 7.3.4).
$***$: For this component, no clear identification was possible.

8 The transient black hole candidate XTE J1550–564 as seen by RXTE

D. Altamirano and M. van der Klis

Astrophysical Journal, to be submitted

Abstract

We have analyzed the power spectra of 427 observations of the black hole candidate XTE J1550–564. We investigate how the frequency, coherence and strength of each power spectral component evolves in time and varies as a function of spectral hardness and intensity and find that it is generally possible to follow components as they shift in frequency and vary in strength and coherence. We use this information to identify the different components and find that the frequencies of power spectral components correlate with each other. We compare these correlations with previous frequency–frequency relations that have been suggested to hold for all sources and find that many of our correlations coincide with these previous relations, but that some are at variance with one previously proposed relation.

8.1 Introduction

Observations with the *Rossi X-ray Timing Explorer* (RXTE) have led to extraordinary progress in the knowledge of the variability properties of many different types of sources, particularly of black hole candidates (or just black hole, BH) and neutron stars that are found in low-mass X-ray binaries (see, e.g, van der Klis 2006). Mass transfer between the companion and compact object in these systems is mainly via Roche-lobe overflow, with the material forming an accretion disk around the compact object through conservation of angular momentum.

Many of the quasi-periodic oscillations (QPOs) observed in these types of systems are thought to originate in the innermost regions of the accretion disk and therefore have been the subject of many previous studies (see Remillard & McClintock 2006 and van der Klis 2006, for the latest reviews). In the case of neutron star systems, QPOs have been found at frequencies as low as mHz (e.g Revnivtsev et al. 2001; Altamirano et al. 2008b) and as high as 1260 and 1329 Hz (Jonker et al. 2007; van Straaten et al. 2000, respectively), with the so called "kHz QPOs" cover the highest frequency region (300–1329 Hz) of the power density spectra. In the case of black hole candidates, QPOs have also been found with frequencies as low as mHz, but the maximum QPO frequency reported is 450 Hz (Strohmayer 2001b). In some models, this difference is interpreted as due to the difference in masses between neutron stars and black holes (see, e.g., the review by van der Klis 2006).

Although the high frequency QPOs ($\gtrsim$ 100 Hz) are particularly interesting given that they might be produced close to the innermost stable orbit (Syunyaev 1973, but also see Kluźniak & Abramowicz 2001; Bursa et al. 2004; Kluźniak & Abramowicz 2005, for some alternative models), the study of the properties and behavior of lower frequency QPOs ($\lesssim$ 50 Hz) may also provide important clues to the physics of accretion onto the compact objects (see, e.g., Wijnands & van der Klis 1999; Psaltis et al. 1999; Casella et al. 2004; Homan et al. 2001; Belloni et al. 2005; van der Klis 2006).

Not only the study of the QPOs, but also the study of the broad band noise found in the power spectra of neutron stars can provide important information that can be used to understand the nature of these systems. For example, van der Klis et al. (1985), Di Salvo et al. (2003), van Straaten et al. (2002), van Straaten et al. (2003) and Altamirano et al. (2006) have shown that the characteristic frequency of the broad band noise and QPOs correlate, and do so in the same manner among different neutron star systems, which means that the mechanisms that produce QPOs and broad band noise are connected.

In the case of black hole candidates, while many works investigated the broad band noise in terms of the total fractional rms amplitude in a given frequency range, no systematic quantitative study of the behavior of the individual broad band components and their relation with the observed QPOs and with source state has been reported as yet across several outbursts of a given source. As we describe in Section 8.5, in this work we decompose the power spectra using a multi-Lorentzian model in such a way that both broad band noise components and QPOs can be described using the same model. As part of a larger program including a range of black hole and neutron star sources (see also Klein-Wolt & van der Klis 2008), in this paper we report on the behavior of the broad band noise and its relation with the QPO behavior and source state for the black hole candidate XTE J1550–56. In the next section we introduce in more detail the current thinking on black hole states as it was developed in the works by Homan et al. (2001), Belloni et al. (2005), Homan & Belloni (2005) and Klein-Wolt & van der Klis (2008), (see also reviews by McClintock & Remillard 2003; Remillard & McClintock 2006, for a different point of view), in Section 8.3 we introduce the methodology used in this paper, and in Section 8.4 we provide an introduction to XTE J1550–564, the object of our current study.

8.2 Black hole states

In black holes the X-ray spectrum can be decomposed into two main components: (i) a hard, non-thermal, power-law component with photon index in the range 1.5–2 ; when this component dominates, it is usually attributed to a corona containing energetic electrons, and (ii) a soft, thermal, black-body like component with temperature $kT \lesssim 1\,\mathrm{keV}$ (Mitsuda et al. 1984); this component is attributed to thermal emission from an optically thick but geometrically-thin accretion disk (Shakura & Sunyaev 1976). See, e.g., Tananbaum et al. (1972), White & Marshall (1984), Życki et al. (2001); Gierliński & Done (2003); McClintock & Remillard (2003); Kubota & Makishima (2004) and Remillard & McClintock (2006) for further discussion of the X-ray spectrum as a function of source state. Based on these two components, it is possible to describe the spectral evolution of a black hole outburst in time. A complete description would of course include the X-ray time variability, other X-ray spectral components as well as the emission at other wavelengths.

In Figure 8.1 (*left panel*) we schematically show the roughly square pattern in the hardness–intensity diagram that a typical BH tends to trace out during an outburst (this figure was taken from van der Klis 2006). The arrows show the direction in which the source evolves in time. First, it has a period in which the intensity increases by a large factor as the hardness slightly decreases. This region in the hardness–intensity diagram is generally called the *low/hard state* (or just *low state* – hereafter LS). At some point, the source 'turns the corner': the intensity stops increasing and the source moves at approximately constant intensity towards a softer state usually known as the *high/soft state* (or just *high state* – hereafter HS). In between the low and the high states, there is the intermediate state (IMS) which links both extremes and where complex behavior, including sometimes large flares in intensity, occur. After the source reaches the HS, it usually shows a decrease of intensity at approximately constant hardness (with some excursions to harder or softer states) until it reaches a level in which it moves back in the direction of the LS at approximately constant intensity. The hardening of the spectra continues until it reaches values that are approximately the same as those observed at the beginning of the outburst. At this point the hardening stops, the intensity rapidly decreases and the source returns to quiescence.

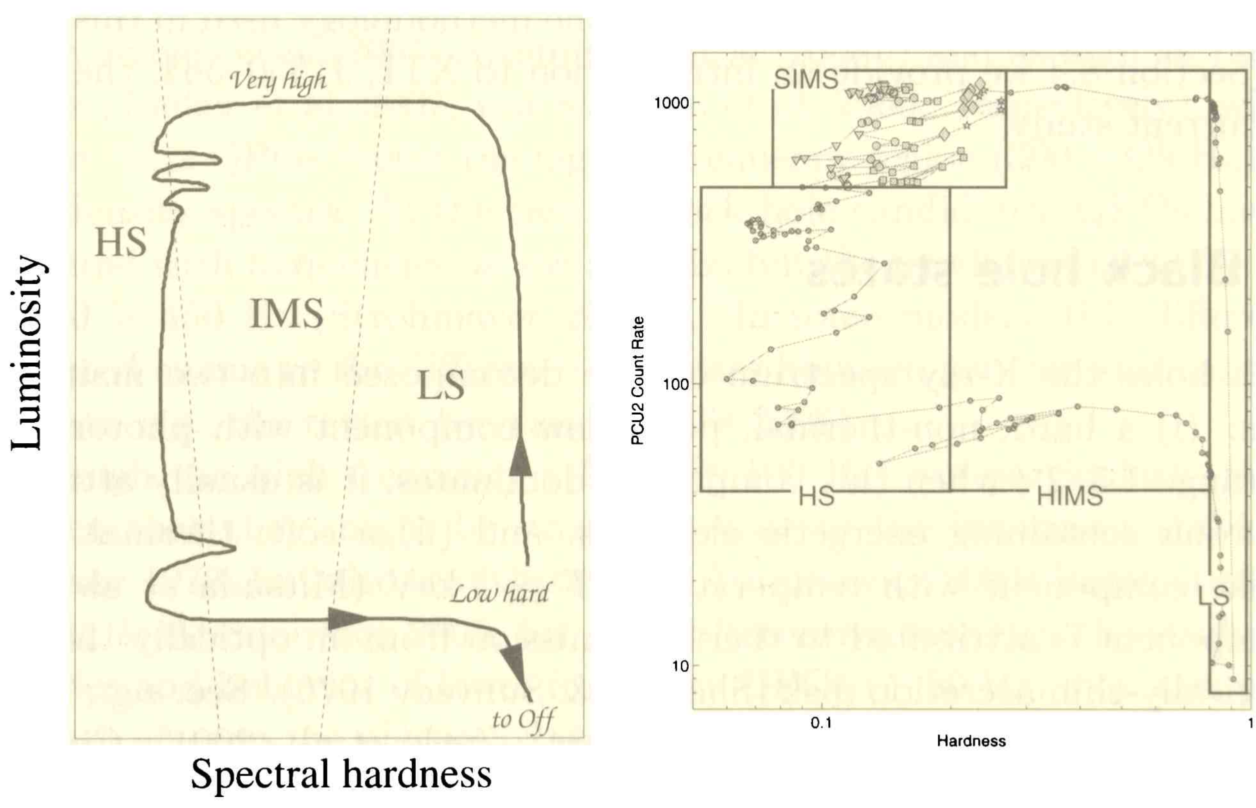

Figure 8.1: *Left:* Schematic Hardness-intensity diagram that shows the main black hole states: the *Low state* (LS), the *Intermediate state* (IMS) and the *high state* (HS). This figure was taken from van der Klis (2006) and was inspired by observations of the black holes XTE J1550–564 (Homan et al. 2001) and GX 339–4 (Belloni et al. 2005). *Right:* Hardness-intensity diagram as shown by Belloni et al. (2005) for all observations of the 2002/2003 outburst of the black hole GX 339–4. These authors subdivided the IMS into the Soft IMS (SIMS) and the hard IMS (HIMS).

In Figure 8.1 (*right panel*) we show the track drawn by the black hole candidate GX 339–4 during its 2002/2003 outburst (this figure was taken from

Belloni et al. 2005). The source shows a pattern such as that presented in the schematic in the *left panel* of Figure 8.1, although it does not always move smoothly in the hardness–intensity diagram. While black hole low-mass X-ray binaries show behavior which differs between sources and can even change between outbursts of the same source (see, e.g., Homan & Belloni 2005; Remillard & McClintock 2006), the loop in the hardness–intensity diagram is usually recognizable. As discussed by Belloni et al. (2005), in the case of the 2002/2003 outburst of GX 339–4 the intermediate state can be usefully subdivided into the Soft Intermediate State (SIMS) and the Hard Intermediate state (HIMS) based on the X-ray time variability.

The intermediate states are associated with state transitions and show strong and fast variations in their properties (see, e.g., Miyamoto et al. 1991, 1993, 1994; Belloni et al. 2005; Homan & Belloni 2005, and references within). These state transitions are important for the understanding of accretion onto black holes since it is thought that during these intervals strong structural changes take place in the accretion flow. For example, there is evidence that the ejection of relativistic jets takes place during some of these transitions (e.g., Fender & Belloni 2004; Corbel et al. 2004; Belloni 2007).

In describing black hole source states it is essential to consider the X-ray time variability. The power spectra of the LS and the HIMS are dominated by a strong band-limited noise that can reach fractional rms amplitudes of up to $\sim 50\%$ (see van der Klis 2006, and references within). Sometimes, low frequency QPOs are observed with frequencies in the range of $\sim 10^{-3}$ – 20 Hz. The characteristic frequencies (see Section 8.5 for a definition) of these QPOs and noise components are found to correlate (see, e.g., Wijnands & van der Klis 1999; Belloni et al. 2002b), generally increasing towards softer states. The SIMS shows no strong band-limited noise; transient QPOs appear whose frequencies are rather stable (see, e.g, Casella et al. 2004, 2005, and references within). In the HS, only weak power-law noise is observed in the power spectrum and sometimes a QPO with frequency in the range 10–20 Hz (see, e.g., the HS of XTE J1550–564 – Homan et al. 2001). In Figure 8.2 we show characteristic power spectra for each of the four black hole states described above.

High frequency ($100 < \nu < 450$ Hz) QPOs have been reported in seven black holes (see review by van der Klis 2006). They are weak (0.5 to 2% rms in the 2–60 keV range), transient, energy dependent (rms amplitudes increasing with energy) and detected only at high count rates. For two sources (XTE J1550–564 and GRO J1655–40) two simultaneous high frequency QPOs have been observed. Otherwise, these QPOs are found alone, at either the frequency of the lower frequency peak or that of the upper one. In either case, in a given

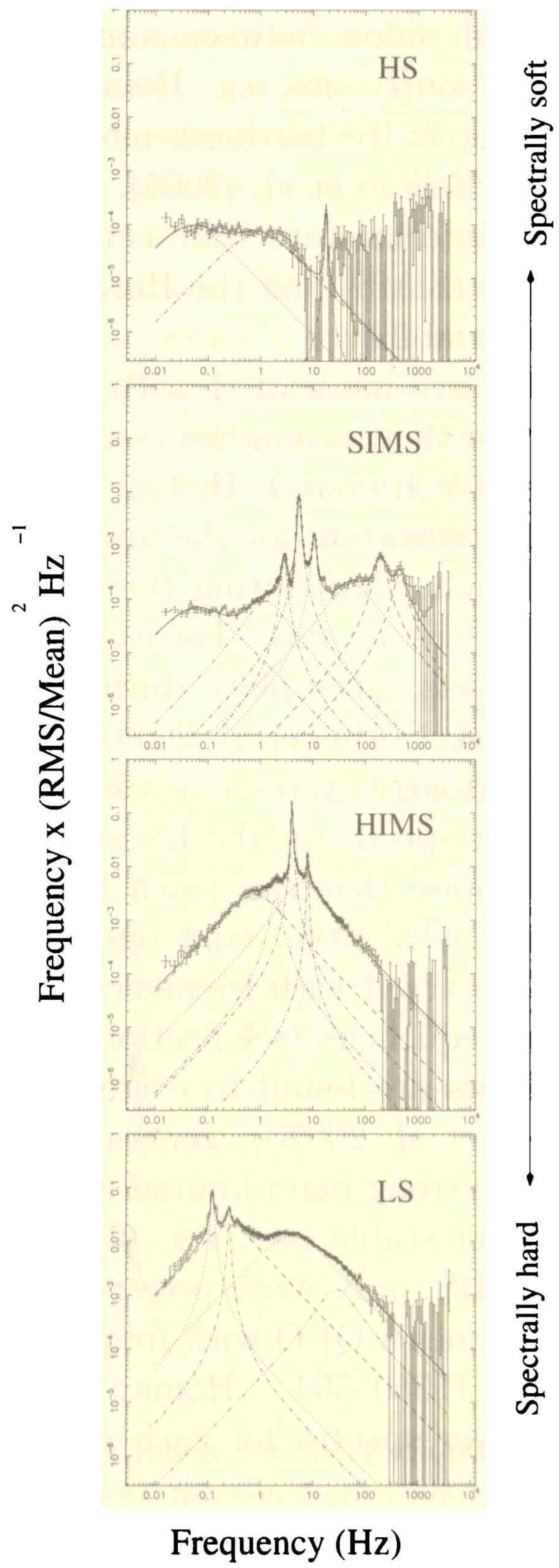

Figure 8.2: The characteristic power spectra of the black hole source states. From top to bottom the X-ray spectrum becomes harder. HS, SIMS, HIMS and LS stand for *high state*, *soft intermediate state*, *hard intermediate state*, and *low state*, respectively

source the frequency is rather constant. Finding high frequency QPOs is not always straightforward, as special selections on time or energy are necessary (e.g Strohmayer 2001a).

8.3 Identification and evolution of power spectral components

The study of low frequency QPOs ($\lesssim$ 20 Hz) in previous works has led to a proposed classification into 3 main types (A, B and C) based on coherence, frequency, time lags and the presence or absence of simultaneous strong broad band noise (see e.g Wijnands et al. 1999; Homan et al. 2001; Remillard et al. 2002a; Casella et al. 2004, 2005; Belloni et al. 2005). A classification method for also the broad band noise components based on that for neutron stars (van Straaten et al. 2003) was discussed by Belloni et al. (2002b). Klein-Wolt & van der Klis (2008) further studied this scheme, that names the different QPOs as well as broad band components as L_i, where L stands for Lorentzian and i for the name of the component. For example, L_b stands for "Lorentzian at the break", L_{LF} for "Low frequency QPO", L_h for hump, L_ℓ for the lower kHz QPO, etc. This classification and way of labeling was used successfully to identify the different components in the power spectra of neutron star systems (see, e.g., van Straaten et al. 2002, 2003, 2005; van der Klis 2006; Klein-Wolt & van der Klis 2008) and has been proven to be a practical way of comparing power spectral components of different neutron star systems (van Straaten et al. 2002; Belloni et al. 2002b; van Straaten et al. 2003, 2005; Altamirano et al. 2006) and between neutron stars and black hole systems (Psaltis et al. 1999; Belloni et al. 2002b; Klein-Wolt & van der Klis 2008).

As in this work we study both QPOs and broad band components, we use the L_i classification. For completeness, references to the types A, B and C are given throughout the paper based on previous works. When a change between types occurs in time, we use a note in the form "(Type ? $\rightarrow$ Type ?, Reference)". For example, (Type B $\rightarrow$ Type C, Homan et al. 2001) refers to a change from Type B to C QPO as reported by Homan et al. (2001). Later in this paper, we explain the relation between the Type A, B and C and the L_i classifications.

Independently of the labeling used, in order to understand the phenomenology we observe in the power spectra of black holes and neutron stars, it is important to study the characteristics of power spectral components as they evolve in time and as a function of spectral hardness and intensity. Correlations that exist between the characteristic frequencies of most of their power spectral components can be useful in this. As we describe below, there are two main relations that are known to hold for black hole variability: the PBK relation (after Psaltis et al. 1999) and the WK relation (after Wijnands et al. 1999).

Psaltis et al. (1999) found an approximate frequency correlation involving a low-frequency QPO and a broad noise component (L_{LF} and L_h, respectively, see Section 8.8), the lower kHz QPO frequency and a broad noise component interpreted as low-frequency version of this QPO (L_ℓ). This correlation spans nearly three decades in frequency, where bright neutron star sources populate the >100 Hz range and black holes and weak neutron star the <10 Hz range. As already noted by Psaltis et al. (1999), because (i) the correlation combines features from different sources which show either peaked or broad components with relatively little overlap, and (ii) the correlation is composed of a subset of data points per source and hence can be biased by the sampling, the data are suggestive but not conclusive with respect to the existence of a single correlation covering this wide frequency range (van der Klis 2006). Interestingly, Warner & Woudt (2002) and Mauche (2002) show that the PBK relation may be extended to white dwarf systems. If true, this implies that the mechanism producing the frequency–frequency correlations must be generic to a broad class of accretion flows.

Wijnands et al. (1999) found that there is a relation between the break frequency of the band-limited noise (L_b) and the centroid frequency of a low-frequency QPO above this break (L_{LF}). Similarly to the PBK relation case, the WK relation is composed of a subset of data points per source.

van Straaten et al. (2002), together with the L_i labeling scheme referenced to above, have proposed for the neutron star variability a 'universal scheme' of correlations between the thus labeled frequencies which encompass the WK and PBK relations. (see also Di Salvo et al. 2003; van Straaten et al. 2003, 2005; Altamirano et al. 2005; Linares et al. 2005; Altamirano et al. 2006) but which has also been recently used to compare black hole variability with that of neutron star systems (Klein-Wolt & van der Klis 2008).

In Section 8.7 we describe the evolution of the power spectral components as a function of time, spectral hardness and intensity independently of their classification. Using these results and the classification proposed by Klein-Wolt & van der Klis (2008) and others, in Section 8.8 we study how the time variability measured XTE J1550–564 fits in the classifications and frequency–frequency relations described above.

8.4 The black hole XTE J1550–56

XTE J1550–564 was first detected by the All-Sky Monitor (ASM) on board RXTE on September 7th, 1998 (Smith 1998). Shortly after that the optical (Orosz et al. 1998) and radio (Campbell-Wilson et al. 1998) counterparts were discovered.

This first outburst was the longest, lasting for about 250 days and was composed of two phases which are separated by a deep and broad intensity dip (see, e.g., Homan et al. 2001; Remillard et al. 2002a, see also Section 8.7.1). On September 20th 1998, approximately 13 days after the first detection of the source, XTE J1550–564 exhibited one of the brightest flares (~ 6.8 Crab) ever observed with RXTE (Remillard et al. 1998). Extensive spectral analysis of this first outburst has been reported by Sobczak et al. (1999, 2000) while an extensive analysis of the time variability has been reported by Homan et al. (2001) and Remillard et al. (2002a). Of particular interest for our current work are the results of Homan et al. (2001), who interpreted the variability observed in XTE J1550–564 as evidence that spectral states are set not only by the mass accretion rate $\dot{M}$ as it had been generally assumed (e.g., Tanaka & Lewin 1995; van der Klis 1995b), but that changes in at least one other physical parameter are also required to explain the overall behavior of the source.

Multiwavelenght observations were also performed during this outburst. The radio outburst lagged the X-ray outburst by 1.8 days and reached a maximum flux of 375 mJy at 843 MHz (Hannikainen et al. 2001a,b) while optical observations showed that there is no strong correlation between optical and X-ray flux (Jain et al. 2001c). From the first observations it was already suspected that XTE J1550–564 is a black hole X-ray binary (based on the spectral and temporal properties, see Sobczak et al. 1999; Cui et al. 1999; Homan et al. 2001), and this was confirmed when Orosz et al. (2002) reported the mass of the compact object to be $M = 10.5 \pm 1.0 M_{\odot}$ based on optical spectroscopic observations of the companion star. The distance to the source is likely ~ 5.3 kpc (see discussion by Orosz et al. 2002), the orbital period is ~ 1.54 days (Jain et al. 2001b; Orosz et al. 2002) and the inclination of the system is between 67 and 77 degrees (Orosz et al. 2002).

On April 6th 2000 XTE J1550-564 became active again (Smith et al. 2000; Masetti & Soria 2000). This outburst was not as bright as the first one, reaching a maximum luminosity of approximately 1 Crab. Miller et al. (2001) reported on the analysis of the high frequency timing properties of this outbursts while the spectral evolution was studied by Tomsick et al. (2001a) and Rodriguez et al. (2003). The correlations between optical, infrared and X-ray variability were studied by Jain et al. (2001b).

Further outbursts were detected in 2001 (Tomsick et al. 2001b; Jain et al. 2001a), 2002 (Swank et al. 2002; Bailyn 2002; Belloni et al. 2002a) and most recently in 2003 (Dubath et al. 2003; Woudt et al. 2003; Miller & Homan 2003; Kuulkers et al. 2003b). These outbursts were short and much dimmer than the previous two, reaching intensities not higher than 10% of the Crab. Swank et al. (2002) have reported low-level activity between the 2001 and 2002 outbursts. Radio observations for the 2001 outburst were reported by Corbel et al. (2001), who found a flat radio spectrum, consistent with a black hole low state. Aref'ev et al. (2004) reported on the broadband X-ray spectrum using INTEGRAL (International Gamma-Ray Astrophysics Laboratory) and RXTE X-ray observations of XTE J1550–564 during the 2003 outburst.

Both low ($\sim 0.01 - 20$ Hz) and high ($\sim 100 - 270$ Hz) frequency QPOs have been studied for this source (see, e.g., Wijnands et al. 1999; Remillard et al. 1999a, 2002a; Cui et al. 2000; Sobczak et al. 2000; Homan et al. 2001; Kalemci et al. 2001; Miller et al. 2001; Rodriguez et al. 2004) but the broad-band noise was only studied in some detail (in terms of a decomposition of the broad band noise into components) by Belloni et al. (2002a) for the 2002 outburst. Results on time variability during the 2001 and 2003 outbursts are presented for the first time in the present work. XTE J1550–564 and GRO J1655–40 are the two black hole sources which occasionally show 2 high frequency ($>$ 100 Hz) peaks simultaneously and at an approximate 2:3 frequency ratio (see review by van der Klis 2006). In the case of XTE J1550–56, the QPOs were found at 188 ± 3 and 268 ± 3 Hz during the 2000 outburst (Miller et al. 2001).

XTE J1550–564 is also an interesting source since it shows large-scale moving jets which have been detected at both X-ray and radio wavelengths (Corbel et al. 2002; Tomsick et al. 2003; Kaaret et al. 2003a). The broadband spectrum of the jets is consistent with synchrotron emission from high-energy particles that were accelerated either in the shock waves formed within the relativistic ejecta or by the interaction of the jets with the interstellar medium (Corbel et al. 2002).

8.5 Observations and data analysis

We use data from the Rossi X-ray Timing Explorer (RXTE) Proportional Counter Array (PCA; for instrument information see Zhang et al. 1993; Jahoda et al. 2006). There were a total of 427 pointed observations in sixteen data sets (30188-06, 30191-01, 30435-01, 30514-03, 40142-04, 40401-01, 40501-01, 50134-01, 50134-02, 50135-01, 50137-02, 50427-01, 60428-01, 70402-01, 80135-01, 80412-01) which sample all the outbursts of XTE J1550–564 detected with

RXTE. Each observation comprises from a fraction of one to several entire satellite orbits, for ~ 1 to ~ 14 ksec of useful data per observation.

We use the 16-s time-resolution Standard 2 mode data to calculate X-ray colors. For each of the five PCA detectors (PCUs) we calculate a soft and a hard color defined as the count rate in the 6.0–16.0 keV band divided by the rate in the 2.0–6.0 keV band and the 16.0–20.0 keV rate divided by the 2.0–6.0 keV rate, respectively and the intensity, defined as the count rate in the 2.0–20 keV band. To obtain the count rates in these exact energy ranges, we interpolate linearly between PCU channels. We then perform dead-time corrections, subtract the background contribution in each band using the standard bright source background model for the PCA, version 2.1e[1], remove instrumental drop-outs and finally obtain colors and intensity for each time interval of 16s. The RXTE gain epoch changes with each new high voltage setting of the PCUs (Jahoda et al. 2006). In order to correct for these gain changes as well as the differences in effective area between the PCUs, we used the method introduced by Kuulkers et al. (1994, when analyzing EXOSAT[2] data): for each PCU we calculate, in the same manner as for XTE J1550–564, the colors of the Crab, which can be supposed to be constant. We then average the 16s Crab colors and intensity for each PCU for each day. For each PCU we divide the 16s color and intensity values obtained for XTE J1550–564 by the corresponding average Crab values that are closest in time but in the same RXTE gain epoch. Then, we average the colors and intensity over all PCUs. Finally, we average the 16s colors per observation.

In order to better constrain the intensity behavior of the different outbursts, we also extracted the All-Sky Monitor (ASM) data (Levine et al. 1996). The ASM is sensitive in the range 2 to 12 keV and it performs sets of 90s pointed observations, covering $\sim 80\%$ of the sky every ~ 90 minutes.

For the Fourier timing analysis we used data from the PCA's Event, Good Xenon and Single Bit modes. Leahy-normalized power spectra were constructed using data segments of 128, 256, 512 or 1024 seconds and a time resolution such that the lowest available frequency is 1/128, 1/256, 1/512 or 1/1024 Hz and the Nyquist frequency was either 2048 or 4096 Hz. (The choice of data segment length depended on the data structure and the type of variability present – see also Appendix I for more information). No background or deadtime corrections were made prior to the calculation of the power spectra. We first averaged the power spectra *per observation.* We inspected the shape of the average power spectra at high frequency (> 1500 Hz) for unusual features in addition to the usual Poisson noise and found none. We then sub-

[1]PCA Digest at http://heasarc.gsfc.nasa.gov/ for details of the model

[2]A European Space Agency X-ray Observatory Satellite

tracted a predicted dead-time modified Poisson noise spectrum estimated from the power at frequencies higher than 1500 Hz, where neither intrinsic noise nor QPOs are known to be present, using the method developed by Klein-Wolt (2004) based on the analytical function of Zhang et al. (1995). In most cases, this method correctly modeled the Poisson noise spectrum. However, in a few cases we found significant excess of power which was well fitted with a broad Lorentzian with characteristic frequency higher than 400 Hz. It is possible that these power excesses are instrumental, but since we cannot exclude the possibility that they are real, we included them in our results. The resulting power spectra were converted to squared fractional rms (van der Klis 1995a). In this normalization the square root of the integrated power density equals the fractional rms of the intrinsic variability in the source count rate.

To fit the power spectra, we used a multi-Lorentzian function: the sum of several Lorentzians, each denoted as L_i, where i denotes the type of component. The characteristic frequency (ν_{max}, see definition below) of L_i is denoted ν_i. We mostly only include those Lorentzians in the fits whose single-trial significance exceeds 3σ based on the negative error bar on the power integrated from 0 to ∞. In a few cases, extra ($< 3\sigma$) components were needed. In Appendix II we describe those cases in detail. We give the frequency of the Lorentzians in terms of characteristic frequency ν_{max} (the frequency where the component contributes most of its variance per logarithmic frequency interval) as introduced by Belloni et al. (2002b): $\nu_{max} = \sqrt{\nu_0^2 + (FWHM/2)^2} = \nu_0\sqrt{1 + 1/4Q^2}$. For the quality factor Q we use the standard definition $Q = \nu_0/FWHM$. $FWHM$ is the full width at half maximum and ν_0 the centroid frequency of the Lorentzian.

In some cases in which QPOs were very coherent (high values of Q), we find that the multi-Lorentzian function is not able to correctly model the peak, and therefore the χ^2/dof was high ($Q \gtrsim 2$; examples of such cases in the current work can be seen in panel A12 in Figure 8.20 and panel B7 in Figure 8.21). Three possible solutions to this problem are: (i) to use several Lorentzians to model a single peak, (ii) to use a combination of Gaussians and Lorentzians for some of the features or (iii) to fit each peaked feature with one Lorentzian even if the final χ^2/dof is high. We find that (i) is not a good solution, as an unrealistic number of components are needed to model the high Q features well, while the use of one Gaussian plus one Lorentzian [i.e. method (ii)] to fit each peaked feature would significantly improve the χ^2/dof (based on an F-test). The problem of using method (ii) however, is that sometimes the frequency of the Gaussian nor that of the Lorentzian represent the peak of the feature. Estimating the true quality factor Q represents an additional problem with this method. Therefore, we opted to use the multi-Lorentzian function in which one Lorentzian is used per peaked feature [method (iii)]. We note that for narrow QPOs, the Q value of the QPO we report can be slightly underestimated and the fractional rms amplitude slightly overestimated. Since the broad band noise is the main subject of this paper, we checked how using methods (ii) and (iii) for the QPOs affect our results on the noise components. We find that the fractional rms amplitude and characteristic frequency of the broad band noise components did not depend significantly on the description of the QPOs. Although the Q values generally also remained the same within errors, we found a few cases where Lorentzians with $Q \lesssim 0.5$ had to be fixed to $Q = 0$ when using method (ii) but were well described with a freely fitted Q in method (iii). None of these differences affect our conclusions (see Section 8.8).

8.6 General description of the main figures used in this work

Each component we fit in a power spectrum is characterized by 3 values: the frequency, the quality factor and the rms amplitude. Furthermore, each component can be different at different intensities and colors of the source. Generally, in previous works the complex phenomenology defined by these variables is presented as two–dimensional projections, in which two variables are plotted versus each other. In this work we introduce multi-dimensional plots, in which the extra dimensions are encoded in the size, shape and color of the symbols. In the following sections we describe the general characteristics of the main diagrams used in the rest of this work.

8.6.1 Fractional rms amplitude as a function of spectral state

In order to follow the power spectral variations and the total rms amplitude as a function of the energy spectral changes, we plotted the hardness–intensity diagram (and details in sub-figures) of each outburst in Figures 8.3–8.7. In each figure, small grey squares represent the average colors for each of the 427 observations we have analyzed in this work. The colored symbols represent the observations of the specific outburst the figure focuses on, colors representing the averaged rms amplitude in the 0.008–10 Hz range. Open circles, stars and triangles were used when the integrated power in this frequency range was $< 2.5\sigma$, between 2.5 and 3σ and $> 3\sigma$ significant, respectively. Blue lines link observations in time order. It is important to note that the color scale here denotes the fractional rms amplitude in a fixed frequency range and hence has a different meaning from that in the figures described in Section 8.6.2.

8.6.2 Power spectral characteristics as a function of time, color and fractional rms amplitude

For each outburst we have fitted the average power spectrum of each observation with a multi-Lorentzian model as described in Section 8.5 and plotted the frequencies of all fitted components versus time (Figures 8.8–8.13) and versus hard color (Figures 8.14–8.18).

In all these figures, we have encoded the value of the quality factor Q in the shape and size of the symbol representing each component. All the components with $Q < 1.8$ are represented by squares, with $1.8 \leq Q \leq 2$ by diamonds and with $Q > 2$ by circles. In this way it is possible to differentiate broad band noise, $Q < 1.8$, from QPOs, $Q > 2$, with the diamonds representing components which, given uncertainties are often straddling the two definitions. The quality factor is encoded such that the linear size of the symbol S follows the relation $S = 3.5 \times \ell og_{10}(Q + 3.5)$. This relation has no physical meaning but allows to visualize the quality factor Q of all components in the power spectra.

The fractional rms amplitude of each component is encoded in the color of the symbol. The color scale differs between outbursts, but in a given outburst is the same between figures.

8.6.3 Power spectra

As reference to be used with the figures described above, we show representative power spectra for each outburst (Figures 8.20–8.23). The panels in each Figure are ordered numerically in time, but note that similar spectra could recur at different times during the outbursts. The times of occurrence of these representative power spectra are marked with white stars on the top margin of Figures 8.8, 8.10, 8.11 and 8.13 (see Section 8.6.2).

For plotting the power spectra in each panel, we use the power times frequency representation (νP_ν), where each power spectral density estimate P_ν is multiplied by its Fourier frequency ν. For a Lorentzian this representation helps to visualize the characteristic frequency ν_{max}, as in νP_ν the Lorentzian's maximum occurs at ν_{max}. The area below the Lorentzian equals the integrated power of the component and is proportional to the square of the fractional rms amplitude. In all figures, the ordinate is in units of rms normalized power density [in (rms/Mean)^2 Hz^{-1} times frequency (in Hz), i.e., dimensionless] and the range is always $3 \times 10^{-7} - 1$. This makes it easier to compare the changes in total fractional rms amplitude between source states and source outbursts.

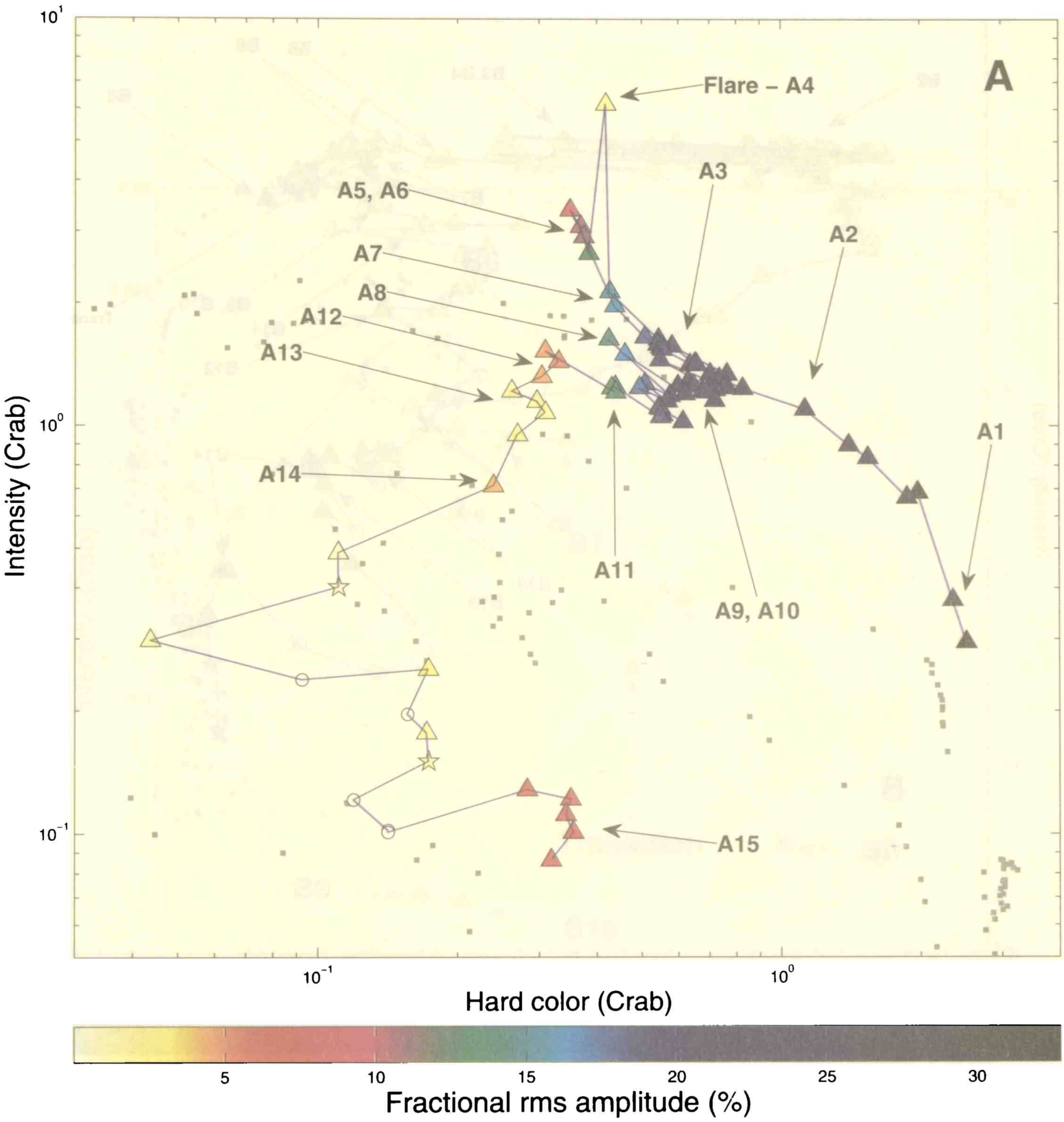

Figure 8.3: Hardness–Intensity diagram for observations during outburst A. Small grey square symbols represent the average colors during other outbursts of XTE J1550–56. Colored symbols represent the observations during this outburst. Open circles, stars and triangles were used when the integrated power in the 0.008–10 Hz range was $< 2.5\sigma$, between 2.5 and 3σ and $> 3\sigma$ significant, respectively. Color bar with the rms amplitude scale is plotted.

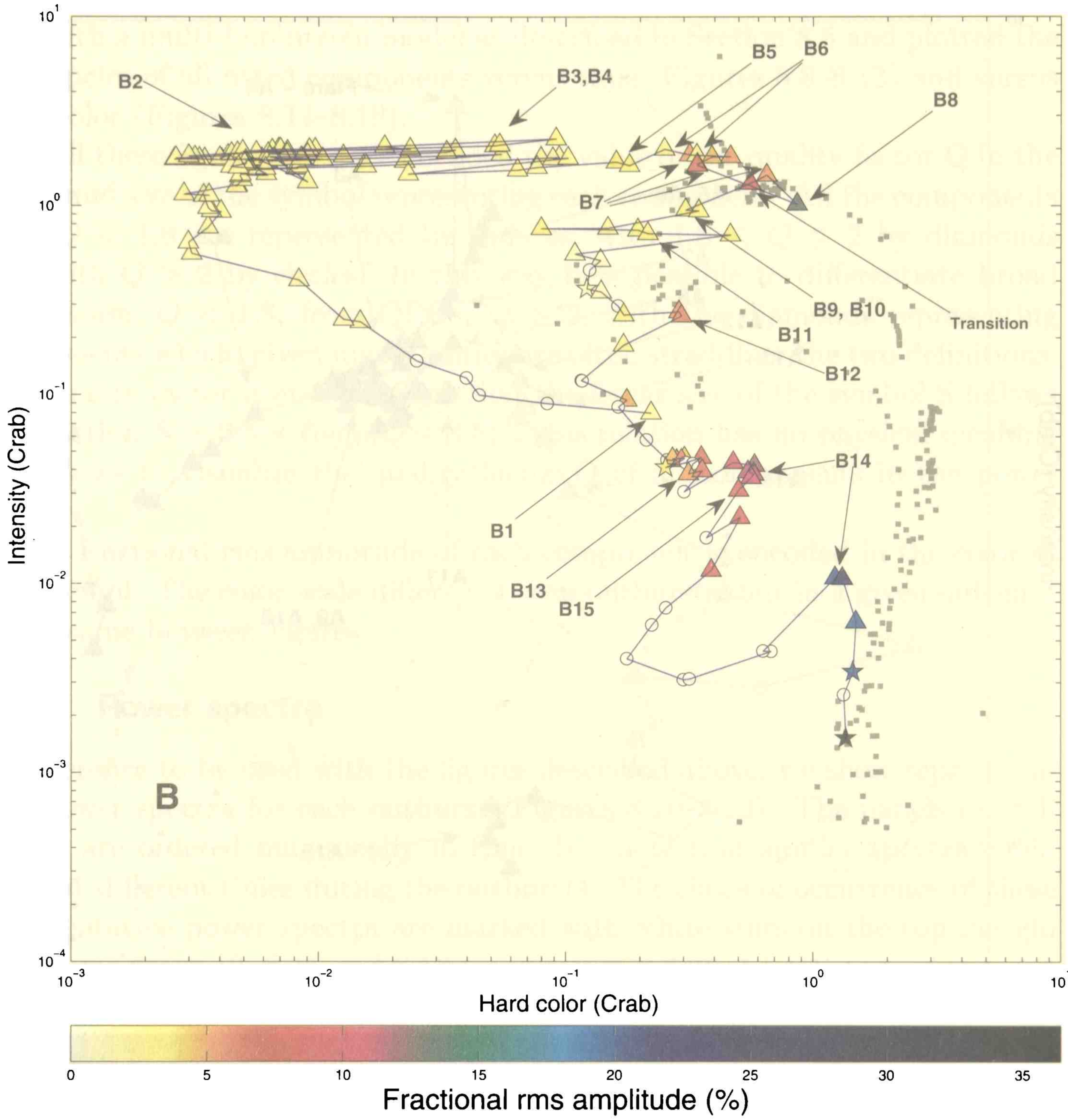

Figure 8.4: Hardness–Intensity diagram for observations during outburst B. Small grey square symbols represent the average colors during other outbursts of XTE J1550–56. Colored symbols represent the observations during this outburst. Open circles, stars and triangles were used when the integrated power in the 0.008–10 Hz range was $< 2.5\sigma$, between 2.5 and 3σ and $> 3\sigma$ significant, respectively. Color bar with the rms amplitude scale is plotted.

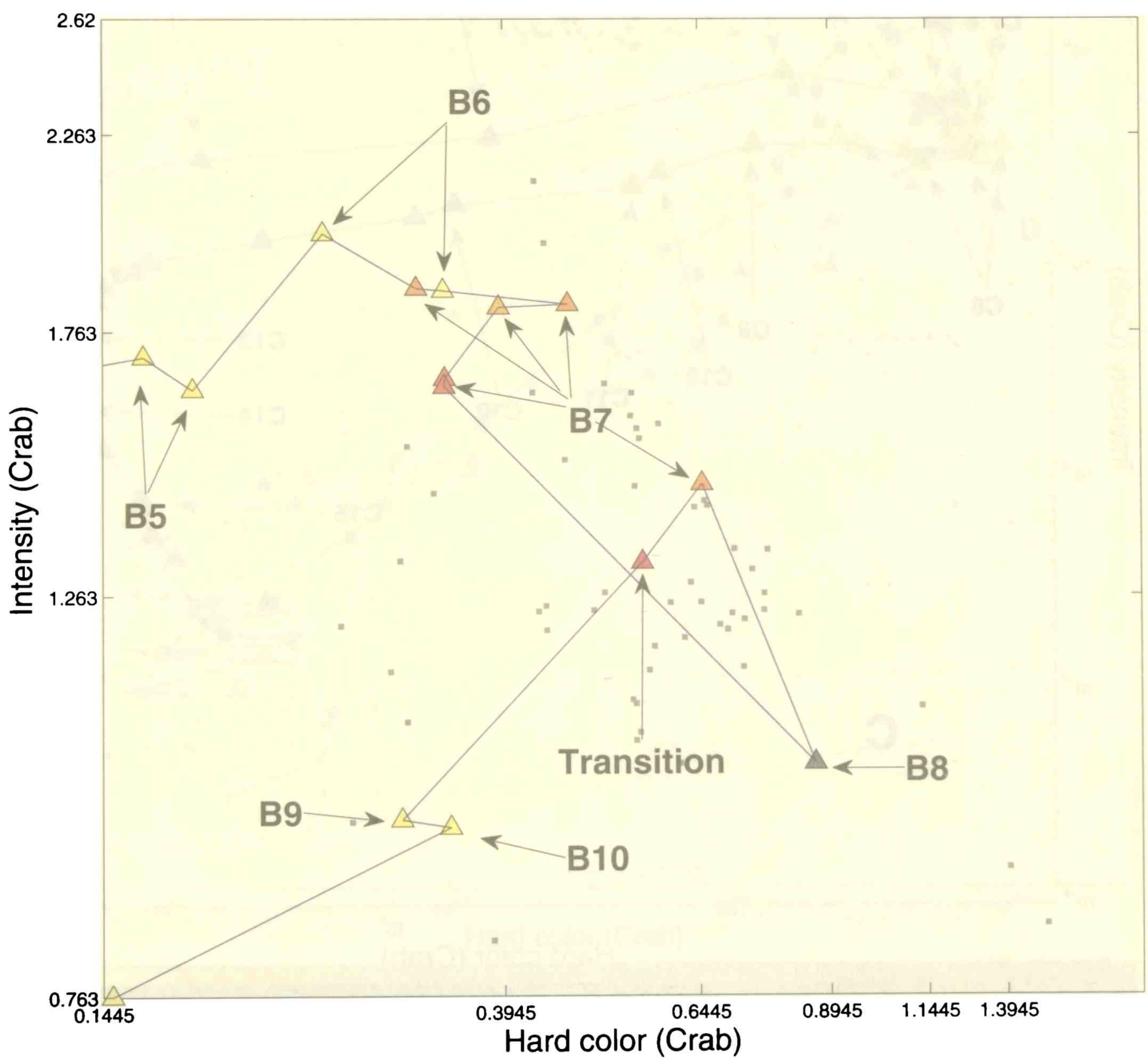

Figure 8.5: Zoom of Figure 8.4. Typically errors in the hard color and intensity are 10^{-3} and $5 \cdot 10^{-4}$ Crab.

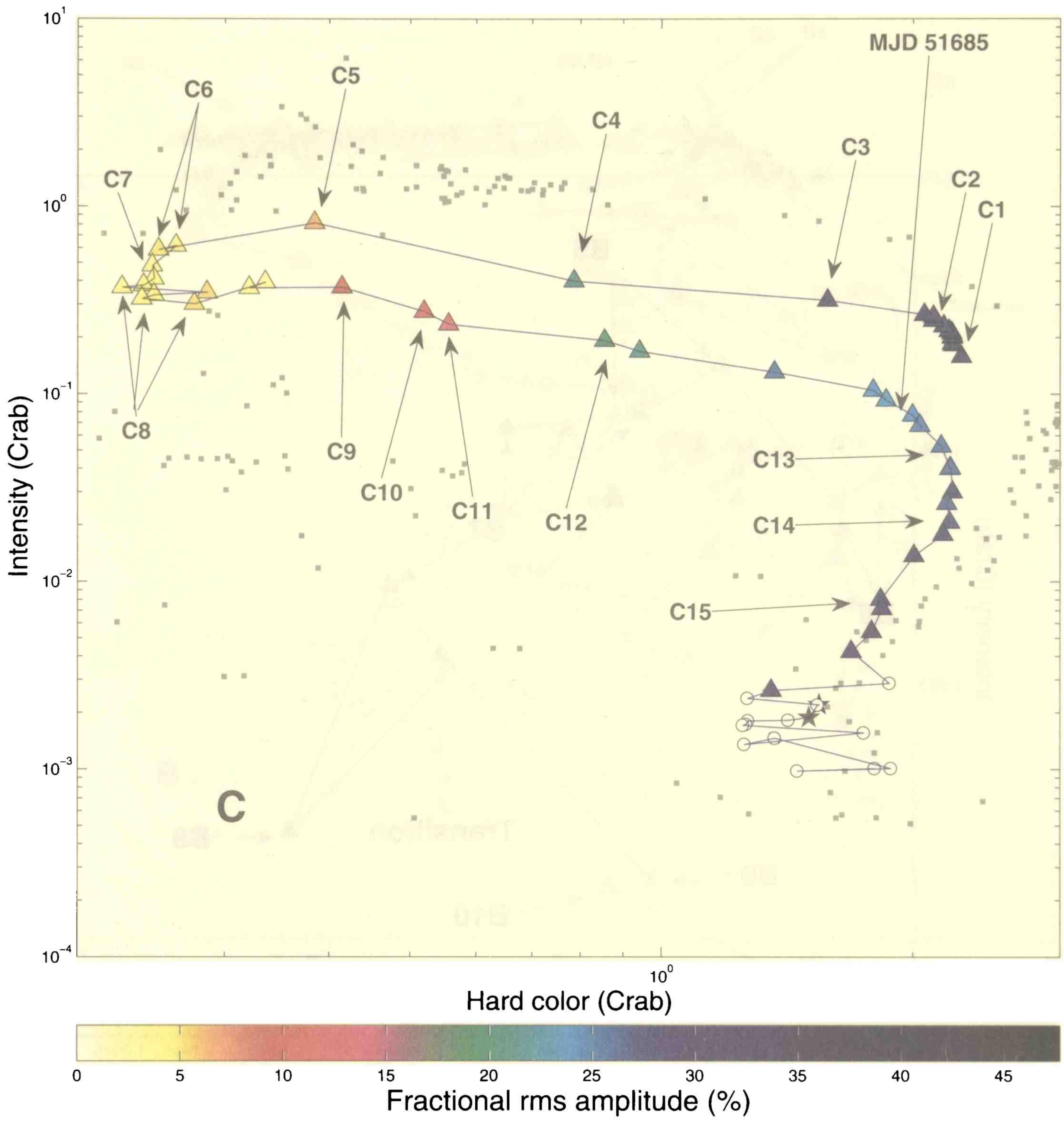

Figure 8.6: Hardness–Intensity diagram for observations during outburst C. Small grey square symbols represent the average colors during other outbursts of XTE J1550–56. Open circles, stars and triangles were used when the integrated power in the 0.008–10 Hz range was $< 2.5\sigma$, between 2.5 and 3σ and $> 3\sigma$ significant, respectively. Color bar with the rms amplitude scale is plotted.

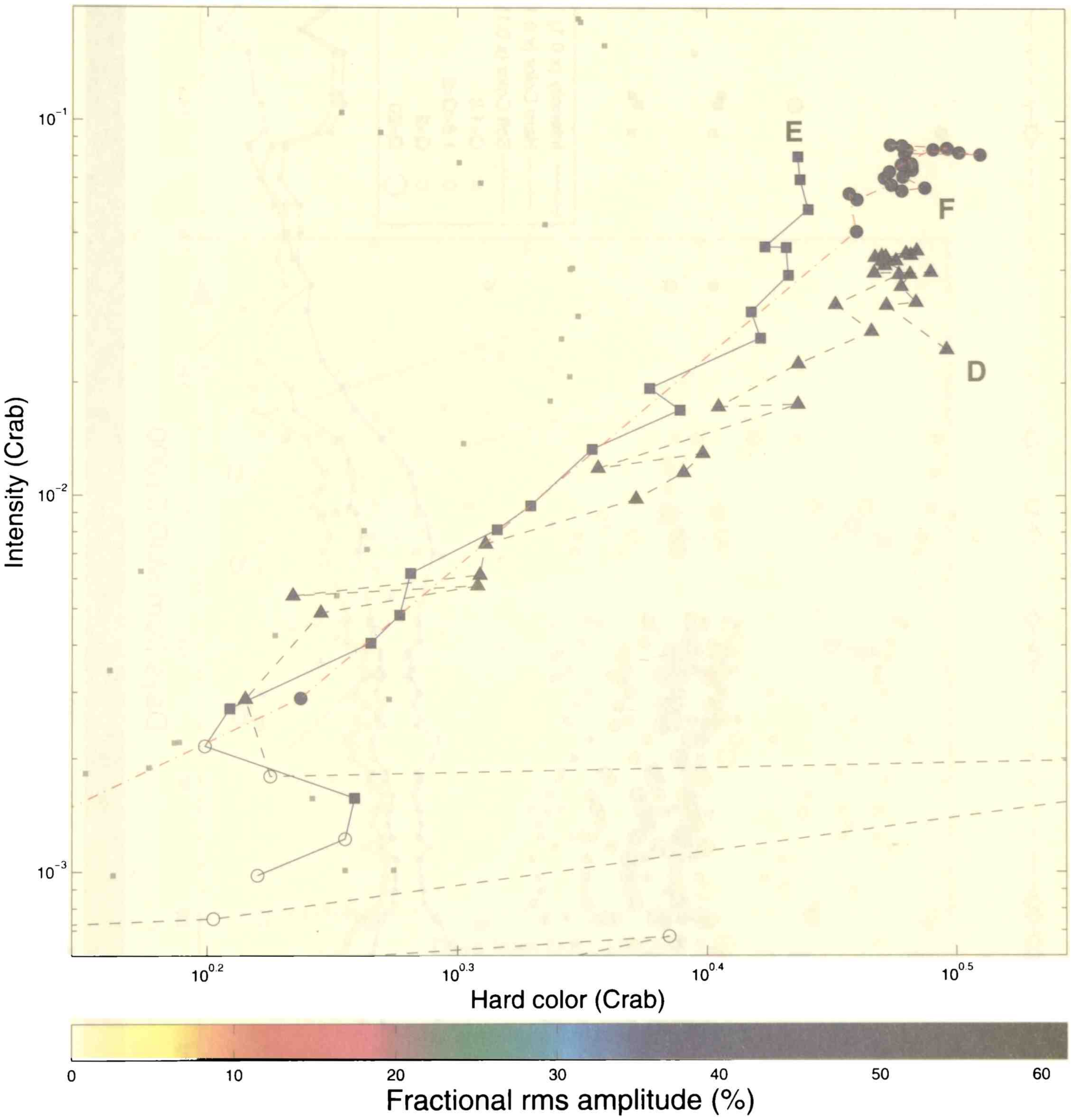

Figure 8.7: Hardness–Intensity diagram for observations during outbursts D, E and F. Small grey square symbols represent the average colors during other outbursts of XTE J1550–56. Colored symbols represent the observations during the three outbursts. Open circles, stars and triangles were used when the integrated power in the 0.008–10 Hz range was $< 2.5\sigma$, between 2.5 and 3σ and $> 3\sigma$ significant, respectively. Color bar with the rms amplitude scale is plotted.

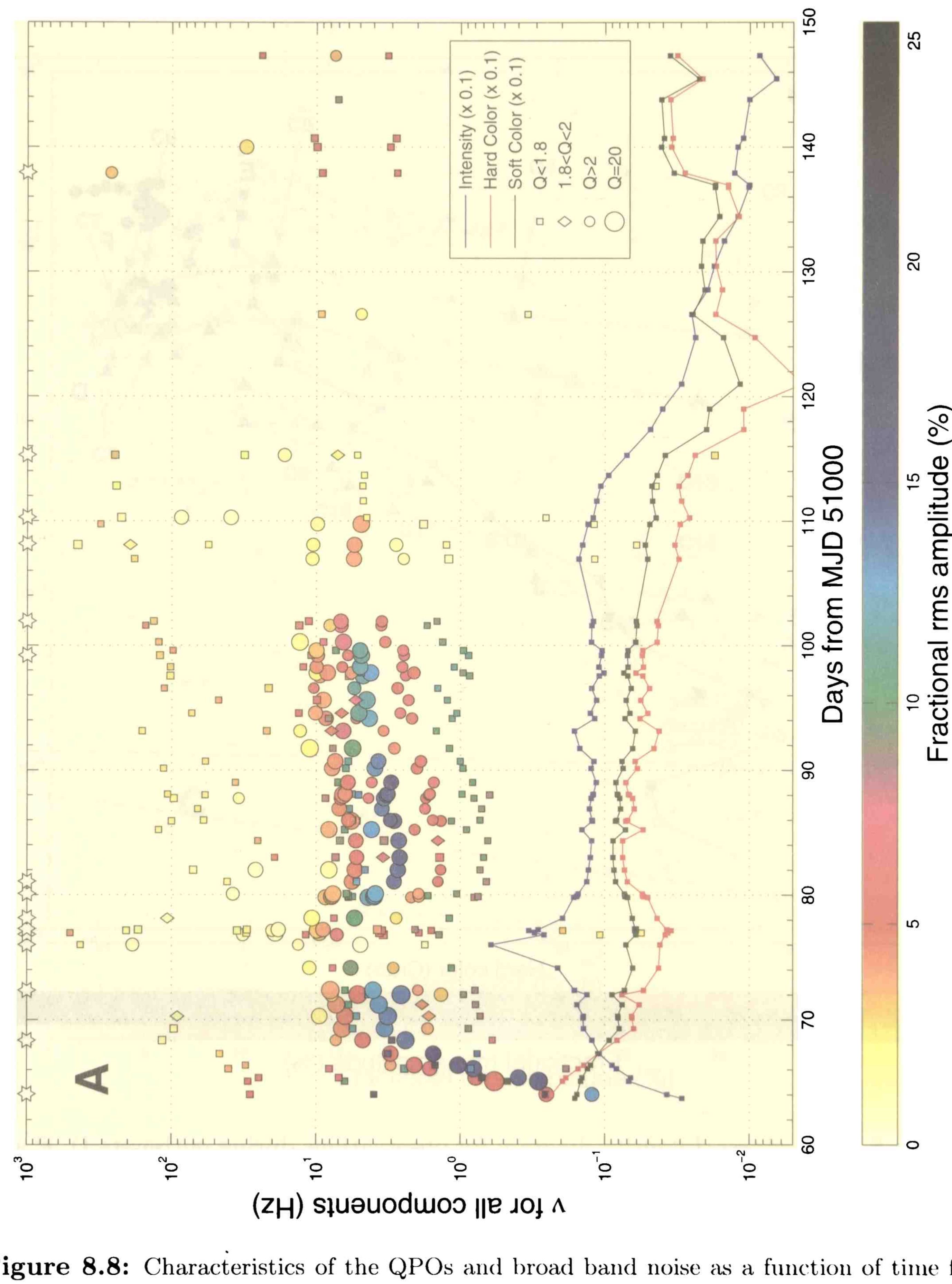

Figure 8.8: Characteristics of the QPOs and broad band noise as a function of time for outburst A. The ordinate marks the characteristic frequency of the components, the abscissa the time of the observation, the type of symbol the quality factor (see also inset) and the color of the symbol the fractional rms amplitude of the component. The color bar gives the rms amplitude. Blue, red and black lines connect the intensity, hard and soft color measurements, respectively. Note that these values have been scaled by the factor indicated in the inset. See Section 8.6 for a further description of the symbols and colors used.

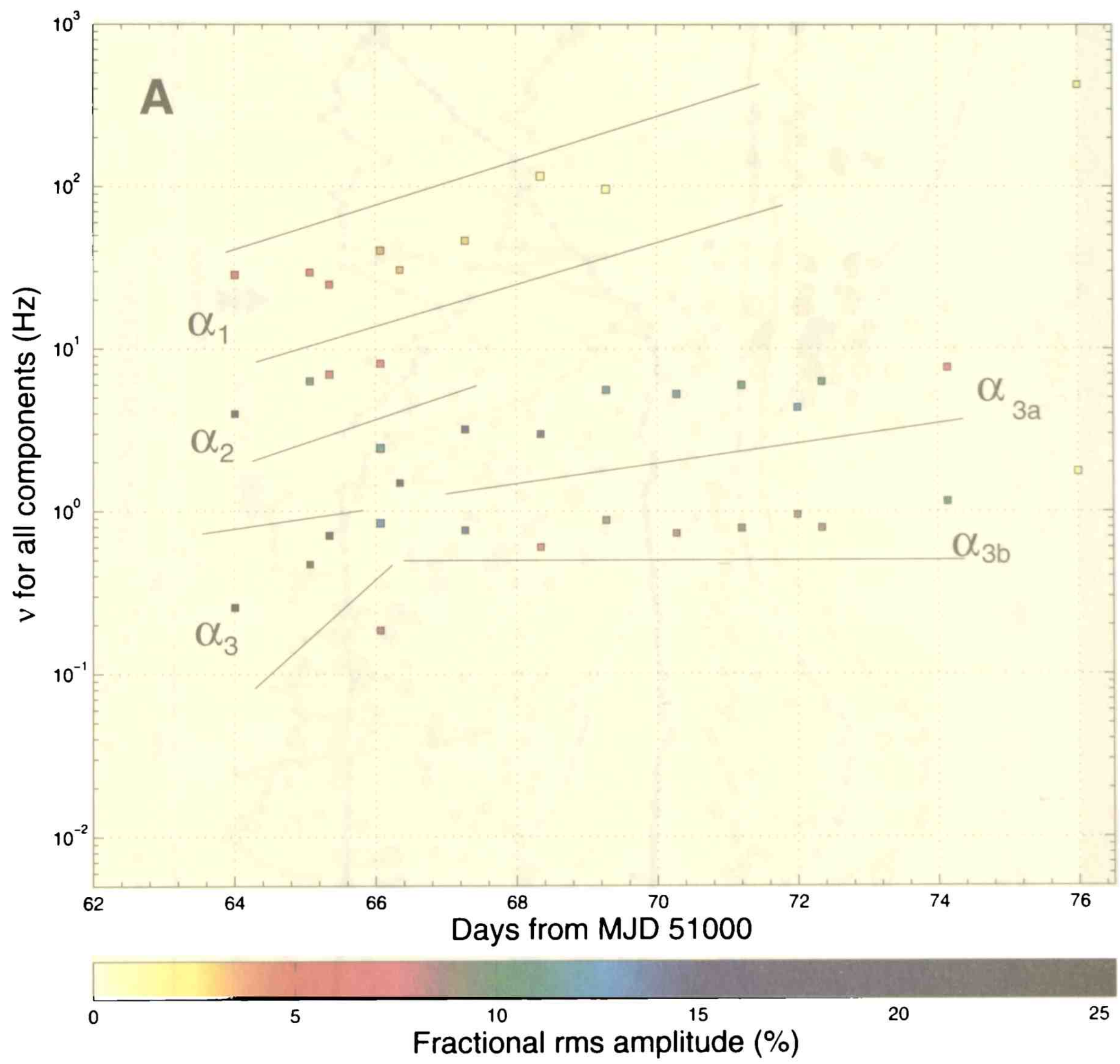

Figure 8.9: Similar to Figure 8.8, but only for the noise components in the period MJD 51062–51075.

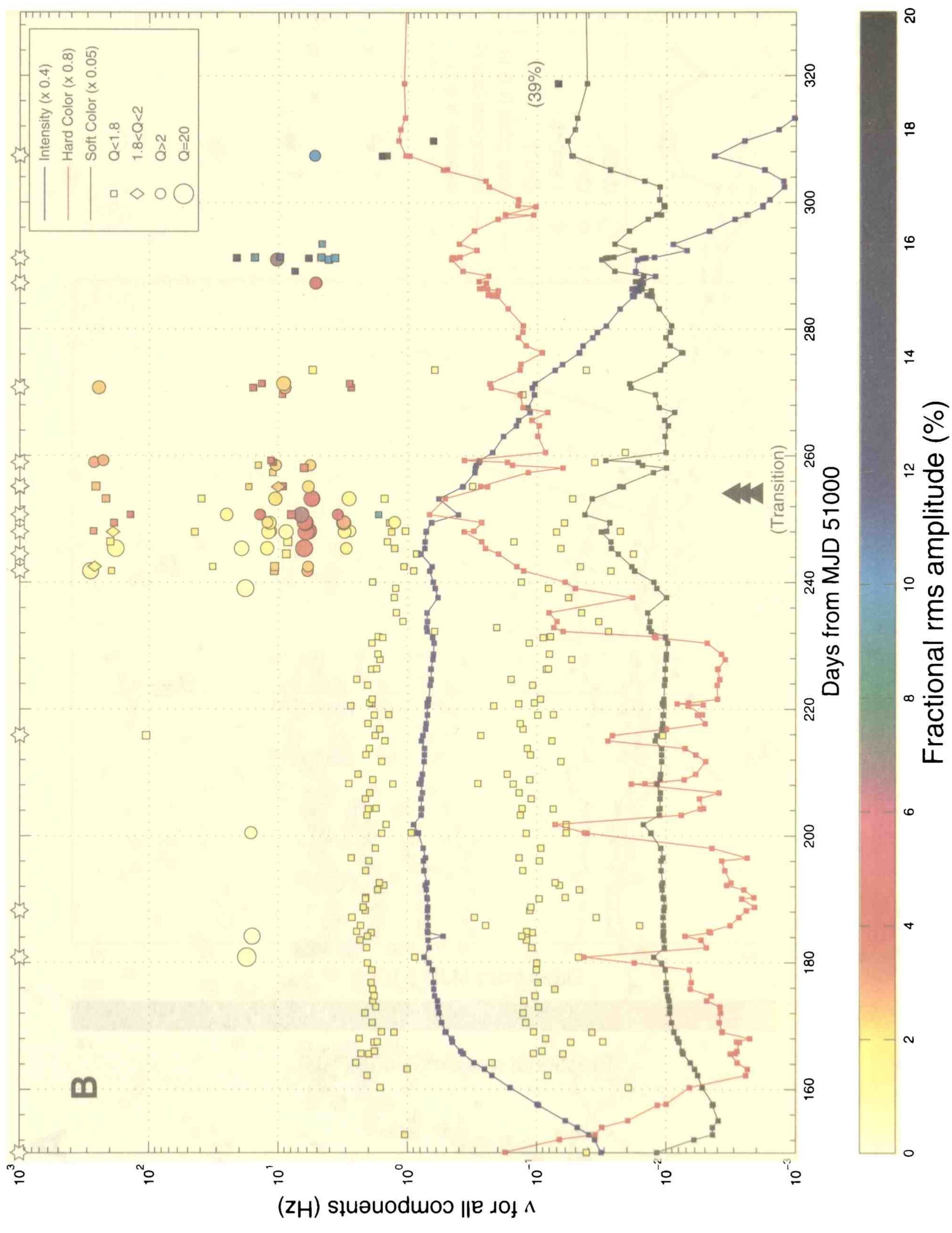

Figure 8.10: Characteristics of the QPOs and broad band noise as a function of time for outburst B. The ordinate marks the characteristic frequency of the components, the abscissa the time of the observation, the type of symbol the quality factor (see also inset) and the color of the symbol the fractional rms amplitude of the component. The color bar gives the rms amplitude for all symbols except for the square at MJD 51319.5, which has an rms amplitude of 39%. Blue, red and black lines connect the intensity, hard and soft color measurements, respectively. Note that these values have been scaled by the factor indicated in the inset. See Section 8.6 for a further description of the symbols and colors used. See Section 8.7.6 for a description on a power spectral transition that occurred at the time marked with the arrow.

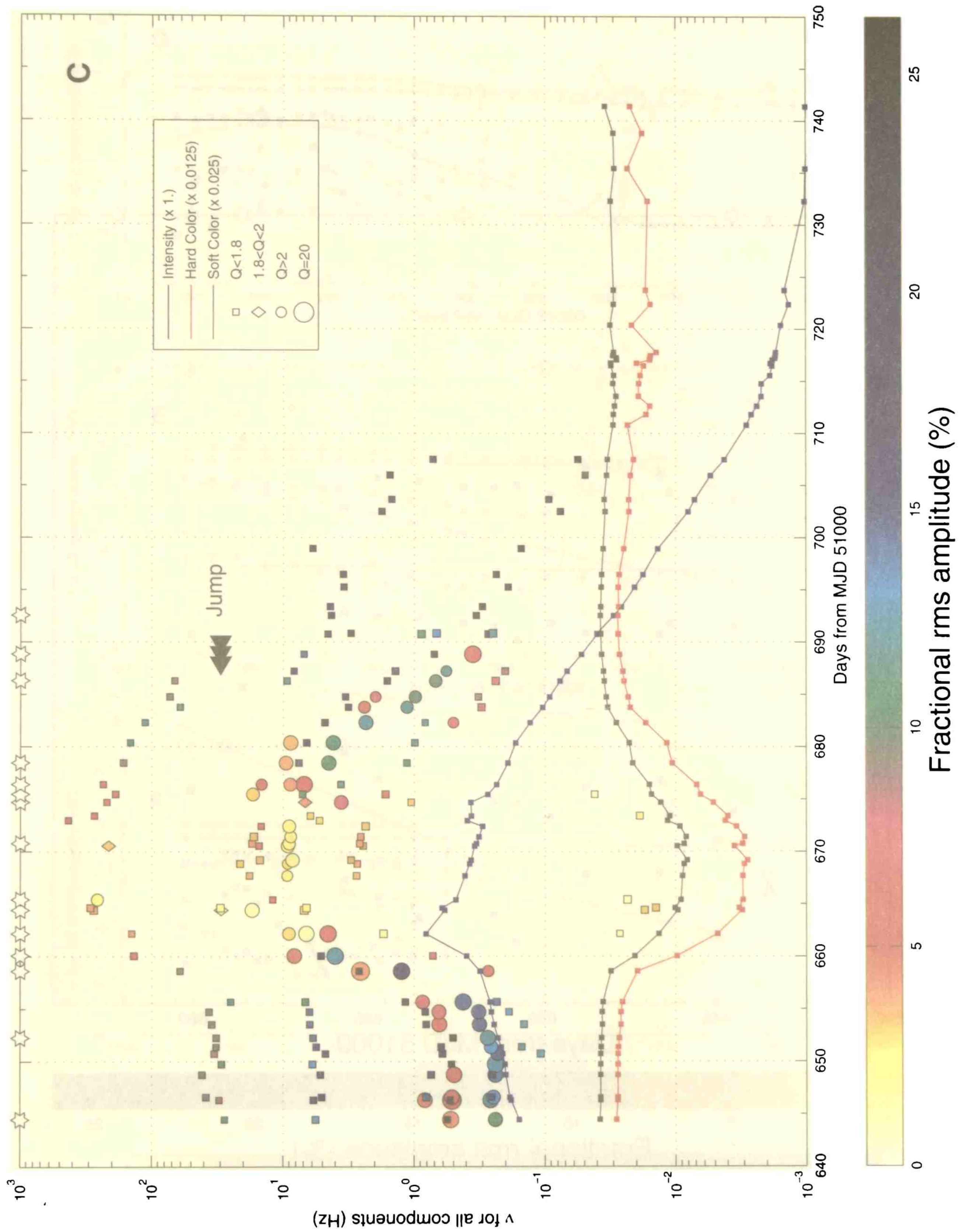

Figure 8.11: Characteristics of the QPOs and broad band noise as a function of time for outburst C. The ordinate marks the characteristic frequency of the components, the abscissa the time of the observation, the type of symbol the quality factor (see also inset) and the color of the symbol the fractional rms amplitude of the component. The color bar gives the rms amplitude. Blue, red and black lines connect the intensity, hard and soft color measurements, respectively. Note that these values have been scaled by the factor indicated in the inset. See Section 8.6 for a further description of the symbols and colors used. See Section 8.7.4 for a description on the frequency jump that occurred at the time marked with the arrow.

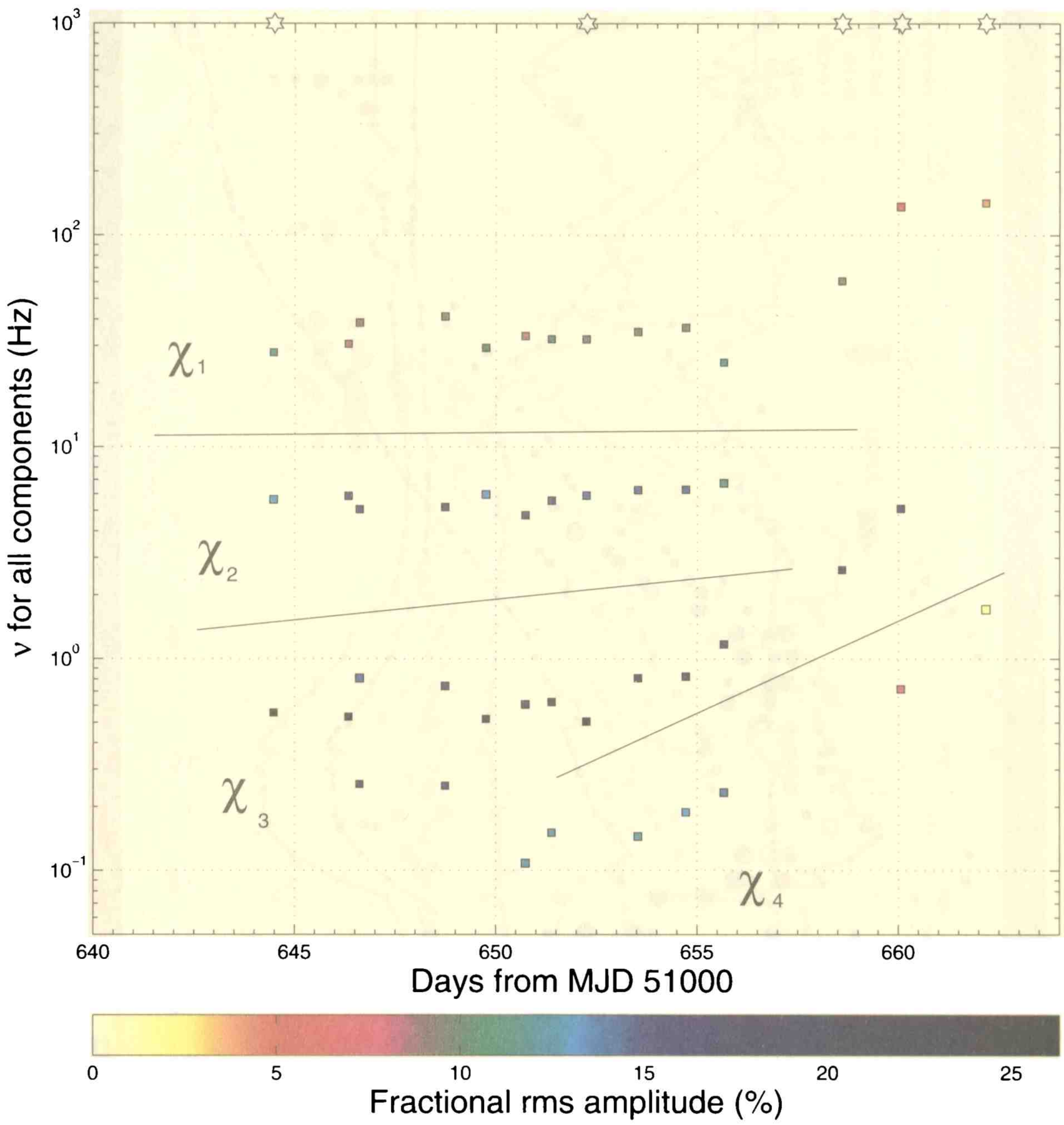

Figure 8.12: Similar to Figure 8.11, but for the period MJD 51640 51665. Note that we only plot the points for the broad components.

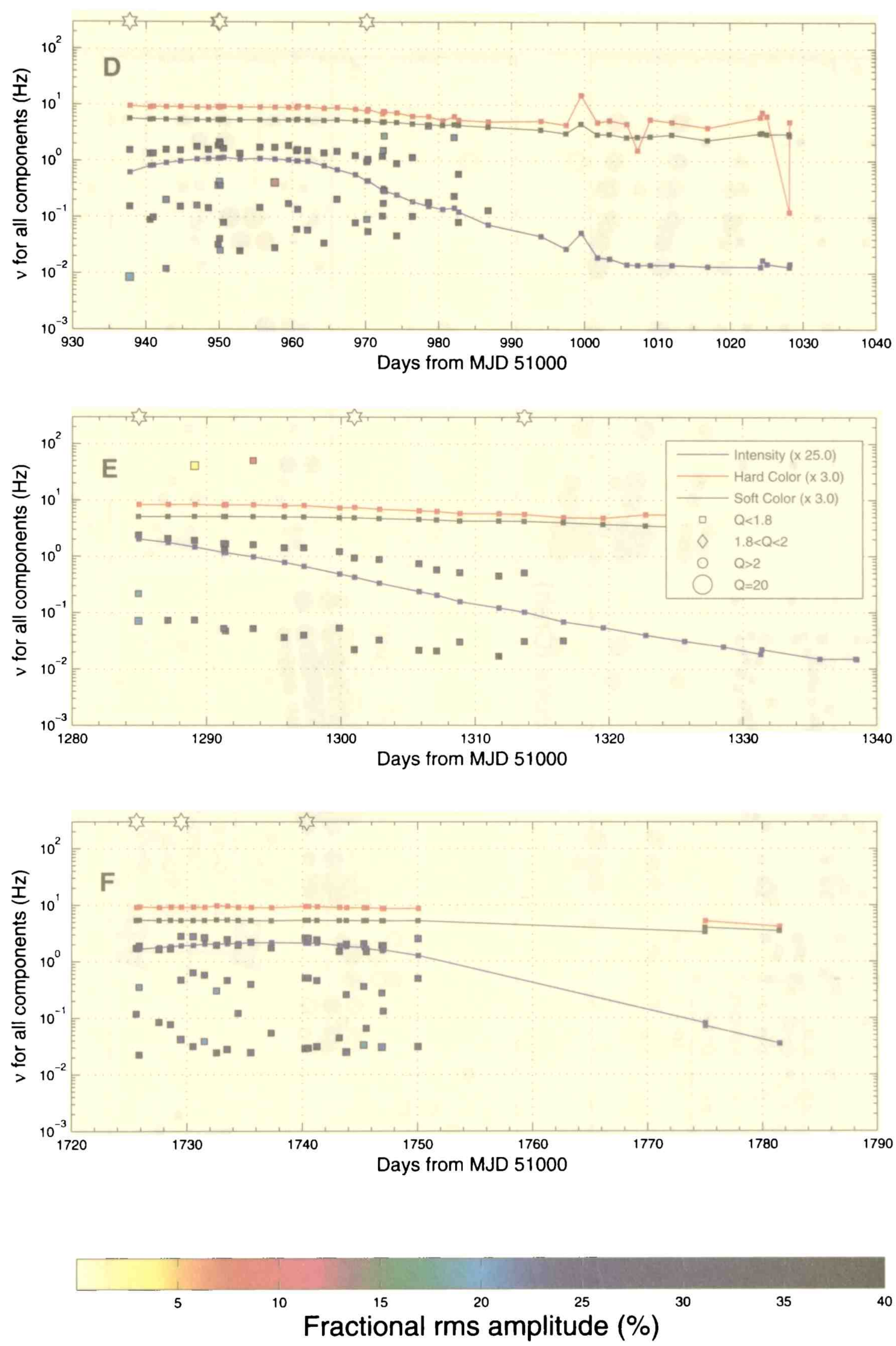

Figure 8.13: Characteristics of the QPOs and broad band noise as a function of time for outbursts D, E and F. The ordinate marks the characteristic frequency of the components, the abscissa the time of the observation, the type of symbol the quality factor (see also inset) and the color of the symbol the fractional rms amplitude of the component. The color bar gives the rms amplitude. Blue, red and black lines connect the intensity, hard and soft color measurements, respectively. Note that these values have been scaled by the factor indicated in the inset. See Section 8.6 for a further description of the symbols and colors used.

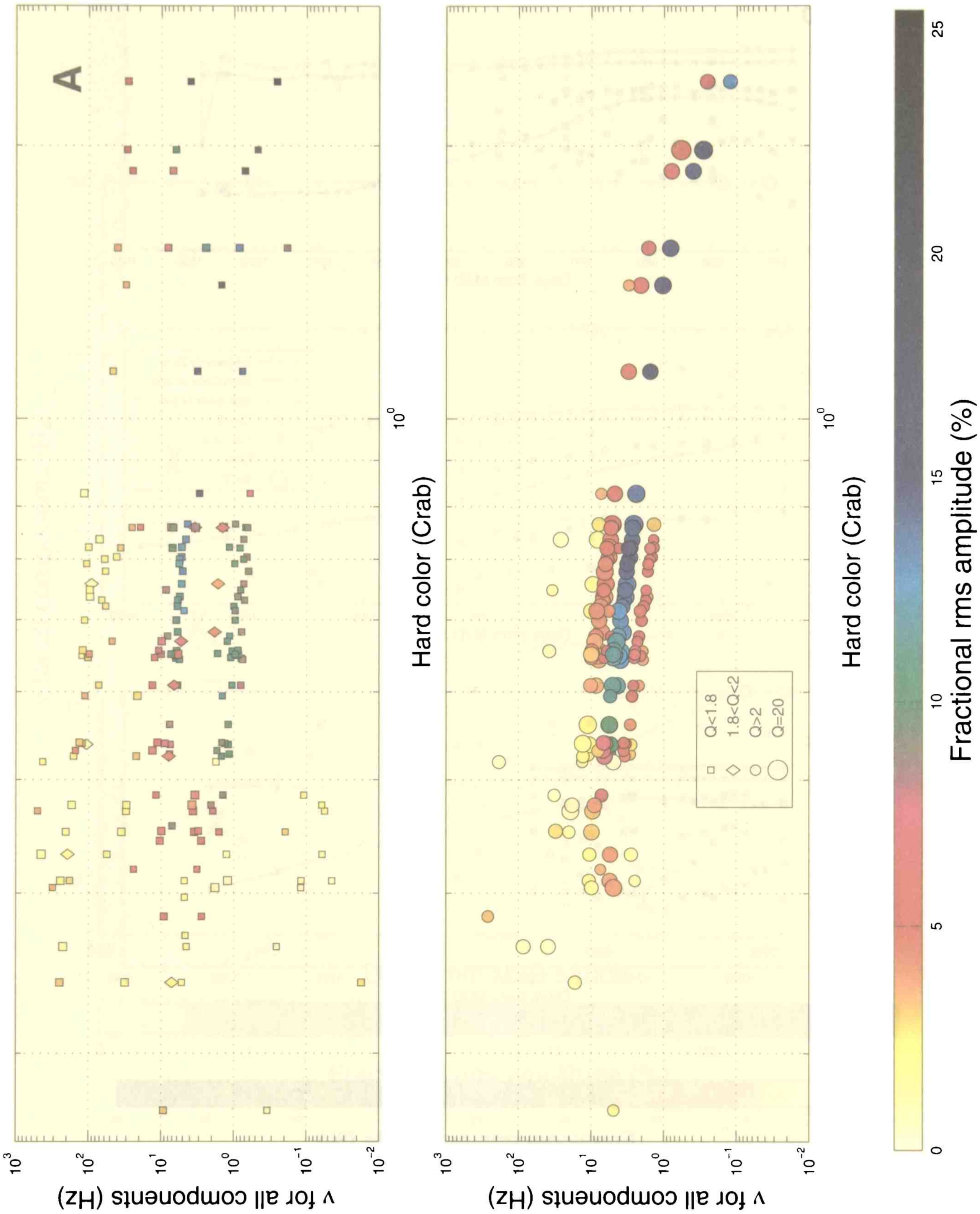

Figure 8.14: Characteristics of the QPOs (lower panel) and broad band noise (upper panel) as a function of Hard color for outburst A. Symbols are as in Figure 8.8 (see also Section 8.6).

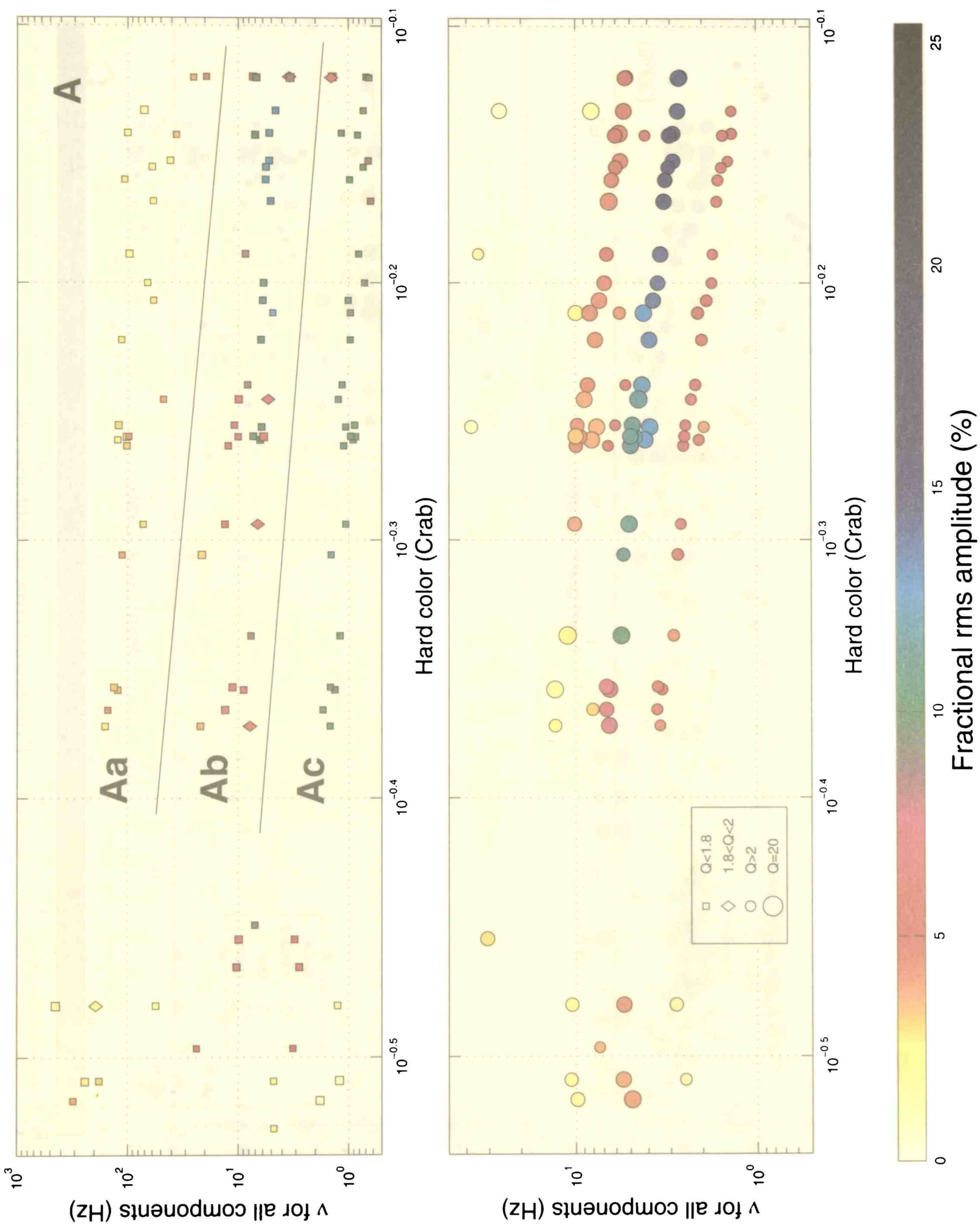

Figure 8.15: The same as Figure 8.14, but only for the time interval MJD 51080-51120

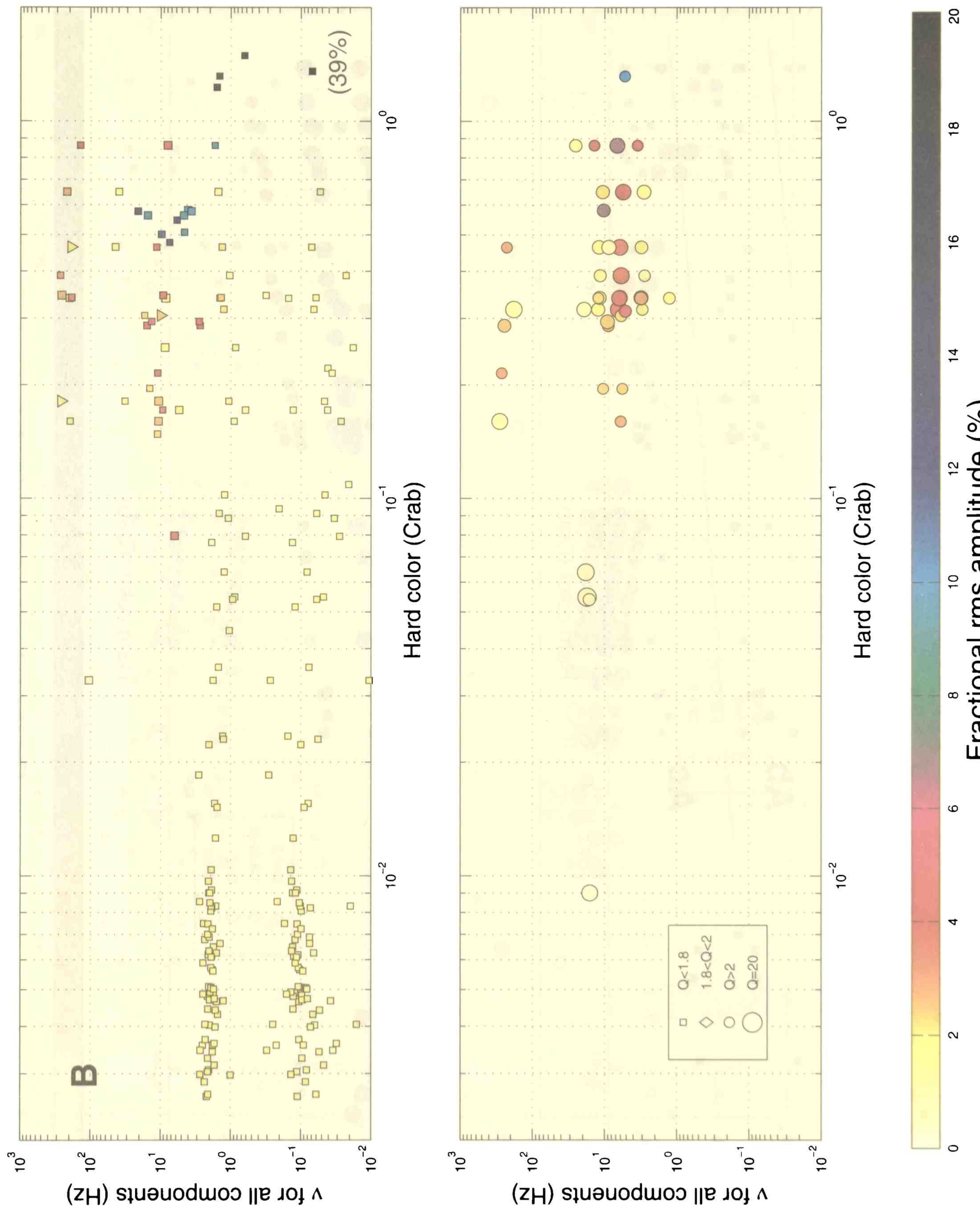

Figure 8.16: Characteristics of the QPOs (lower panel) and broad band noise (upper panel) as a function of Hard color for outburst B. Symbols are as in Figure 8.10 (see also Section 8.6).

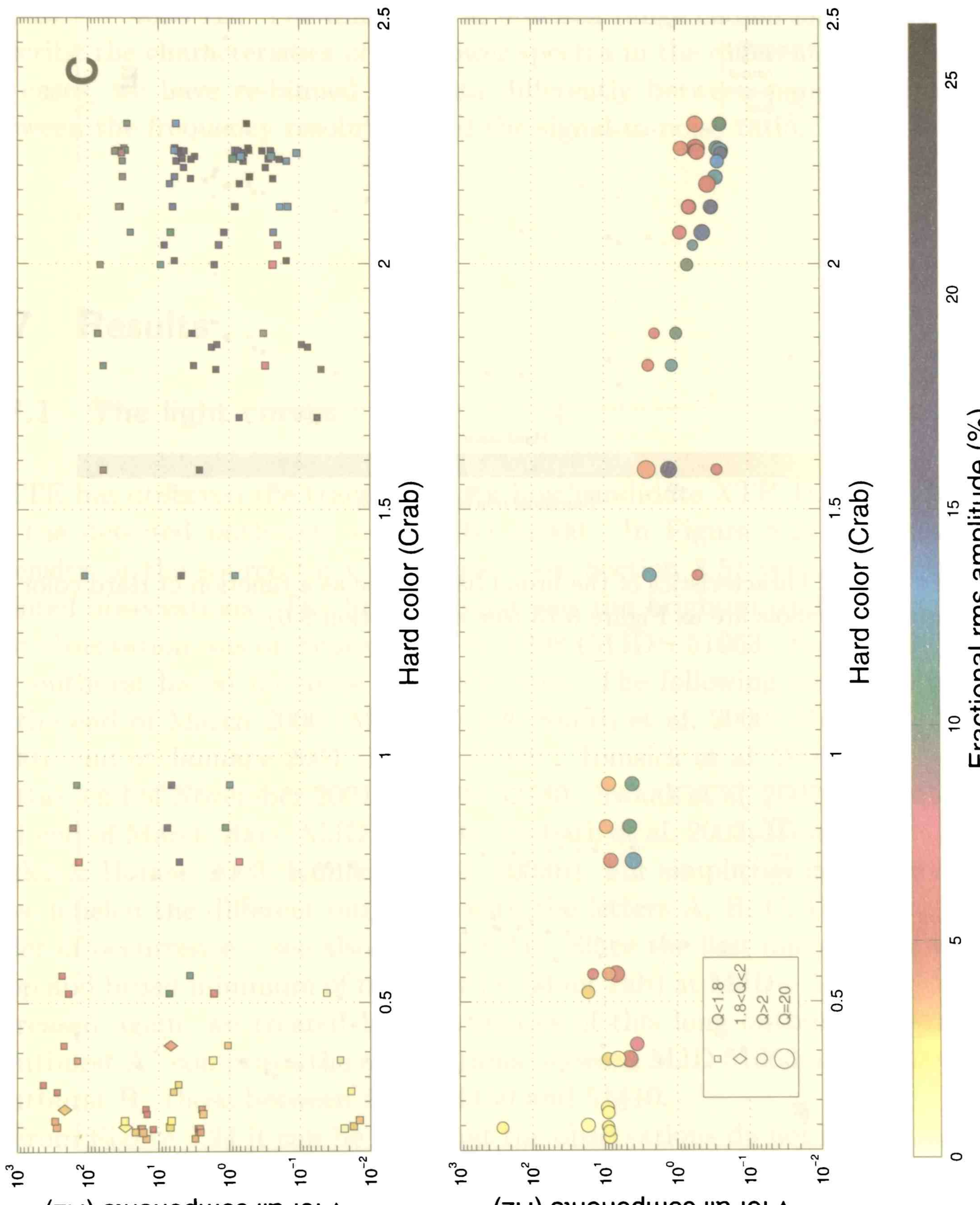

Figure 8.17: Characteristics of the QPOs (lower panel) and broad band noise (upper panel) as a function of Hard color for outburst C. Symbols are as in Figure 8.11 (see also Section 8.6).

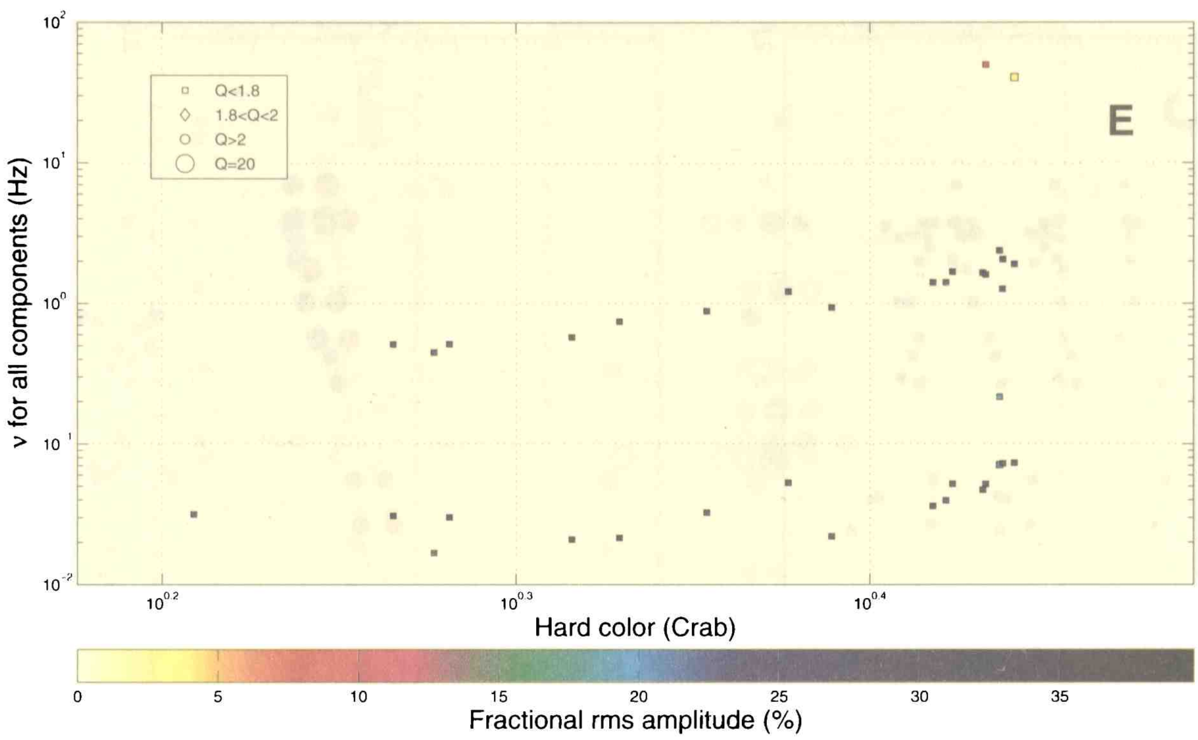

Figure 8.18: Characteristics of the broad band noise as a function of Hard color for outburst E. Symbols are as Figure 8.13 (see also Section 8.6).

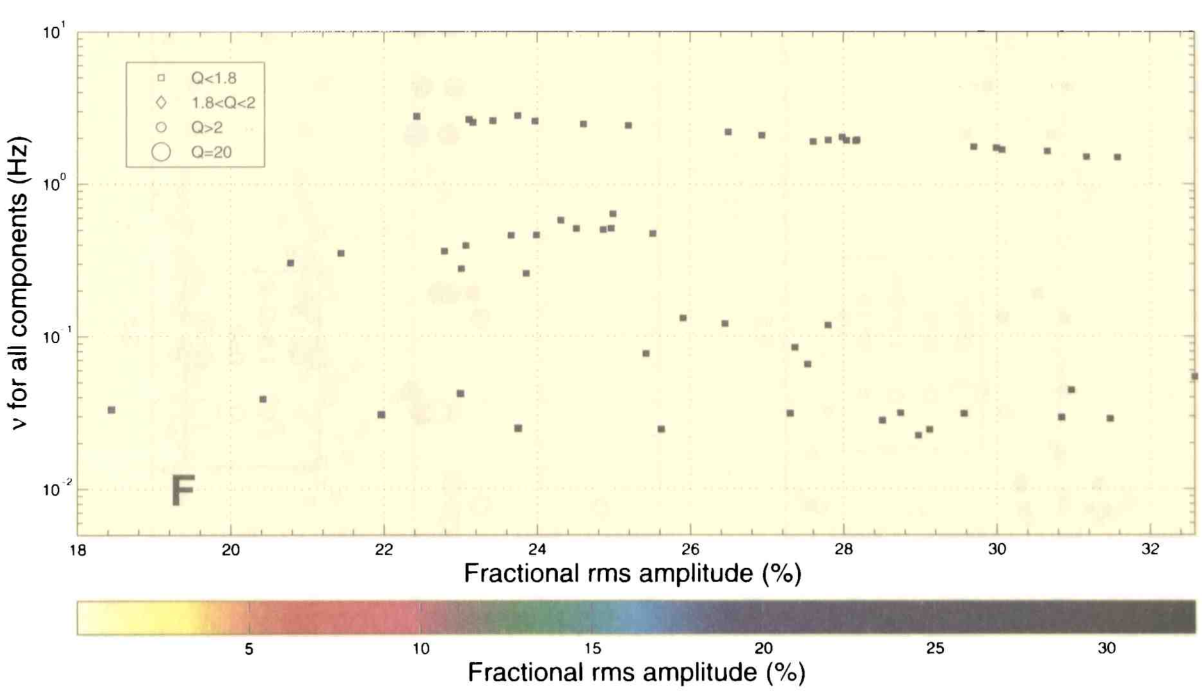

Figure 8.19: Characteristics of the broad band noise measured during outburst F, as a function of the component's fractional rms amplitude. Symbols are as in Figure 8.13 (see also Section 8.6).

In the same figures, the abscissa is in units of Hz and for outbursts A, B and C is in the $3 \times 10^{-3} - 4096$ Hz range, while for outbursts D, E and F is in the $3 \times 10^{-4} - 4096$ Hz. The difference in abscissa range chosen allows to better describe the characteristics of the power spectra in the different outbursts. In all cases, we have re-binned the data differently between panels to balance between the frequency resolution and the signal-to-noise ratio.

8.7 Results

8.7.1 The light curves

RXTE has observed the transient black hole candidate XTE J1550–56 during all the detected outbursts since MJD 51000. In Figure 8.24 we show the intensity of the source (in Crab units – see Section 8.5) versus time for all pointed observations. The first outburst was the brightest and longest. The first observation was on September 7th, 1998 (MJD$\simeq$ 51063, Smith 1998) and the outburst lasted for more than 260 days. The following outbursts began at the end of March 2000 (MJD$\simeq$ 51630 Smith et al. 2000; Masetti & Soria 2000), end of January 2001 (MJD$\simeq$ 51930, Tomsick et al. 2001b; Jain et al. 2001a), end of November 2001 (MJD$\simeq$ 52240, Swank et al. 2002; Bailyn 2002) and end of March 2003 (MJD$\simeq$ 52720, Dubath et al. 2003; Woudt et al. 2003; Miller & Homan 2003; Kuulkers et al. 2003b). For simplicity, in this work we have labeled the different outbursts with the letters A, B, C, D, E and F (in order of occurrence – see also Figure 8.24). Since the first outburst showed a deep and broad minimum of intensity ($\sim$ 60 mCrab) at MJD$\sim$ 51150 and then increased again, we treated the two phases of this long outburst separately. "Outburst A" comprises the observations between MJD 51063 and 51150, and "outburst B" those between MJD 51150 and 51410.

From Figure 8.24 it can be seen that the observations do not always sample the whole outburst, but usually cover the last part of the rise and most of the decay. In Figure 8.25 we plot the ASM light curve (drawn lines) and the average intensity per PCA observation (symbols) in units chosen to approximately match the ASM countrates. Although the ASM and PCA light curves generally match well, sometimes there are clear differences. For example, the flare at MJD 51075 during outburst A is larger in the PCA than in the ASM, indicating that the flare was stronger at higher energies (Remillard et al. 1998), where the PCA (2–60 keV) is more sensitive than the ASM (1.5–12 keV).

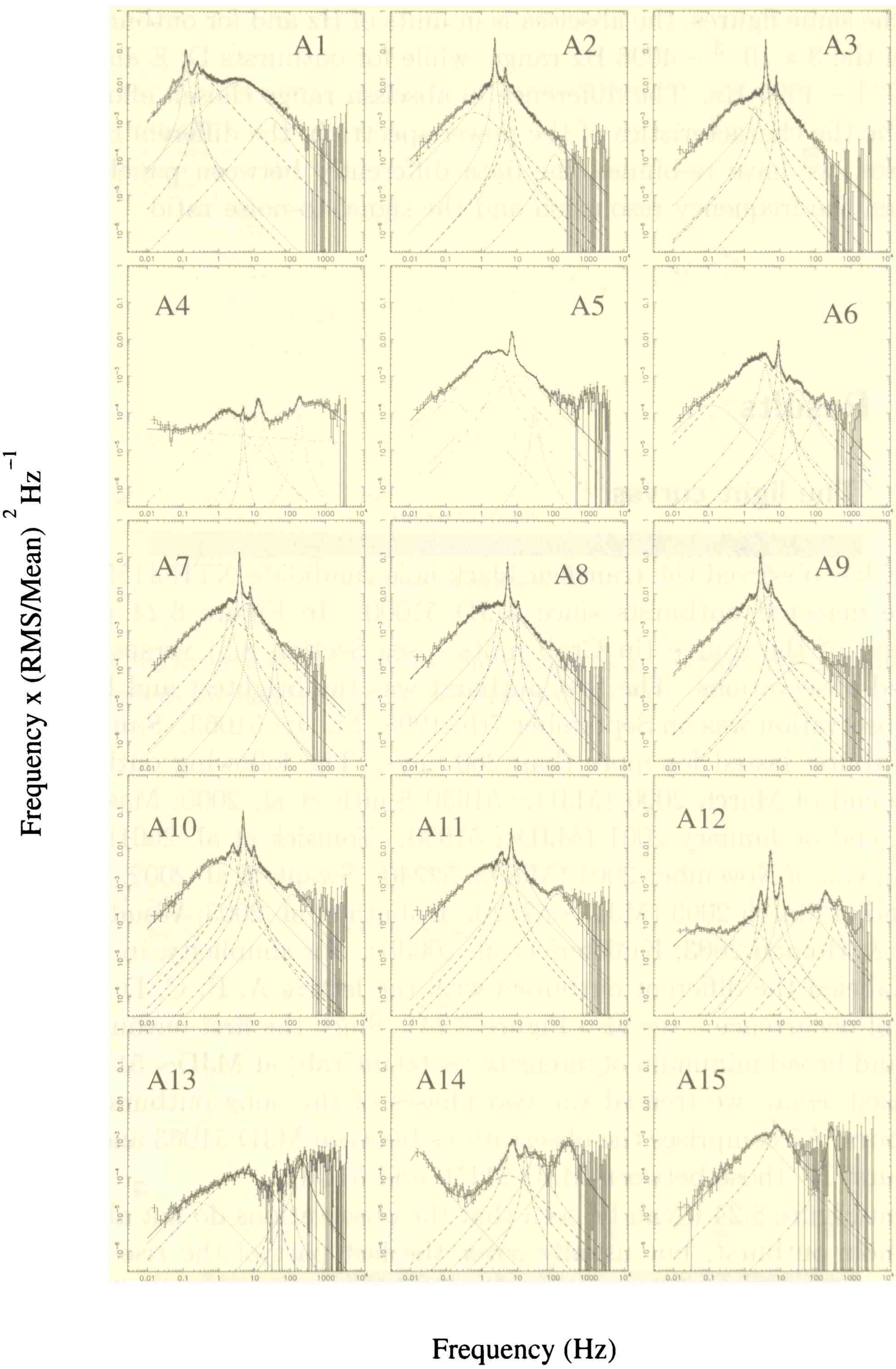

Figure 8.20: Representative power spectra for outburst A. See Section 8.6 for further description of this Figure. The time of each power spectrum is marked with a white star at the top Figure 8.8. The re-binning varies between the panels to balance the frequency resolution with the signal-to-noise ratio.

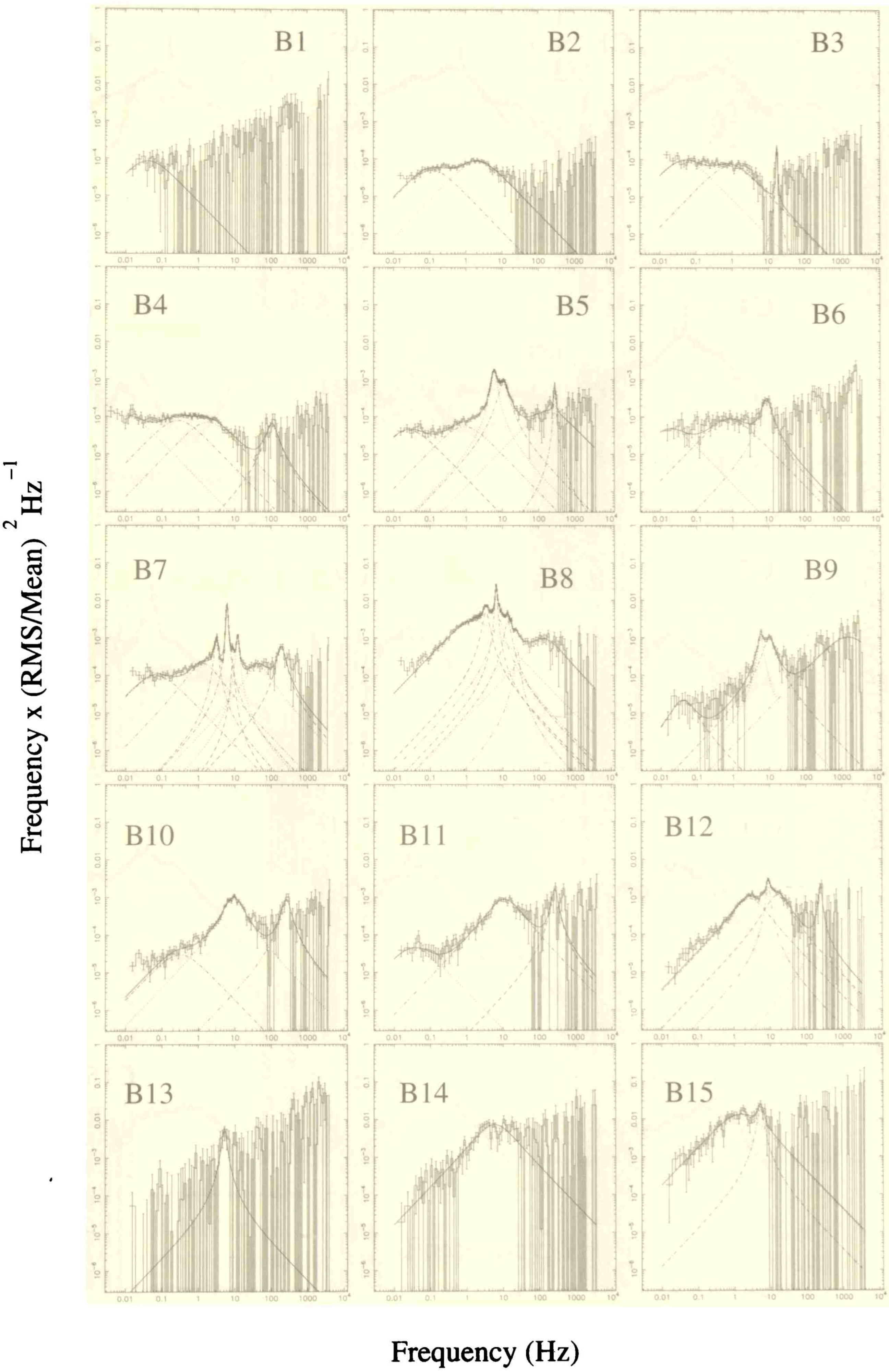

Figure 8.21: Representative power spectra for outburst B. See Section 8.6 for further description of this Figure. The time of each power spectrum is marked with a white star at the top Figure 8.10. The re-binning varies between the panels to balance the frequency resolution with the signal-to-noise ratio.

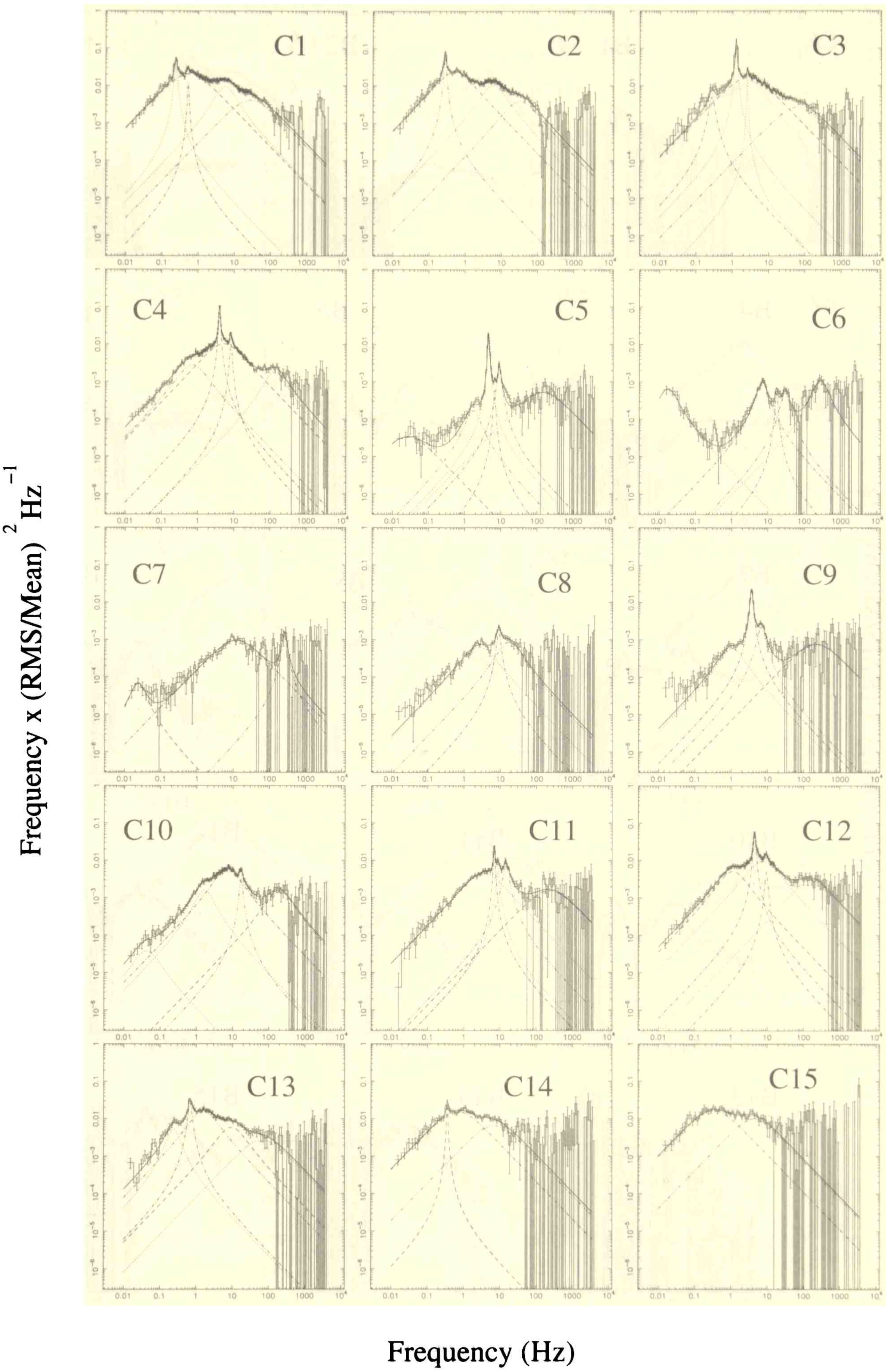

Figure 8.22: Representative power spectra for outburst C. See Section 8.6 for further description of this Figure. The time of each power spectrum is marked with a white star at the top Figure 8.11. The re-binning varies between the panels to balance the frequency resolution with the signal-to-noise ratio.

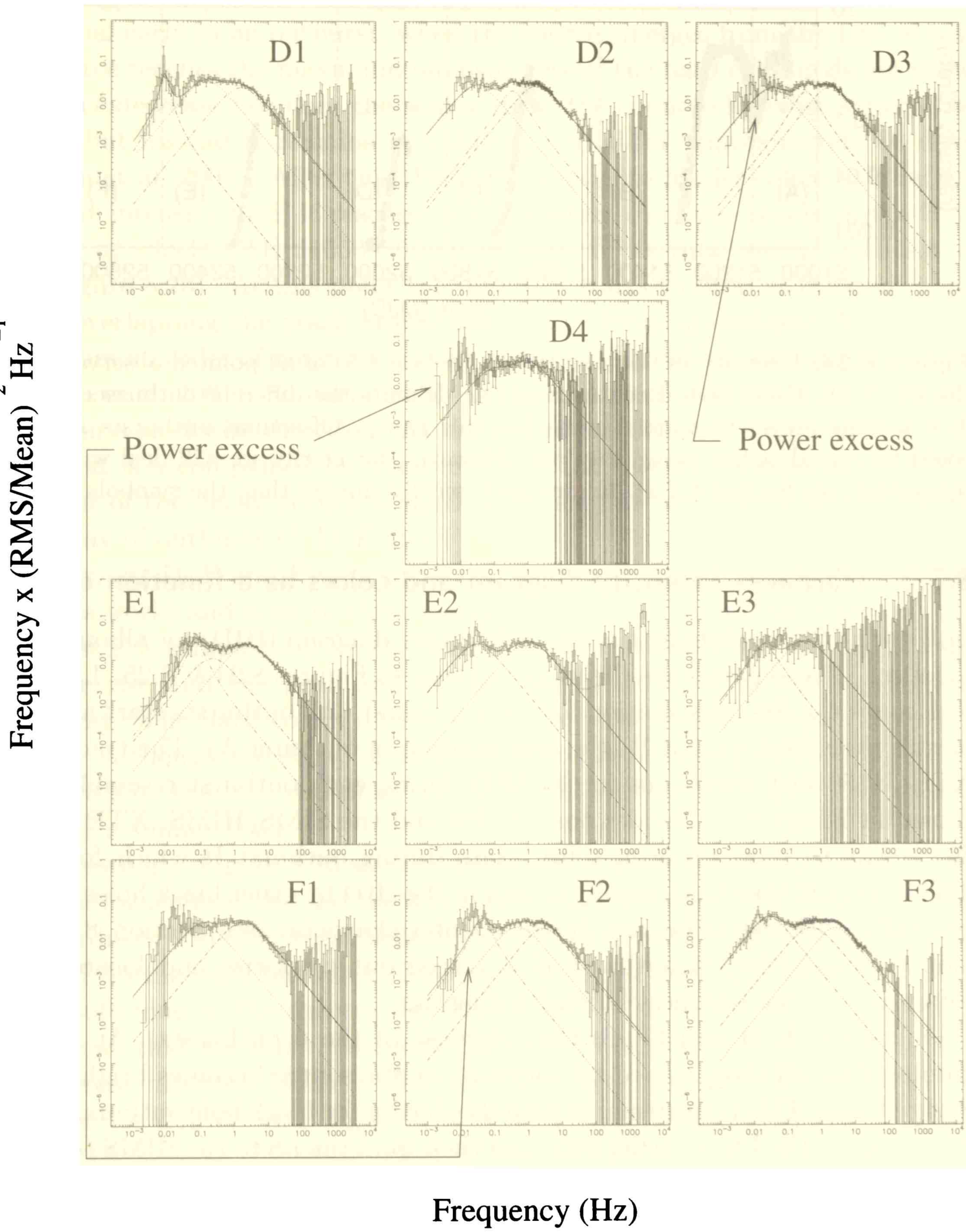

Figure 8.23: Representative power spectra for outbursts D (D1-D4), E (E1-E3) and F (F1-F3). See Section 8.6 for further description of this Figure. The time of each power spectrum is marked with a white star at the top Figure 8.13. The re-binning varies between the panels to balance the frequency resolution with the signal-to-noise ratio.

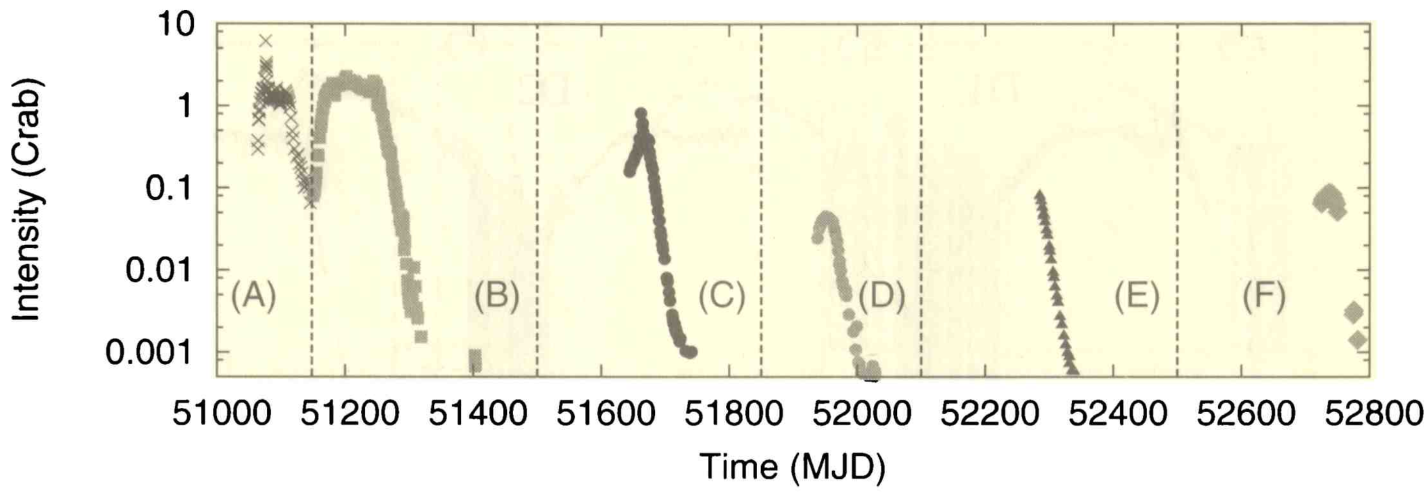

Figure 8.24: Intensity in Crab units (see Section 8.5) of all pointed observations of the BH XTE J1550–564. Each vertical line delimits the different outbursts (named A–F in time order) that are discussed in this paper. Of course, outbursts A and B could be considered as being only one. However, for clarity we will deal with them separately (see Section 8.7.1). Errors are typically smaller than the symbols.

8.7.2 Hardness–intensity diagram and colors as a function of time

In Figure 8.26 we plot the Hardness–Intensity diagram (HID) for all outbursts together. The symbols are the same as those in Figures 8.24 & 8.25. Labels A to F mark the first observation for each outburst. All outbursts start at colors harder than Crab except B (the continuation of outburst A). The tracks that XTE J1550–564 traces out in the HID during each outburst resemble those shown in Figure 8.1. Besides the LS, HS and the SIMS/HIMS, XTE J1550–564 seems to show an even softer state during outburst B which follows a different track than that usually drawn in the HID by other black holes. While generally outburst loops are drawn counter-clockwise (see Section 8.2), the loop corresponding to outburst B is traced out clockwise and located in a softer area of the hardness–intensity diagram.

Outbursts A, B and C are the brightest of the 6 outbursts. At the beginning they all show a spectral softening as the source becomes brighter (see Figure 8.26). This is the usual observed behavior for black hole outbursts when they move in the LS to higher flux, and then from the LS to the HIMS (see Section 8.2 and references within). Their further time evolution differs. Outburst C smoothly traces the square–like HID pattern in a counterclockwise direction following the LS→IMS→HS→IMS→LS sequence as expected for a typical BH outburst (see Section 8.2). Although outburst A draws a similar pattern, its intensity decay was interrupted at a level of $\sim 7 \times 10^{-2}$ Crab by outburst B and did not reach the LS. Probably because outburst B is the continuation of outburst A, we find that the evolution of outburst B is entirely different from that of A (see also Homan et al. 2001; Remillard et al. 2002a). At the beginning of outburst B, the intensity increases as the hardness decreases (as it is usual early in an outburst, when the source emerges from the LS). When the source reaches the maximum intensity levels, the hard color does not show a further decrease nor does the source draw the counterclockwise square-like shape, but instead it remains in a flaring period for approximately 80 days (Homan et al. 2001). After this the source moves to harder colors at a rather constant intensity until it reaches approximately the same region in the HID as that in which XTE J1550–564 spent most of its time during outburst A (see Figure 8.26). At this point the intensity starts to drop at constant hard color, overlapping the track drawn during the decay of outburst A, down to intensities an order of magnitude lower than those at which outburst B started (Homan et al. 2001). So outburst B, as the continuation of outburst A, traces a loop in a clockwise direction. At the end of the decay, it shows an intensity flare that is accompanied by a hardening of the spectra (Homan et al. 2001). The rest of the decay occurs at hard colors similar to those measured during the decay of outburst C, D, E and F.

Outbursts D, E and F were hard and weak outbursts (Belloni et al. 2002a, and this work) and none of them reached hard colors lower than Crab. While outburst E is sampled during the decay, outburst D and F are sampled during the late rise and the peak and in the case of outburst D, during most of the decay. The hard colors during the decay of outbursts D and E are very similar. Although the decay of outburst F was barely sampled by RXTE (see Figure 8.25), the last two observations of this outburst suggest that it also followed a similar track.

Interestingly, Figure 8.26 shows that for all outbursts (if we consider A and B as one) when near the end the flux drops below several 0.001 Crab, the spectral hardness is similar regardless of the duration and the maximum intensity reached during each outburst. Moreover, near the end all outbursts show a slight softening of the spectra (see also Figures 8.4, 8.6 & 8.7). Figure 8.26 also shows that the main hard–soft (LS–HS) transitions and vice versa occur at different intensity levels in different outbursts. Consistent with what was reported for GX 339–4, a higher flux in the LS–HS transition predicts a lower one for the reverse transition (Belloni et al. 2006).

In order to allow to follow the time evolution of the intensity and colors in correlation to the power spectral evolution, in Figures 8.8, 8.10, 8.11 & 8.13 we plot the average intensity (blue), the average hard (red) and the average soft (black) color versus time. For clarity, we have scaled the intensity and the colors (in Crab units) differently for each figure. The multiplicative factors are reported in the figures. Similar figures using PCA data can be found in Cui et al. (1999) for the first part of outburst A and in Homan et al. (2001)

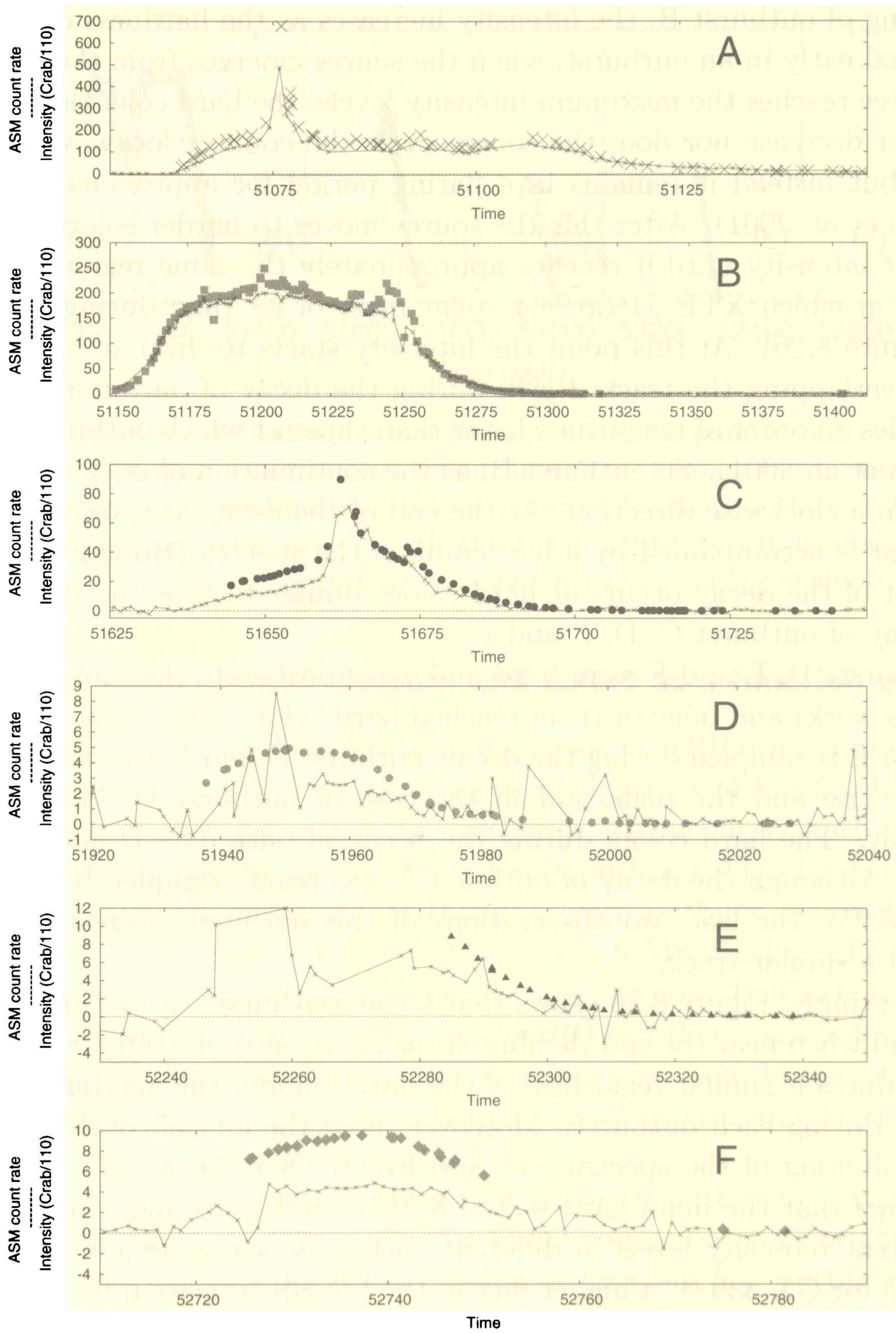

Figure 8.25: ASM light curve (crosses connected by lines, no errors plotted) of each outburst of the BH XTE J1550–564 separately. Also plotted is the averaged intensity in Crab units per PCA observation (symbols are the same as Figure 8.24; errors are typically smaller than the symbols) in units chosen to approximately match the ASM countrates. Although the ASM light curve generally matches the intensity as seen from the PCA pointed observations, sometimes there are clear differences, probably due to the fact that the PCA (2–60 keV) is more sensitive at high energies than the ASM (1.5–12 keV).

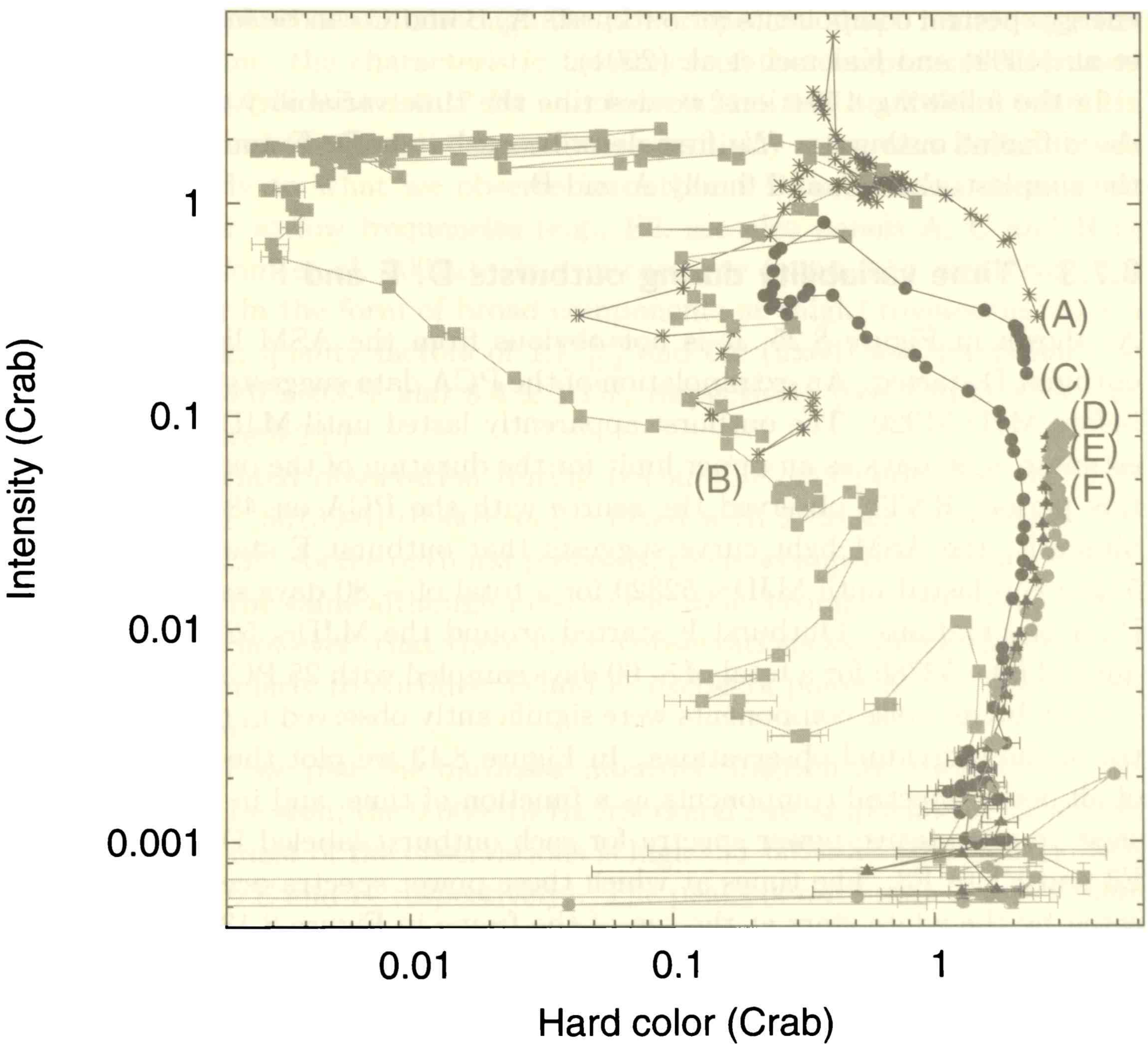

Figure 8.26: Hardness vs. Intensity in units of Crab for all pointed observation of the BH XTE J1550–564. The labels A–F refer to the 6 outburst shown in Figures 8.24 & 8.25. The position of each label shows the point in the HID in which the corresponding outburst starts. By following the lines that connect the points it is possible to follow the change in color/intensity with time (see also Figures 8.3–8.7). The symbols are the same as in Figure 8.24. Errors are plotted.

for outburst B. Additional similar figures have been reported by Kubota & Done (2004) for outbursts A and B and Miller et al. (2001) for outburst C, but these used the ASM, which is much less sensitive than the PCA. (For example, figure 1 in Kubota & Done 2004 shows that the ASM did not detect the soft-state flaring studied by Homan et al. 2001). The time evolution of energy spectral components for outbursts A, B and C can be found in Sobczak et al. (1999) and Kalemci et al. (2001).

In the following 4 sections we describe the time variability as measured in the different outbursts. We first describe outbursts D, E and F as they are the simplest, then C, and finally A and B.

8.7.3 Time variability during outbursts D, E and F

As shown in Figure 8.25, it is not obvious from the ASM lightcurve when outburst D started. An extrapolation of the PCA data suggests that it was not before MJD 51920. The outburst apparently lasted until MJD$\sim$ 52000 so we estimate $\sim$ 80 days as an upper limit for the duration of the outburst. During this period, RXTE observed the source with the PCA on 48 opportunities. Similarly, the ASM light curve suggests that outburst E started on MJD$\sim$ 52240 and lasted until MJD$\sim$ 52320 for a total of $\sim$ 80 days sampled with 27 PCA observations. Outburst F started around the MJD$\sim$ 52720 and lasted until MJD$\sim$ 52780 for a total of $\sim$ 60 days sampled with 25 PCA observations.

Only broad noise components were significantly observed in the power spectra of the individual observations. In Figure 8.13 we plot the characteristics of all power spectral components as a function of time, and in Figure 8.23 we show representative power spectra for each outburst labeled D1 to D4, E1 to E3 and F1 to F3. The times at which these power spectra occurred are indicated by the white stars at the top of the frame in Figure 8.13. One to three Lorentzian components were needed to fit the different power spectra during these outbursts. All power spectra are consistent with those expected for the LS of black holes: they are strong ($\sim 40 - 60\%$ rms over 0.001–100 Hz), and tend to have a flat-top at low frequencies, a break in the 0.01–0.1 Hz range and an additional bump or knee in the 1–10 Hz range.

The first pointed observation during outburst D was performed on MJD 51937.7 (ObsId: 50427-01-01-00) and is well fitted with 3 broad Lorentzians at frequencies 1.5$\pm$0.1, 0.15$\pm$0.02 and 0.008$\pm$0.001 Hz (see D1 in Figure 8.23). As the outburst proceeds, the power spectra remain approximately the same although only 2 components were sometimes needed (e.g., D4) for a good fit. In many cases (e.g., D3 and D4) there is power excess in the form of broad feature at frequencies lower than 0.05 Hz and in the form of a QPO with frequencies between 10 and 30 Hz (e.g D2 and D3). In most cases statistics were not sufficient to measure these power excesses. After MJD 51990, no significant power is observed in the power spectra.

The first pointed observation during outburst E was performed on MJD 52284.9 (ObsId: 60428-01-01-00) and is fitted with 3 broad Lorentzians (see E1). As the source evolves in time, the power spectra are well fitted with only two broad components and although the power spectral shape remain approximately the same, the characteristic frequency of the components decreases (from 2.37 ± 0.07 to 0.51 ± 0.17 Hz and from 0.21 ± 0.07 to 0.030 ± 0.009 Hz for the upper and the lower component, respectively – see also Belloni et al. 2005). Similarly to what we observe in outburst D, sometimes there is an excess of power at low frequencies (e.g., E2, see also panels A, C and H in figure 1 of Belloni et al. 2002a). In two cases we found 3.1σ significant excesses of power in the form of broad components at (high) frequencies 40 ± 5 and 50 ± 25 Hz, quality factors of $1.7^{+1.6}_{-0.9}$ and 0.0 (fixed) and fractional rms amplitudes of $4.0 \pm 0.6\%$ and $8.4 \pm 1.1\%$, respectively (see Figure 8.13, not plotted in Figure 8.23.).

The first pointed observation during outburst F was performed on MJD 52725.6 (ObsId: 80135-01-01-00) and is fitted with 2 broad Lorentzians (see F1 in Figure 8.23). As the outburst proceeds, the power spectral shape remains approximately the same although most of the time 3 components needed for a good fit. Note, however, that there are no observations sampling the decay of outburst F. Similarly to outburst D and E, excess of power at low frequencies sometimes occurs.

In Figure 8.7 we plot the hardness–intensity diagram for these three outbursts. As can be seen, the 0.008–10 Hz fractional rms amplitude of the power spectra during most of the observations is high (35–60%, 35–50% and 42–46% for ourbursts D, E and F, respectively). The peaks of outbursts D and F were mostly sampled at the same hardness but their intensities are a factor of ~ 2 different (F being the brightest). The observations of outburst E, whose peak was not covered with the pointed observations, show that the source reached levels at least as bright as outburst F, but at similar flux levels it was softer. All 3 outbursts show a slight softening of the spectra during the decay. Significant power is measured until the source becomes dimmer than $\sim 2 \times 10^{-3}$ Crab.

We find a positive correlation between the frequency of the $\nu \sim 1$ Hz broad component and hard color during outburst E (see Figure 8.18). The frequency of the $\nu > 1$ Hz broad component measured during outburst F anti-correlates with this component's amplitude (see Figure 8.19). We find no significant relations between the characteristic frequencies and either colors or intensity during outbursts D and F, nor between the characteristic frequencies and their components' rms amplitudes during outbursts D and E (not plotted).

So, the frequencies, fractional rms amplitudes and colors we find during outbursts D, E and F are typical of the black hole low state. The fact that the power spectra can be fitted with a simple model consisting of two or three Lorentzian components, mostly with zero centroid frequency, is consistent with findings by Belloni et al. (2002b) for the hard states of black hole sources. Contrary to what we will report below for the other outbursts, for outburst E we find that the frequency of the $\nu \sim 1$ Hz component increases with color (this work) and decreases in time (see Figure 8.13 and Belloni et al. 2002a).

8.7.4 Timing variability during Outburst C

Outburst C started on MJD 51630 and lasted until MJD$\sim$ 51730 for a total of $\sim$ 100 days sampled with 67 pointed PCA observations. One to six Lorentzian components were needed to fit each power spectrum. In Figure 8.11 we plot the characteristics of all components as a function of time while in Figure 8.22 we show 15 representative power spectra for this outburst. They are labeled from C1 to C15 and are time ordered. The times at which these power spectra occurred are indicated by the white stars at the top of the frame in Figure 8.11. Similar spectra to these can recur at different times during the outburst. Figure 8.6 illustrates where in the hardness–intensity diagram these 15 power spectra were observed. The track traced during this outburst in the hardness–intensity diagram is different than in that for outbursts D, E and F except in the decay, during which all outbursts show the slight softening of the spectra (see Section 8.7.2).

The first pointed observation in outburst C corresponds to ObsId 50137-02-01-00 and was performed on MJD 51644.49. As can be seen in Figure 8.25, this observation was performed about 15 days after the beginning of the outburst. As often found in the low state of black holes, the power spectrum contains 2 QPOs at low frequencies (between 0.1 and 1 Hz, Type C, Rodriguez et al. 2004) plus 3 broad Lorentzians that fit the broad band noise (see C1 in Figure 8.22). In Figure 8.12 we show the characteristics of the broad band components as they evolve in time during the period MJD 51640–61665 (see also Figure 8.11). There are two clear groups of components, namely χ_1 and χ_2, whose frequency is rather constant (at $\sim$ 30 Hz and $\sim$ 6 Hz) until MJD 51657, when the frequency of χ_1 seems to start to increase, while χ_2 is not significantly detected anymore. As can be seen in Figure 8.12, the behavior of the component in χ_3 during the first $\sim$ 7 days is complex, as the component observed in the first two observations (MJD< 51646) seem to split in two between MJD 51646.5 and 51649, to become again one component (when only one component, its fractional rms amplitude is higher than that of any of the "split" components, suggesting that the rms was distributed over the two). At MJD 51650.5 a new component at frequencies lower than 0.02 Hz is significantly detected (group χ_4), and simultaneously with this the frequencies of the components in both χ_3 and χ_4 start to increase. Panels C1–C4 are representative of the time evolution described above, in which the source moves from the LS to the HIMS. C4 is the power spectrum of an observation taken on MJD 51660.08 (ObsId: 50134-02-01-01, see also Figure 8.6). On MJD$\sim$ 51662.1 (ObsId 50134-02-02-00) and after a data gap of $\sim$ 2 days, we find that the power spectral characteristics have changed from typical HIMS power spectra to the typical SIMS shape shown in C5, in which the 0.008–10 Hz fractional rms amplitude has dropped from 20.88 ± 0.09 to $6.71 \pm 0.03\%$ mainly due to a drop in noise amplitudes, and the QPO frequencies slightly increased (the strongest QPO frequency changed from 4.009 ± 0.005 to 4.53 ± 0.01 Hz; Type C $\rightarrow$ Type B, Rodriguez et al. 2004). As can be seen from Figures 8.6 & 8.11, the transition coincides with the highest intensity point sampled by the RXTE pointed observations but not with an extreme value of the hardness.

On MJD$\sim$ 51664.4 (ObsId:50134-02-02-01) and after a decrease in intensity and a further decrease of colors, the power spectral characteristics change from C5 to C6. The same power spectral characteristics are also seen in a second observation performed the same day (50134-02-03-00). These power spectra are well fitted with 6 Lorentzians at 276 ± 21, 29 ± 1.3, 17.1 ± 0.5, 6.9 ± 0.1 and 0.017 ± 0.002 Hz and quality factors 0.9 ± 0.3, 1.8 ± 0.5, $6.1^{+6.2}_{1.9}$, 1.37 ± 0.09 and 0.7 ± 0.1, respectively. This is the only observation in outburst C in which we observe very low frequency noise in the form of a steep power law at frequencies lower than 0.1 Hz. This power is well modeled by the Lorentzian at 0.017 Hz. (These power spectra were not reported by Rodriguez et al. 2004; we nevertheless note that the QPO at 17.1 Hz cannot be unambiguously classified as either type A, B or C). Coincident with this type of power spectrum, the decrease in intensity continues, but at a rather constant hardness and during a period of $\sim$ 8 days, in which the power spectra change from consisting of just a single broad component at frequencies lower than 50 Hz (not plotted), to power spectra that can be fitted with 3 components (a QPO in between two broad Lorentzians, see power spectrum C8). This period is the closest approach to the HS of the source during this outburst, reaching rms amplitudes as low as $\sim$ 4% (softer colors and lower rms amplitudes than these are observed during outburst B, see Sections 8.7.2 & 8.7.6).

On MJD 51674.7 and as the source hardens again as it enters the HIMS and the power spectral shape changes to C9 (Type B or C, see discussion by Rodriguez et al. 2004). As can be seen in Figures 8.6, 8.11 & 8.22, C5 and C9 are very similar in both color and power spectrum and characteristic of the SIMS, although the 0.008–10 Hz fractional rms amplitude in C9 is higher than in C5 (9.49 ± 0.05 and $6.71 \pm 0.03\%$, respectively).

On MJD 51675.4 the power spectrum changes to C10 (50134-01-03-00). This power spectrum is different from all the other ones in outburst C (but see power spectra A5 and A6 in Section 8.7.5); the QPO reaches its maximum frequency (16.9 ± 0.1 Hz) and this is the only time we detect more than two broad components at frequencies lower than that of the QPO. On MJD 51676 the power spectrum changes to the typical HIMS shape seen in C11 (50134-01-04-00), in which the QPO is now detected at frequencies lower than 10 Hz (as it is the case for all power spectra except C10).

So starting on MJD 51676 and as the intensity decreases and the colors increase, the power spectral components evolve to lower frequencies in a similar but inverse pattern to that observed in the first part of the outburst (i.e. from the HIMS to the LS, although at lower intensities). Power spectra C11–C15 synopsize this evolution which can also be followed in Figure 8.11 (QPOs when present, are Type C, Rodriguez et al. 2004). This evolution finishes on MJD 51707.5, after which no significant features are present in the power spectra.

As can be seen in Figure 8.11, starting on MJD 51673 the hard color starts to increase (the decay of the outburst started about 10 days earlier) and the characteristic frequencies of the broad band noise components decrease with time. At 51685, the highest-frequency broad band component in each power spectrum jumps in both frequency and fractional rms amplitude. Between MJD 51673 and 51685, the component has rms amplitudes lower than $\sim 10\%$ and characteristic frequencies higher than 50 Hz, while after the jump it has rms amplitudes higher than $\sim 15\%$ and characteristic frequencies less than 10 Hz (down to 0.8 Hz). There is one observation which shows two components simultaneously, suggesting that there are two different components in the power spectra which dominate at different times of the evolution of the source (we note that power spectra made up of sub-datasets of the same observation also show the two components). The time of the jump coincides with the time at which the hard color stops its steep increase (which started on MJD 51673) suggesting that it can be related with a spectral state change. In Figure 8.6 we mark this point with the label "MJD 51685" and in Figure 8.11 with "Jump". Klein-Wolt & van der Klis (2008) also reported on this (see their figure 6). In their interpretation the components measured before the jump are the blend of two broad components that are at similar frequency and cannot be resolved with the statistics of the present data. After the jump the two components' frequency difference is large enough to resolve them. When the lower frequency component dominates, the higher frequency component is not significant (except in one case, see above) but its 95% confidence upper limits are relatively high, between 3 and 10% (Klein-Wolt & van der Klis 2008).

During the period MJD 51673–51705, the characteristic frequency of the low frequency components in the power spectra also decrease in time, but no frequency or rms amplitude jump is seen such as that discussed for the high frequency component.

In Figure 8.17 we show that during this outburst, the relation between hardness and characteristic frequency of the QPOs can be divided in two: (i) there is an anti-correlation between hardness and frequency at colors harder than 1.5, which may flatten around this value of the hard color and (ii) at hard colors less than 1, the frequency of the different features shows no clear trend. Between hard color values of 1 and 1.5 there is insufficient data to tell. In the case of the broad components, the distribution of data points is more complex. At colors harder than 2, there are 4 tracks: the top two and bottom one being at approximately constant frequency while for the one but lowest one, frequency anti-correlates with color. At hard colors between 1.5 and 2, there might be 4 tracks as well, but the sparseness and dispersion of the data prevent us to connect them with the previous ones. At colors between 0.6 and 1.5 three tracks are present, and at colors softer than 0.6 four tracks are again visible. The data plotted in this figure do not allow for an obvious connection between tracks. (We note that separating the data corresponding to the rise from those corresponding to the decay has no effect on the description mentioned above).

From Figure 8.17, it is also possible to see the dependence of the rms amplitude of the different components with hardness. In the case of the QPOs, the fractional rms amplitudes increase with color. The relation, however, is not strict. Depending on the assumed connection between the tracks observed in the upper panel of Figure 8.17, the same is true for the broad components. Using the data points before the peak of the outburst separately from those after the peak of the outburst smooths the correlation between hard color and rms amplitude of the components although it is still not strict (not plotted).

8.7.5 Time variability during Outburst A

Outburst A started on MJD 51063 and lasted until MJD 51150 for a total of 87 days sampled with 78 PCA observations. One to eight Lorentzian components were needed to fit each power spectrum. In Figure 8.8 we plot the characteristics of all components as a function of time while in Figure 8.20 we show 15 representative power spectra for this outburst. They are labeled from A1 to A15 and are time ordered. The times at which these power spectra occurred are indicated by the white stars at the top of the frame in Figure 8.8

and in Figure 8.3 we illustrate where in the HID these power spectra were observed.

During the first $\sim$ 12 days of the outburst corresponding to the period prior to the 6.8 Crab X-ray flare (see below), the intensity increased as the hard and soft colors decreased (see Figure 8.8). The power spectra are well fitted with 2 to 5 broad Lorentzians and 1 to 3 sharp Lorentzians to fit broad band noise and QPOs, respectively. These power spectra are typical of the LS and are similar to those observed during the LS of outburst C (e.g., C1-C3). A1, A2 and A3 summarize the evolution during this period. The characteristic frequencies of the two QPOs that can be seen in A1 (Type C, Remillard et al. 2002a), as well as those of the broad components at frequencies $>$ 10 Hz (group α_1, see below), increase with time. For the low frequency ($<$ 10 Hz) components, the $\sim$ 12-day period can be divided in two. In Figure 8.9 we plot the characteristics of the broad components as a function of time for this $\sim$ 12-day period. (Note that groups α_1 and α_2 have frequencies that are always higher that those of the two QPOs, while α_{3a} is in between the 2 QPOs and α_{3b} below them; the first data point of α_3 has a frequency higher than that of the 2 QPOs, while the other two data points have frequencies in between those of the QPOs). In the first $\sim$ 2.5 days, there are two groups of broad band components whose characteristic frequencies increase with time (α_2 from $\sim$ 4 to $\sim$ 9 Hz and α_3 from $\sim$ 0.25 to $\sim$ 0.9 Hz, see Figure 8.9). During the the remaining $\sim$ 8.5 days, α_2 is not significantly detected and α_3 seems to split into two different groups, one with frequencies increasing from $\sim$ 2 to $\sim$ 8 (α_{3a}) and another one with approximately constant frequency between $\sim$ 0.6 to $\sim$ 1 Hz (α_{3b}). This component splitting is similar to that we observe during the rise of outburst C (see Section 8.7.4). As the power spectra evolve from A1 to A3, it is necessary to add to our model an extra broad component with frequencies lower than that of the strong QPO, which in A1, and similarly during 3 other observations following A1, is either not detectable or blended with another component, possibly due to lack of statistics (see also Klein-Wolt & van der Klis 2008). As can be seen in Figure 8.9, the fractional rms amplitude of the components in α_3 is always $>$ 23% while it is always $\lesssim$ 18% for α_{3a} and α_{3b}. We note that it is also possible that α_{3a} is the continuation of α_2, if a frequency jump occurs. We consider this unlikely because there is one observation, at MJD 51066, which shows both components simultaneously, and because after the flare we also find power spectra with two components at higher frequencies (similar to α_1 and α_2), one with frequencies in between (similar to α_{3a}) and one with frequencies below (similar to α_{3b}) those of the 2 QPOs.

On MJD $\sim$ 51075.9 a $\sim$ 6.8 Crab flare occurs and a 3 ksec observation during this time shows that the power spectral shape has changed completely (power spectrum A4, ObsId 30191-01-02-00, also see Remillard et al. 1999a). This observation shows 3 clear QPOs (at 186 ± 3, 13.26 ± 0.08 and 4.93 ± 0.05 Hz) and broad band power much weaker than before ($\sim 2\%$ rms down from $\sim 15\%$ rms, in the 0.001–10 Hz range).

that is well fitted with 2 broad Lorentzians at (426 ± 42 and 1.75 ± 0.04 Hz) and a power law to account for the low frequency noise (with index $\alpha = 1.06 \pm 0.05$, we note that this is the only case in our sample that a power law was needed, instead of a low frequency broad Lorentzian, for a stable fit). This is the first time a QPO at frequencies higher than 100 Hz was detected for this source (Remillard et al. 1998, 1999a). The zero-centered Lorentzian at characteristic frequency of 426 Hz is more than 11σ significant. However, since the Poissonian noise is affected by deadtime effects associated with the extremely high count rate during the flare (13 kcounts/PCU) and our model may not be able to well estimate the deadtime modified Poisson spectrum accurately (see, e.g., discussions in Zhang et al. 1995; Klein-Wolt 2004; Jahoda et al. 2006), we cannot exclude the possibility that this power excess is instrumental.

The first two observations taken after the flare (MJD=51076.8 and 51076.9, see power spectrum A5 and A6) shows a HIMS power spectral shape similar to those during the pre-flare period but in these cases the QPO reaches its maximum in frequency (~ 10 Hz) and 3 broad components are significantly detected at frequencies lower than that of the QPO. These power spectra are similar to that shown in C10 during outburst C (see Section 8.7.4). However, it is interesting that while A5 and A6 occurred right after the flare, suggesting a relation between flare and the QPO reaching its maximum frequency, C10 occurred at low intensity during the HIMS.

In the period MJD 51077–51102, for a total of 25 days, the source remains within a relatively small region in the hardness–intensity diagram, while moving from higher intensity/softer energy spectra to lower intensity/harder spectra (see Figure 8.3, power spectra A5–A11). Depending on the position in the HID, the 0.008–10 Hz rms amplitude varies (it is higher at harder colors) and so does the rms amplitude of the components and the power spectral shape. Generally, at harder colors the characteristic frequencies are found to be lower than at softer colors. Power spectra A5-A11 in Figure 8.20 are representative of this period. Figure 8.3 illustrates where in the HID these power spectra are observed.

On MJD=51106.9 (and after almost 5 days without PCA or ASM information), we observe that the intensity has increased and the colors decreased from those during the previous observation. In this observation as well as in the other two performed between MJD 51106.9 and 51110 (Obs-Ids: 30191-01-32-00/33-00/34-01), the 0.008–10 Hz fractional rms amplitude ($4.78 \pm 0.2\%$) is much lower than in A11 ($13.33 \pm 0.06\%$ rms, last seen at MJD 51102 – ObsId 30191-01-31-01) and the power spectra (in all 3 cases) resemble that shown in panel A12. The A11 $\rightarrow$ A12 transition is another example of the HIMS$\rightarrow$SIMS Type C $\rightarrow$ Type B QPO transition (Remillard et al. 2002a); the frequency of the strongest QPO decreases from 6.75 ± 0.01 to 5.49 ± 0.02 Hz. The A12 power spectra are all found at hard colors between 0.3 and 0.34 (see description of Figure 8.14 below).

Simultaneously with a a small dip in the hard and soft color at MJD 51110.2 the power spectrum changes from A12 to A13 and then to broad band noise than can be fitted with one or two broad Lorentzians (not plotted). Power spectrum A13 (ObsId30191-01-34-00) resulted from 3.2 ksec of data at an averaged source count rate of $\sim$ 3050 c/s/PCU where all 5 PCUs were turned on. The 0.008–100 Hz fractional rms is $4.90 \pm 0.03\%$ and is fitted with 5 Lorentzians: 2 zero centered at 0.25 ± 0.06 and 4.48 ± 0.3 Hz, and 3 QPOs at $\sim 38.99 \pm 1.39$, $\sim 85.9 \pm 2.2$ and 223 ± 20 Hz. All components have less than 1.5% fractional rms amplitude and are $> 3\sigma$ significant, except the broad component at 4.9 Hz, which was 2.7σ (this component was necessary for a stable fit). A14 is the power spectrum of an observation performed on MJD 51115.28, before the steep decrease in colors that can be seen in Figures 8.3 & 8.8 (hard color ~ 0.265). This is the only observation in outburst A in which we observe very low frequency noise in the form of a steep power law at frequencies lower than 0.1 Hz (see A14). The characteristics of power spectrum A14 are similar to those in C6 and interestingly, both power spectra were found when the source starts the steep decrease in intensity at soft spectrum (see Figure 8.3).

In the period MJD 51115.5–51137 we find almost no power (see Figures 8.3 & 8.8) until the last observations of this outburst, in which the hard color has increased and power is detectable again, with periods of insignificant power in between, in the form of a QPO at 4.9 ± 0.1 Hz and two broad components at 9.2 ± 0.9 and 0.3 ± 0.1 Hz at MJD 51126.6, 2 broad components at 9.1 ± 0.3 and 2.7 ± 0.5 Hz and a high frequency QPO at 263 ± 16 Hz at MJD 51137.9 (power spectrum A15), 2 broad components at 9.9 ± 0.5 and 3.1 ± 0.3 Hz and a QPO at 30 ± 1 Hz at MJD 51140.0 (and a similar power spectrum but without the QPO at MJD 51140.9), 1 broad component at 7.07 ± 0.49 Hz at MJD 51143 and 2 broad components at 23 ± 9 and 3.2 ± 0.4 Hz and QPO at 7.4 ± 0.2 Hz at MJD 51147.4 (this power spectrum is similar to that shown in C8, see Figure 8.22).

As we show in Figure 8.8, the characteristic frequencies of both QPOs and broad band noise at $\nu \lesssim 20$ Hz during most of the outburst seem to change together and in anti-correlation with the hard color. A similar anti-correlation but only between QPO frequency and hard color is shown in Figure 8.17 for outburst C data, and has been reported in previous works, see, e.g., Homan et al. (2001).

To further investigate this, in Figure 8.14 we plot the frequency of all components versus the hard color. The symbols and the color scale in Figure 8.14 are the same as those in Figure 8.8. As can be seen in the bottom panel there is a clear anti–correlation between the characteristic frequency of the QPOs and hard color. The 3 high frequency QPOs (see yellow circles at hard colors ~ 0.55, ~ 0.65 and ~ 0.72) also seem to anti-correlate with the hard color (see also Homan et al. 2001, for a similar correlation detected during outburst B). In the upper panel we plot the characteristic frequency of the broad band components ($Q < 2$). Between hard color 0.4 and 0.8, three groups of components can be distinguished whose frequencies also anti-correlate with hard color. The anti-correlation might continue beyond the 0.4–0.8 range, but the dispersion of the points is high.

To separate data with the same hardness but from different stages of the outburst, in Figure 8.15 we show the same as in Figure 8.14, but we only plot data points in the range MJD 51080–51120, i.e. after the 6.8 Crab flare. In the case of the broad band components, we separate between the three groups distinguished above by lines, and we call them Aa, Ab and Ac in order of decreasing frequency. The time selection does not significantly improve either the rms amplitude or the frequency anti-correlation with hardness, indicating that the dispersion seen in Figure 8.15 is not caused by mixing outburst stages. In the case of the QPOs, in Figure 8.15 there is a data gap between hard colors 0.32 and 0.42 which is filled in, in Figure 8.14 with data points from observations before the flare (i.e. A1–A3). This gap represents the A11→A12 HIMS→SIMS transition from the Type C to Type B QPO described above (at harder and softer colors, respectively; Remillard et al. 2002a). The rms amplitude of the Type B QPO follows the rms amplitude/hard color anti-correlation.

In three observations between MJD=51076.9 and 51077.41 (ObsIds 30191-01-04-00/05-00/06-00) we find that the power spectral characteristics change significantly within each observation. These changes are coincident with a clear change ($\sim 15\%$) in count rate. In Figure 8.27 we plot the the dynamical power spectra (lower panel) and the total count rate (upper panel) of observation 30191-01-06-00, to show the changes in power spectra as a function of time (the other two observations show similar changes, although there the transition occurs from lower to higher count rate). The observation is divided in three data segments corresponding to three satellite orbits. The count rate in the

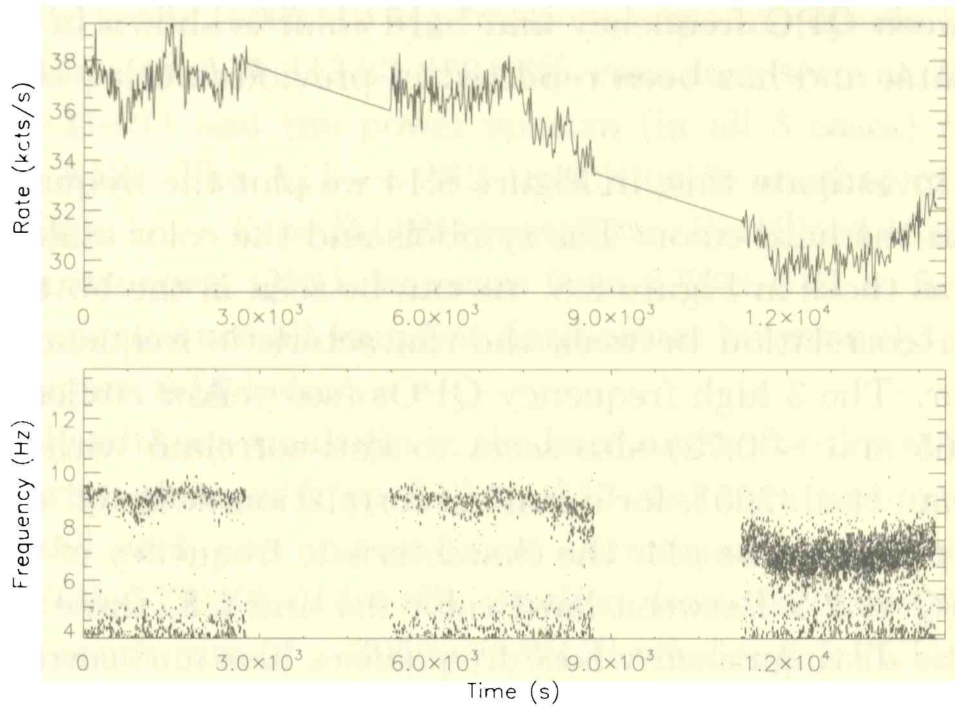

Figure 8.27: Dynamical power spectrum (bottom panel) and light curve (top panel) of observation 30191-01-06-00.

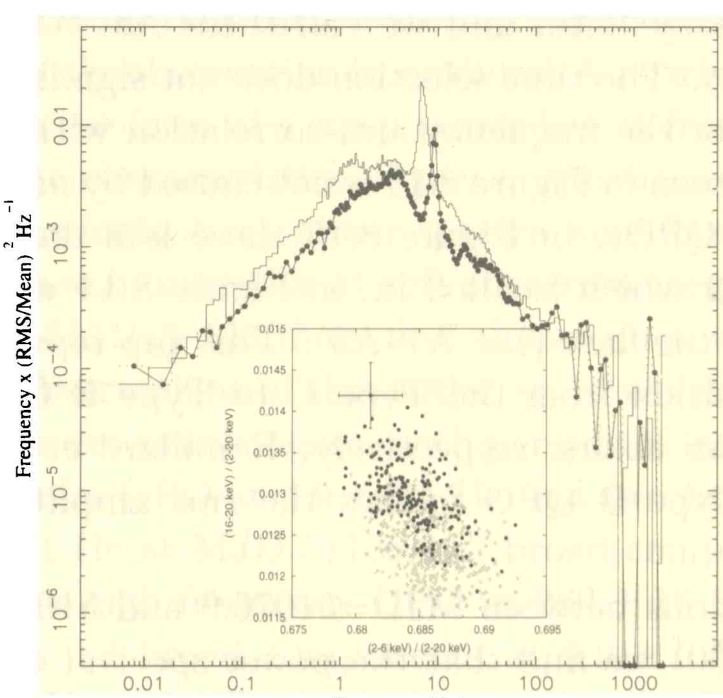

Figure 8.28: Power spectra of the first (bullets) and third (grey histogram) orbits of observation 30191-01-06-00 (see Figure 8.27). Inset: (2–6 keV)/(2–20 keV) versus (16–20 keV)/(2–20 keV) deadtime and background corrected count rates. Grey and black circles mark 16s averages for the data of the first and the third orbit, respectively. Typical error bars are plotted for one point.

first two orbits is similar and so are the frequency and the rms amplitude of the QPO at $\sim$ 9 Hz. The count rate in the third orbit is lower, and so is the frequency of the QPO, but the rms amplitude is higher. In Figure 8.28 we show the power spectra of the first and third orbit data segments (PDS1 and PDS3, respectively). As can be seen, the drop in intensity does not only affect the frequency of the QPOs and broad components, but also their rms amplitudes. While in PDS1 there is clear structure at frequencies higher than the QPO, in PDS3 the power decreases more smoothly above the QPO frequency. Furthermore, while in PDS3 two components are clearly necessary to fit the double bump in power at frequencies between 0.8 and 4 Hz, the double bump is not as clear in PDS1. In the inset of Figure 8.28 we plot the (2–6 keV)/(2–20 keV) versus (16–20 keV)/(2–20 keV) count rate. The black filled and black open circles represent the 16s average for the PDS3 and PDS1 data, respectively. The data for PDS3 seems to be harder than those of PDS2, although only marginally. For clarity, in Figures 8.8 & 8.14 we plot one power spectrum per observation, corresponding to the one with higher number of components.

8.7.6 Time variability during Outburst B

Outburst B started on MJD 51150 as a continuation of outburst A (see Section 8.7.1 and Figure 8.24) and lasted until MJD 51325 for a total of $\sim$ 175 days sampled with 171 pointed PCA observations. One to seven Lorentzian components were needed to fit the power spectra. In Figure 8.10 we plot the characteristics of all components as a function of time while in Figure 8.21 we show 15 representative power spectra for this outburst. They are labeled from B1 to B15 and are time ordered. The times at which these power spectra occurred are indicated by the white stars at the top of the frame in Figure 8.10 and in Figure 8.4 we illustrate where in the HID these power spectra were observed.

The first observation in outburst B corresponds to ObsId 30435-01-06-00 and was performed on MJD 51150.08. The power spectrum of this observation is noisy and only a 1.6% rms amplitude Lorentzian is present (see B1). At this point, the intensity starts to increase as the soft and the hard color decrease and almost no significant power is found until MJD 51160, when the power is well fitted with a broad Lorentzian (see Figures 8.4 & 8.10). At this point, the source reaches the so called high state (HS, see Homan et al. 2001) when the hard color reaches a minimum of about $\sim$ 0.02 Crab, more than an order of magnitude lower than the minimum hardness reached during the HS of outburst A and C and almost 3 orders of magnitude softer than the minima registered during outbursts D,E and F (during the LS). Starting on MJD

51160 and for a total of $\sim$ 80 days (i.e. until until MJD 51240), the source is in a flaring period in which the power spectra can be fitted with 2 or 3 broad Lorentzians (power spectra B2, B3 and B4). On several occasions we find excess power in the form of a QPO at frequencies higher than 10 Hz. This excess was significantly fitted only 3 times with frequencies between 15 and 20 Hz (e.g., power spectrum B3). As Homan et al. (2001) shows, the flares are stronger in the hard color and the QPOs appear at the peaks of the flares (Figure 8.10). During this period, the total rms amplitude remains low and approximately constant and so does the fractional rms amplitude of the components (1 – 2% rms, see Figure 8.10). On MJD 51215.8 (ObsId 40401-01-31-00) the power spectrum is well fitted with 3 broad Lorentzians and a 3.7σ Lorentzian at 105 ± 17 Hz (Q= $1.3^{+1.0}_{-0.4}$ – see power spectrum B4) which also coincides with the peak of one of the hard flares.

On MJD 51241.8, and as the hardness increases in the form of another flare, the power spectral shape completely changes into B5 (Type A, Remillard et al. 2002a). Although the hard and soft colors are higher in B5 than in the previous observation (and the hardest since the flaring period started), we note that there is no abrupt change in colors during these observations (as it was the case during the flares in the period MJD 51170–51230), but the hard and soft color have increased smoothly since MJD$\sim$ 51237. We also note that the fractional rms amplitude in the 0-1 Hz range is similar in B5 as in the previous observations. The most significant difference between B5 and previous power spectra is the appearance of the QPOs at 6 and 11 Hz (with $\sim$ 3 and $\sim$ 2.6% rms) and of significant power at frequencies higher than 100 Hz. The power spectrum of an observation taken on MJD 51242.5 still resembles that of B5.

As the colors increase and the intensity decreases, the power changes as follows: on MJD 51244.49 we find B6, on MJD 51245.36 the power spectrum changes to B7, on MJD 51246.4 back to B6 and on MJD 51247.97 back to B7. The shape of the power spectra in the 3 following observations resembles that of B7, but the rms amplitude increases while hardness and intensity decrease (see Figure 8.5 for the evolution in the HID during this time). Power spectra B6 were classified as (probably) Type A QPO, and B7 as Type B QPO (Remillard et al. 2002a). On MJD 51250.7, the 0.008–100 Hz rms amplitude of the power spectra increases from $6.84 \pm 0.01\%$ (B7, ObsId 40401-01-56-01) to $14.56 \pm 0.04\%$ (B8, ObsId 40401-01-57-00). The characteristic frequency of the strongest QPO also increases, but slightly, from 6.27 ± 0.07 to 6.68 ± 0.01 Hz. The power spectral changes are simultaneous with a sudden increase in colors and a decrease of intensity (Type B $\rightarrow$ Type C QPO, Remillard et al. 2002a). As the intensity slightly increases and the colors start to decrease, on MJD 51253.2 the power spectra resemble B7 again. This complex behavior is summarized in Figures 8.4 & 8.5.

B8 (Type C QPO Remillard et al. 2002a) is observed at a local maximum of the hard color as well as a local minimum of the intensity. This appears to be associated with the change between B7 and B8 power spectra. From our data it is not clear what is the reason for the change between B6 and B7. There are B7 power spectra at softer and harder colors and at higher and lower intensities than those when B6 is observed. Similar results are found from the soft color vs. intensity and soft color vs. hard color diagrams (not plotted).

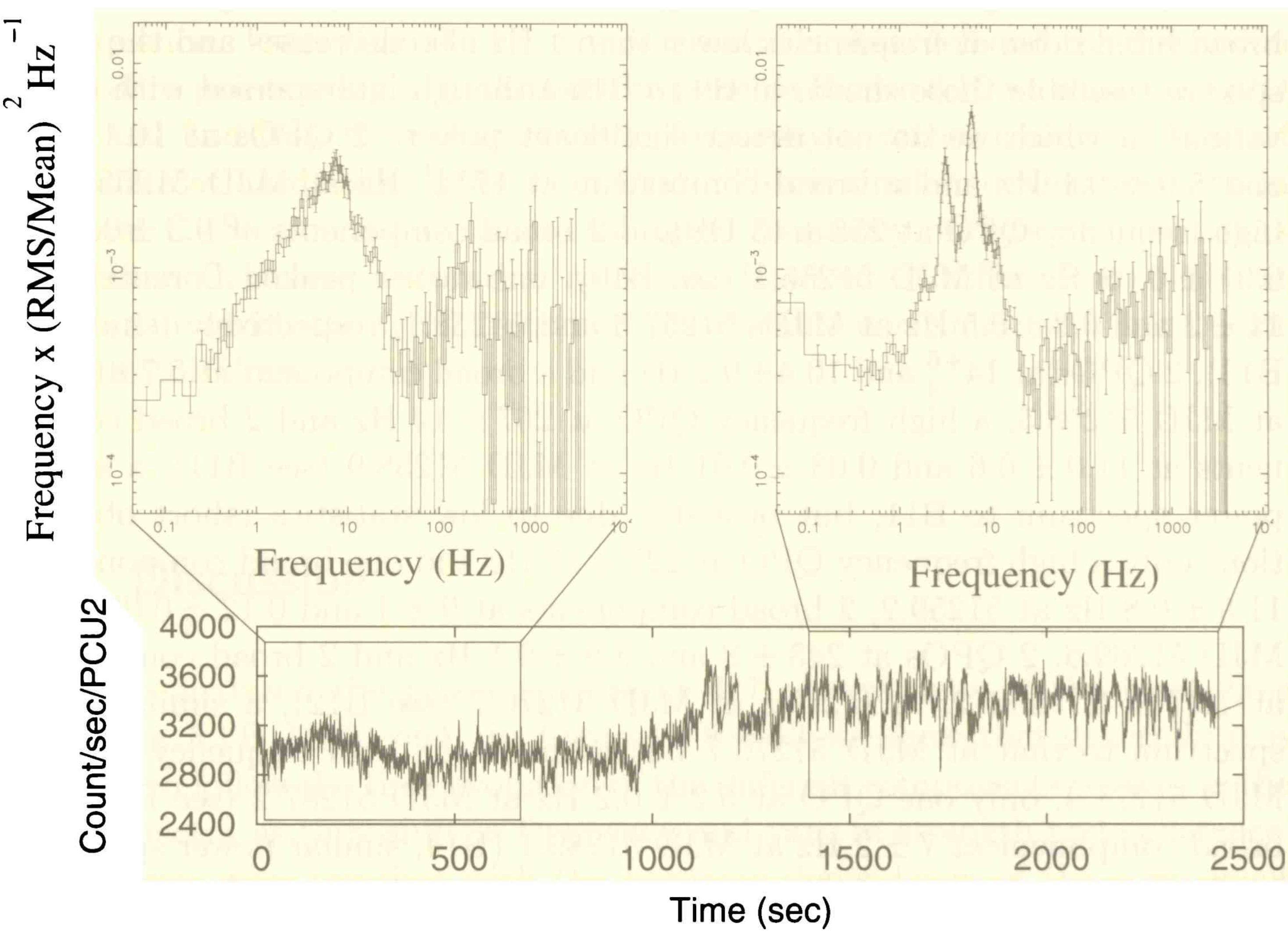

Figure 8.29: *Bottom panel*: 1–second PCU2 light curve of observation 40401-01-58-01 (MJD 51254.09). *Upper-left panel*: Power spectrum from the first 650 seconds of data. *Upper-right panel*: power spectrum of the data in the 1400–2500 seconds range. See Section 8.7.6 and Homan et al. (2001).

On MJD 51254.09 (ObsId:40401-01-58-01), we find that within one observation, the power spectral shape changes from one which is similar to B10 to one that resembles B7 with an intermediate power spectrum similar to B9. Homan et al. (2001) studied this observation; in their interpretation the source is undergoing a transition from the Type A QPO to the Type B QPO. These authors plotted the dynamical power spectra showing the QPOs appearing (see figure 19 in Homan et al. 2001). In Figure 8.29 we plot the 1 second Standard 1 (PCU2) lightcurve and two representative power spectra. About $\sim$ 1000 seconds after the beginning of the observation, the count rate increases and the flickering is stronger. This is probably the point of transition where the power spectrum changes. Homan et al. (2001) show in their figure 17, that at this same time the hard color starts to decrease (the soft color remains approximately constant). In Figures 8.4 & 8.5 we mark the point in the hardness–intensity diagram at which this transition occurs (see label "Transition").

As the intensity decreases after MJD 51255.09, the rms amplitude of the broad band noise at frequencies lower than 1 Hz also decreases and the power spectra resemble those shown in B9 to B15 although interspersed with observations in which we do not detect significant power: 2 QPOs at 10.1 ± 0.3 and 5.9 ± 0.1 Hz and a broad component at 17^{+11}_{-5} Hz at MJD 51255.09, a high frequency QPO at 258 ± 13 Hz and 2 broad components at 9.3 ± 0.1 and 0.31 ± 0.08 Hz at MJD 51255.1 (see B10), one rather peaked Lorentzian at 11 ± 2 and 6.3 ± 0.5 Hz at MJDs 51257.3 and 51258.1, respectively (similar to B13), 2 QPOs at 14^{+6}_{-4} and 10.4 ± 0.2 Hz and a broad component at 5.7 ± 0.1 Hz at MJD 51258.5, a high frequency QPO at 267 ± 14 Hz and 2 broad components at 11.0 ± 0.6 and 0.03 ± 0.01 Hz at MJD 51258.9 (see B11), a similar power spectrum to B11, but probably due to low statistics (short observation) only a high frequency QPO at 227 ± 17 Hz and one broad component at 11.5 ± 0.8 Hz at 51259.2, 2 broad components at 9 ± 1 and 0.12 ± 0.03 Hz at MJD 51269.6, 2 QPOs at 245 ± 8 and 8.9 ± 0.1 Hz and 2 broad components at 15.7 ± 1.7 and 2.7 ± 0.2 Hz at MJD 51270.7 (see B12), a similar power spectrum to that at MJD 51270.7 but without the high frequency QPO at MJD 51271.4, only one QPO at 5.2 ± 0.2 Hz at MJD 51287.2 (see B13), one broad component at 7 ± 2 Hz at MJD 51289.1 (B14, similar power spectra at MJDs 51291.1, 51291.3, 51293.4, 51307.3 and 51309.7) a QPO and a broad Lorentzian at 10.3 ± 0.3 and 4.1 ± 0.3 Hz, respectively, at MJD 51290.9, 2 broad components at 21 ± 8 and 3.6 ± 0.5 Hz at 51291.2 and similarly but at 15 ± 3 and 4.6 ± 0.6 Hz at MJD 51291.3, a QPO and a broad component at 5.2 ± 0.3 and 1.4 ± 0.1 Hz, respectively, at MJD 51307.4 (see B15) and a broad Lorentzian at 0.068 ± 0.009 Hz at MJD 51318.8.

These changes in time and colors are summarized in Figures 8.4 & 8.10. As can be seen in these figures, the detection of significant power usually coincides with periods in which the energy spectrum hardens, but not always. For example, the hard color starts to increase at MJD 51300, but it is not until $\sim$ 8 days later that we find significant power.

So, during the first $\sim$ 85 days of this outburst we detect broad band noise with approximately constant characteristics and rarely, QPOs at frequencies higher than 10 Hz. During the following $\sim$ 20 days, and accompanied with a hardening of the spectrum, we detect much more variability in the form of both broad band components and QPOs. As can be seen in Figure 8.10, we find no relation between the characteristic frequency of the components and their fractional rms amplitude.

In Figure 8.16 we plot the characteristics of the different components versus hard color. In the upper panel of this figure we show that the characteristic frequency of the broad band noise at frequencies higher than 0.5 Hz may anti–correlate with color, although only marginally. In the case of the components at frequencies lower than 0.5 Hz, no clear trend is observed and the dispersion of the data points is high. In the bottom panel of Figure 8.16 we show the QPO data, and find that their characteristic frequency is rather constant. Most of these data at hard colors lower than Crab. This is similar to what was seen in outburst C (Section 8.7.4), where the QPO frequency of data at hard colors lower than Crab was also rather constant. However, it differs from outburst A data, in which the QPO frequency clearly anti–correlates with hard color down to 0.4 Crab.

8.8 Discussion

We have analyzed the power spectra of 427 observations of the black hole candidate XTE J1550–564. In Figures 8.8–8.13 we show that generally it is possible to follow the time evolution of the different components we find in the power spectra as they shift in frequency and vary in strength and coherence. This information together with the hardness dependency of the component characteristics (Figures 8.14–8.18) helps identifying the different components.

In this section we assume that each power spectrum is composed of a small number ($<$ 10) of components which evolve smoothly in time (although they do not need to be always present) and whose identity can be established based on following this evolution and the correlated motions through the HID. The correct identification is a critical issue, as up to 8 simultaneous significant components with variable frequency are found in the 0.01–500 Hz range. Incorrect identification will lead to spurious frequency-frequency relations and therefore wrong physical interpretations. We first identify QPOs and broad components based on how the characteristics of the power spectral components evolve in time and vary as a function of hard color. Then, we discuss our results in the context of the PBK and WK frequency–frequency relations.

8.8.1 Low frequency QPO identification

From the component identification point of view, the low frequency QPOs (< 20 Hz) are the easiest to recognize. Figures 8.14 & 8.15 show that in outburst A there are mainly 3 different tracks of QPOs with frequencies anti-correlating with hard color. However, the 3 QPOs are not always detected (e.g., at colors harder than 1) and sometimes a fourth QPO is also detected at higher or lower frequencies (e.g., B8).

Following Klein-Wolt & van der Klis (2008) we call the QPO in the middle track show in Figures 8.14 and 8.16 L_{LF}, where LF stands for low frequency. This QPO is easy to identify, as it is the strongest of the three. The QPOs at higher and lower frequency of L_{LF} are called L^+_{LF} and L^-_{LF}, respectively. Note that the + and – only denote that the frequency of the component is higher or lower than that of the strongest QPO, respectively. It has been suggested (e.g. Wijnands et al. 1999; Homan et al. 2001; Remillard et al. 2002a) that these QPOs are harmonically related, where L^+_{LF} and L^-_{LF} are the second harmonic and the sub-harmonic of L_{LF}, respectively. To the best of our knowledge, no systematic study of this issue has been made as yet. It would require to refit all the power spectra with Lorentzians (in terms of centroid frequencies) and is beyond the aim of this paper. In the case of outburst C, there are only two clear tracks (Figure 8.17). The lower one corresponds to the strongest QPO and therefore we call it L_{LF}. The upper one, which has a similar separation as that between L_{LF} and L^+_{LF} in outburst A, we call L^+_{LF}. Note finally, that we do not make a distinction between Type C and Type B QPOs. In both the Type C and Type B QPO power spectra, we identify the middle QPO as L_{LF} and those on the sides as L^+_{LF} and L^-_{LF} (see also Klein-Wolt & van der Klis 2008). This is justified by the fact that the Type B QPOs seem to extend the anti-correlation between the Type C QPO frequencies and hard color measured in LS and HIMS power spectra, as well as the anti–correlation between the QPO fractional rms amplitude and hard color (see, e.g., Figures 8.14 & 8.15 for outburst A).

8.8.2 Broad components identification

The classification of the broad components is more difficult. The clearest case of three separate simultaneous components, Aa, Ab and Ac, is shown in Figure 8.15 for a subset of data during outburst A. Comparing these data with the shape of the power spectra, we find that the Ac components (i.e. the ones with lowest frequency) are the Lorentzians which fit the the *break* in power detected at low frequencies, Ab are the Lorentzians which fit the *hump* in power found at characteristic frequencies near, but usually slightly higher than those for the low frequency QPO L_{LF}, and Aa are the Lorentzians fitting the power excess with highest characteristic frequencies. Comparing our results with those of Klein-Wolt & van der Klis (2008), we find that these components clearly correspond to L_b, L_h and L_ℓ (or L_u, see below), respectively.

The Lorentzian at the break (L_b) and at the hump (L_h)

As the source evolves from the LS to the HIMS (i.e. to softer states in outbursts A and C), ν_{LF} increases, sometimes we detect its harmonic and/or subharmonic and most importantly, we generally detect only one broad component at frequencies lower than ν_{LF}. In these cases (see, e.g., group Ac in Figure 8.15 and during most of outburst C decay) we identify this component as L_b. We find that in this subset of data the $\nu_{LF} - \nu_b$ pairs correlate. In the rest of this work we assume that correlation always holds, so when more than one component is detected with frequency $< \nu_{LF}$, we use it to identify L_b.

As noted by Belloni et al. (2002b, see also Klein-Wolt & van der Klis 2008), L_{LF} and L_h are often close in frequency, separated by no more than a few Hz, and seem to form a closely coupled set of features. (This was also noted by van Straaten et al. 2002, 2003 for two similar components in neutron star power spectra). As shown in Section 8.7, QPOs are only detected during outbursts A, B and C. These QPOs can appear on top of strong (e.g., A1/A3, A5/A11, B8, C1/C4, C12/C13) or weak (e.g., A12, B7, C5) broad band noise and then have typically been called Type C or B QPOs, respectively. In the first cases, L_h is significantly detected, but when the noise is weak, there is no need for that component (see, e.g., figure 4 by Klein-Wolt & van der Klis 2008).

As shown in Sections 8.7.4 and 8.7.5, at the beginning of the outbursts A and C (i.e., in the LS) the power spectra do not show a significant component at frequencies lower than ν_{LF}. This might be because the data lack sufficient statistics to detect it. As a result, it is probable that L_b blends with L_h into a broad (Q=0) component with characteristic frequency in between ν_b and ν_h (Klein-Wolt & van der Klis 2008), although always higher than ν_{LF}. So, the components identified as L_h in our work might be the blend of two components, when L_b is not significantly detected, i.e. in the period MJD 51063–51067 (α_3 during outburst A, see Figure 8.9) in outburst A, and only for observations 50137-02-01-00/02-00/03-01G/05-00 and 50134-02-01-00 in the period MJD 51644.5–51664.4 in outburst C.

During observations of the outburst B HS, QPOs appear at frequencies between 10 and 20 Hz when no broad band noise is detectable in their frequency range (see, e.g., B3). It has been suggested that the QPO in these observations is another manifestation of L_{LF}, i.e. a Type C QPO that is detected in the HS (Homan et al. 2005) at higher frequencies than those measured in the IMS.

Power spectra like B6 can be similarly interpreted. Klein-Wolt & van der Klis (2008) tentatively identified the components in this type of power spectrum as follows: the QPO is L_{LF} and the broad components with frequency $< \nu_{LF}$ are L_h, L_b and VLFN (for very low frequency noise) in order of decreasing frequency, respectively.

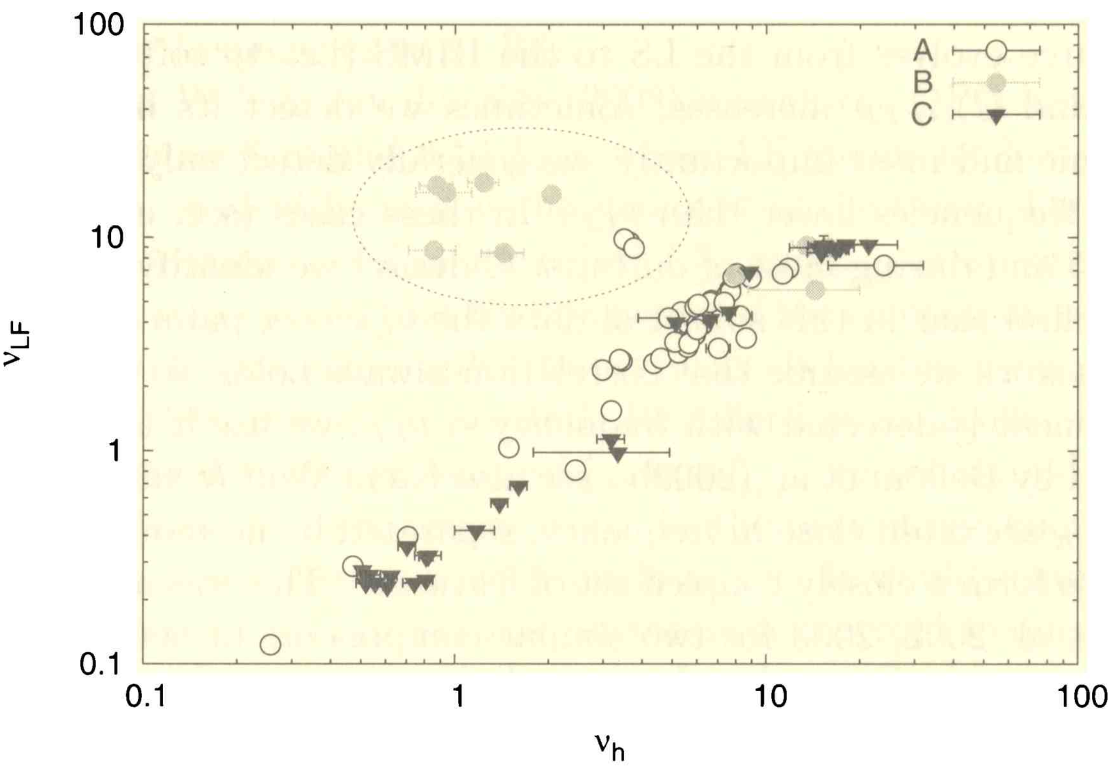

Figure 8.30: L_{LF} characteristic frequency versus that of L_h during outbursts A, B and C, as indicated. The points marked by the ellipse clearly do not follow the main correlation. See Section 8.8.2 for a discussion.

In Figures 8.30 & 8.31 we plot ν_{LF} vs. ν_h and ν_{LF} vs. ν_b, respectively, using the classifications described above. We find that our identifications follow a narrow relation except for a groups of points which correspond to power spectra like B3 and B6 (filled grey circles). In Figures 8.30 & 8.31 we enclose these points with an ellipse. These data are not consistent with either of the correlations. If instead we identify ν_h as ν_b, these power spectra fit better to the ν_{LF} vs. ν_b plot but still do not match well.

The data points from outburst A which do not follow the relation ν_{LF} vs. ν_h (also enclosed within the ellipse in Figure 8.30) correspond to the power spectra similar to A6, for which $\nu_h < \nu_{LF}$. However, our identifications do follow the ν_{LF} vs. ν_b (3 open circles at $\nu_b \sim 1.5 - 2$, at the upper end of the correlation shown in Figure 8.31). These power spectra correspond to those observations that followed the 6.8 Crab flare observed during outburst A. We find 3 significant components at frequencies lower than ν_{LF} (see, e.g., A5 and A6 – see also C10). In these power spectra we measure the highest values of

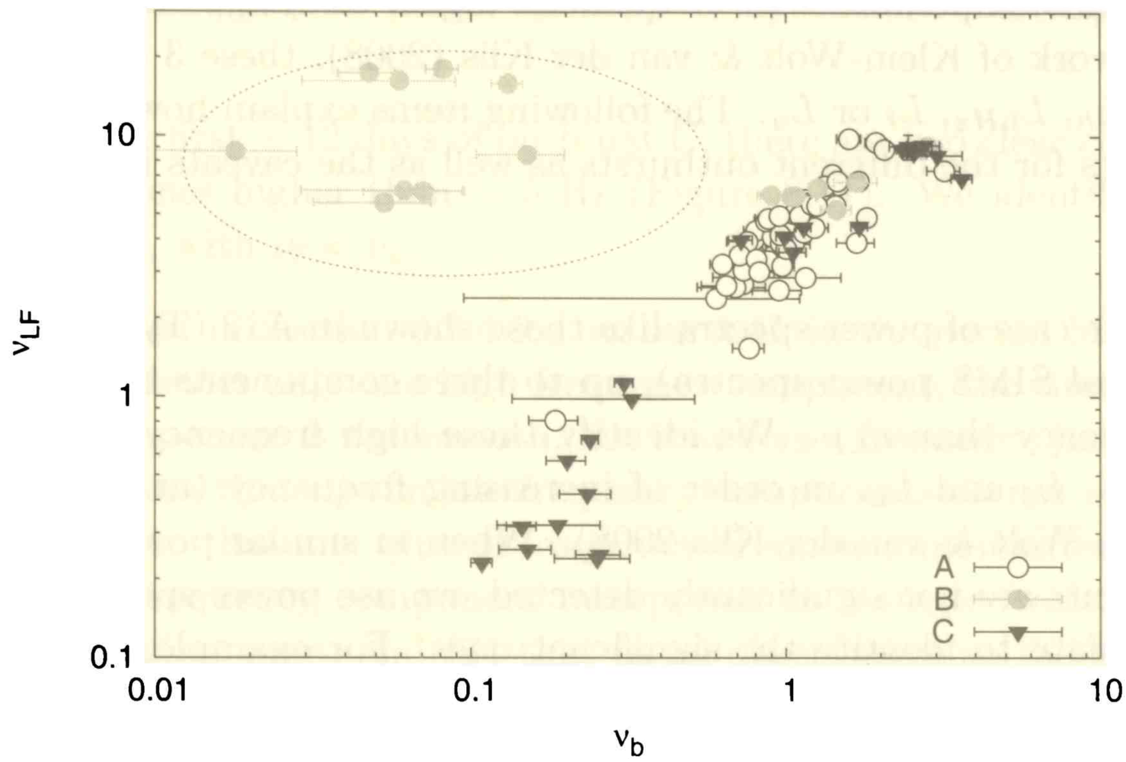

Figure 8.31: L_{LF} characteristic frequency versus that of L_b during outbursts A, B and C, as indicated. The points marked by the ellipse clearly do not follow the main correlation. See Section 8.8.2 for a discussion.

ν_{LF} (see Sections 8.7.5 & 8.7.4). We assume that in these observations ν_{LF} has switched to slightly higher frequencies than ν_h and this is why the points do not follow the $\nu_{LF} - \nu_h$ correlation. Another possibility is that L_h is one of the two broad components at higher frequency than ν_{LF}. Identifying ν_h with the highest of the two does not move the data points onto the correlation. Identifying ν_h with the other high frequency component might extend the correlation. However, we find that correlation $\nu_{LF} - \nu_h$ would flatten (not plotted). As we discuss in the following section, the two high frequency components are probably L_ℓ and L_u. Therefore, in order of decreasing frequency we identify L_{LF}, L_h, L_b and the VLFN as the QPO and the three broad components at $\leq \nu_{LF}$, respectively. As only 4 observations show this type of power spectra, our identifications should be considered only tentative.

The high frequency components L_{hHz}, L_ℓ and L_u

As discussed by Klein-Wolt & van der Klis (2008), the possible blends between broad components imply several caveats regarding their identification, particularly in the case of high frequency components. In order to identify the high frequency components we take ν_{LF} as a reference frequency and we use the information on the evolution of the components that we present in Figures 8.8, 8.9, 8.10 and 8.11. We find that in our sample there are no more than 3 broad components with frequencies higher than ν_{LF}. Reasoning within the framework of Klein-Wolt & van der Klis (2008), these 3 components can be either L_h, L_{hHz}, L_ℓ or L_u. The following items explain how we identify the components for the different outbursts as well as the caveats in the identifications.

(I) In the case of power spectra like those shown in A12 (Type B QPOs, i.e. typical SIMS power spectra), up to three components appear at higher frequency than ν_{LF}. We identify these high frequency components as L_{hHz}, L_ℓ and L_u, in order of increasing frequency (at $\nu \gtrsim 40$ Hz, see Klein-Wolt & van der Klis 2008). When in similar power spectra components are not significantly detected, we use power spectrum A12 as a template to identify the significant ones. For example, in B7 we identify as L_{hHz} and L_ℓ the two high frequency components based on their characteristic frequency. We note that L_{hHz} only appears in this type of power spectra and fits the power in between the low frequency and the high frequency QPOs. It is identified as a different component than L_h, as ν_{hHz} is much higher than ν_{LF} and does not follow the correlation presented in Figure 8.30. (However, we note that as discussed in Section 8.8.2, the relation between ν_{LF} and ν_h might flatten at high values of ν_{LF}. If L_{hHz} is actually L_h, then the relation would have a break, after which ν_{LF} and ν_h anti-correlate. Although this is possible, we cannot confirm it, as A12 or B7 power spectra are a small subset of our data. Therefore, to be consistent with the work of Klein-Wolt & van der Klis 2008, we use the L_{hHz} identification). We also note that the L_ℓ and L_u in the SIMS can be highly coherent (Q$>$ 4) compared with those measured in the typical HIMS and LS power spectra, which are usually broad Lorentzians. As it is not yet clear whether the high frequency QPOs are a particular manifestation of the high frequency broad components at a certain spectral state or if they represent unrelated phenomena, in the rest of this section we are consistent with the work of Klein-Wolt & van der Klis (2008) and call the high frequency QPOs at the SIMS L_ℓ and L_u.

(II) As discussed in Section 8.7.5 and shown in Figure 8.9, during the pre-flare period in outburst A there are two high frequency components that are sometimes simultaneously detected (α_1 and α_2). Based on the time evolution presented in Figure 8.9, we interpret α_1 as L_u and α_2 as L_ℓ.

(III) B8 is the only power spectrum of HIMS/LS type during outburst B. We detect two high frequency components which we identify as L_ℓ and L_u

based its similarity to power spectra during outburst A (e.g., A10 and A11).

(IV) During the first $\sim$ 12 days of outburst C, there are two clear components at frequencies higher than $\sim$ 5 Hz (Figure 8.11). We identify them as L_ℓ and L_u, with $\nu_\ell < \nu_u$.

(V) As we report in Section 8.7.4 for outburst C, in the period MJD 51672–51705 we detect only one high frequency component; the time evolution of this component is not smooth, but it suffers a frequency jump at MJD 51685. Given that (i) the low frequency components do not show a similar jump, so that any type of frequency–frequency correlation involving this high frequency component interpreted as a single feature will also show a similar jump and (ii) that in an observation at the time of the jump, we find two simultaneous high frequency components that can be identified as L_ℓ and L_u, we conclude that before the jump we are measuring L_u and after the jump L_ℓ. Note, that this is a different interpretation from that chosen by Klein-Wolt & van der Klis (2008), who also noticed this jump but followed Psaltis et al. (1999) when identifying the components and therefore assigned most of these components to L_ℓ.

(VI) Given [4] and [5] and Figure 8.11, we identify the high frequency components in the period MJD 51660–51672 (outburst C) as L_u (note that only one is present, always at $\nu > 100$ Hz, and apparently connecting the ν_u tracks at times < 51660 and > 51672.

During the post–flare period in outburst A, and except for the A12 type of power spectra [see point (1) above], we detect only one broad component at high frequency which can be either L_ℓ or L_u (or even L_{hHz}). The time evolution nor the dependency on color allows an unambiguous identification. We use the frequency–frequency relations that we find from the data in which we could unambiguously identify the components, and find that all these components were more consistent with being L_u than L_ℓ. In Figure 8.32 we show the relations between ν_u and ν_{LF} (upper panel) and between ν_ℓ and ν_{LF} (lower panel). As is obvious from this figure, the relations are relatively broad collections of points not well fitted with a power law. Note that these figures compare the same frequencies as the PBK relation (Section 8.8.3) which was found to be broad in previous works as well (Belloni et al. 2002b).

Broad components in outbursts B, C, D, E and F when L_{LF} is not present

As described in previous sections, during the decay of outburst C we find that the ν_{LF} decreases with time and so do ν_h and ν_b, the frequencies of the broad

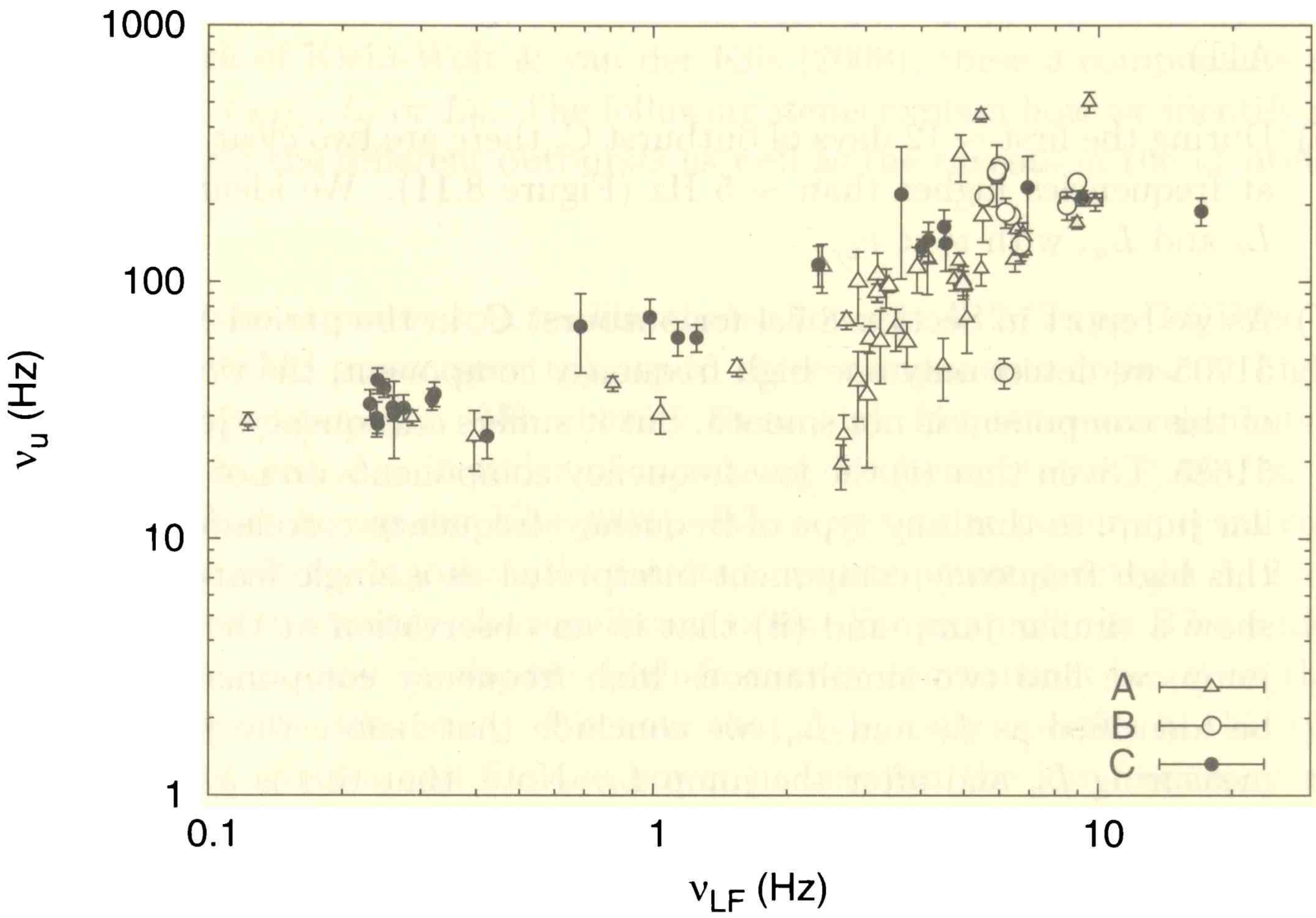

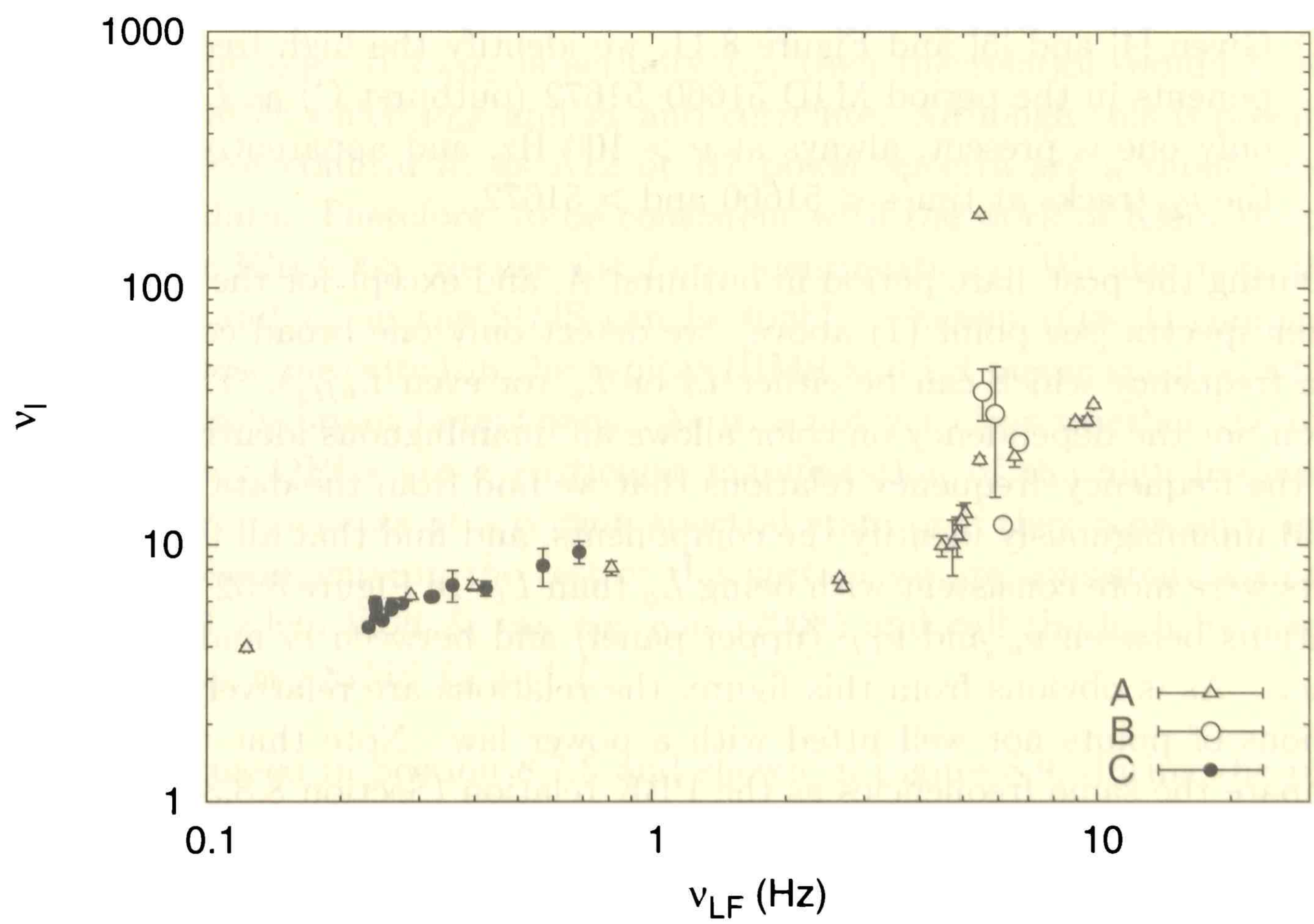

Figure 8.32: ν_u vs. ν_{LF} (upper panel) and ν_ℓ vs. ν_{LF} (lower panel) for data during outbursts A, B and C, as indicated. Both panels have the same scale. See Section 8.8.2 for a discussion on the identifications.

components at both sides of L_{LF}. We also find that L_u is detected during the first part of the decay, and L_ℓ during the second, for a total of 3 broad components (i.e. L_b, L_h and either L_ℓ or L_u). The last time the QPO is detected in MJD 51690 (C14, the source is already in its low–luminosity LS), after which we only detect two (broad) significant components in power spectra (C15) whose frequencies keep decreasing with time, although not smoothly, until they are not detected anymore. Extrapolating in time the evolution of ν_ℓ, ν_h and ν_b (see Figure 8.11, we find that the transition from 3 to 2 broad components is probably explained as either (i) the blend of L_b with L_h (see also Figure 7a in Klein-Wolt & van der Klis 2008) or (ii) that L_b is not significantly detected anymore. So, the two broad components can be identified as the pair $\nu_{b+h} - \nu_\ell$ or $\nu_h - \nu_\ell$.

As shown in Section 8.7.3, during outbursts D, E and F we find that the power spectra are similar to those in the low–luminosity LS of outburst C, and can be fitted with 2 to 3 broad components. Given this, and the fact that they represent the variability of the source in the same spectral state (i.e., in the low state), it is reasonable to assume that the power spectral components are the same as in C, i.e. L_b, L_h and L_ℓ, possibly blended. When only two significant components are present in the power spectra, they can be the couple $\nu_b - \nu_h$, $\nu_{b+h} - \nu_\ell$, $\nu_b - \nu_{h+\ell}$, $\nu_h - \nu_\ell$ or $\nu_b - \nu_\ell$ (where the subindices $b+h$, and similarly with the other combinations, indicate the blend of the components L_b and L_h). When 3 components are significant, they should unambiguously be $\nu_b - \nu_h - \nu_\ell$.

In Figure 8.33 we plot ν_b vs. ν_h (lower correlation) and ν_ℓ vs ν_h (upper correlation) for the data during outbursts A, C, D, E and F. The components corresponding to all data in outburst A and in the period MJD 51640–51690 of outburst C (black points) are as defined in Sections 8.8.2 & 8.8.2. For outburst C data after 51690, we use the classification as described above ($\nu_h - \nu_\ell$). With red, orange and grey we mark the data from outbursts D, E and F, respectively, when only 2 components were significantly detected. With blue and green we mark the data from D and F, respectively, when 3 components were significantly detected. As can be seen in the $\nu_\ell - \nu_h$ correlation, at high frequencies there are a few points that are off the relation that the rest of the data follow. These points are marked with an arrow in Figure 8.33 and represent the power spectra similar to A6, i.e. those in which we interpret that ν_h has switched to lower frequencies than ν_{LF}.

If it is assumed that when 3 broad components are found in the power spectra, they are L_b, L_h and L_ℓ with $\nu_b < \nu_h < \nu_\ell$, we find that the data follow the correlations expected from outbursts A and C data, suggesting that our identifications are correct (see blue and green in Figure 8.33). However,

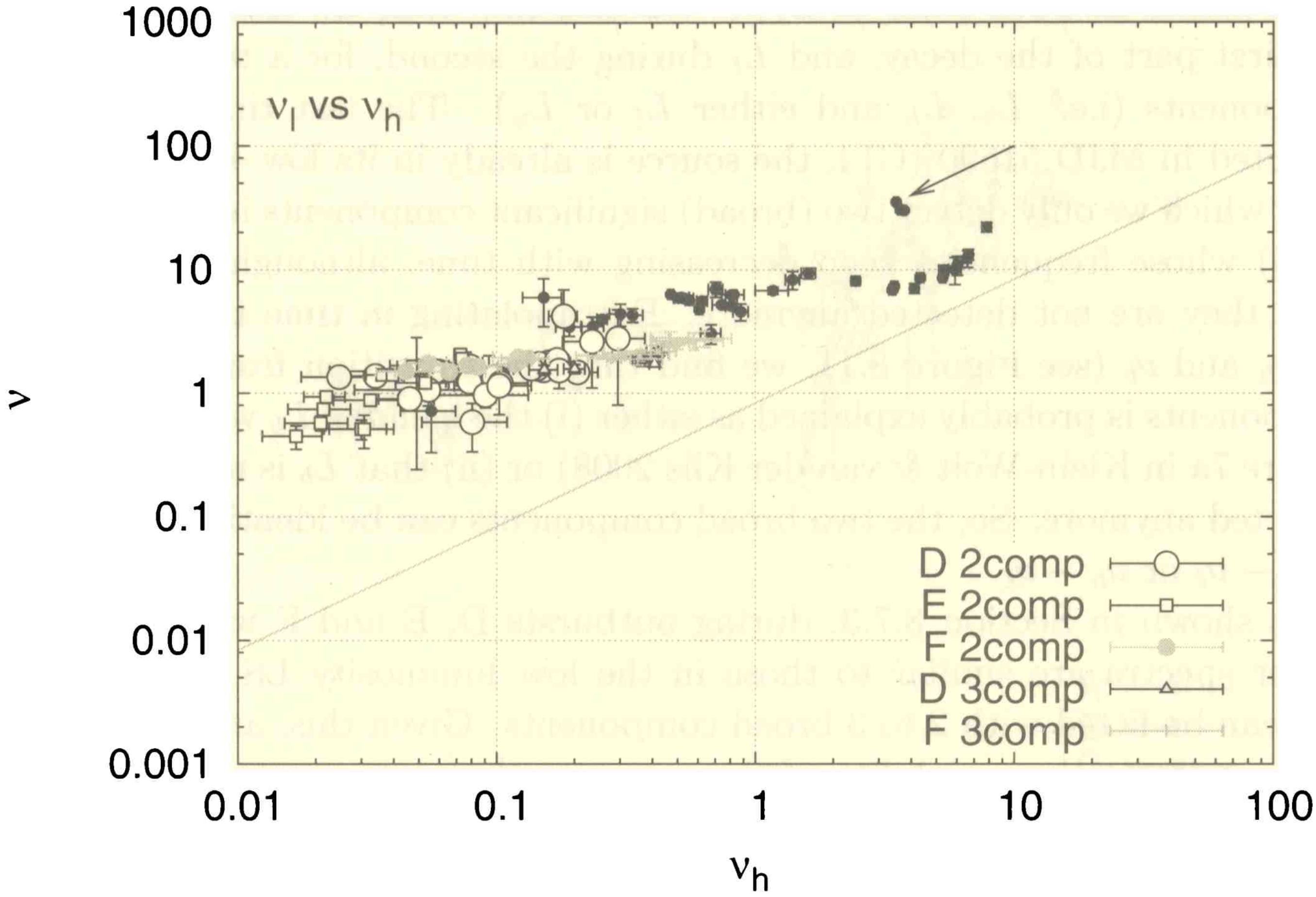

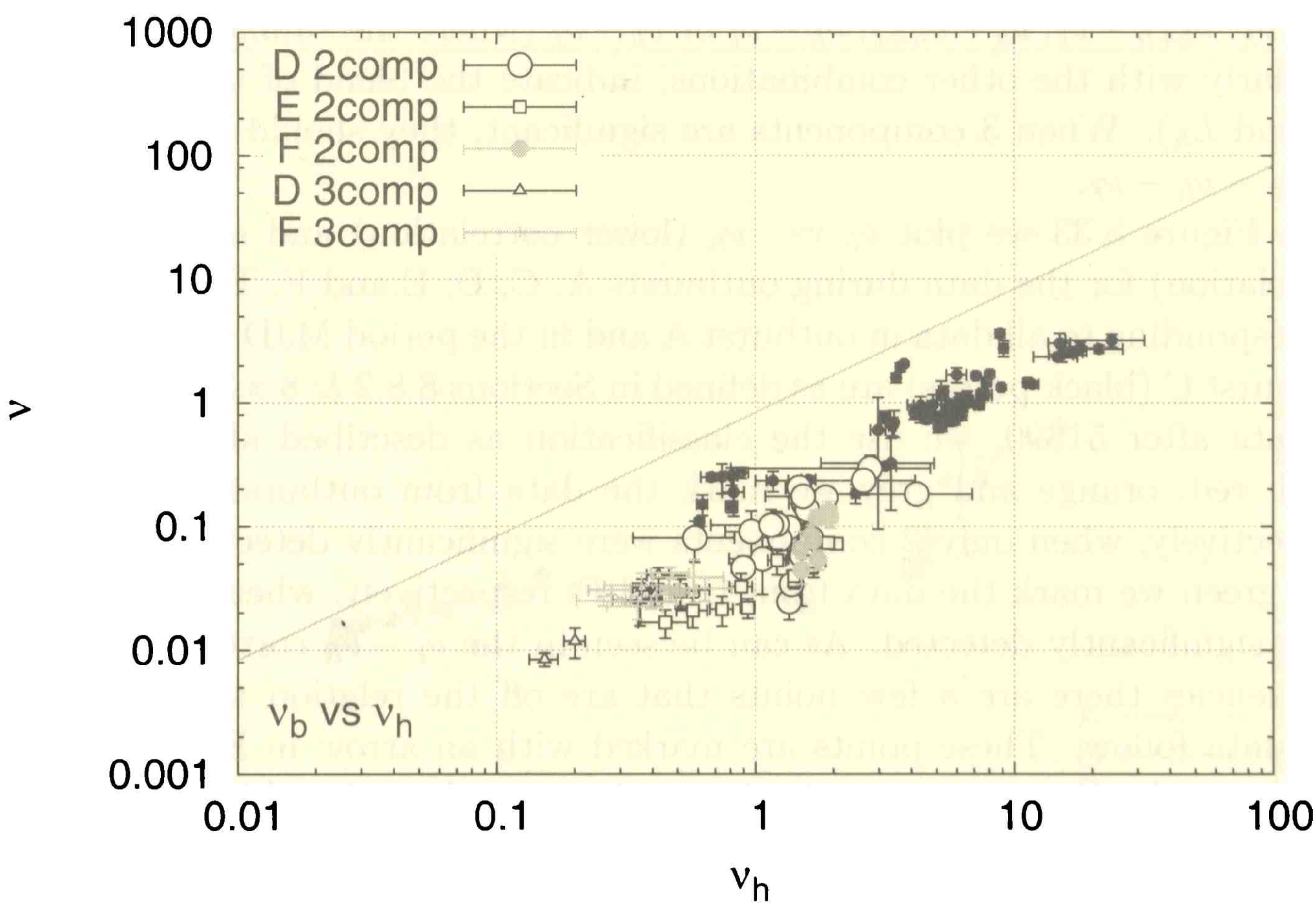

Figure 8.33: ν_b vs. ν_h (bottom panel) and ν_ℓ vs. ν_h (upper panel) for the data during outburst A, C, D, E and F as indicated. Different symbols are used for power spectra with 2 or 3 significant broad components. See Section 8.8.2 for a discussion on the identifications.

we also find that different pair combinations also follow the correlations to similar accuracy. For instance, the pairs ν_h vs. ν_b for outburst D extend the upper correlation in Figure 8.33 (not plotted) to lower frequencies, i.e. extend the ν_ℓ vs. ν_h correlation as marked by the data of outbursts A and C.

The situation is more complex when only two components are present (red, orange and grey). If they are the pair $\nu_b - \nu_h$, we find that they fall on the lower correlation in Figure 8.33. However, if we consider them as the pair $\nu_h - \nu_\ell$, they fall on the upper one.

In Section 8.7.6 we show that during the flaring period in outburst B, and when the source is in a spectral state about 4 orders of magnitude softer and more than an order of magnitude brighter (in terms of count rate) than those reported for D, E and F, we find that the power spectrum is also fitted with 2 to 3 broad Lorentzians (plus, sometimes, a sharp Lorentzian for a QPO) with characteristic frequencies approximately constant at $\sim$ 2 and $\sim$ 0.1 Hz (see Figures 8.10 & 8.16). When 3 components are significantly detected, Klein-Wolt & van der Klis (2008) identified them as VLFN, L_b and L_h (with $\nu_{VLFN} < \nu_b < \nu_h$) based on the evolution of the different power spectral components as the black hole sources move in the LS→IMS→HS direction. We find the $\nu_b - \nu_h$ pairs as suggested by these authors follow the corresponding correlation in Figure 8.33. However, as the power spectral shape is similar to that during the LS of outburst D, E and F, and there is no smooth time evolution of the components from the HIMS to the HS in our data that can be used to identify the components, in principle other identifications are also possible. If the two broad components with highest frequency are interpreted as the pair $\nu_h - \nu_\ell$ (instead of the pair $\nu_b - \nu_h$), we find that the frequency points fall on the upper correlation shown in Figure 8.33. Furthermore, for those cases in which three broad components are significant, the pair $\nu_{VLFN} - \nu_b$ can also be interpreted as $\nu_b - \nu_h$ as they fall on top of the lower correlation in Figure 8.33.

Given the above, we conclude that for the HS power spectra of outbursts B, and the LS power spectra of D, E and F, it is not possible to unambiguously identify the broad components based on the frequency–frequency correlations we find between power spectral components during outburst A and C. However, if the outburst D, E and F power spectra are the same as those during the decay of outburst C, then the components probably are $\nu_h - \nu_\ell$ (or $\nu_{b+h} - \nu_\ell$) or $\nu_b - \nu_h - \nu_\ell$, depending on whether the power spectra are well fitted with two or three significant components, respectively.

8.8.3 XTE J1550–564 and the PBK relation

From the point of view of component classification, the PBK relation relates the ν_{LF} or ν_h with that of ν_ℓ.

In the 6 panels in Figure 8.34 we plot the PBK relation (grey circles) as reported by Belloni et al. (2002b) (see also grey points in figure 11 in Klein-Wolt & van der Klis 2008). In Figure 8.34a we over-plot the pairs $\nu_{LF} - \nu_\ell$ and $\nu_h - \nu_\ell$ measured in outburst C power spectra. As can be seen, our data are on top of the PBK relation and follow its general power-law trend.

In Figure 8.34b, we over-plot the pairs $\nu_{LF} - \nu_\ell$ (black triangles) measured in outburst A power spectra, in which both L_u and L_ℓ are simultaneously significant. (We note that since ν_h is generally higher than ν_{LF}, the pairs $\nu_h - \nu_\ell$ form a similar pattern as that shown in Figure 8.34b but at higher frequencies in the abscissa. For clarity, these data are not plotted). As can be seen, the data at $\nu_{LF} < 2$ Hz seem to fall on top of the correlation, although with a steeper slope. The data at $\nu_{LF} > 4$ Hz do not fall on the correlation. In principle, if the PBK relation holds for all sources, this could mean that one of the components that we are plotting has been wrongly identified. As all the components with frequencies lower than our ν_ℓ are well defined (particularly L_{LF}, see Sections 8.8.1 & 8.8.2) the only possibility is that what we identify as L_u is L_ℓ and that what we identify as L_ℓ is another component, like L_{hHz} or one that has not yet been identified. To further investigate this, in Figure 8.34b we also over plot the $\nu_{LF} - \nu_u$ pairs (open circles). As can be seen, the data at $\nu_{LF} < 2$ Hz do not fall on the correlation, while those at $\nu_{LF} > 4$ Hz are closer to the correlation but appear to define a correlation that is less steep. The two points at ν_ℓ and ν_u higher than 100 Hz correspond to the power spectra A12 (the so-called Type B QPO) and do not seem to follow the correlation either. This is probably because the high frequency QPOs in black holes have rather constant frequency (see Section 8.2; see also van der Klis 2006, for a review) while ν_{LF} varies. Figure 8.34c we over-plot outburst A data when only L_u is significantly detected (note that as discussed in Section 8.8.2, when only one high frequency component is detected during outburst A, we identify it with L_u). The $\nu_{LF} - \nu_u$ pairs seem to follow the track marked by the PBK relation, although not on top, but parallel to it (in this case, the pairs $\nu_h - \nu_u$ do fall on the relation – not plotted).

In Figures 8.34d we compare the PBK relation with our $\nu_h - \nu_\ell$ pairs found during outbursts D and F when 3 broad components were simultaneously detected (see Section 8.8.2) and similarly in Figure 8.34e, but for outbursts D, E and F when only two broad components were simultaneously detected. In the first case, the data fall near to the relation and in the second case, the data seem to extend the relation. We note however, that as a priori we

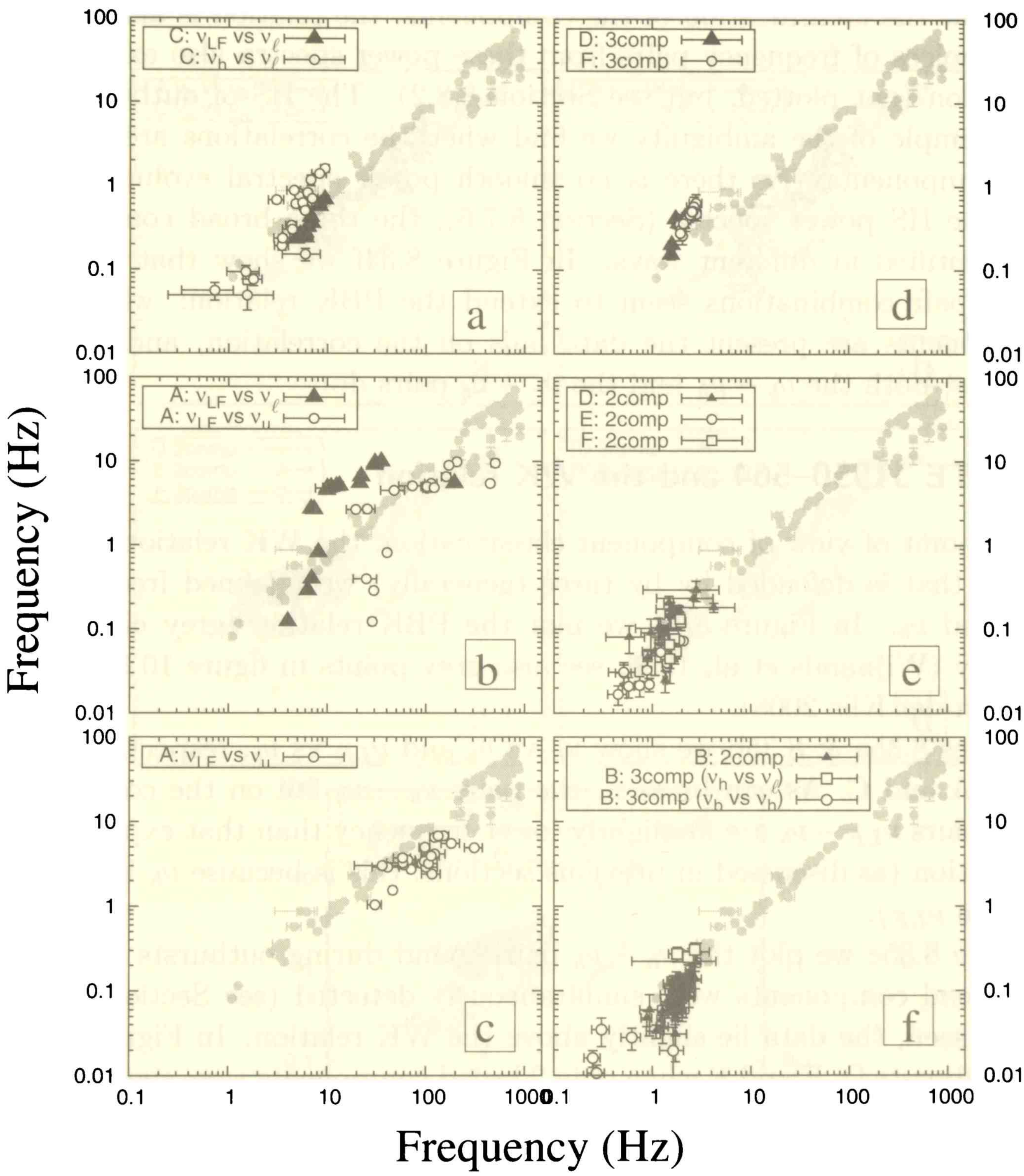

Figure 8.34: PBK relation as reported by Belloni et al. 2002b (grey circles, see also figure 11 by Klein-Wolt & van der Klis 2008). *Panel a:* ν_{LF} vs. ν_ℓ (triangles) and ν_h vs. ν_ℓ (open circles) measured in outburst C power spectra. *Panel b:* ν_{LF} vs. ν_ℓ (triangles) and ν_{LF} vs. ν_u (open circles) measured in outburst A power spectra, in which both L_u and L_ℓ are simultaneously significant. *Panel c:* ν_{LF} vs. ν_u measured in outburst A power spectra when only L_u is significantly detected (note that as discussed in Section 8.8.2, when only one high frequency component is detected, we identify it as L_u). *Panel d:* ν_h vs. ν_ℓ during outbursts D and F power spectra when 3 broad components were simultaneously detected. *Panel e:* ν_h vs. ν_ℓ during outbursts D, E and F power spectra when only two broad components were simultaneously detected. *Panel f:* HS outburst B data. Three different frequency pair combinations seem to extend the PBK relation: when only two components are present, they fall on the correlation, and when 3 components are present, both the ν_b vs. ν_h and the ν_h vs. ν_ℓ pairs do.

do not know the identification of the components, the relation is ambiguous, as other choices of frequency pairs from these power spectra also extend the PBK relation (not plotted, but see Section 8.8.2). The HS of outburst B is a good example of the ambiguity we find when the correlations are used to identify components. As there is no smooth power spectral evolution that leads to the HS power spectra (Section 8.7.6), the three broad components can be identified in different ways. In Figure 8.34f we show that different frequency pair combinations seem to extend the PBK relation: when only two components are present the data falls on the correlation, and when 3 components, both the $\nu_b - \nu_h$ and the $\nu_h - \nu_\ell$ pairs do.

8.8.4 XTE J1550–564 and the WK relation

From the point of view of component classification, the WK relation has the advantage that is defended by by three (generally) well defined frequencies: ν_{LF}, ν_h and ν_b. In Figure 8.35 we plot the PBK relation (grey circles) as reported by (Wijnands et al. 1999; see also grey points in figure 10 in Klein-Wolt & van der Klis 2008).

In Figures 8.35a & 8.35b we show ν_h vs ν_b and ν_{LF} vs ν_b, respectively, for outbursts A and C. As can be seen, the pairs $\nu_h - \nu_b$ fall on the correlation while the pairs $\nu_{LF} - \nu_b$ are at slightly lower frequency than that expected by the correlation (as discussed in previous sections, this is because ν_h is usually higher than ν_{LF}).

In Figure 8.35c we plot the $\nu_h - \nu_b$ pairs found during outbursts D and F when 3 broad components were simultaneously detected (see Section 8.8.2). As can be seen, the data lie slightly above the WK relation. In Figure 8.35d we plot outbursts D, E and F when only 2 broad components were significantly detected. In this case the data seem to extend the WK relation. In Figure 8.35e we plot the HS outburst B data. When only 2 components are present, the data seem to lie slightly above the WK relation. The pairs $\nu_\ell - \nu_h$ and $\nu_h - \nu_b$ both seem to lie on the correlation.

8.8.5 Power spectra that do not fit the previous classifications

In this section we describe the power spectra that are not included in the classifications proposed in this paper and therefore do not appear in any of the frequency–frequency relations discussed above. This specifically concerns power spectra similar to A4, A13, A14, B10, B11, B13, B14, C6, C7 and C8.

Power spectra A14 and C6 occur at approximately the same time the source starts a decrease in intensity at rather constant hardness (see Sections 8.7.4 & 8.7.5, respectively). As can be seen in Figures 8.20 & 8.22, their power spectral

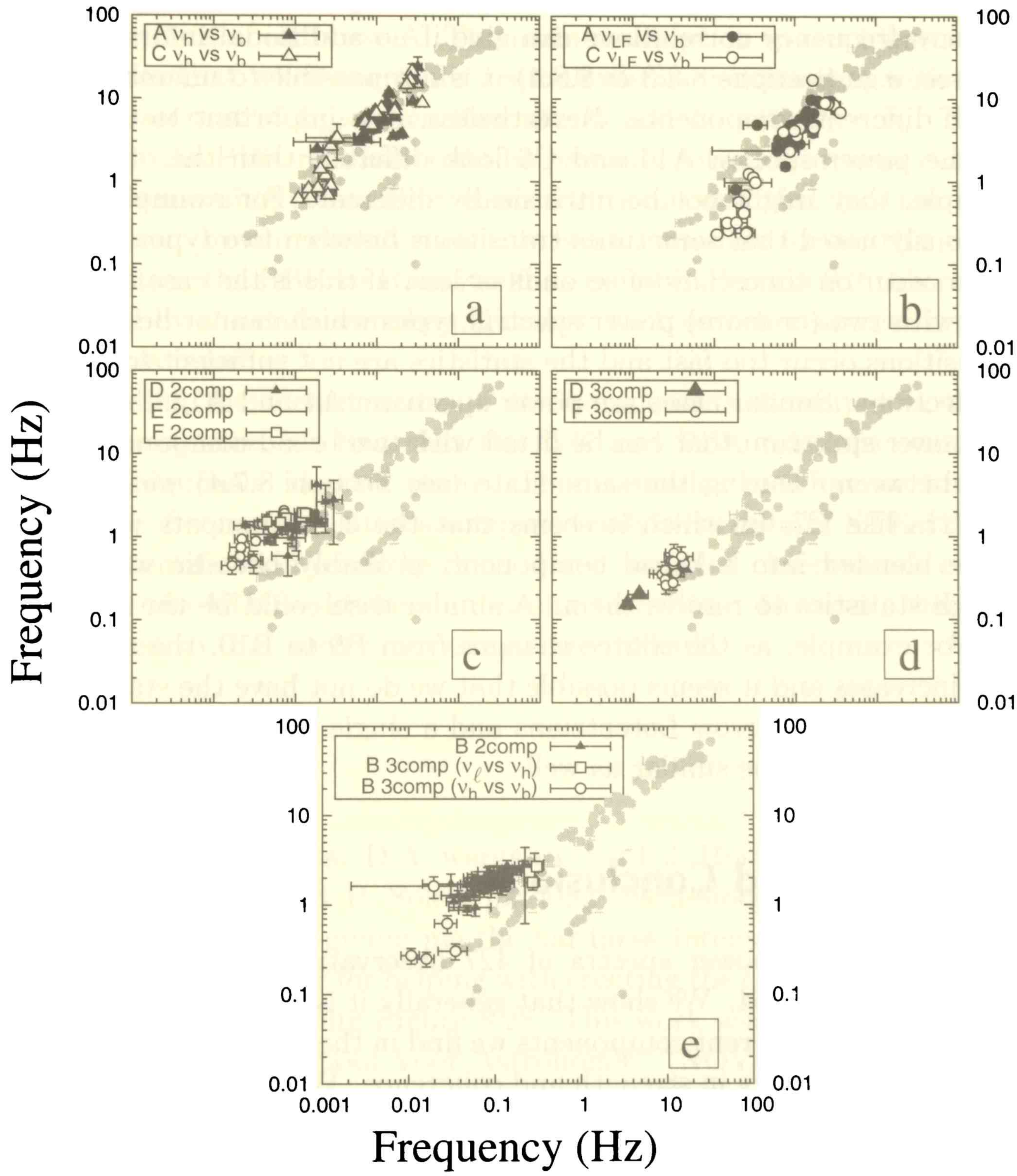

Figure 8.35: WK relation as reported by Wijnands et al. (1999) (grey circles, see also figure 10 by Klein-Wolt & van der Klis 2008). *Panel a:* ν_h vs. ν_b data for outburst A (filled black triangles) and C (open triangles). *Panel b:* ν_{LF} vs. ν_b data for outbursts A (filled black circles) and C (open circles). *Panel c:* outbursts D, E and F data when only 2 broad components were significantly detected. *Panel d:* ν_h vs. ν_b during outbursts D and F power spectra when 3 broad components were simultaneously detected. *Panel e:* HS outburst B data when only 2 (triangles) and 3 (squares and circles) components are significantly detected. Squares represent the pairs ν_ℓ vs. ν_b, circles the ν_h vs. ν_b ones.

shape is almost identical. As the power spectral shape does not resemble any of the other ones sampled in our data set, and given the ambiguity that the frequency–frequency correlations can give if no additional information is available (see, e.g., Sections 8.8.3 & 8.8.4) it is not possible to unambiguously identify the different components. Nevertheless, it is important to note that although the power spectra A14 and C6 look different than the other ones in our sample, they might not be intrinsically different. For example, it has been previously noted that sometimes transitions between two types of power spectra can occur on timescales of seconds or less. If this is the case, we could be dealing with two (or more) power spectral types which cannot be resolved, as the transitions occur too fast and the statistics are not sufficient to do time or color selections. Similar cases are power spectrum A4 and A13.

C8 is a power spectrum that can be fitted with two broad components with a QPO in between. During the same state (see Section 8.7.4) we also find power spectra like C7, in which it seems that the 3 components we detect in C8 have blended into a broad component, probably because we do not have enough statistics to resolve them. A similar case could be the sequence B9–B15. For example, as the source changes from B9 to B10, the total rms amplitude increases and it seems possible that we do not have the statistics to distinguish between 2 narrow Lorentzians and a single broad one. B11→B12 and B14→B15 seem to be similar as well.

8.9 Summary and Conclusions

We have analyzed the power spectra of 427 observations of the black hole candidate XTE J1550–564. We show that generally it is possible to follow the time evolution of the different components we find in the power spectra as they shift in frequency and vary in strength and coherence. We use this information together with the hardness dependency of the component characteristics to identify the different components. We show that with our identifications, the frequencies of most of the power spectral components measured in the HIMS and LS correlate with each other.

By comparing the observed correlations with each other and with previous works it is possible to confirm the identifications we made. However, in the sense of these correlations some of our identifications are ambiguous, as other component identification combinations sometimes prove to follow the same correlation. In particular this is the case for the high-state components observed during outburst B and for the low-state components observed in outbursts D, E and F.

Finally we have compared our identifications with the WK and PBK relations. We find that the frequencies of our identified components follow the WK relation, but this is not always the case for the PBK relation, e.g., the post-flare data of outburst A. The main assumption in our identification procedure was that when there are 2 simultaneous components with frequencies higher than that of L_{LF}, then they are L_ℓ and L_u with $\nu_\ell < \nu_u$. The discrepancy with the PBK relation could be partially solved if in some cases L_ℓ is L_u and the remaining component is an additional one that has not been taken into account by our classification. It is also possible to use this result to all into question the PBK relation itself; as noted in Section 8.3 this relation may be biased by the data sampling. Further work on other sources is required to decide this issue.

Regarding the identification of the components measured in the HS and LS power spectra, we find that the WK and PBK relations cannot be used to unambiguously identify them. This is similar to what we find with the frequency–frequency relations composed only with data of XTE J1550–564. A proper identification could be done if well–sampled observations could be obtained of the HIMS→LS low-luminosity transition. However, this transitions can be fast so that such observations are difficult.

Acknowledgments: D.A. wants to thank J. Homan for discussions on BH states, P. Casella and P. Soleri for long discussions about BH timing variability, T. Belloni for giving me the hardness–intensity diagram of GX 339–4 (Figure 8.1), Asaf Peer for helping with creating the color figures and P. Casella for helping with creating Figure 8.28. This work was supported by the "Nederlandse Onderzoekschool Voor Astronomie" (NOVA), i.e., the "Netherlands Research School for Astronomy"

8.10 Appendix I: on the $< 3\sigma$ fitted components

In this appendix we describe the cases in which we included components that were less than 3σ significant.

During outburst A: From a total of 382 Lorentzians fitted, 9 were less than 3σ significant. 4 out of these 9 cases fitted a clear excess of power at frequencies $\sim$ 96, $\sim$ 115, $\sim$ 167 and $\sim$ 263 Hz with significances of 2.92, 2.86, 2.63 and 2.98σ, respectively (in observations 30188-06-06-00, 30188-06-05-00, 30191-01-05-00 and 30514-03-41-00, respectively). The remaining 5 were components that were needed for a stable fit. Their frequencies were $\sim$ 0.96, $\sim$ 5.91, $\sim$ 26.2, $\sim$ 30.72, $\sim$ 39.0 Hz and had significances of 2.49, 2.11, 2.92, 2.72 and 2.86σ, respectively (in observations 30191-01-28-00, 30191-01-28-01, 30191-01-12-00, 30435-01-01-01 and 30191-01-34-00, respectively).

During outburst B: From the 278 Lorentzians fitted, 5 were less than 3σ significant. In 3 out of the 5 cases the components were needed for a stable fit. These Lorentzians had characteristic frequencies of 0.22, 0.04 and 25 Hz and significances of 2.97, 2.8 and 2.4σ, respectively (Obs-Ids: 30435-01-14-01, 40401-01-73-00 and 40401-01-57-00, respectively). In the 2 remaining cases, the Lorentzians have frequencies of 15.9 and 16.3 Hz and significances of 2 and 2.8σ, respectively (Obs-Ids: 40401-01-06-01 and 40401-01-18-01, respectively). These components were kept since they proved to significantly improve the χ^2/dof. Furthermore, Homan et al. (2001) have shown that these components are significant when several observations are added together to improve the signal to noise ratio.

During outburst C: From a total of 177 Lorentzians fitted, 8 were less than 3σ significant. In 5 out of the 8 cases, the components were needed for a stable fit. They were at frequencies $\sim$ 2.4, $\sim$ 1.9, $\sim$ 0.7, $\sim$ 0.8 and $\sim$ 17.2 Hz and had significances of 2.7, 2.1, 2.9, 2.3 and 2.7σ, respectively (in observations 50135-01-03-00, 50135-01-04-00, 50137-02-03-00, 50137-02-07-00 and 50134-02-02-01, respectively). The remaining 3 cases correspond to features fitted in 2 continuous observations. The power spectra of these observations are similar to power spectrum B12 (see Figure 8.21). If averaged together we find 3 significant components at $\sim$ 3, $\sim$ 9 and $\sim$ 21 Hz. However if studied separately we find that in the case of observation 50134-02-04-01, the components at $\sim$ 9 and $\sim$ 21 Hz are 2.4 and 2.9σ significant, respectively and for observation 50134-02-05-00 the component at $\sim$ 9 Hz is 2.7σ.

During outburst D: From a total of 68 Lorentzians fitted, 2 were less than 3σ significant but were needed for a stable fit. The characteristic frequencies of these Lorentzians were 0.29 and 2.62 Hz with significances of 2.97 in both cases (in observations 50137-02-25-00 and 50137-02-30-00, respectively).

During outburst E and F we fitted a total of 36 and 58 Lorentzians, respectively. All of them were significant at to the 3σ level.

8.11 Appendix II: observing modes

Outburst A started on MJD 51063 and lasted until MJD 51150 for a total of 87 days covered with 78 PCA observations. The first observation was performed on MJD 51063.71 (ObsId: 30188-06-02-00) with the Good Xenon mode. Unfortunately, the source was too bright and data were lost due to insufficient telemetry rate. We therefore excluded this observation from our timing analysis. The remaining 77 observations were observed using a combination of Single Bit and Event modes in order to prevent similar problems: ObsId 30188-06 and most of ObsId 30191-01 were observed using the modes SB_125us_0_17_1s, SB_125us_18_35_1s and E_16us_16B_36_1s. These combination lead to a maximum time resolution of 1/8192 sec and a Nyquist frequency of 4096 Hz. The remaining observations (30191-01-04-00/05-00/06-00/09-00/09-01/09-02/10-00) were observed with a combination of the modes SB_125us_0_13_1s, SB_125us_14_17_1s, SB_125us_18_23_1s, E_125us_64M_24_1s and SB_250us_0_249_2s_2LLD. We first calculated the power spectra without the 2LLD mode for a Nyquist frequency of 4096 Hz and searched for features at frequencies higher than 2000 Hz. None were found, then we recalculated the power spectra adding together the 1LLD events and twice the 2LLD events in order to improve our sensitivity. These are the modes used in this paper; the power-spectra final Nyquist frequency is 2048 Hz.

Outburst B started on MJD 51150 as a continuation of outburst A (see Section 8.7.1 and Figure 8.24) and lasted until MJD 51325 for a total of $\sim$ 175 days. During this period, RXTE observed XTE J1550–564 on 171 opportunities with the PCA. ObsId 30435-01 and most of ObsId 40401-01 were observed using a combination of the modes SB_125us_0_17_1s, SB_125us_18_35_1s and E_16us_16B_36_1s. This combination led to a maximum time resolution of 1/8192 sec and a Nyquist frequency of 4096 Hz. The remaining observations (40401-01-91/99 and 40501-01-01-00) were observed using the Good Xenon mode. Observation 40501-01-01-00 was performed when the source was too bright and data were lost due to the high intensity of the source. We therefore excluded this observation from our timing analysis (as it was the case of observation 30188-06-02-00 in outburst A). The rest of the observations which were recorded in using the Good Xenon mode were performed during the decay of the outburst and did not suffer from telemetry problems. The intensity points in Figure 8.25 at MJD$\sim$ 51403 correspond to the slew observations 40142-04-01-01R, 40142-04-01-02R, 40142-04-01-03R and were excluded from our timing analysis.

Outburst C started on MJD 51630 and lasted until MJD$\sim$ 51730 for a total of $\sim$ 100 days covered by 67 PCA observations and 3 different types of mode combinations. Observations 50134-01-01/05, 50134-02-04-00/08-01 and 50135-01/02 were observed using the single bit modes SB_125us_0_13_1s and SB_125us_14_35_1s in combination with the event mode E_8us_32M_36_1s. Given the low time resolution of the event mode, in the observations 50134-01-01/05 we only used the single bit modes. Observations 50134-02-01/02-03 were observed using the modes SB_125us_0_17_1s, SB_125us_18_35_1s and E_16us_16B_36_1s. Observations 50135-01-03/30 were observed using the event mode E_125us_64M_0_1s. In all cases, the combination of modes led to a maximum time resolution of 1/8192 sec and a Nyquist frequency of 4096 Hz.

Outbursts D, E and F were sampled with 48, 27 and 25 observations, all recorded using the event mode *E_125us_64M_0_1s* which led to a maximum time resolution of 1/8192 sec and a Nyquist frequency of 4096 Hz. We searched each observation for data anomalies and found that 50137-02-34-00 on MJD 51999.5 (outburst D) showed a sudden increase of count rate which was significantly different between the 3 PCUs which were on. We therefore interpret this increase in the count rate as probably instrumental and therefore excluded it from our analysis. The power spectrum of this observation is well described with a power law with index 2.01 ± 0.06 Hz.

8.12 Appendix III

For each outburst we have shown representative power spectra in the νP_ν representation (see Figures 8.20–8.23) which is useful as it allows to easily visualize the relative importance of Lorentzian components. Another representation of power spectra is the P_ν representation, i.e. the power spectral density estimate P_ν is plotted versus the frequency ν. This representation is useful as well, as it allows to visualize flat tops (white noise ranges) of power spectra at low frequencies and also how the power spectrum deviates from a broken power law. As this representation has been widely used in the past. In Figures 8.36–8.39 of this Appendix we re-plot Figures 8.20–8.23 in the P_ν representation so that it is possible to compare the plots with previous works. In all figures, the ordinate is in units of rms normalized power density [in $(\text{rms/Mean})^2\ \text{Hz}^{-1}$] and the range is always $3 \times 10^{-7} - 1$ for outbursts A, B and C, and in the range $3 \times 10^{-7} - 40$ for outbursts D, E and F. This makes it easier to compare the changes in total fractional rms amplitude between source states and source outbursts. In the same figures, the abscissa is in units of Hz and for outbursts A, B and C is in the $3 \times 10^{-3} - 4096$ Hz range, while for outbursts D, E and F is in the $3 \times 10^{-4} - 4096$ Hz range. The difference in abscissa range chosen allows to better describe the characteristics of the power spectra in the different outbursts. In all cases, we have re-binned the data differently between panels to balance between the frequency resolution and the signal-to-noise ratio.

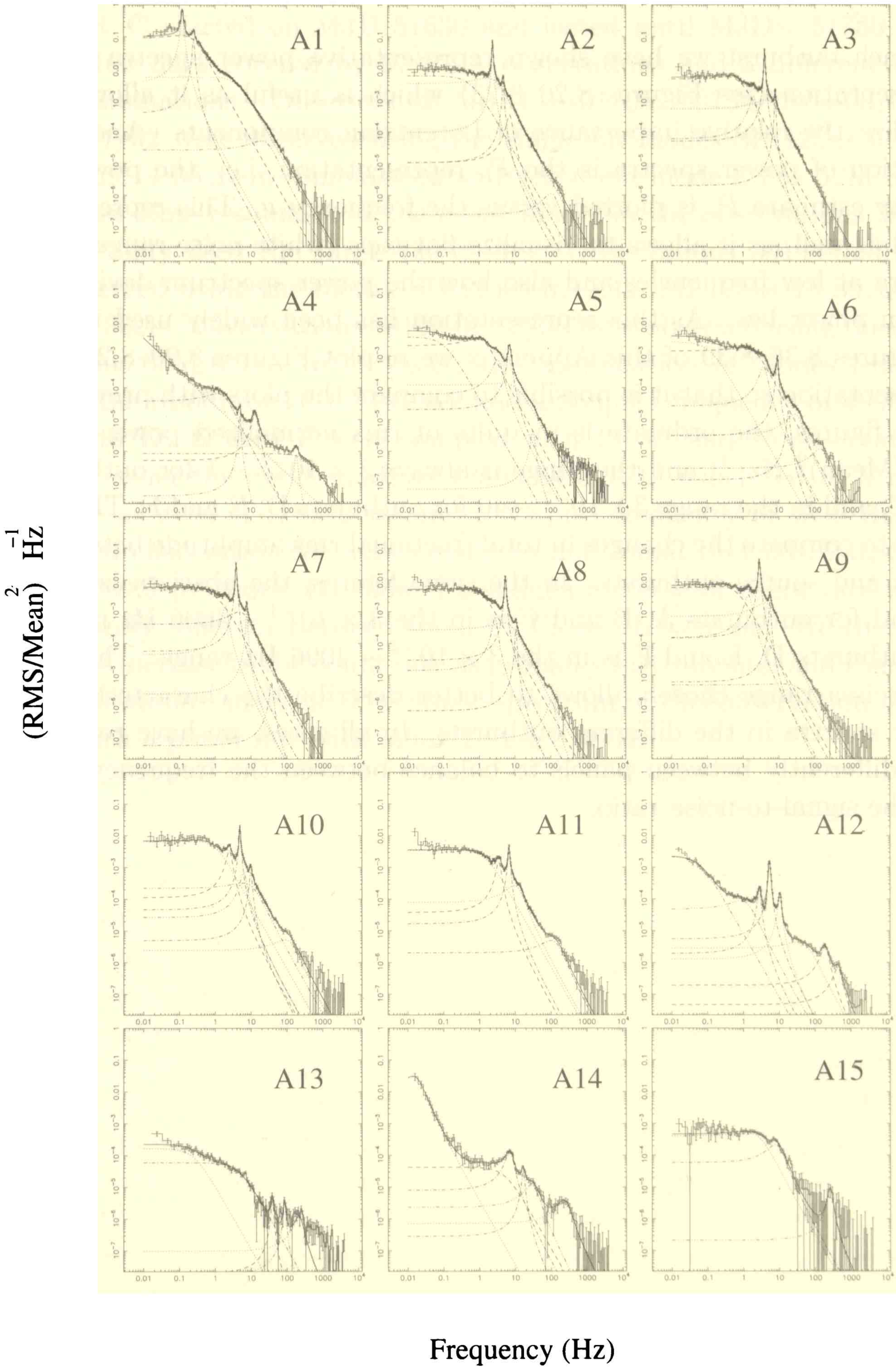

Figure 8.36: The same as Figure 8.20 but all panels are in the $P\nu$ representation See Appendix III

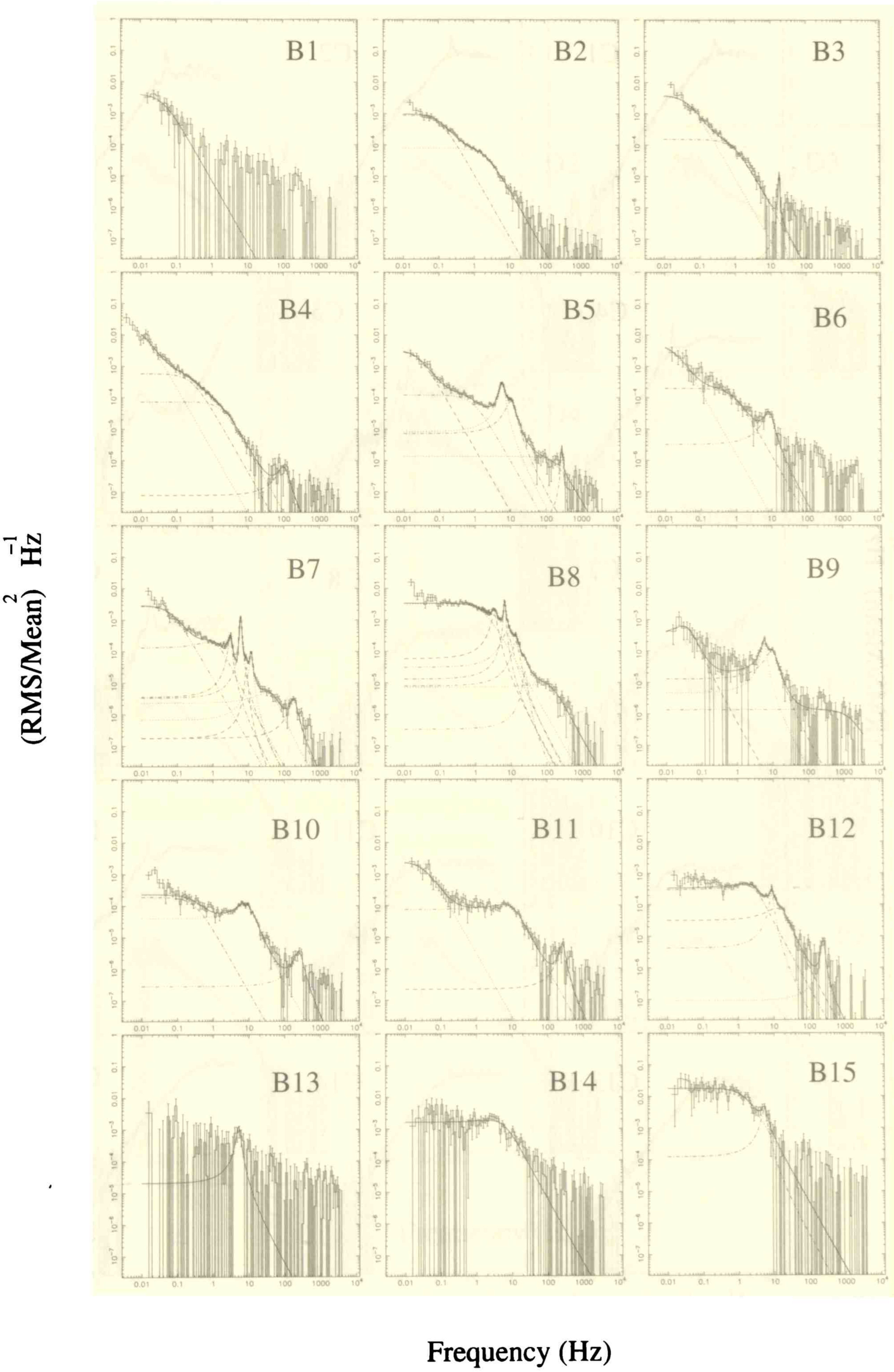

Figure 8.37: The same as Figure 8.21 but all panels are in the $P\nu$ representation. See Appendix III

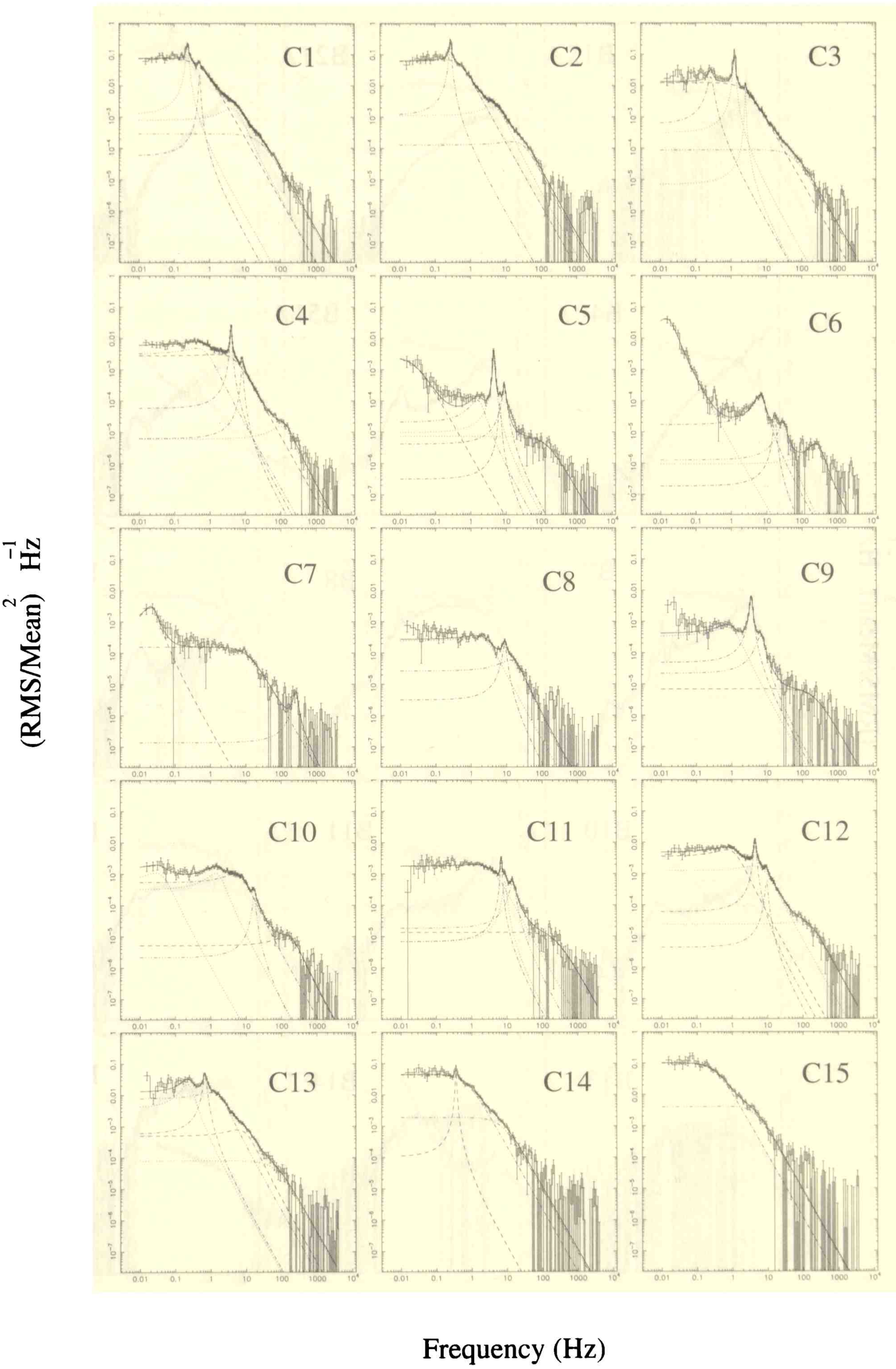

Figure 8.38: The same as Figure 8.22 but all panels are in the $P\nu$ representation – See Appendix III

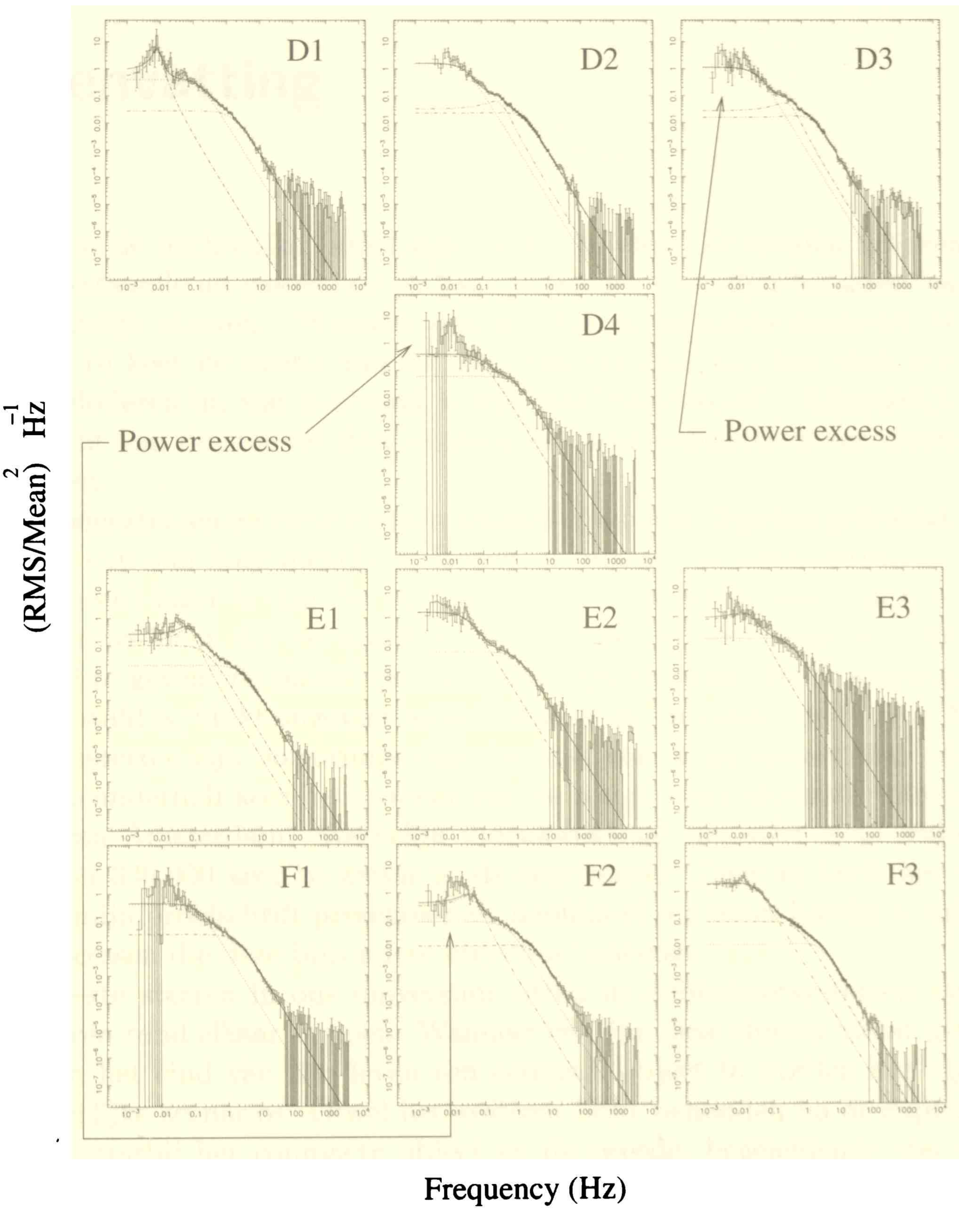

Figure 8.39: The same as Figure 8.23 but all panels are in the $P\nu$ representation - See Appendix III

Samenvatting

Overal aan de nachtelijke hemel zijn sterren te zien. Ze worden geboren uit wolken bestaande uit gas en stof en leven miljoenen tot miljarden jaren waarna ze uiteindelijk sterven. Wanneer een ster bij de geboorte zwaarder is dan ongeveer 10 keer de massa van de zon, dan zal deze aan het eind van zijn leven exploderen in, wat genoemd wordt, een "Supernova". Afhankelijk van het gewicht van de ster zal deze explosie een neutronenster of een zwart gat achterlaten.

Neutronensterren en zwarte gaten worden compacte objecten genoemd vanwege hun extreem hoge dichtheid. Hoewel de massa van neutronensterren (in het algemeen) lager is dan die van zwarte gaten, is het volume van een neutronenster zo klein dat de dichtheid nog steeds extreem hoog is. Om een voorbeeld te geven: de massa van neutronensterren, zoals die in sommige gevallen bepaald is, blijkt ongeveer anderhalf keer die van onze zon te zijn. Maar neutronensterren zijn bolvormige objecten met een straal kleiner dan 15 km. Dit is dus anderhalf keer het gewicht van de zon in een bolvormig volume ter grootte van Amsterdam. Werkelijk indrukwekkend, wanneer je je realiseert dat de zon 330.000 keer zo zwaar is als onze aarde. Daarom heeft het werk dat ik in mijn proefschrift presenteer als hoofddoel een beter inzicht te krijgen in de processen die deze bijzondere objecten beheersen.

De meeste sterren in ons universum zitten in dubbelstersystemen waarin twee sterren rond elkaar draaien. Wanneer één van deze sterren zwaar genoeg is om aan het eind van zijn leven een compact object te worden dan zijn er twee mogelijke scenarios. Ofwel het systeem blijft behouden na de supernova explosie, waarbij het compacte object en de tweede, begeleidende ster rond elkaar blijven draaien, ofwel het systeem valt uiteen als gevolg van de explosie.

Als het dubbelstersysteem na de explosie behouden blijft en als ook de afstand tussen het compacte object en de begeleidende ster niet al te groot is, dan zal het gas van de begeleidende ster aangetrokken worden door de sterke zwaartekracht van het compacte object. Dit gas zal naar het compacte object vallen en door de rotatie van het systeem een spiraliserende beweging maken en een zogenoemde accretieschijf vormen. Dit traject van het gas is zicht-

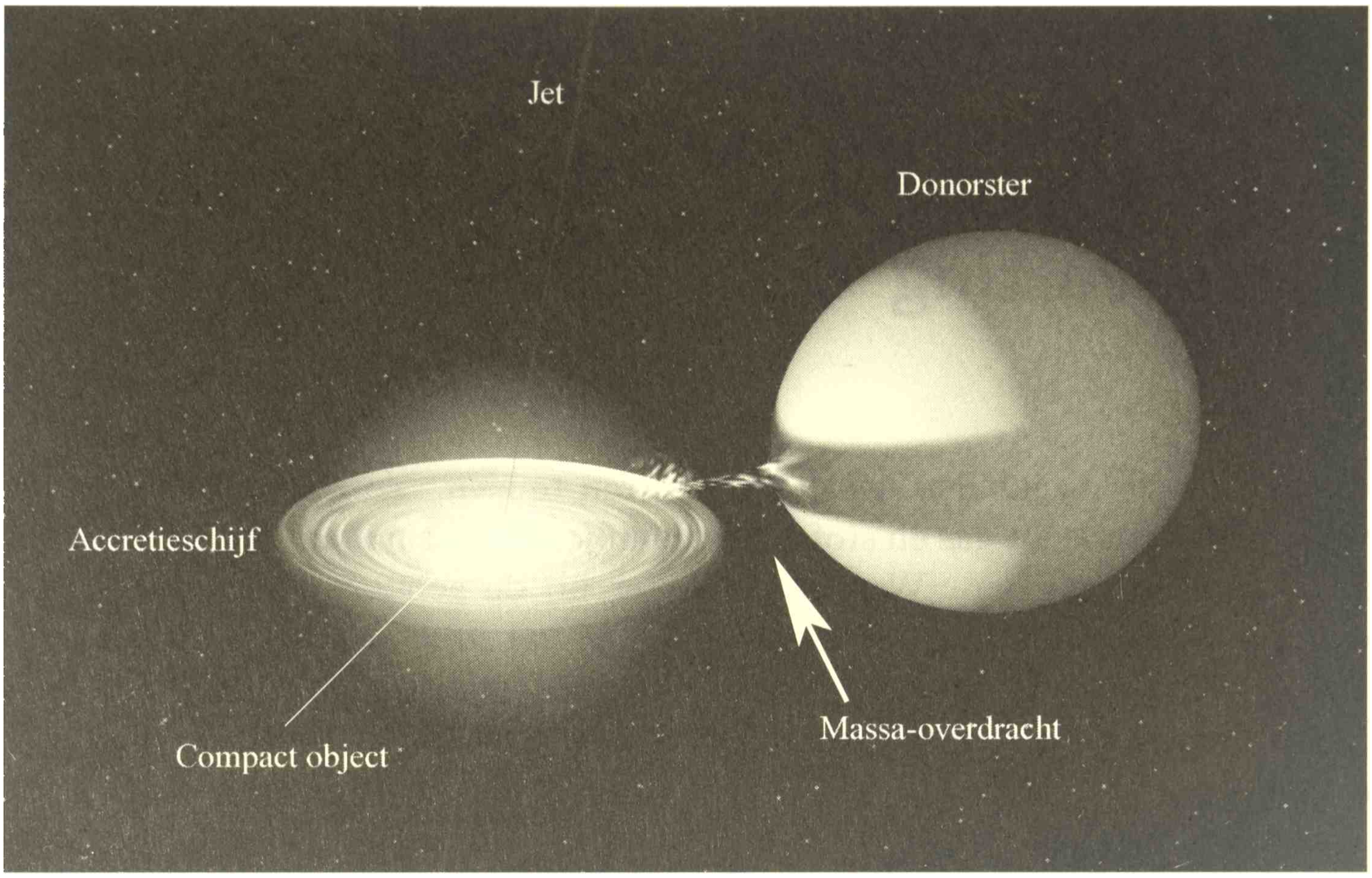

Figuur 1: Een tekening van een lage-massa röntgendubbelster. De gewone ster wordt ook wel donorster genoemt aangezien hij zijn massa overdraagt aan het compacte object.

baar in verschillende vormen van licht, maar is voornamelijk waarneembaar als röntgen straling. Een schets van zo'n systeem is te zien in Figuur 1. In mijn proefschrift beschrijf ik het onderzoek van enkele van de verschillende manifestaties van dit accretieproces zoals die in röntgenstraling worden waargenomen.

Om deze objecten te bestuderen maak ik gebruik van waarnemingen die zijn gedaan met de Rossi X-ray Timing Explorer satelliet. Dit is een telescoop die röntgenfotonen registreert die van deze objecten afkomstig zijn. Hierbij worden zowel het aantal fotonen als hun energie geregistreerd per tijdseenheid, waarbij de aankomsttijd van de fotonen zeer nauwkeurig bepaald wordt. Met deze informatie is het mogelijk om periodieke of quasi-periodieke tijdsfluctuaties in de röntgenhelderheid van accreterende compacte objecten te onderzoeken, die weer gebruikt kunnen worden om deze systemen beter te kunnen begrijpen.

Eén van de voorspelde eigenschappen van zwarte gaten is dat ze geen oppervlak hebben (dit is misschien wel het grootste verschil tussen een zwart gat en een neutronenster), waardoor het alleen mogelijk is om het naar het zwarte gat toe spiraliserende gas te bestuderen. In hoofdstuk 8 presenteer ik een volledige analyze van de alle Rossi gegevens van het röntgendubbelstersysteem XTE J1550–564 waarin het compacte object zeer waarschijnlijk een zwart gat is. Tijdens deze studie heb ik vele verschijnselen bestudeerd die quasiperiodiek zijn. De eigenschappen van deze verschijnselen zich hangen af van de röntgenhelderheid van het systeem.

In het geval van neutronensterren is het mogelijk om zowel het naar binnen vallende gas te bestuderen alswel te zien wat er gebeurt wanneer het gas het oppervlak van de neutronenster raakt. Twee interessante voorbeelden die ik in mijn proefschrift heb bestudeerd, zijn:

(I) Thermonucleaire uitbarstingen: wanneer er zich genoeg gas op het oppervlak van de neutronenster heeft verzameld en daarmee de druk en ook de temperatuur in deze laag gas is toegenomen, zijn de omstandigheden dusdanig dat er waterstof- of helium-kernfusie geïnitieerd kan worden. Deze kernreactie manifesteert zichzelf als een 'nucleaire explosie' en wordt een röntgenflits genoemd. Deze flitsen duren slechts een paar seconden, herhalen zich verscheidene keren per dag, zijn onvoorspelbaar en produceren meer energie in 10 seconden dan de zon in één week.

(II) Accreterende milliseconde pulsars: pulsars zijn roterende neutronensterren waarbij er zeer regelmatige lichtpulsen opgewekt worden met een tussenpoos gelijk aan de rotatieperiode van de neutronenster. Deze lichtpulsen kunnen worden verklaard met behulp van het vuurtorenmodel: de pulsars zenden bundels van straling uit die periodiek over de Aarde scheren. Pulsars zijn extreem regelmatig en kunnen ook als de pulsen zeer zwak zijn nog worden waargenomen.

Er wordt onderscheid gemaakt tussen radiopulsars en röntgenpulsars afhankelijk van de soort straling die ze uitzenden. Voor röntgenpulsars wordt aangenomen dat de pulsen onstaan daar waar het geaccreterende gas de neutronenster raakt. In plaats van dat het gas uniform naar de neutronenster toevalt, wordt het gas gekanaliseerd door het aanwezige magnetisch veld van de pulsar. Het gas wordt naar de magnetische polen van de neutronenster gedreven en resulteert in hete plekken op het oppervlak van de neutronenster. Deze hete plekken zijn helderder in röntgenstraling dan de rest van het oppervlak van de neutronenster. Doordat de neutronenster roteert zullen deze hete plekken röntgenpulsaties veroorzaken in de waargenomen helderheid van het object met een periode gelijk aan de rotatieperiode van de neutronenster.

In hoofdstukken 5, 6 en 7 bestudeer ik de quasi-periodieke helderheidsvariaties die zich voordoen tijdens het accretieproces. Hieruit blijkt dat voor verschillende neutronensterren de manier waarop de materie naar de neutronenster toe spiraleert zeer veel overeenkomsten vertoond. In hoofdstuk 3 en 4 komen twee bijzondere accreterende milliseconde pulsars aan de orde. Deze pulsars zijn met tussenpozen actief, wat vergelijkbaar is met een vuurtoren waarbij de lamp het soms wel doet en soms niet. In hoofdstuk 2 bestudeer ik een bijzonder type helderheidsfluctuatie. Hoewel de aard van deze fluctuatie nog niet zeker is, lijkt het erop dat deze van het oppervlak van de neutronster komt en dat het gehele neutronensteroppervlak quasi-periodiek in helderheid varieert. In het begin zijn de schommelingen zeer snel, maar ze worden steeds langzamer en trager tot het punt bereikt wordt waarop een thermonucleaire flits kan plaatsvinden. Dit is de eerste keer dat we een waarneembaar verschijnsel kunnen gebruiken om het moment van de terugkerende flitsen te voorspellen. In andere woorden, we hebben voor het eerst een klok gevonden die ons kan vertellen wanneer de bom opnieuw gaat ontploffen.

Glossary

- **AMXPs**: Accreting millisecond X-ray pulsars (see, e.g., Chapters 3 & 4).
- **ASM**: All Sky Monitor (Levine et al. 1996). See also Section 1.2.1, page 2, for more details.
- **BH/BHC**: Black hole / Black hole candidate.
- **BLN**: Band Limited Noise.
- **BS**: Banana state, usually subdivided into LLB, LB and UB (used in the context of neutron star Atoll sources – See Figure 1.8 on page 13).
- **CD**: Color-diagram.
- **EIS**: Extreme island state (used in the context of neutron star Atoll sources – See Figure 1.8 on page 13).
- **FWHM**: Full width at half maximum.
- **GC**: Globular Cluster.
- **HEXTE**: High Energy X-ray Timing Experiment (Gruber et al. 1996; Rothschild et al. 1998). See also Section 1.2.1, page 2, for more details.
- **HBO**: Horizontal Branch Oscillation (used in the context of neutron star Z-sources).
- **HID**: Hardness-Intensity Diagram.
- **HIMS**: Hard Intermediate State (used in the context of BHC source states – See Section 1.4, page 12, and Section 8.2, page 141, for more details).
- **HMXB**: High-mass X-ray Binary.

- **HS**: High state (or 'high/soft state', used in the context of BHC source states – See Section 1.4, page 12, and Section 8.2, page 141, for more details).
- **IS**: Island state (used in the context of neutron star Atoll sources – See Figure 1.8 on page 13).
- **LB**: Lower banana (used in the context of neutron star Atoll sources' states – See Figure 1.8 on page 13).
- **LFN**: Low-frequency noise.
- **LLB**: Lower-left banana (used in the context of neutron star Atoll sources' states – See Figure 1.8 on page 13).
- **LMXB**: Low-mass X-ray Binary.
- **LS**: Low state (or 'low/hard state', used in the context of BHC source states – See Section 1.4, page 12, and Section 8.2, page 141, for more details).
- $\mathbf{L}_x$: X-ray Luminosity.
- $\mathbf{L}_{Edd}$: Eddington Luminosity.
- $\mathbf{L}_i$: Power spectral features are usually fitted with a function consisting of one or multiple Lorentzians, each denoted as L_i, where i determines the type of component. The characteristic frequency (ν_{max}) of L_i is denoted ν_i. In this thesis I use:
  - L_u for upper kHz QPO.
  - L_ℓ for lower kHz QPO.
  - $L_{\ell ow}$ for a feature that might be the same as L_ℓ, when $\nu_\ell \lesssim 50$ Hz (see also Section 7.3.6, page 124, for more details).
  - L_h for hump.
  - L_b for break.
  - L_{b2} for the second break.
  - L_{LF} for Low Frequency QPO.
  - $L_{LF/2}$ for the subharmonic of the Low Frequency QPO (in the context of NS, see Section 6.4.2, page 94, for more details).
  - L_{LF}^{+} **or** L_{LF}^{-} for the QPOs at higher and lower frequency than L_{LF} (in the context of BHC).

- L_{VLFN} for the Very-low frequency noise.

- $\dot{m}$: Local accretion rate (see Chapter 2).
- $\dot{m}_{Edd}$: Local Eddington accretion rate (see Chapter 2).
- **NS**: Neutron star.
- ν_0: centroid frequency of the Lorentzian (see also ν_{max}).
- ν_s: spin frequency of the neutron star.
- ν_{max}: Characteristic frequency of a Lorentzian L_i, defined as $\nu_{max} = \sqrt{\nu_0^2 + (FWHM/2)^2} = \nu_0\sqrt{1 + 1/4Q^2}$. See also L_i and Belloni et al. (2002b).
- **PCA**: Proportional Counter Array (Jahoda et al. 2006). See also Section 1.2.1, page 2, for more details.
- **PCU**: Proportional Counter Unit (Jahoda et al. 2006). See also Section 1.2.1, page 2, for more details.
- **PDM**: Phase dispersion minimization technique (Stellingwerf 1978). See also Section 1.2.1, page 7, for more details.
- **Q**: Quality factor of a Lorentzian. It is defined as $Q = \nu_0/FWHM$.
- **QPO**: Quasi-periodic oscillation.
- **RXTE**: Rossi X-ray Timing Explorer (Jahoda et al. 2006). See also Section 1.2.1, page 2, for more details.
- **SIMS**: Soft Intermediate State (used in the context of BHC source states – See Section 1.4, page 12, and Section 8.2, page 141, for more details).
- $t_{thermal}$: Thermal timescale is defined as $t_{thermal} = c_pT/\epsilon$ where c_p, T and ϵ are the heat capacity at constant pressure , the temperature and the nuclear energy generation rate, respectively
- t_{accr}: Accretion timescale is defined as $t_{accr} = y/\dot{m}$ where y and $\dot{m}$ are the column density of the burning layer and local accretion rate, respectively.
- **UB**: Upper banana (used in the context of neutron star Atoll sources' states – See Figure 1.8 on page 13).

- **VLFN**: Very-low frequency noise.
- y_f: column depth of the fuel layer (in the context of burning of material on the neutron star surface).

Bibliography

Abramowicz M.A., Karas V., Kluzniak W., Lee W.H., Rebusco P., 2003, PASJ, 55, 467
Alpar M.A., Cheng A.F., Ruderman M.A., Shaham J., 1982, Nature, 300, 728
Altamirano D., van der Klis M., Méndez M., et al., 2005, ApJ, 633, 358
Altamirano D., van der Klis M., Méndez M., et al., 2006, Submitted to ApJ
Altamirano D., Casella P., Patruno A., Wijnands R., van der Klis M., Feb. 2008a, ApJ, 674, L45
Altamirano D., van der Klis M., Wijnands R., Cumming A., Jan. 2008b, ApJ, 673, L35
Aref'ev V.A., Revnivtsev M.G., Lutovinov A.A., Sunyaev R.A., 2004, Astronomy Letters, 30, 669
Backer D.C., Kulkarni S.R., Heiles C., Davis M.M., Goss W.M., 1982, Nature, 300, 615
Bailyn C., 2002, IAU Circ., 7792, 2
Bardeen J.M., Petterson J.A., 1975, ApJ, 195, L65+
Barret D., Grindlay J.E., Harrus I.M., Olive J.F., 1999, A&A, 341, 789
Barret D., Olive J.F., Boirin L., et al., 2000a, ApJ, 533, 329
Barret D., Olive J.F., Boirin L., et al., 2000b, Advances in Space Research, 25, 383
Barret D., Kluźniak W., Olive J.F., Paltani S., Skinner G.K., 2005a, MNRAS, 357, 1288
Barret D., Olive J.F., Miller M.C., 2005b, MNRAS, 361, 855
Barret D., Olive J.F., Miller M.C., 2005c, Astronomische Nachrichten, 326, 808
Belloni T., 2007, ArXiv e-prints, 705
Belloni T., Colombo A.P., Homan J., Campana S., van der Klis M., 2002a, A&A, 390, 199
Belloni T., Psaltis D., van der Klis M., 2002b, ApJ, 572, 392
Belloni T., Homan J., Casella P., et al., 2005, A&A, 440, 207
Belloni T., Parolin I., Del Santo M., et al., 2006, MNRAS, 367, 1113
Berger M., van der Klis M., van Paradijs J., et al., 1996, ApJ, 469, L13+

Bhattacharya D., 2002, Journal of Astrophysics and Astronomy, 23, 67

Bhattacharya D., van den Heuvel E.P.J., 1991, Phys. Rep., 203, 1

Bildsten L., 1998, In: Buccheri R., van Paradijs J., Alpar A. (eds.) NATO ASIC Proc. 515: The Many Faces of Neutron Stars., 419–+

Bildsten L., Chakrabarty D., 2001, ApJ, 557, 292

Bloser P.F., Grindlay J.E., Kaaret P., et al., 2000, ApJ, 542, 1000

Bradt H.V., Rothschild R.E., Swank J.H., Jan. 1993, A&AS, 97, 355

Brainerd J., Lamb F.K., Jun. 1987, ApJ, 317, L33

Brian P. Flannery P. Saul A. Teukolsky, Vetterling W.T., 1989, Numerical Recipes (Fortran Version), Cambridge University Press

Bursa M., Abramowicz M.A., Karas V., Kluźniak W., 2004, ApJ, 617, L45

Campana S., Stella L., Mereghetti S., et al., May 1998, ApJ, 499, L65+

Campbell-Wilson D., McIntyre V., Hunstead R., et al., 1998, IAU Circ., 7010, 3

Casella P., Belloni T., Homan J., Stella L., 2004, A&A, 426, 587

Casella P., Belloni T., Stella L., 2005, ApJ, 629, 403

Casella P., Altamirano D., Patruno A., Wijnands R., van der Klis M., Feb. 2008, ApJ, 674, L41

Chakrabarty D., Morgan E.H., Wijnands R., et al., Mar. 2003, In: Bulletin of the American Astronomical Society, vol. 35 of Bulletin of the American Astronomical Society, 657–+

Chevalier C., Ilovaisky S.A., 1991, A&A, 251, L11

Colgate S.A., Petschek A.G., Sep. 1981, ApJ, 248, 771

Cook G.B., Shapiro S.L., Teukolsky S.A., 1994, ApJ, 424, 823

Corbel S., Kaaret P., Jain R.K., et al., 2001, ApJ, 554, 43

Corbel S., Fender R.P., Tzioumis A.K., et al., 2002, Science, 298, 196

Corbel S., Fender R.P., Tomsick J.A., Tzioumis A.K., Tingay S., 2004, ApJ, 617, 1272

Cui W., Zhang S.N., Chen W., 1998, ApJ, 492, L53+

Cui W., Zhang S.N., Chen W., Morgan E.H., 1999, ApJ, 512, L43

Cui W., Zhang S.N., Chen W., 2000, ApJ, 531, L45

Cumming A., Zweibel E., Bildsten L., 2001, ApJ, 557, 958

Di Salvo T., Burderi L., Jan. 2003, A&A, 397, 723

Di Salvo T., Méndez M., van der Klis M., Ford E., Robba N.R., 2001, ApJ, 546, 1107

Di Salvo T., Méndez M., van der Klis M., 2003, A&A, 406, 177

Dib R., Ransom S.M., Ray P.S., Kaspi V.M., Archibald A.M., Jun. 2005, ApJ, 626, 333

Dubath P., Revnivtsev M., Goldoni P., et al., 2003, IAU Circ., 8100, 1

Eggleton P.P., 1983, ApJ, 268, 368

Emelyanov A.N., Revnivtsev M.G., Aref'ev V.A., Sunyaev R.A., 2002, Astronomy Letters, 28, 12

Falanga M., Titarchuk L., Jun. 2007, ApJ, 661, 1084

Fender R., Belloni T., 2004, ARA&A, 42, 317

Fiocchi M., Bazzano A., Ubertini P., federici M., 2006, ArXiv Astrophysics, astro-ph/0610320

Ford E.C., van der Klis M., Méndez M., et al., 2000, ApJ, 537, 368

Fragile P.C., Mathews G.J., Wilson J.R., 2001, ApJ, 553, 955

Galloway D.K., Jun. 2006, In: Braga J., D'Amico F., Rothschild R.E. (eds.) The Transient Milky Way: A Perspective for MIRAX, vol. 840 of American Institute of Physics Conference Series, 50–54

Galloway D.K., Muno M.P., Hartman J.M., et al., 2006, ArXiv Astrophysics, astro-ph/0608259

Galloway D.K., Morgan E.H., Krauss M.I., Kaaret P., Chakrabarty D., 2007, ApJ, 654, L73

Gavriil F.P., Strohmayer T.E., Swank J.H., Markwardt C.B., 2006, In: Bulletin of the American Astronomical Society, vol. 38 of Bulletin of the American Astronomical Society, 336–+

Gavriil F.P., Strohmayer T.E., Swank J.H., Markwardt C.B., 2007, ApJ, 669, L29

Geldzahler B.J., 1983, ApJ, 264, L49

Giacconi R., Murray S., Gursky H., et al., 1974, ApJS, 27, 37

Gierliński M., Done C., 2002, MNRAS, 337, 1373

Gierliński M., Done C., 2003, MNRAS, 342, 1083

Giles A.B., Hill K.M., Strohmayer T.E., Cummings N., 2002, ApJ, 568, 279

Girardi L., Bressan A., Bertelli G., Chiosi C., 2000, A&AS, 141, 371

Göğüş E., Alpar M.A., Gilfanov M., 2007, ApJ, 659, 580

Grindlay J., Gursky H., Schnopper H., et al., 1976, ApJ, 205, L127

Grindlay J.E., Marshall H.L., Hertz P., et al., 1980, ApJ, 240, L121

Gruber D.E., Blanco P.R., Heindl W.A., et al., 1996, A&AS, 120, C641+

Hannikainen D., Campbell-Wilson D., Hunstead R., et al., 2001a, Astrophysics and Space Science Supplement, 276, 45

Hannikainen D., Wu K., Campbell-Wilson D., et al., 2001b, In: Gimenez A., Reglero V., Winkler C. (eds.) Exploring the Gamma-Ray Universe, vol. 459 of ESA Special Publication, 291–294

Hasinger G., van der Klis M., 1989, A&A, 225, 79

Hatchett S.P., Begelman M.C., Sarazin C.L., 1981, ApJ, 247, 677

Heger A., Cumming A., Woosley S.E., 2007, ApJ, 665, 1311

Hessels J.W.T., Ransom S.M., Stairs I.H., et al., Mar. 2006, Science, 311, 1901

Hoffman J.A., Lewin W.H.G., Doty J., 1977, ApJ, 217, L23

Homan J., Belloni T., 2005, Ap&SS, 300, 107
Homan J., van der Klis M., 2000, ApJ, 539, 847
Homan J., Wijnands R., van der Klis M., et al., 2001, ApJS, 132, 377
Homan J., van der Klis M., Jonker P.G., et al., 2002, ApJ, 568, 878
Homan J., Miller J.M., Wijnands R., et al., 2005, ApJ, 623, 383
Homan J., van der Klis M., Wijnands R., et al., Feb. 2007, ApJ, 656, 420
Illarionov A.F., Sunyaev R.A., Feb. 1975, A&A, 39, 185
in 't Zand J.J.M., Verbunt F., Strohmayer T.E., et al., 1999, A&A, 345, 100
in't Zand J.J.M., van Kerkwijk M.H., Pooley D., et al., 2001, ApJ, 563, L41
in't Zand J.J.M., Jonker P.G., Markwardt C.B., 2007, A&A, 465, 953
Ivanov P.B., Illarionov A.F., 1997, MNRAS, 285, 394
Jahoda K., Markwardt C., Radeva Y., et al., 1996, Proc. SPIE, 2808, 59
Jahoda K., Markwardt C.B., Radeva Y., et al., 2006, ApJS, 163, 401
Jain R., Bailyn C., Tomsick J., 2001a, IAU Circ., 7575, 3
Jain R.K., Bailyn C.D., Orosz J.A., McClintock J.E., Remillard R.A., 2001b, ApJ, 554, L181
Jain R.K., Bailyn C.D., Orosz J.A., et al., 2001c, ApJ, 546, 1086
Jonker P.G., Nelemans G., Oct. 2004, MNRAS, 354, 355
Jonker P.G., Méndez M., van der Klis M., 2000a, ApJ, 540, L29
Jonker P.G., van der Klis M., Homan J., et al., 2000b, ApJ, 531, 453
Jonker P.G., van der Klis M., Homan J., et al., 2001, ApJ, 553, 335
Jonker P.G., Méndez M., van der Klis M., 2002a, MNRAS, 336, L1
Jonker P.G., van der Klis M., Homan J., et al., 2002b, MNRAS, 333, 665
Jonker P.G., Méndez M., van der Klis M., Jul. 2005, MNRAS, 360, 921
Jonker P.G., in't Zand J.J.M., Méndez M., van der Klis M., 2007, MNRAS, 378, 1187
Kaaret P., Piraino S., Bloser P.F., et al., 1999, ApJ, 520, L37
Kaaret P., Corbel S., Tomsick J.A., et al., Jan. 2003a, ApJ, 582, 945
Kaaret P., i. Zand J.J.M., Heise J., Tomsick J.A., 2003b, ApJ, 598, 481
Kaaret P., Morgan E.H., Vanderspek R., Tomsick J.A., 2006, ApJ, 638, 963
Kalemci E., Tomsick J.A., Rothschild R.E., Pottschmidt K., Kaaret P., 2001, ApJ, 563, 239
King A., Sep. 2006, ArXiv Astrophysics, astro-ph/0609811
Kirsch M.G.F., Mukerjee K., Breitfellner M.G., et al., 2004, A&A, 423, L9
Kitamoto S., Tsunemi H., Miyamoto S., Roussel-Dupre D., 1993, ApJ, 403, 315
Klein-Wolt M., 2004, PhD.Thesis
Klein-Wolt M., van der Klis M., Mar. 2008, ApJ, 675, 1407
Kluźniak W., Abramowicz M.A., 2001, ArXiv Astrophysics, astro-ph/0105057
Kluźniak W., Abramowicz M.A., 2005, Ap&SS, 300, 143

Kubota A., Done C., Sep. 2004, MNRAS, 353, 980
Kubota A., Makishima K., 2004, ApJ, 601, 428
Kuulkers E., van der Klis M., Oosterbroek T., et al., 1994, A&A, 289, 795
Kuulkers E., van der Klis M., Oosterbroek T., van Paradijs J., Lewin W.H.G., 1997, MNRAS, 287, 495
Kuulkers E., den Hartog P.R., in't Zand J.J.M., et al., 2003a, A&A, 399, 663
Kuulkers E., Remillard R., Miller J.M., 2003b, The Astronomer's Telegram, 134, 1
Kuznetsov S.I., 2002, Astronomy Letters, 28, 73
Kylafis N.D., Klimis G.S., Dec. 1987, ApJ, 323, 678
Leahy D.A., Darbro W., Elsner R.F., et al., 1983, ApJ, 266, 160
Levine A.M., Bradt H., Cui W., et al., 1996, ApJ, 469, L33+
Linares M., van der Klis M., Altamirano D., Markwardt C.B., Dec. 2005, ApJ, 634, 1250
Linares M., van der Klis M., Wijnands R., May 2007, ApJ, 660, 595
Liu Q.Z., van Paradijs J., van den Heuvel E.P.J., Jul. 2007, A&A, 469, 807
Lomb N.R., 1976, Ap&SS, 39, 447
Méndez M., 2002, In: The Ninth Marcel Grossmann Meeting, 2319–2320
Méndez M., van der Klis M., 1999, ApJ, 517, L51
Méndez M., van der Klis M., Ford E.C., 2001, ApJ, 561, 1016
Markert T.H., Backman D.E., Canizares C.R., Clark G.W., Levine A.M., 1975, Nature, 257, 32
Markwardt C.B., Swank J., 2004, The Astronomer's Telegram, 237, 1
Markwardt C.B., Swank J.H., 2005, The Astronomer's Telegram, 495, 1
Markwardt C.B., Swank J.H., Strohmayer T.E., i. Zand J.J.M., Marshall F.E., 2002, ApJ, 575, L21
Markwardt C.B., Smith E., Swank J.H., 2003, IAU Circ., 8080
Marti J., Mirabel I.F., Rodriguez L.F., Chaty S., 1998, A&A, 332, L45
Masetti N., Soria R., 2000, IAU Circ., 7399, 2
Mauche C.W., 2002, ApJ, 580, 423
McClintock J.E., Remillard R.A., 2003, ArXiv Astrophysics, astro-ph/0306213
Méndez M., 2000, Proc 19th Texas Symposium on Relativistic Astrophysics and Cosmology, ed. J. Paul, T. Montmerle, & E. Aubourg (Amsterdam: Elsevier), 15/16
Méndez M., van der Klis M., van Paradijs J., et al., 1997, ApJ, 485, L37+
Méndez M., van der Klis M., van Paradijs J., et al., 1998a, ApJ, 494, L65+
Méndez M., van der Klis M., Wijnands R., et al., 1998b, ApJ, 505, L23+
Meszaros P., Riffert H., Berthiaume G., Feb. 1988, ApJ, 325, 204
Migliari S., Fender R.P., 2006, MNRAS, 366, 79
Migliari S., Fender R.P., Rupen M., et al., 2004, MNRAS, 351, 186

Migliari S., Fender R.P., van der Klis M., 2005, MNRAS, 363, 112
Miller J.M., Homan J., 2003, The Astronomer's Telegram, 135, 1
Miller J.M., Wijnands R., Homan J., et al., 2001, ApJ, 563, 928
Miller M.C., 1999, ApJ, 515, L77
Miller M.C., Lamb F.K., Psaltis D., 1998, ApJ, 508, 791
Mitsuda K., Inoue H., Koyama K., et al., 1984, PASJ, 36, 741
Miyamoto S., Kimura K., Kitamoto S., Dotani T., Ebisawa K., 1991, ApJ, 383, 784
Miyamoto S., Iga S., Kitamoto S., Kamado Y., 1993, ApJ, 403, L39
Miyamoto S., Kitamoto S., Iga S., Hayashida K., Terada K., 1994, ApJ, 435, 398
Morgan E.H., Remillard R.A., Greiner J., 1997, ApJ, 482, 993
Morrison R., McCammon D., 1983, ApJ, 270, 119
Narayan R., Cooper R.L., Aug. 2007, ApJ, 665, 628
Nelemans G., Jonker P.G., Marsh T.R., van der Klis M., 2004, MNRAS, 348, L7
Nelson R.P., Papaloizou J.C.B., 2000, MNRAS, 315, 570
Nowak M.A., 2000, MNRAS, 318, 361
Olive J.F., Barret D., Boirin L., et al., 1998, A&A, 333, 942
Orosz J., Bailyn C., Jain R., 1998, IAU Circ., 7009, 1
Orosz J.A., Bailyn C.D., 1997, ApJ, 477, 876
Orosz J.A., Groot P.J., van der Klis M., et al., 2002, ApJ, 568, 845
Ortolani S., Barbuy B., Bica E., 1994, A&AS, 108, 653
Ortolani S., Bica E., Barbuy B., 1997, A&A, 326, 614
Osaki Y., 1985, A&A, 144, 369
Paczynski B., 1983, ApJ, 264, 282
Papitto A., Menna M.T., Burderi L., et al., 2005, ApJ, 621, L113
Piro A.L., Bildsten L., Mar. 2004, ApJ, 603, 252
Piro A.L., Bildsten L., Feb. 2006, ApJ, 638, 968
Pooley D., Lewin W.H.G., Verbunt F., et al., 2002, ApJ, 573, 184
Pottschmidt K., Wilms J., Nowak M.A., et al., 2003, A&A, 407, 1039
Press et al., 1992, Numerical Recipes: The Art of Scientific Computing, Cambridge University Press, Cambridge (UK) and New York, 2nd edn.
Priedhorsky W., Terrell J., 1984a, ApJ, 284, L17
Priedhorsky W.C., Terrell J., 1984b, ApJ, 280, 661
Prins S., van der Klis M., 1997, A&A, 319, 498
Psaltis D., Chakrabarty D., 1999, ApJ, 521, 332
Psaltis D., Belloni T., van der Klis M., 1999, ApJ, 520, 262
Rappaport S., Ma C.P., Joss P.C., Nelson L.A., 1987, ApJ, 322, 842
Reerink T.J., Schnerr R.S., van der Klis M., van Straaten S., 2005, A&A

submitted
Reig P., Méndez M., van der Klis M., Ford E.C., Feb. 2000, ApJ, 530, 916
Reig P., van Straaten S., van der Klis M., 2004, ApJ, 602, 918
Remillard R., Morgan E., McClintock J., Sobczak G., 1998, IAU Circ., 7019, 1
Remillard R.A., McClintock J.E., 2006, ARA&A, 44, 49
Remillard R.A., McClintock J.E., Sobczak G.J., et al., 1999a, ApJ, 517, L127
Remillard R.A., Morgan E.H., McClintock J.E., Bailyn C.D., Orosz J.A., 1999b, ApJ, 522, 397
Remillard R.A., Sobczak G.J., Muno M.P., McClintock J.E., 2002a, ApJ, 564, 962
Remillard R.A., Swank J., Strohmayer T., 2002b, IAU Circ., 7893
Revnivtsev M., Sunyaev R., 2003, A&A, 399, 699
Revnivtsev M., Churazov E., Gilfanov M., Sunyaev R., 2001, A&A, 372, 138
Revnivtsev M.G., Trudolyubov S.P., Borozdin K.N., 2002, Astronomy Letters, 28, 237
Rodriguez J., Corbel S., Tomsick J.A., 2003, ApJ, 595, 1032
Rodriguez J., Corbel S., Kalemci E., Tomsick J.A., Tagger M., 2004, ApJ, 612, 1018
Rothschild R.E., Blanco P.R., Gruber D.E., et al., Mar. 1998, ApJ, 496, 538
Rots A.H., Jahoda K., Lyne A.G., 2004, ApJ, 605, L129
Salgado M., Bonazzola S., Gourgoulhon E., Haensel P., 1994, A&A, 291, 155
Santos J.J.F.C., Piatti A.E., 2004, A&A, 428, 79
Scargle J.D., 1982, ApJ, 263, 835
Schnerr R.S., Reerink T., van der Klis M., et al., 2003, A&A, 406, 221
Schulz N.S., 1999, ApJ, 511, 304
Shahbaz T., van der Hooft F., Casares J., Charles P.A., van Paradijs J., 1999, MNRAS, 306, 89
Shakura N.I., Sunyaev R.A., 1976, MNRAS, 175, 613
Shih I.C., Bird A.J., Charles P.A., Cornelisse R., Tiramani D., 2005, MNRAS, 361, 602
Simon V., 2003, A&A, 405, 199
Smale A.P., Zhang W., White N.E., 1997, ApJ, 483, L119+
Smith D.A., 1998, IAU Circ., 7008, 1
Smith D.A., Levine A.M., Remillard R., et al., 2000, IAU Circ., 7399, 1
Sobczak G.J., McClintock J.E., Remillard R.A., et al., 1999, ApJ, 517, L121
Sobczak G.J., McClintock J.E., Remillard R.A., et al., 2000, ApJ, 531, 537
Stella L., White N.E., Rosner R., Sep. 1986, ApJ, 308, 669
Stella L., Priedhorsky W., White N.E., 1987, ApJ, 312, L17
Stellingwerf R.F., 1978, ApJ, 224, 953

Strohmayer T., Bildsten L., 2003, astro-ph/0301544
Strohmayer T., Bildsten L., Apr. 2006, Compact stellar X-ray sources, 113–156
Strohmayer T.E., 2001a, Advances in Space Research, 28, 511
Strohmayer T.E., 2001b, ApJ, 552, L49
Strohmayer T.E., Brown E.F., 2002, ApJ, 566, 1045
Strohmayer T.E., Markwardt C.B., 2002, ApJ, 577, 337
Swank J., Markwardt K., 2001, in ASP Conf. Ser. 251, New Century of X-ray Astronomy, eds. H. Inoue & H. Kunieda (San Francisco: ASP), 94
Swank J., Smith E., Markwardt C., 2002, IAU Circ., 7792, 1
Swank J.H., Becker R.H., Boldt E.A., et al., 1977, ApJ, 212, L73
Syunyaev R.A., 1973, Soviet Astronomy, 16, 941
Tanaka Y., Lewin W.H.G., 1995, In: X-ray binaries, p. 126 - 174, 126–174
Tananbaum H., Gursky H., Kellogg E., Giacconi R., Jones C., 1972, ApJ, 177, L5+
Titarchuk L., Cui W., Wood K., 2002, ApJ, 576, L49
Titarchuk L., Kuznetsov S., Shaposhnikov N., Sep. 2007, ApJ, 667, 404
Tomsick J.A., Corbel S., Kaaret P., 2001a, ApJ, 563, 229
Tomsick J.A., Smith E., Swank J., Wijnands R., Homan J., 2001b, IAU Circ., 7575, 2
Tomsick J.A., Corbel S., Fender R., et al., 2003, ApJ, 582, 933
Tout C.A., Pols O.R., Eggleton P.P., Han Z., 1996, MNRAS, 281, 257
van der Klis M., 1989, In: Ögelman H., van den Heuvel E.P.J. (eds.) Timing Neutron Stars, 27–+
van der Klis M., 1995a, Proceedings of the NATO Advanced Study Institute on the Lives of the Neutron Stars, held in Kemer, Turkey, August 19-September 12, 1993. Editor(s), M. A. Alpar, U. Kiziloglu, J. van Paradijs; Publisher, Kluwer Academic, Dordrecht, The Netherlands, Boston, Massachusetts, 301
van der Klis M., 1995b, In: X-ray binaries, p. 252 - 307, 252–307
van der Klis M., 2000, ARA&A, 38, 717
van der Klis M., 2001, ApJ, 561, 943
van der Klis M., 2004, in "Compact Stellar X-ray Sources", eds. W.H.G. Lewin and M. van der Klis, in press.
van der Klis M., 2006, in Compact Stellar X-Ray Sources, ed. W. H. G. Lewin & M. van der Klis (Cambridge: Cambridge Univ. Press), in press
van der Klis M., Jansen F., van Paradijs J., et al., 1985, Nature, 316, 225
van der Klis M., Wijnands R.A.D., Horne K., Chen W., 1997, ApJ, L97+
van Paradijs J., van der Klis M., van Amerongen S., et al., 1990, A&A, 234, 181
van Straaten S., Ford E.C., van der Klis M., Méndez M., Kaaret P., 2000, ApJ, 540, 1049

van Straaten S., van der Klis M., di Salvo T., Belloni T., 2002, ApJ, 568, 912
van Straaten S., van der Klis M., Méndez M., 2003, ApJ, 596, 1155
van Straaten S., van der Klis M., Wijnands R., 2005, ApJ, 619, 455
van Zyl L., Charles P.A., Arribas S., et al., 2004, MNRAS, 350, 649
Verbunt F., van Kerkwijk M.H., in't Zand J.J.M., Heise J., 2000, A&A, 359, 960
Wachter S., Hoard D.W., Bailyn C.D., Corbel S., Kaaret P., 2002, ApJ, 568, 901
Warner B., Woudt P.A., 2002, MNRAS, 335, 84
Welsh W.F., Robinson E.L., Young P., 2000, AJ, 120, 943
Wen L., Levine A.M., Corbet R.H.D., Bradt H.V., 2006, ApJS, 163, 372
Whelan J., Iben I.J., Dec. 1973, ApJ, 186, 1007
White N.E., Marshall F.E., 1984, ApJ, 281, 354
White N.E., Peacock A., Hasinger G., et al., 1986, MNRAS, 218, 129
Wijnands R., 2005, ArXiv Astrophysics, astro-ph/0501264
Wijnands R., van der Klis M., 1998a, Nature, 394, 344
Wijnands R., van der Klis M., Nov. 1998b, ApJ, 507, L63
Wijnands R., van der Klis M., 1999, ApJ, 514, 939
Wijnands R., Homan J., van der Klis M., 1999, ApJ, 526, L33
Wijnands R., Guainazzi M., van der Klis M., Méndez M., 2002a, ApJ, 573, L45
Wijnands R., Heinke C.O., Grindlay J.E., 2002b, ApJ, 572, 1002
Wijnands R., van der Klis M., Homan J., et al., 2003, Nature, 424, 44
Wijnands R.A.D., van der Klis M., 1997, ApJ, 482, L65+
Wijnands R.A.D., van der Klis M., van Paradijs J., et al., 1997, ApJ, 479, L141+
Willmore A.P., Mason K.O., Sanford P.W., et al., 1974, MNRAS, 169, 7
Woudt P., Charles P., Shih I.C., 2003, IAU Circ., 8102, 2
Yoshida K., Mitsuda K., Ebisawa K., et al., 1993, PASJ, 45, 605
Yu W., van der Klis M., 2002, ApJ, 567, L67
Zhang S.N., Yu W., Zhang W., Feb. 1998a, ApJ, 494, L71+
Zhang W., Giles A.B., Jahoda K., et al., 1993, In: Proc. SPIE Vol. 2006, p. 324-333, EUV, X-Ray, and Gamma-Ray Instrumentation for Astronomy IV, Oswald H. Siegmund; Ed., 324–333
Zhang W., Jahoda K., Swank J.H., Morgan E.H., Giles A.B., 1995, ApJ, 449, 930
Zhang W., Lapidus I., Swank J.H., White N.E., Titarchuk L., 1997, IAU Circ., 6541, 1
Zhang W., Jahoda K., Kelley R.L., et al., Mar. 1998b, ApJ, 495, L9+
Zhang W., Smale A.P., Strohmayer T.E., Swank J.H., 1998c, ApJ, 500, L171+

Życki P.T., Done C., Smith D.A., 2001, MNRAS, 326, 1367

Publication list

Refereed journal papers
(accepted and submitted)

- **Altamirano, D.**; Casella, P.; Patruno, A.; Wijnands, R.; van der Klis, M., 2008, ApJL, Volume 674, pp. 45
  'Intermittent Millisecond X-Ray Pulsations from the Neutron Star X-Ray Transient SAX J1748.9-2021 in the Globular Cluster NGC 6440'

- Casella, P.; **Altamirano, D.**; Patruno, A.; Wijnands, R.; van der Klis, M., 2008, ApJL, Volume 674, pp. 41
  'Discovery of Coherent Millisecond X-Ray Pulsations in Aquila X-1'

- **Altamirano, D.**; van der Klis, M.; Wijnands, R.; Cumming, A., 2008, ApJL, Volume 673, pp. 35
  'Millihertz Oscillation Frequency Drift Predicts the Occurrence of Type I X-Ray Bursts'

- Patruno, A.; **Altamirano, D.**; Hessels, J. W. T.; Casella, P.; Wijnands, R.; van der Klis, M., 2008, Submitted to ApJ
  'Phase-coherent timing of the accreting millisecond pulsar SAX J1748.9-2021'

- **Altamirano, D.**; van der Klis, M. ; Méndez, M. ; Wijnands, R. ; Markwardt, C.; Swank, J., 2007, Submitted to ApJ
  'Discovery of kilohertz quasi-periodic oscillations and state transitions in the low-mass X-ray binary 1E 1724–3045 (Terzan 2)'

- Boutloukos, S.; van der Klis, M.; **Altamirano, D.**; Klein-Wolt, M.; Wijnands, R.; Jonker, P. G.; Fender, R. P., 2006, ApJ, Volume 653, pp. 1435
  'Discovery of Twin kHz QPOs in the Peculiar X-Ray Binary Circinus X-1'

- **Altamirano, D.**; van der Klis, M.; Méndez, M.; Jonker, P.G.; Klein-Wolt, M.; Lewin, W.H.G., 2006, Submitted to ApJ
'X-ray time variability across the atoll source states of 4U 1636–53'

- Linares, M.; van der Klis, M.; **Altamirano, D.**; Markwardt, C. B., 2005, ApJ, Volume 634, pp. 1250
'Discovery of Kilohertz Quasi-periodic Oscillations and Shifted Frequency Correlations in the Accreting Millisecond Pulsar XTE J1807-294'

- **Altamirano, D.**; van der Klis, M.; Méndez, M.; Migliari, S.; Jonker, P. G.; Tiengo, A.; Zhang, W., 2005, ApJ, Volume 633, pp. 358
'The Island State of the Atoll Source 4U 1820-30'

Other publications

- Soleri, P; **Altamirano, D.**; Fender, R; Casella, P; Tudose, V.; Maitra, D; Wijnands, R. ; Belloni, R; Miller-Jones, J; Klein-Wolt, M.; van der Klis, M., 2008, proceedings of "A Population Explosion: The Nature and Evolution of X-ray Binaries in Diverse Environments"
'Multiwavelength observations of the black hole candidate Swift J1753.5-0127'

- **Altamirano, D.**; Wijnands, R.; Degenaar, N.; Casella, P.; Homan, J.; Belloni, T.; Campana, S., 2007, Astronomer Telegram 1178
'Following the neutron star transient XTE J1701-462 as it turns into quiescence'

- Homan, J.; Wijnands, R.; **Altamirano, D.**; Belloni, T., 2007, Astronomer Telegram 1165
'Rapid decay of the neutron star transient XTE J1701-462'

- Boutloukos, S.; van der Klis, M.; **Altamirano, D.**; Klein-Wolt, M.; Wijnands, R., 2007, proceedings of the 11th Marcel Grossman meeting
'kHz QPO pairs expose the neutron star of Circinus X-1'

- Kuulkers, E.; in't Zand, J.; Homan, J.; van Straaten, S.; **Altamirano, D.**; van der Klis, M., 2004, X-ray Timing 2003: Rossi and Beyond. AIP Conference Proceedings, Vol. 714, held 3-5 November, 2003 in Cambridge, MA.
'X-ray spectral and timing properties of the 2001 superburst of 4U 1636-536'

Accepted observing proposals

(Only listed those where I am the Principal Investigator)

- **Altamirano, D.**; Cackett, E.; Wijnands, R.; van der Klis, M.
'Observations during the rare dips observed on the X-ray binary SLX 1735-269', **Chandra observatory**, 2007.

- **Altamirano, D.**; Wijnands, R.; Degenaar, N.; Hessels, J.; Markwardt, C.; van der Klis, M.
'First Chandra observation of the ultra-compact X-ray binary 4U 1850-087 during its high luminosity state', **Chandra observatory**, 2007.

- **Altamirano, D.**; Homan, J. ; Wijnands, R.; van der Klis, M.
'RXTE observations of the next outburst of a bright neutron star transient', **RXTE**, 2007.

- **Altamirano, D.**; Wijnands, R.; van der Klis, M.; Méndez, M.; Cumming, A.
'RXTE/XMM-NEWTON simultaneous observations of 4U 1608-52 OR AQL X-1', **RXTE**, 2007.

- **Altamirano, D.**; Wijnands, R.; van der Klis, M.
'Observations of three persistent, but not well-studied neutron star LMXBS', **RXTE**, 2007.

- **Altamirano, D.**, Wijnands, R.; Degenaar, N.; Casella, P.; Homan, J.; Belloni, T.; Campana, S.
'Observing Campaign for the bright transient neutron star XTE J1701-462', **Swift Observatory** (ToO proposal), 2007.

- **Altamirano, D.**, Wijnands, R.; Soleri, P.; Casella, P.; van der Klis, M.; Tudose, V.
'Multiwavelenght quasi-simultaneous observations of the black hole candidate Swift J1753.5-0127', **Swift Observatory** (ToO proposal), 2007.

- **Altamirano, D.**, Migliari, S.; Wijnands, R.; van der Klis, M., Casella, P.
  'Simultaneous RXTE/Radio GO Observations of the neutron star low mass X-ray binary 4U 1820-30', **RXTE**, 2006.

- **Altamirano, D.**, Wijnands, R.; van der Klis, M.; Méndez, ; Cumming, A.
  'First high resolution spectral studies from marginally stable nuclear burning', XMM-Newton, 2005.

To all of you, and nobody else

The future belongs to those who believe in the beauty of their dreams.

Eleanor Roosevelt

Coming to Amsterdam to do and finish my PhD was a dream that came true. But it did not just happen because all planets aligned in a magical way (or may be yes?), it was the combination of many things that happened one after the other one; it was the effort of many people which I inevitably thank with all my soul.

En Argentina tengo que agradecer particularmente a Diego (Dbagu), Nico (Duronga), Pete (y no Pitt), Vero, Ramirex, Anahi, Ceci, Pato (fisico.. no podia ser perfecto), Tibu y a Mariana. Todos estuvieron conmigo durante mis estudios universtarios, y siguien estando junto a mi, lejos pero cerca. Otros, como Marito (ahora brazuca!), Negro Terri, El Conde, Negro Seba (y toda la banda del club, cuya lista me llevaria medio libro), Natalia R. (de vuelta en argentina?), Pancho V. (ahora en Svalbard?), Caro C., Giselle, Magali, los Botino, la Tia Miriam, Elena, Gustavo y tantos otros, que no estuvieron muy relacionados con el estudio, pero que ayudaron en muchas formas a que mi sueño se haga realidad. Los quiero mucho! Un agradecimiento particular pa el Chino de los hornos! nunca me olvidaria de vos! desde antes y durante estos años, quien mas para sacarme una sonrisa con tus mails!.

And of course, when in Argentina many other people collaborated for this dream. Specials thanks to Virpi Niemela for helping me with my master project, M. Corcoran for being the first "international astronomer" I met who, in some way, made me see that there was a lot out there!!. Also a big thanks to the COSPAR people, particularly to Peter Wiltmore for organizing the X-ray meeting in Brazil. If I hadn't gone to that school, I doubt I would have done X-ray astronomy at all!. Particularly in that meeting, Randall, Mariano and Carlos made a big impression on me (many reasons, could not go through all of them now...). Special thanks to Mariano, who afterwards accepted to be

my Master Co-promotor (que coraje!), who was the person who smoothed my way to Europe and who is today a great collaborator (and who seemed not to have enough with me, that now he hired my girlfriend as a his PhD!).

These four years have been amazing for me, from both the scientific and the non-scientific point of view. Someone once said that those who have problems at work cannot enjoy their free time, and that those who have problems enjoying there free time, cannot enjoy their work life. I cannot agree more with whoever said that. For this reason I have to (and I must) thank Juan(ote, mi poeta), Nacho (y a toda su flia que me a integrado a su mundo! Cuando nos vamos al Borda?), Annemarieke, Miriam, Jordi, Salvo, Beike, Manu, Santiago (poker o futbol?), Pg, pazzo Patruno (idolo!), Paolo, Paola, Nanda, Truike (and all the salsa gang), Maryem (cuando hablamos?), Elena (Bella!), Simone (I miss you man! where r u?), Ruben, Raul (climbing freak!), Viney, Nacho G., Daniele (Daniele, Daniele – quien mas si no DDD?), Timi, Leonid, Maria, Jorge, Juan (cuando hacemos otra vaca?), Laura (vas a ser mama!!), Javier (en alta mar?) and so many others for the dinners, parties, meetings, drinks, etc etc etc etc and 100 times more etc!. I also have to thank the ping pong gang, the Coffee Mafia, the Meerkamp secret society, the XRT sect, the squash brotherhood, the secretary crew and all of the people that is not part of any of these groups (what a pity!!), but still make the Anton Pannekoek institute a great place to work: Minou, Pg, Peter (I love you!), Nathalie, Atakan, Martin, Huib, Jason, Gemma (the office feels so lonely without you...), Marc, Michiel, Alex, Casey, Manux, Eva, Dipankar, Lianne, Ale, Nicole, Nanda, Eduardo, David, Maciek, Paolo, Lide, Valeriu (el Conde), Alexander, Klaas, Rhaana, Arjan, Anna and last but not least, Rudy.

Scientifically speaking, three persons and one group show me the way into the "research world". Mariano, thanks a lot for all your long emails, questions and answers!!!!, Rudy... I have no words!! thanks a lot for the patience, comments, etc, etc.. basically, thanks for everything!!. Michiel, one billion thanks for everything. I learned a lot from you and I hope I can keep learning much (very much) more in the next years. I must say that I was amazed by the amount of time you manage to give to science after you became director of the institute. I really hope that you keep finding more and more time for science in the near future!. And for the group, for the XRT group, I can only say that it has been great to have all those discussions. Hopefully, we will keep having more of those in the future (It is not a question of how well each person works, but how well they all work together).

So, I cannot finish with this crazy list without mentioning the two beauties I have as paranimfen. Miriam, muchas gracias por todo todo y mucho mas... pero sobre todo, muchas gracias por estar a mi lado en este dia. Beike, mi LaLoCa, what can I say? Should I write a book with all the things I wanna say? Ok, I keep it simple: Thank you very very strawberry much for all the amazing time we have spent together and particularly, for being on my side during the defense day. Please, never stop jumping around (and always dance like nobody's watching) and most important, don't forget to "Relax!, take it eeeeasy....". :-)

Finalmente, y que los ultimos sean los primeros, quiero agradecer a mi familia por todo el apoyo que me han dado durante estos años. Tata, Nona (si, aunque no estes, siempre estas conmigo), Má, Pá, Ivan y Eugue, que les puedo decir! no tengo palabras pa decirles todo lo que los quiero y lo que los extraño. Pero aca va, este libro, se los dedico a ustedes, los quiero, los amo, y les agradezco de nuevo por por todo, todo, y por mucho mas!

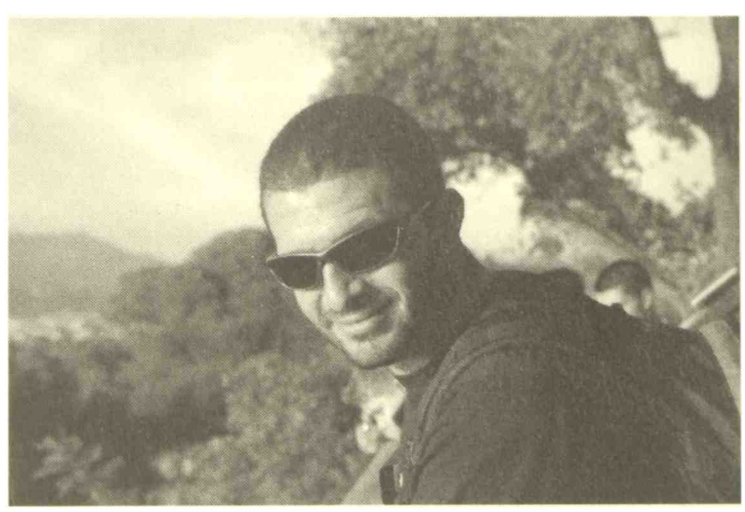

Lots of kisses to all of you, and nobody else.
Diego Altamirano

(si, lo se.. me olvide de la mayoria de los acentos... pero asi soy yo)

Limitations live only in your mind, nowhere else........ so come on! free your imagination! write down your ideas!

If at first the idea is not absurd, then there is no hope for it

Albert Einstein

All exact science is dominated by the idea of approximation

Bertrand Russell

You have to have an idea of what you are going to do, but it should be a vague idea

Pablo Picasso

Every now and then, each and everyone of us has a great idea, one which could change our lives... one that could change the way we see the world... Unfortunately, in most cases if not all, we just stop for a tiny moment, we smile to our thoughts as if we could feel their greatness... to then continue with our lives... as if those ideas had never existed in our minds. What a waste!